Rayonnement thermique à l'échelle nanométrique : Effets de champ proche et d'interférences dans les structures multicouches et sur les performances électriques des cellules thermophotovoltaïques

Etienne Blandre

▶ **To cite this version:**

Etienne Blandre. Rayonnement thermique à l'échelle nanométrique : Effets de champ proche et d'interférences dans les structures multicouches et sur les performances électriques des cellules thermophotovoltaïques. Thermique [physics.class-ph]. Université de Lyon, 2016. Français. NNT : 2016LYSEI103 . tel-01940935

HAL Id: tel-01940935
https://theses.hal.science/tel-01940935

Submitted on 30 Nov 2018

HAL is a multi-disciplinary open access archive for the deposit and dissemination of scientific research documents, whether they are published or not. The documents may come from teaching and research institutions in France or abroad, or from public or private research centers.

L'archive ouverte pluridisciplinaire **HAL**, est destinée au dépôt et à la diffusion de documents scientifiques de niveau recherche, publiés ou non, émanant des établissements d'enseignement et de recherche français ou étrangers, des laboratoires publics ou privés.

N°d'ordre NNT : 2016LYSEI103

THESE de DOCTORAT DE L'UNIVERSITE DE LYON
opérée au sein de
L'INSA de Lyon

Ecole Doctorale 162
Mécanique-Energétique-Génie Civil-Acoustique

Spécialité de doctorat : Thermique et Energétique

Soutenance prévue le 14/10/2016, par :
Etienne Blandre

Thermal radiation at the nanoscale: near-field and interference effects in few-layer structures and on the electrical performances of thermophotovoltaic devices

---

Devant le jury composé de :

Joulain, Karl	Professeur	Université de Poitiers	Rapporteur
Rubi, Miguel	Professeur	Universitat de Barcelona	Rapporteur
Taliercio, Thierry	Professeur	Université Montpellier 2	Examinateur
Paire, Myriam	Ingénieur-chercheur	EDF	Examinatrice
Vaillon, Rodolphe	Directeur de recherche	CNRS	Directeur de thèse
Chapuis, Pierre-Olivier	Chargé de recherche	CNRS	Co-directeur de thèse
Shimizu, Makoto	Assistant professor	Tohoku University	Invité

Cette thèse est accessible à l'adresse : http://theses.insa-lyon.fr/publication/2016LYSEI103/these.pdf
© [E. Blandre], [2016], INSA Lyon, tous droits réservés

Cette thèse est accessible à l'adresse : http://theses.insa-lyon.fr/publication/2016LYSEI103/these.pdf
© [E. Blandre], [2016], INSA Lyon, tous droits réservés

INSA Direction de la Recherche - Liste des Écoles Doctorales

SIGLE	ÉCOLE DOCTORALE	NOM ET COORDONNÉES DU RESPONSABLE
CHIMIE EDA 206	**CHIMIE DE LYON** http://www.edchimie-lyon.fr Sec. : Renée EL MELHEM Bât. Blaise Pascal 3ème étage Tél. : 04 72 43 80 46 Insa : R. GOURDON secretariat@edchimie-lyon.fr	**M. Jean-Marc LANCELIN** Université de Lyon - Collège Doctoral Bât. ESCPE 43 bd du 11 novembre 1918 69622 VILLEURBANNE Cedex Tél. : 04 72 43 13 95 directeur@edchimie-lyon.fr
E.E.A. EDA 160	**ÉLECTRONIQUE, ÉLECTROTECHNIQUE, AUTOMATIQUE** http://edeea.ec-lyon.fr Sec. : M. C. HAVGOUDOUKIAN ecole-doctorale.eea@ec-lyon.fr	**M. Gérard SCORLETTI** École Centrale de Lyon 36, avenue Guy de Collongue 69134 ECULLY Tél. : 04 72 18 60 97 / Fax. : 04 78 43 37 17 gerard.scorletti@ec-lyon.fr
E2M2 EDA 341	**ÉVOLUTION, ÉCOSYSTEME, MICROBIOLOGIE, MODÉLISATION** http://e2m2.universite-lyon.fr Sec. : Bât. Atrium - UCB Lyon I Tél. : 04 72 44 83 62 Insa : S. REVERCHON secretariat.e2m2@univ-lyon1.fr	**M. Fabrice CORDEY** Laboratoire de Géologie de Lyon Université Claude Bernard Lyon I Bât. Géode - Bureau 225 43, bvd du 11 novembre 1918 69622 VILLEURBANNE Cedex Tél. : 04 72 44 83 74 fabrice.cordey@univ-lyon1.fr
EDISS EDA 205	**INTERDISCIPLINAIRE SCIENCES-SANTÉ** http://ediss-lyon.fr Bât. Atrium - UCB Lyon I Tél. : 04 72 44 83 62 infomaths@univ-lyon1.fr	**Mme Emmanuelle CANET-SOULAS** INSERM U1060, CarMeN lab, Univ. Lyon I Bâtiment IMBL 11, avenue Jean Capelle 69621 VILLEURBANNE Cedex Tél. : 04 72 11 90 13 emmanuelle.canet@univ-lyon1.fr
INFOMATHS EDA 512	**INFORMATIQUE ET MATHÉMATIQUES** http://infomaths.univ-lyon1.fr Sec. : Renée EL MELHEM Bât. Blaise Pascal - 3ème étage infomaths@univ-lyon1.fr	**Mme Sylvie CALABRETTO** LIRIS - INSA de Lyon - Bât. Blaise Pascal 7, avenue Jean Capelle 69622 VILLEURBANNE Cedex Tél. : 04 72 43 80 46 / Fax. : 04 72 43 16 87 sylvie.calabretto@insa-lyon.fr
Matériaux EDA 034	**MATÉRIAUX DE LYON** http://ed34.universite-lyon.fr Sec. : M. LABOUNE-DAHMANI Bât. Direction - 1er étage Tél. : 04 72 43 71 70 ed.materiaux@insa-lyon.fr	**M. Jean-Yves BUFFIERE** MATEIS - INSA de Lyon - Bât. Saint Exupéry 7, avenue Jean Capelle 69621 VILLEURBANNE Cedex Tél. : 04 72 43 71 70 / Fax. : 04 72 43 85 28 ed.materiaux@insa-lyon.fr
MEGA EDA 162	**MÉCANIQUE, ÉNERGÉTIQUE, GÉNIE CIVIL, ACOUSTIQUE** http://mega.universite-lyon.fr Sec. : M. LABOUNE-DAHMANI Bât. Direction - 1er étage Tél. : 04 72 43 71 70 mega@insa-lyon.fr	**M. Philippe BOISSE** LAMCOS - INSA de Lyon Bât. Jacquard 25 bis, avenue Jean Capelle 69621 VILLEURBANNE Cedex Tél. : 04 72 43 71 70 / Fax. : 04 72 43 72 37 philippe.boisse@insa-lyon.fr
ScSo EDA 483	**AMÉNAGEMENT, URBANISME, ARCHÉOLOGIE, SCIENCES POLITIQUES, SOCIOLOGIE, ANTHROPOLOGIE** http://recherche.univ-lyon2.fr/scso/ Sec. : Viviane POLSINELLI Brigitte DUBOIS Insa : Jean-Yves TOUSSAINT viviane.polsinelli@univ-lyon2.fr	**Mme Isabelle VON BUELTZINGLOEWEN** Université Lyon II 86, rue Pasteur 69365 LYON Cedex 07 Tél. : 04 78 77 23 86 / Fax. : 04 37 28 04 48 isavonb@dbmail.com

Cette thèse est accessible à l'adresse : http://theses.insa-lyon.fr/publication/2016LYSEI103/these.pdf
© [E. Blandre], [2016], INSA Lyon, tous droits réservés

Cette thèse est accessible à l'adresse : http://theses.insa-lyon.fr/publication/2016LYSEI103/these.pdf
© [E. Blandre], [2016], INSA Lyon, tous droits réservés

Pre-acknowledgments

Je voudrais remercier Dr. Mathieu Francoeur qui m'a fourni la base du code de transfer radiatif en champ proche, ainsi que pour son aide précieuses sur ces simualtions. Je remercie Dr. Makoto Shimizu pour sa proche collaboration sur les structures multicouches, ainsi que Dr. Jean-Philippe Perez, Pr. Thierry Taliercio et Pr. Eric Tournié pour les discussions fructueuses sur les photodetecteurs PIN, ainsi que pour nous avoir fourni les paramètres de ces jonctions et les propriétés physiques de l'InSb.

Cette thèse est accessible à l'adresse : http://theses.insa-lyon.fr/publication/2016LYSEI103/these.pdf
© [E. Blandre], [2016], INSA Lyon, tous droits réservés

Cette thèse est accessible à l'adresse : http://theses.insa-lyon.fr/publication/2016LYSEI103/these.pdf
© [E. Blandre], [2016], INSA Lyon, tous droits réservés

Abstract

This thesis manuscript deals with the study of near-field radiation thermophotovoltaic (TPV) systems. TPV systems convert thermal energy from a hot radiator into electricity in a photovoltaic cell via. The advantage of those systems compared to conventional solar PV systems is that it is possible to control the emission properties of the radiator to increase the performances of the system. One way to control the radiative heat transfer between two bodies is near-field thermal radiation. It is a regime that occurs when two bodies are separated by a distance smaller than the thermal wavelength (10 μm at 300 K). In this case, the radiative heat flux between the two bodies is significantly enhanced, and the spectrum of emission can be tuned using surface polaritons. In the far field, interference effects occurring in multilayer structures also allow controlling the thermal radiation emitted.

The fundamentals of thermal radiation and photovoltaics are first reminded. Results of numerical simulations of the thermal emission of few-layer structures supporting interference phenomena are then presented. These phenomena allow tuning the spectrum of emission, and therefore make possible the optimal design of a selective emitter for TPV applications. The impact of temperature on the spectral and total hemispherical emissivities of the same type of structure is then investigated. The importance of the temperature dependence of the optical properties of the materials constituting the emitters is highlighted. It is demonstrated that the control of interferences using few-layer structures allow increasing the total hemispherical emissivity by a factor 20 compared to a single metallic substrate.

The following chapter focuses on near-field thermal radiation between a semi-infinite emitter and a flat film. This configuration was chosen because it is close to the configuration of a near-field TPV system, where the semi-infinite emitter can be considered as a radiator and the film as a PV cell. The behavior of the resonances between two silicon carbide bodies is studied. Spatial absorption of near-field radiative power inside the film is analyzed. This chapter is concluded by the analysis of interferences that appear in the near-to-far field transition regime.

Results of numerical simulations of TPV systems with near field interactions between the radiator and the PV cell (NFR-TPV) are presented in the last chapter. NFR-TPV systems performances are evaluated by means of a coupled model taking into account their radiative, electric and thermal behavior. A focus is made on the models based on the low-injection approximation generally used to simplify the electrical charge transport problem in the PV cells. The validity of these approximations is assessed in details with a specifically developed physical and numerical model that is able to account for high-injection phenomena. Eventually different cell architectures that optimize the performances of the system are proposed.

Cette thèse est accessible à l'adresse : http://theses.insa-lyon.fr/publication/2016LYSEI103/these.pdf
© [E. Blandre], [2016], INSA Lyon, tous droits réservés

All these results shed new light on thermal radiation of multilayers and their application to thermophotovoltaic conversion.

Keywords: Nanoscale heat transfer, Near-field thermal radiation, Thermophotovoltaic energy conversion, Interferences, Few-layer structures.

Cette thèse est accessible à l'adresse : http://theses.insa-lyon.fr/publication/2016LYSEI103/these.pdf
© [E. Blandre], [2016], INSA Lyon, tous droits réservés

Résumé

Ce manuscrit aborde l'étude de systèmes thermophotovoltaïques (TPV). Un système TPV sert à convertir de l'énergie thermique provenant d'un corps rayonnant en énergie électrique, à l'aide d'une cellule photovoltaïque. Comparé au PV solaire classique, l'avantage de ces systèmes est qu'il est possible de contrôler les propriétés d'émission du radiateur pour augmenter les performances de conversion énergétique du système. Il est également possible de contrôler le transfert radiatif entre deux corps en utilisant le régime de rayonnement en champ proche, qui apparaît lorsque que deux corps sont séparés par une distance inférieure à la longueur d'onde du rayonnement thermique (10 μm à 300 K). Dans cette situation, le flux radiatif entre les deux objets est grandement augmenté, et le spectre d'émission peut être contrôlé en impliquant des polaritons de surface. En champ lointain, les phénomènes d'interférence dans des structures multicouches permettent aussi de contrôler le rayonnement thermique émis.

Les bases du rayonnement thermique et de la conversion photovoltaïque sont tout d'abord rappelées. Les flux rayonnés par des émetteurs multicouches supportant des phénomènes d'interférence sont ensuite calculés numériquement. Les phénomènes d'interférence permettent de contrôler le spectre d'émission et donc l'optimisation d'un émetteur sélectif pour des applications TPV. L'impact de la température sur l'émissivité totale hémisphérique du même type de structure est ensuite analysé. Il s'avère important de prendre en compte l'évolution en température des propriétés optiques des matériaux constituant l'émetteur. Il est ensuite démontré que le contrôle des phénomènes d'interférences au sein des structures multicouches permet d'augmenter les émissivités spectrale et totale hémisphérique de ces structures d'un facteur 20 par rapport à un simple substrat métallique.

La partie suivante du manuscrit est dédiée au rayonnement thermique en champ proche entre un émetteur semi-infini et une couche mince. Cette configuration est proche d'un système TPV, où l'émetteur semi-infini peut être assimilé au corps rayonnant, et le film à une cellule PV. Le comportement des résonances de polaritons de surface est étudié dans le cas du carbure de silicium. L'absorption spatiale de la puissance radiative en champ proche au sein du film est ensuite analysée. Une analyse des phénomènes d'interférence apparaissant dans le régime de transition champ proche-champ lointain conclut ce chapitre.

Dans le dernier chapitre, des résultats des simulations numériques des performances de systèmes TPV en champ proche (TPV-CP) sont présentés. Les performances des systèmes TPV-CP sont évaluées grâce à un modèle couplé prenant en compte leurs comportements radiatif, électrique et thermique. Les modèles basés sur l'hypothèse de faible injection utilisés généralement pour simplifier le problème du transport des charges électriques dans la cellule PV sont évalués en détails.

Cette thèse est accessible à l'adresse : http://theses.insa-lyon.fr/publication/2016LYSEI103/these.pdf
© [E. Blandre], [2016], INSA Lyon, tous droits réservés

Leur validité est étudiée en développant et mettant en oeuvre un modèle physique et numérique qui prend en compte les phénomènes de forte injection. Pour finir, nous proposons différentes architectures de cellules permettant d'optimiser les performances du système. Ces travaux offrent un nouvel éclairage sur le rayonnement des structures multicouches et leur application à la conversion thermophotovoltaïque.

Mots clés : Nanothermique, Rayonnement en champ proche, Conversion thermophotovoltaïque, Interférences, Structures multicouches.

Cette thèse est accessible à l'adresse : http://theses.insa-lyon.fr/publication/2016LYSEI103/these.pdf
© [E. Blandre], [2016], INSA Lyon, tous droits réservés

Cette thèse est accessible à l'adresse : http://theses.insa-lyon.fr/publication/2016LYSEI103/these.pdf
© [E. Blandre], [2016], INSA Lyon, tous droits réservés

Cette thèse est accessible à l'adresse : http://theses.insa-lyon.fr/publication/2016LYSEI103/these.pdf
© [E. Blandre], [2016], INSA Lyon, tous droits réservés

Contents

Cette thèse est accessible à l'adresse : http://theses.insa-lyon.fr/publication/2016LYSEI103/these.pdf
© [E. Blandre], [2016], INSA Lyon, tous droits réservés

Cette thèse est accessible à l'adresse : http://theses.insa-lyon.fr/publication/2016LYSEI103/these.pdf
© [E. Blandre], [2016], INSA Lyon, tous droits réservés

Cette thèse est accessible à l'adresse : http://theses.insa-lyon.fr/publication/2016LYSEI103/these.pdf
© [E. Blandre], [2016], INSA Lyon, tous droits réservés

Cette thèse est accessible à l'adresse : http://theses.insa-lyon.fr/publication/2016LYSEI103/these.pdf
© [E. Blandre], [2016], INSA Lyon, tous droits réservés

List of Figures

Cette thèse est accessible à l'adresse : http://theses.insa-lyon.fr/publication/2016LYSEI103/these.pdf
© [E. Blandre], [2016], INSA Lyon, tous droits réservés

Cette thèse est accessible à l'adresse : http://theses.insa-lyon.fr/publication/2016LYSEI103/these.pdf
© [E. Blandre], [2016], INSA Lyon, tous droits réservés

Cette thèse est accessible à l'adresse : http://theses.insa-lyon.fr/publication/2016LYSEI103/these.pdf
© [E. Blandre], [2016], INSA Lyon, tous droits réservés

Cette thèse est accessible à l'adresse : http://theses.insa-lyon.fr/publication/2016LYSEI103/these.pdf
© [E. Blandre], [2016], INSA Lyon, tous droits réservés

Cette thèse est accessible à l'adresse : http://theses.insa-lyon.fr/publication/2016LYSEI103/these.pdf
© [E. Blandre], [2016], INSA Lyon, tous droits réservés

Cette thèse est accessible à l'adresse : http://theses.insa-lyon.fr/publication/2016LYSEI103/these.pdf
© [E. Blandre], [2016], INSA Lyon, tous droits réservés

Cette thèse est accessible à l'adresse : http://theses.insa-lyon.fr/publication/2016LYSEI103/these.pdf
© [E. Blandre], [2016], INSA Lyon, tous droits réservés

Cette thèse est accessible à l'adresse : http://theses.insa-lyon.fr/publication/2016LYSEI103/these.pdf
© [E. Blandre], [2016], INSA Lyon, tous droits réservés

Introduction

The way of life of a modern human being is based on the consumption of energy under various forms (electrical, mechanical, thermal...). This is why the control of energy has a paramount importance for the future. The energy flow chart of United States released by the Lawrence Livermore National Laboratory in 2015 [9] highlights two alarming facts. First, 35% of the energy produced in 2014 came from petroleum, a non-renewable and non-environmentally friendly source of energy, while less than 1% came from the renewable and more environmentally friendly solar energy. Second, 60% of the energy produced this year was rejected, leaving only 40% available for consumption. In this context, it is absolutely crucial to find new sources of green and renewable energy, and to increase the efficiency of energy converters.

The fast advances of nanotechnologies in the past decades introduced new concepts to control energy. Heat transfer at the nanoscale can be involved in these new concepts. This led over the past decades to the conception of promising energy conversion nanodevices, such as nanostructured thermoelectric materials based on the Seebeck effect [10], or PV cells with nanotextured surfaces [11].

In this manuscript, we investigate the possibilities of tailoring radiative heat transfer between bodies using nanostructures, in order to increase the energy conversion performances of thermophotovoltaic (TPV) systems. The latter convert thermal energy (thermo) into electricity (voltaic) via its radiative form (photo). They consist in a hot source (radiator) emitting thermal radiation toward a PV cell. Thermal power is supplied to the radiator by waste heat sources (coming for instance from an engine), or from absorbing sun's radiation for solar thermophotovoltaic (STPV) systems. The advantage of thermophotovoltaic converters is that it is possible to control the spectral distribution of the emission of the hot source in order to increase the energy conversion performances of the system [12]. The theoretical limit for the efficiency of STPV systems has been evaluated at 85% [13], which is more than twice larger than the Shockley–Queisser limit [14] (33%) for a monojunction solar cell illuminated by the AM1.5 solar spectrum [15]. STPV systems constitute therefore a potential alternative to classical solar PV. However, the maximum efficiency obtained experimentally for a STPV system remains very low (6.2%) [16]. A deeper understanding of the phenomena involved in TPV converters, new concepts and breakthroughs are needed to reach high-efficiency TPV systems.
In this thesis, phenomena occurring at the nanoscale will be under consideration to control radiative heat transfer from the hot source to the PV cell. It is possible to tailor the far-field emission

Cette thèse est accessible à l'adresse : http://theses.insa-lyon.fr/publication/2016LYSEI103/these.pdf
© [E. Blandre], [2016], INSA Lyon, tous droits réservés

of few-layer structures using interference phenomena. Another way to tune the emission of a body is near-field thermal radiation, a radiative heat transfer regime arising when two bodies are separated by a distance much smaller than the characteristic wavelength of thermal radiation [17]. Several effects occurring in the near field can be potentially used to increase the efficiency of TPV systems, such as the increase of the radiative heat flux between the two bodies [17] and the spectral tuning due to surface polaritons [18]. The concept of TPV systems where the radiator and the photovoltaic cell are separated by a subwavelength distance was introduced in 2002 [19]. By decreasing the distance between the hot source and the PV cell to a subwavelength distance, it is in theory possible to enhance the energy conversion performances of TPV systems due to near-field effects. These systems are referred to as near-field radiation mediated thermophotovoltaic (NFR-TPV devices). Despite the realization of two experimental works on this topic [20, 21], the experimental proof of the concept of NFR-TPV systems has not been performed yet: the increase of the performances of the system due to near-field effects reported in both studies was marginal. In addition to the technological challenge that is the control of a subwavelength distance between the radiator and the cell, there is obviously a need for optimizations of NFR-TPV systems through numerical simulations of their physical behavior.

The fundamentals of thermal radiation at nanoscale are presented in Chapter I. We recall the basics of the classical model for thermal radiation between bodies based on Planck's law. After showing that this model is insufficient to describe accurately the radiative heat transfer between closely-spaced bodies, we detail the Fluctuational Electrodynamics (FE) approach in particular configurations involving layered materials. The FE model allows taking into account near-field and interference effects, and thus will be used to simulate radiative heat transfer between bodies along this manuscript.
In Chapter II, we recall the working principles of a photovoltaic cell under illumination, and present the different equations that model its electrical behavior. This chapter constitutes a theoretical basis for the modeling of charge transport in NFR-TPV cells, that will be used to simulate the performances of NFR-TPV systems in Chapter V.

The far-field emission of few-layer structures supporting interference phenomena is investigated in Chapter III. The great potential for this kind of structure as spectral selective radiator for TPV applications was already been highlighted. However, if Fabry-Pérot interferences inside a single cavity are very well understood [22], it is not fully the case yet when multiple layers are involved. We thus focus on this topic. Extending the understanding of interferences inside few-layer structures, the optimization of the spectral hemispherical emissivity of few-layer structures for a TPV application is performed thereafter.
Calculation of the emission of high-temperature emitters for TPV requires the optical properties of the emitting material: the values of the dielectric function are needed for the frequency range where the spectrum of emission extends. Generally, these values are measured or modeled at ambient temperature, which is obviously much lower than the operating temperature of a TPV radiator. In the following section, we thus study the impact of the variations with temperature of the optical properties of the emitting material by analyzing the dependence on temperature of the

Cette thèse est accessible à l'adresse : http://theses.insa-lyon.fr/publication/2016LYSEI103/these.pdf
© [E. Blandre], [2016], INSA Lyon, tous droits réservés

spectral and total emissivities of few-layer structures. This study is performed in a temperature between 0 and 500 K, which is in principle lower than that required for TPV, but provides already an example of the importance of the temperature dependence of the optical properties. Another application of this study is thermal rectification between two bodies, a phenomena that takes place when a thermal diode behavior can be observed, i.e. when different heat fluxes are transferred when the temperatures of the two bodies are inverted. Indeed, the key point to evaluate and control radiative rectification phenomena between two bodies is the variation with temperature of the radiative heat transfer between them. We end this chapter by studying the impact of interferences on the total hemispherical emissivty of these structures.

One of the major phenomena that needs to be fully understood to optimize the performances of NFR-TPV systems is near-field radiative heat transfer between the emitter and the PV cell. The spectral tuning of the thermal radiation exchanged between planar bodies was extensively studied in the past years [17, 18, 23, 24], but several important effects that have a large impact of the performances of NFR-TPV systems have been neglected. One of these phenomena is the spatial distribution of the absorption of radiative power [25]. Furthermore, it was recently shown that spectral modifications of the radiative heat flux exchanged between two planar bodies due to interferences could also occur in the near-to-far field transition regime [26]. Chapter IV thus deals with near-field thermal radiation in a configuration close to a TPV system: a semi-infinite radiator emitting toward a flat film. We focus on the spatial distribution of the near-field radiative power inside the film. Then, we investigate interferences in the near-to-far field transition regime and explore the possibilities of tuning the spectrum of emission using interference phenomena.

To solve numerically the charge transport problem inside NFR-TPV systems, the low-injection approximation is usually assumed [27, 4, 25, 28]. One of the main reason is that applying the low-injection approximation drastically simplifies the numerical resolution of the charge transport problem in PV cells. However, no one ever questioned the validity of this approximation in the case of NFR-TPV systems, despite the fact that the radiative energy absorbed by the PV devices in the near field can be orders of magnitude larger than in the case non-concentrated solar cells. The uncertainty on the validity of this model is a barrier for a realistic optimization of NFR-TPV systems. Furthermore, the low-injection approximation model does not allow simulating the electrical behaviors of PIN cells, because of the presence of an intrinsic region where high-injection phenomena are very likely to occur. We present in Chapter V a numerical model that solves the charge transport problem inside PV cells without applying the low-injection approximation. We use this model to assess the validity of the low-injection approximation in the case of NFR-TPV systems. Optimizations of the doping levels and the thicknesses of the doped regions are performed thereafter. Eventually, we present the first results of a NFR-TPV system close to an experimental configuration, with an InSb PV cell based on a PIN architecture, illuminated by a source at relatively low temperature (800 K).

The manuscript ends with the main conclusions and provides some prospects for the future.

Cette thèse est accessible à l'adresse : http://theses.insa-lyon.fr/publication/2016LYSEI103/these.pdf
© [E. Blandre], [2016], INSA Lyon, tous droits réservés

Cette thèse est accessible à l'adresse : http://theses.insa-lyon.fr/publication/2016LYSEI103/these.pdf
© [E. Blandre], [2016], INSA Lyon, tous droits réservés

Chapter I

Fundamentals of nanoscale thermal radiation

Contents

In this chapter, a brief summary of the fundamentals of thermal radiation is presented. The classical model of thermal radiation between bodies is recalled first. Then, the physical, mathematical and numerical models used to calculate the radiative heat transfer between bodies at nanoscale is introduced. These models will be used along this thesis to calculate the radiative heat transfer including nanoscale effects.

Heat transfer between two bodies is an exchange of energy due to a temperature difference between them. There are three main processes of heat transfer. Conduction involves solids. In metals, the heat is mainly carried by the free electrons, while in semiconductors and dielectrics, it is transferred by the phonons, the elementary vibrations of the crystalline lattice. In convection, heat is carried by fluid put in motion, either by a external mechanical source (forced convection) or by a self-induced process due to variations of the density of the fluid when the spatial distribution of the temperature is non-uniform (natural convection). The last heat transfer mechanism between bodies is thermal radiation.

Cette thèse est accessible à l'adresse : http://theses.insa-lyon.fr/publication/2016LYSEI103/these.pdf
© [E. Blandre], [2016], INSA Lyon, tous droits réservés

I.1 Classical model of thermal radiation between bodies

When a body is at a temperature larger than 0 K, the electrical charges (like the partial charges on the atoms or ions in polar materials, or the free electrons for metals) inside it oscillate under thermal agitation. It induces the oscillation of electromagnetic dipoles, that radiate electromagnetic waves and therefore dissipate energy. If the waves are propagating, they are sent into space and travel until they are absorbed by a lossy medium. The fundamental base model for thermal radiation emission is the blackbody radiation.

I.1.1 Wavelength and angular frequency distributions of the blackbody intensity

Assuming that the radiating body is the perfect emitter and absorber, Planck's law gives the spectral distribution of the blackbody intensity I^{bb} at a temperature T per unit projected area. It can be expressed as a function of wavelength in vacuum λ_v and the temperature T [29]

$$I^{bb}(\lambda_v, T) = \frac{2hc_v^2}{\lambda_v} \frac{1}{e^{hc_v/(\lambda_v k_b T)} - 1}, \tag{I.1}$$

where h is the Planck constant, k_b is the Boltzmann constant, c_v is the speed of light (in vacuum) and the subscript v refers to vacuum. Electromagnetic waves can be described as being waves or particles. The quantum of energy carried by light is the photon. In photovoltaics, it is convenient to have access to the energy carried by a photon. The energy E carried by a photon is directly proportional to its angular frequency ω, following the Planck-Einstein relation [30]

$$E = \hbar\omega = h\frac{2\pi c_v}{\lambda_v} \tag{I.2}$$

where $\hbar$ is the reduced Planck's constant ($\hbar = \frac{h}{2\pi}$).

It is sometimes more convenient to express Planck's law as a function of the angular frequency, such that [29]

$$I^{bb}(\omega, T) = \frac{\hbar\omega^3}{4\pi^3 c_v^2} \frac{1}{e^{\hbar\omega/(k_b T)} - 1}. \tag{I.3}$$

Furthermore, unlike the wavelength, the frequency of a photon remains constant when traveling through different media.

Eq. I.3 can be reformulated as

$$I^{bb}(\omega, T) = \Theta(\omega, T)\frac{k_v^2}{4\pi^3}, \tag{I.4}$$

where $k_v = \frac{\omega}{c_v}$ is the magnitude of the wavevector in vacuum, and $\Theta(\omega, T)$ is the mean energy of a Planck oscillator

$$\Theta(\omega, T) = \frac{\hbar\omega}{e^{\hbar\omega/(k_b T)} - 1} = E \times n(\omega), \tag{I.5}$$

Cette thèse est accessible à l'adresse : http://theses.insa-lyon.fr/publication/2016LYSEI103/these.pdf
© [E. Blandre], [2016], INSA Lyon, tous droits réservés

where $n(\omega)$ is the Bose-Einstein distribution.

I.1.2 Spectral hemispherical emissive power

The spectral hemispherical emissive power of a blackbody can be obtained by integrating the blackbody intensity over the solid angle in a half space, giving

$$q_{\omega}^{bb}(T) = \Theta(\omega, T)\frac{k_{\nu}^2}{4\pi^2}. \tag{I.6}$$

Fig. I.1 depicts the spectral hemispherical emissive power of a blackbody as a function of the angular frequency for several temperatures. It is worth noticing that the spectra are broadband.

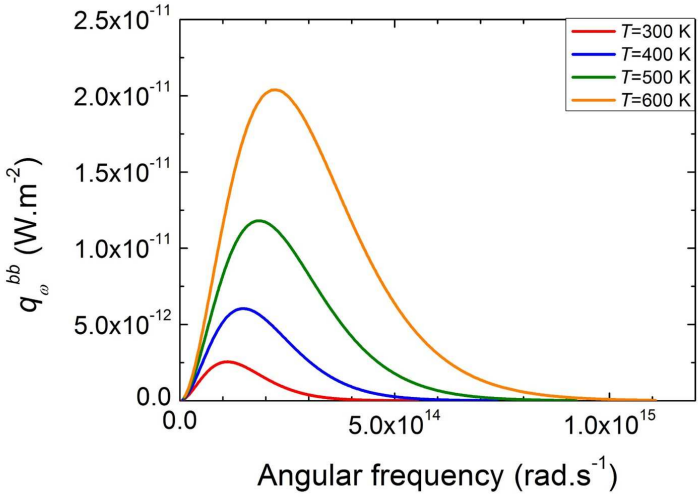

Figure I.1: Spectral hemispherical emissive power of the blackbody q_{ω}^{bb} as a function of the angular frequency ω for several temperatures.

I.1.3 Wien's law

By calculating the derivative of Eq. I.1 and I.3 with respect to λ_{ν} and ω respectively, and equalizing the result to 0, Wien's law that links the wavelength (or angular frequency) where the blackbody intensity is maximum and the temperature can be derived. When considering the wavelength distribution of the blackbody intensity (Eq. I.1), it is written as

$$\lambda_{\text{Wien}}(T) = \frac{C_{\lambda}}{T}, \tag{I.7}$$

where C_{λ} is a constant of value 2.898×10^{-3} m.K. For an angular frequency distribution (Eq. I.3), Wien's law is:

$$\omega_{\text{Wien}}(T) = C_{\omega} \times T, \tag{I.8}$$

Cette thèse est accessible à l'adresse : http://theses.insa-lyon.fr/publication/2016LYSEI103/these.pdf
© [E. Blandre], [2016], INSA Lyon, tous droits réservés

where C_ω is a constant of value 3.697×10^{11} m.K^{-1}.

I.1.4 Total hemispherical radiative heat flux

The total hemispherical radiative heat flux emitted by a blackbody is obtained by integrating Eq. I.6 over all frequencies to give the Stefan-Boltzmann law

$$q^{bb}(T) = \sigma T^4, \tag{I.9}$$

where σ is the Stefan-Boltzmann constant, equal to 5.670×10^{-8} W.m^{-2}.K^{-4}. In reality, bodies are neither perfect absorbers nor perfect emitters. To describe the emission of real bodies, another quantity must be introduced. As the blackbody is the perfect emitter, the ratio of the radiative heat flux emitted by a real body to the radiative heat flux from a blackbody at the same temperature gives a quantity between 0 and 1 called emissivity. The spectral hemispherical emissivity ε_ω of a real body can therefore be written as its spectral hemispherical radiative power q_ω divided by the one of the blackbody at the same temperature (Eq. I.6)

$$\varepsilon_\omega = \frac{q_\omega(\omega, T)}{q_\omega^{bb}(\omega, T)}, \tag{I.10}$$

and the total hemispherical emissivity ε of a real body is expressed as its total hemispherical emitted radiative power divided by the one emitted by the blackbody at the same temperature

$$\varepsilon = \frac{q(T)}{q^{bb}(T)}. \tag{I.11}$$

I.2 Limitations of the classical model: near-field and interference effects

The classical model of thermal radiation is not always valid: it describes properly thermal radiation between two bodies separated by a distance much larger than the thermal wavelength given by Wien's law in Eq. I.8 (far-field regime). Indeed, it takes into account only the participation of the so-called propagating waves to the radiative heat transfer. When the distance between bodies becomes much smaller than the thermal wavelength (near-field regime), the contribution of evanescent waves to the radiative heat transfer has to be accounted for. In addition, at such distances, wave effects occur, such as diffraction and interferences due to coherence effects.
Evanescent waves propagate along the surface of the emitting body. Their amplitude decreases exponentially when moving away from the surface. Their penetration depth is of the same order of magnitude as the thermal wavelength. Therefore, when two bodies are separated by a vacuum gap size larger than the thermal wavelength, they do not participate to radiative heat transfer. When two absorbing bodies are separated by a vacuum gap size smaller than the thermal wavelength, evanescent waves are transferred from the emitting body to the other through a process called "tunneling", and start participating to heat transfer. At a body-vacuum interface, some of

Cette thèse est accessible à l'adresse : http://theses.insa-lyon.fr/publication/2016LYSEI103/these.pdf
© [E. Blandre], [2016], INSA Lyon, tous droits réservés

them are surface modes, i.e. they are evanescent in the emitter and the vacuum. Surface modes can be generated by hybrid modes of a mechanical oscillation and the electric field, called polaritons. For polar and dielectric materials, the mechanical oscillations are the optical phonons, and the surface modes associated are called surface phonon-polaritons (SPhP). In metals, the collective oscillations of the electron cloud are called plasmons, and their interaction with the electric field are called surface plasmon-polaritons (SPP). Evanescent waves can also appear when propagative modes in the body reach the interface between the emitter and vacuum with an incident angle larger than the critical angle for reflection. In this case, propagating waves are totally internally reflected in the body, and become evanescent waves in vacuum. These modes are referred to as "frustrated modes". Fig. I.2 summarizes schematically the three types of modes.

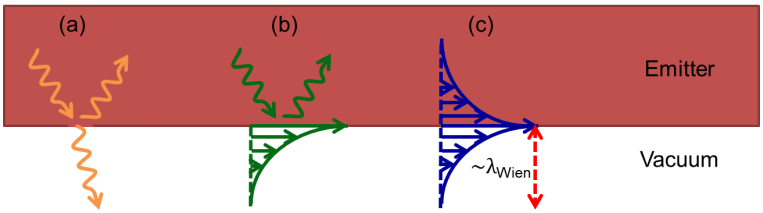

Figure I.2: Schematic of the different modes at a body-vacuum interface.
(a): waves are propagative in the emitter and in vacuum (propagating modes).
(b): waves are propagative in the emitter and evanescent in the vacuum due to total internal reflection (frustrated modes).
(c): these evanescent waves are coupled in the body and in vacuum (surface modes).

The first calculation of near-field radiative heat transfer between two plane-parallel bodies was performed by Polder and Van Hove [17]. They reported an exponential increase of the radiative heat flux between the two bodies when the distance separating them decreases. Later, the impact of surface polaritons on the spectral distribution of the radiative heat flux was underlined in [18, 23]: large peaks in the local density of states were observed due to polariton resonances. Another phenomenon occurring for bodies separated by a small distance or inside thin layers is the coherence of thermal radiation, leading to interference effects [26, 6]. When the distance between two plane-parallel bodies or the thickness of a flat film is of the same order of magnitude as the thermal wavelength, constructive and destructive interferences occur, and can lead to significant modifications of the spectral and total heat flux transferred between them.
As a consequence, neither Planck's nor Stefan-Boltzmann's laws can describe accurately radiative heat transfer between closely-spaced bodies. In the next section, we present the physical, mathematical and numerical models that were used during this thesis to calculate the radiative heat flux between planar bodies, that take into account near-field and interference effects.

Cette thèse est accessible à l'adresse : http://theses.insa-lyon.fr/publication/2016LYSEI103/these.pdf
© [E. Blandre], [2016], INSA Lyon, tous droits réservés

I.3 Physical, mathematical and numerical models

I.3.1 Description of the generic problem

In this manuscript, only one-dimensional geometries will be considered: in Chapter III, the thermal emission of few-layer structures will be calculated. In Chapter IV, the radiative heat transfer between a semi-infinite emitter and a flat film separated by a vacuum gap will be studied. Eventually in Chapter V, the radiator of the NFR-TPV system will be considered as a plane semi-infinite body, and the PV cell as a few-layer structure, each layer corresponding to a doped region. In the following, we present the physical, mathematical and numerical models, as well as the methodology to calculate the radiative heat transfer inside a one-dimensional medium. The Fluctuational Electrodynamics approach will be introduced. This approach allows taking into account near-field and interference effects.

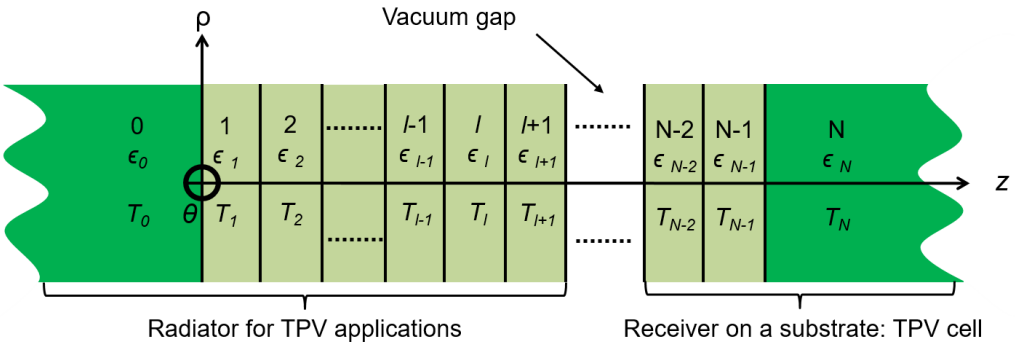

Figure I.3: Schematic representation of the generic system under consideration.

The method we present allows considering the generic configuration depicted in Fig. I.3: $N-1$ layers of finite thickness are sandwiched between two semi-infinite half-spaces labeled 0 and N. Each layer is characterized by its temperature T_l, its optical properties (dielectric function) ϵ_l, its position z_l and its thickness $z_{l+1}-z_l$. Among them, emitting layers are designated with the subscript ss, while z corresponds to the position where the radiative heat flux is calculated.

I.3.2 The Fluctuational Electrodynamics approach

To take near-field and interference effects into account, the Fluctuational Electrodynamics (FE) approach is used when solving the thermal radiation problem [17, 18]. Maxwell's equations are considered with the linear response theory of the Green's tensors and the Fluctuation-Dissipation Theorem (FDT) [31].

I.3.2.1 Theory of the linear response - Green's tensors

Maxwell's equations are the fundamental equations governing the electromagnetic field in a medium with electrical charges and currents: they describe the propagation of electromagnetic

Cette thèse est accessible à l'adresse : http://theses.insa-lyon.fr/publication/2016LYSEI103/these.pdf
© [E. Blandre], [2016], INSA Lyon, tous droits réservés

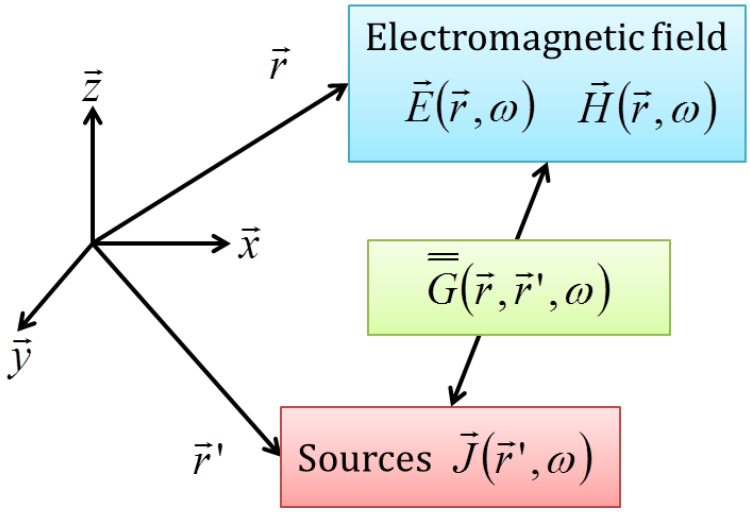

Figure I.4: The Green's tensor $\bar{\bar{G}}$ provides the link between the sources at position $\overrightarrow{r}'$ with the electromagnetic field at position $\overrightarrow{r}$.

waves inside a medium. The Green's tensors provide the relation between the electromagnetic fields at a position $\overrightarrow{r}$ and the sources of the electromagnetic waves generated at position $\overrightarrow{r}'$ (Fig. I.4). Due to the linearity of Maxwell's equations, a linear relation is considered between the electric and magnetic fields at position $\overrightarrow{r}$ and the sources at position $\overrightarrow{r}'$, such that [32]

$$\overrightarrow{E}(\overrightarrow{r},\omega) = i\omega\mu_v \int_V \bar{\bar{G}}^E(\overrightarrow{r},\overrightarrow{r}',\omega)\cdot\overrightarrow{J}(\overrightarrow{r}',\omega)dV, \tag{I.12}$$

$$\overrightarrow{H}(\overrightarrow{r},\omega) = \int_V \bar{\bar{G}}^H(\overrightarrow{r},\overrightarrow{r}',\omega)\cdot\overrightarrow{J}(\overrightarrow{r}',\omega)dV, \tag{I.13}$$

where $\overrightarrow{E}$ and $\overrightarrow{H}$ are respectively the electric and the magnetic fields at position $\overrightarrow{r}$ and angular frequency ω, $\overrightarrow{J}$ the currents of the excitation at position $\overrightarrow{r}'$ and angular frequency ω and μ_v is the magnetic permeability in vacuum. $\bar{\bar{G}}^E$ and $\bar{\bar{G}}^H$ are the electric and magnetic Green's tensors, respectively. The integral over V represent a summation over the volume of the emitting medium. The only unknowns left are the currents $\overrightarrow{J}$ for thermal radiation by a given material at temperature T.

I.3.2.2 Fluctuation-Dissipation Theorem

The source of thermal radiation is the electromagnetic energy dissipated by the electrical charges due to thermal motion. At a non-zero temperature, the spatial position of the electrical charges fluctuates under thermal agitation. The relation that provides the ensemble average of the spatial correlation function of the random currents $\overrightarrow{J}$ is given by the Fluctuation-Dissipation Theorem

Cette thèse est accessible à l'adresse : http://theses.insa-lyon.fr/publication/2016LYSEI103/these.pdf
© [E. Blandre], [2016], INSA Lyon, tous droits réservés

(FDT), that can be written as [31]

$$\left\langle J_\alpha(\overrightarrow{r}',\omega)J_\beta(\overrightarrow{r}'',\omega')\right\rangle = \frac{\epsilon_\nu\epsilon''_{ss}(\omega)}{\pi}\Theta(\omega,T)\delta(\overrightarrow{r}'-\overrightarrow{r}'')\delta(\omega-\omega')\delta_{\alpha\beta}, \tag{I.14}$$

where ϵ''_{ss} is the imaginary part of the dielectric function in the source medium ss at $\overrightarrow{r}$. δ is the Dirac delta function, and ϵ_ν is the permittivity of free space. The subscripts α and β refer to the orthogonal components of the Cartesian system.

I.3.3 Expression of the monochromatic heat flux

The monochromatic radiative heat flux at position z along the $\overrightarrow{e_z}$ direction (Fig. I.3) is given by the time-averaged z-component of the Poynting vector $\overrightarrow{E}\otimes\overrightarrow{H}$ [18]

$$q_\omega(z) = 4\times\frac{1}{2}Re\left[\left\langle E_xH_y^* - E_yH_x^*\right\rangle\right](\overrightarrow{r},\omega) \tag{I.15}$$

where the superscript * denotes the complex conjugate number. The factor 4 comes from the fact that we only consider positive frequencies [18].

The two terms $E_xH_y^*$ and $E_yH_x^*$ of the Poynting vector can be derived by combining Eq. I.12 and I.13

$$\begin{aligned}&\left\langle E_xH_y^*\right\rangle(\overrightarrow{r},\omega) = \\ &\left\langle (i\omega\mu_\nu\int_{V'}G^E_{x\alpha}(\overrightarrow{r},\overrightarrow{r}',\omega)J_\alpha(\overrightarrow{r}',\omega)d^3r'\int_{V''}G^E_{y\beta}(\overrightarrow{r},\overrightarrow{r}'',\omega)J_\beta(\overrightarrow{r}'',\omega)d^3r'')^*\right\rangle \\ &= i\omega\mu_\nu\int_{V'}\int_{V''}G^E_{x\alpha}(\overrightarrow{r},\overrightarrow{r}',\omega)G^{H*}_{y\beta}(\overrightarrow{r},\overrightarrow{r}'',\omega)\left\langle J_\alpha(\overrightarrow{r}',\omega)J_\beta(\overrightarrow{r}'',\omega)\right\rangle d^3r'd^3r''\end{aligned} \tag{I.16}$$

where here the subscripts α and β indicate a summation over the three coordinates x, y and z. Using the FDT relation (Eq. I.14) gives

$$\left\langle E_xH_y^*\right\rangle(\overrightarrow{r},\omega) = i\omega\mu_\nu\frac{\omega\epsilon_\nu}{\pi}\epsilon''_{ss}\Theta(\omega,T)\int_{V'}G^E_{x\alpha}(\overrightarrow{r},\overrightarrow{r}',\omega)G^{H*}_{y\alpha}(\overrightarrow{r},\overrightarrow{r}',\omega)d^3\overrightarrow{r}' \tag{I.17}$$

The same calculation can be applied for $E_yH_x^*$, using the relations $\epsilon_\nu\mu_\nu = \frac{1}{c_\nu^2}$ and $\frac{\omega^2}{c_\nu^2} = k_\nu^2$. Eventually, the monochromatic heat flux can be written as [18]

$$\begin{aligned}&q_\omega(z) = \frac{2k_\nu^2\Theta(\omega,T)}{\pi}\times \\ &Re\left\{i\epsilon''_{ss}(\omega)\int_{V'}\left[G^E_{x\alpha}(\overrightarrow{r},\overrightarrow{r}',\omega)G^{H*}_{y\alpha}(\overrightarrow{r},\overrightarrow{r}',\omega) - G^E_{y\alpha}(\overrightarrow{r},\overrightarrow{r}',\omega)G^{H*}_{x\alpha}(\overrightarrow{r},\overrightarrow{r}',\omega)\right]\right\}d^3\overrightarrow{r}'\end{aligned} \tag{I.18}$$

Cette thèse est accessible à l'adresse : http://theses.insa-lyon.fr/publication/2016LYSEI103/these.pdf
© [E. Blandre], [2016], INSA Lyon, tous droits réservés

I.3.4 Application to the case of one-dimensional layered media

I.3.4.1 Weyl development of the Green's tensor

The Green's tensors can be expressed as a function of their Weyl components $\bar{\bar{g}}$ by applying a two dimensional Fourier transform (plane wave decomposition) [2]

$$\bar{\bar{G}}^{E,H}(\overrightarrow{r},\overrightarrow{r}',\omega)=\int_0^{+\infty}\frac{\overrightarrow{dk_\rho}}{(2\pi)^2}\bar{\bar{g}}^{E,H}(\overrightarrow{k_\rho},z,z',\omega)e^{-i\overrightarrow{k_\rho}(\overrightarrow{R}-\overrightarrow{R}')}, \tag{I.19}$$

where $\overrightarrow{k_\rho}=k_x\overrightarrow{e_x}+k_y\overrightarrow{e_y}$, and $\overrightarrow{R}=x\overrightarrow{e_x}+y\overrightarrow{e_y}$. Eq. I.19 is then used to express the monochromatic heat flux (Eq. I.18) as a function of the Weyl components of the Green's tensors. Using the two-dimensional Fourier transform, the products of the Green's tensors can be written as

$$\begin{aligned}\int_{V''}d^3\overrightarrow{r}'G^E_{x\alpha}G^{H*}_{y\alpha}=\iint_0^{+\infty}\frac{d\overrightarrow{k_\rho}}{(2\pi)^2}\frac{\overrightarrow{dk_\rho}'}{(2\pi)^2}e^{i(\overrightarrow{k_\rho}-\overrightarrow{k_\rho}')}\\ \times\int_{z'}g^E_{x\alpha}(\overrightarrow{k_\rho},z,z',\omega)g^{H*}_{y\alpha}(\overrightarrow{k'_\rho},z,z',\omega)dz'\iint d^2\overrightarrow{R'}e^{(\overrightarrow{k_\rho}-\overrightarrow{k_\rho}')\overrightarrow{R}'}\end{aligned} \tag{I.20}$$

where $\iint d^2\overrightarrow{R'}e^{(\overrightarrow{k_\rho}-\overrightarrow{k_\rho}')\overrightarrow{R}'}=4\pi^2\delta(\overrightarrow{k_\rho}-\overrightarrow{k_\rho}')$ according to a well known identity [18], giving

$$\int_{V'}d^3\overrightarrow{r}'G^E_{x\alpha}G^{H*}_{y\alpha}=\int_{-\infty}^{+\infty}\frac{d\overrightarrow{k_\rho}}{(2\pi)^2}\int_{z'}dz'g^E_{x\alpha}(\overrightarrow{k_\rho},z,z',\omega)g^{H*}_{y\alpha}(\overrightarrow{k_\rho},z,z',\omega) \tag{I.21}$$

As there is an azimuthal symmetry in the problem, it is possible to switch from a Cartesian coordinate system (x,y,z) to a polar coordinate system (ρ,θ,z), and use the following transformation on the integration variable $\overrightarrow{k_\rho}$:

$$\iint_{-\infty}^{+\infty}d\overrightarrow{k_\rho}=\int_{-\infty}^{+\infty}\int_{-\infty}^{+\infty}dk_xdk_y=\int_{k_\rho=0}^{+\infty}\int_{\theta=0}^{2\pi}k_\rho dk_\rho d\theta=2\pi\int_0^{\infty}k_\rho dk_\rho \tag{I.22}$$

where k_ρ is the component of the wavevector parallel to the interface. The component of the wavevector perpendicular to the interface k_z is also introduced. The two components of the wavevector are logically linked with the magnitude of the wavevector k_ν through the relation

$$k_{z_\nu}=\sqrt{k_\nu^2-k_\rho^2}. \tag{I.23}$$

The final expression of the monochromatic heat flux as a function of the Weyl components is

Cette thèse est accessible à l'adresse : http://theses.insa-lyon.fr/publication/2016LYSEI103/these.pdf
© [E. Blandre], [2016], INSA Lyon, tous droits réservés

[2, 1]

$$q_\omega(z) = \frac{k_\nu^2 \Theta(\omega,T)}{\pi} Re\left\{ i\epsilon''_{ss}(\omega) \int_0^\infty k_\rho dk_\rho \int_{V'} \begin{pmatrix} g^E_{\rho\alpha}(k_\rho,z,z',\omega) g^{H*}_{\theta\alpha}(k_\rho,z,z',\omega) \\ -g^E_{\theta\alpha}(k_\rho,z,z',\omega) g^{H*}_{\rho\alpha}(k_\rho,z,z',\omega) \end{pmatrix} dz' \right\}, \tag{I.24}$$

where the integration over the variable z' corresponds to the integration over the volume of the emitter V, while the integration over k_ρ corresponds to the integral over all directions.

I.3.4.2 Expression of the Weyl components of the Green's tensor

Green's tensors can be calculated using Sipe's formalism [33]. Results can be found in the article of Francoeur et al. [2], where the expressions of the Weyl component of the Green's tensors are given. The electric and magnetic tensors can be written as follows

$$\bar{\bar{g}}^E(k_\rho,z,z',\omega) = \begin{pmatrix} g^E_{\rho\rho} & 0 & g^E_{\rho z} \\ 0 & g^E_{\theta\theta} & 0 \\ g^E_{z\rho} & 0 & g^E_{zz} \end{pmatrix}, \tag{I.25}$$

$$\bar{\bar{g}}^H(k_\rho,z,z',\omega) = \begin{pmatrix} 0 & g^H_{\rho\theta} & 0 \\ g^H_{\theta\rho} & 0 & g^H_{\theta z} \\ 0 & g^H_{z\theta} & 0 \end{pmatrix}. \tag{I.26}$$

In Eq. I.24, the summation over $\alpha = \rho, \theta, z$ can be performed, leaving only the non-zero products of the Weyl components of the Green's tensors. The monochromatic heat flux emitted by a layer ss reduces to [2]

$$q_\omega(z) = \frac{k_\nu^2 \Theta(\omega,T)}{\pi^2} Re\left\{ i\epsilon''_{ss}(\omega) \int_0^\infty k_\rho dk_\rho \int_{z_{ss}}^{z_{ss+1}} \begin{pmatrix} g^E_{\rho\rho}(k_\rho,z,z',\omega) g^{H^*}_{\theta\rho}(k_\rho,z,z',\omega) \\ +g^E_{\rho z}(k_\rho,z,\omega) g^{H^*}_{\theta z}(k_\rho,z,z',\omega) \\ -g^E_{\theta\theta}(k_\rho,z,z',\omega) g^{H^*}_{\rho\theta}(k_\rho,z,z',\omega) dz' \end{pmatrix} \right\} \tag{I.27}$$

The emitting layer ss is a distribution along the z-axis of multiple source points z' located between the two interfaces of the source layer z_{ss} and z_{ss+1}. This source layer can emit a field in both forward and backward directions (i.e. in the z-positive and z-negative directions), and this field is then multireflected in each layer of the system. The emitted field can be divided in four contributions, each one corresponding to waves that have been emitted:

- in the z-positive direction, and travelling after multireflections in the z-positive direction, with a corresponding amplitude A,
- in the z-positive direction, and travelling after multireflections in the z-negative direction, with a corresponding amplitude B,
- in the z-negative direction, and travelling after multireflections in the z-positive direction,

Cette thèse est accessible à l'adresse : http://theses.insa-lyon.fr/publication/2016LYSEI103/these.pdf
© [E. Blandre], [2016], INSA Lyon, tous droits réservés

with a corresponding amplitude C,

- in the z-negative direction, and travelling after multireflections in the z-negative direction, with a corresponding amplitude D.

The remaining Weyl components of the Green's tensors in layer l where the heat flux is calculated can be written as [2]

$$g^E_{\rho\rho}(k_\rho,z,z',\omega)=\frac{ik_{z_l}}{2k_{ss}k_l}\left\{\begin{pmatrix}A^p e^{ik_{z_l}(z-z_l)}e^{-ik_{z_{ss}}z'}-B^p e^{-ik_{z_l}(z-z_l)}e^{-ik_{z_{ss}}z'}\\-C^p e^{ik_{z_l}(z-z_l)}e^{ik_{z_{ss}}z'}+D^p e^{-ik_{z_l}(z-z_l)}e^{ik_{z_{ss}}z'}\end{pmatrix}\right\} \tag{I.28}$$

$$g^{H*}_{\theta\rho}(k_\rho,z,z',\omega)=\frac{k_l^*}{2k_{ss}^*}\left\{\begin{pmatrix}-A^p e^{-ik_{z_l}(z-z_l)}e^{ik_{z_{ss}}z'}-B^p e^{ik_{z_l}(z-z_l)}e^{ik_{z_{ss}}z'}\\+C^p e^{-ik_{z_l}(z-z_l)}e^{-ik_{z_{ss}}z'}+D^p e^{ik_{z_l}(z-z_l)}e^{-ik_{z_{ss}}z'}\end{pmatrix}\right\} \tag{I.29}$$

$$g^E_{\rho z}(k_\rho,z,z',\omega)=\frac{ik_{z_l}k_\rho}{2k_{z_{ss}}k_{ss}k_l}\left\{\begin{pmatrix}-A^p e^{-ik_{z_l}(z-z_l)}e^{ik_{z_{ss}}z'}-B^p e^{ik_{z_l}(z-z_l)}e^{ik_{z_{ss}}z'}\\+C^p e^{-ik_{z_l}(z-z_l)}e^{-ik_{z_{ss}}z'}+D^p e^{ik_{z_l}(z-z_l)}e^{-ik_{z_{ss}}z'}\end{pmatrix}\right\} \tag{I.30}$$

$$g^{H*}_{\theta z}(k_\rho,z,z',\omega)=\frac{k_l^*k\rho}{2k_{ss}^*k_{z_{ss}}^*}\left\{\begin{pmatrix}-A^p e^{-ik_{z_l}(z-z_l)}e^{ik_{z_{ss}}z'}-B^p e^{ik_{z_l}(z-z_l)}e^{ik_{z_{ss}}z'}\\+C^p e^{-ik_{z_l}(z-z_l)}e^{-ik_{z_{ss}}z'}+D^p e^{ik_{z_l}(z-z_l)}e^{-ik_{z_{ss}}z'}\end{pmatrix}\right\} \tag{I.31}$$

$$g^E_{\theta\theta}(k_\rho,z,z',\omega)=\frac{i}{2k_{z_{ss}}}\left\{\begin{pmatrix}A^s e^{-ik_{z_l}(z-z_l)}e^{ik_{z_{ss}}z'}+B^s e^{ik_{z_l}(z-z_l)}e^{ik_{z_{ss}}z'}\\+C^s e^{-ik_{z_l}(z-z_l)}e^{-ik_{z_{ss}}z'}+D^s e^{ik_{z_l}(z-z_l)}e^{-ik_{z_{ss}}z'}\end{pmatrix}\right\} \tag{I.32}$$

$$g^{H^*}_{\rho\theta}(k_\rho,z,z',\omega)=\frac{k_{z_l}^*}{2k_{z_{ss}}^*}\left\{\begin{pmatrix}A^s e^{-ik_{z_l}(z-z_l)}e^{ik_{z_{ss}}z'}-B^s e^{ik_{z_l}(z-z_l)}e^{ik_{z_{ss}}z'}\\+C^s e^{-ik_{z_l}(z-z_l)}e^{-ik_{z_{ss}}z'}-D^s e^{ik_{z_l}(z-z_l)}e^{-ik_{z_{ss}}z'}\end{pmatrix}\right\} \tag{I.33}$$

where the superscripts s and p denote the transverse electric and transverse magnetic polarizations, respectively. As the Weyl components of the Green's tensor are calculated in layer l, only the shift between the position of the layer z_l and the position where the heat flux is calculated z' is taken into account.

The integration over the volume of the emitter can be performed analytically to save computation time. If a semi-infinite layer of surface $z_{ss}=0$ is emitting, the integral must be performed from $-\infty$ to 0. In this case the development is rather simple, and leads to the following expression for the monochromatic heat flux [2]

$$q_\omega(z)=\frac{k_\nu^2\Theta(\omega,T)}{2\pi^2}Re\left\{i\epsilon''_{ss}(\omega)\int_0^\infty\frac{k_\rho dk_\rho}{k''_{z_{ss}}}\begin{pmatrix}g^E_{\rho\rho}(k_\rho,z,\omega)g^{H^*}_{\theta\rho}(k_\rho,z,\omega)\\+g^E_{\rho z}(k_\rho,z,\omega)g^{H^*}_{\theta z}(k_\rho,z,\omega)\\-g^E_{\theta\theta}(k_\rho,z,\omega)g^{H^*}_{\rho\theta}(k_\rho,z,\omega)\end{pmatrix}\right\} \tag{I.34}$$

where the term $k''_{z_{ss}}$ denotes the imaginary part of the component of the wavevector perpendicular to the interface, and results from the integration over the volume of the emitter.

If the emitting layer has a finite thickness t, the integration is still straightforward, but cumber-

Cette thèse est accessible à l'adresse : http://theses.insa-lyon.fr/publication/2016LYSEI103/these.pdf
© [E. Blandre], [2016], INSA Lyon, tous droits réservés

some. In the end, the different factors inside the integral are found as

$$g^E_{\rho\rho} g^{H*}_{\theta\rho} + g^E_{\rho z} g^{H*}_{\theta z} = \frac{i k_{z_l} k_l^*}{8|k_{ss}|^2 |k_{z_{ss}}|^2 k'_{z_{ss}} k''_{z_{ss}} k_l} \times$$
$$\begin{pmatrix} k'_{z_{ss}} (e^{2k''_{z_{ss}} t - 1})[-|A^p|^2 e^{-2k''_{z_l}(z-z_l)} - A^p B^{p*} e^{2ik'_{z_l}(z-z_l)} \\ +A^{p*} B^p e^{-2ik'_{z_l}(z-z_l)} + |B^p|^2 e^{2k''_{z_l}(z-z_l)}] \\ +k'_{z_{ss}} (1 - e^{-2k''_{z_{ss}} t})[-|C^p|^2 e^{-2k''_{z_l}(z-z_l)} - C^p D^{p*} e^{2ik'_{z_l}(z-z_l)} \\ +D^p C^{p*} e^{-2ik'_{z_l}(z-z_l)} + |D^p|^2 e^{2k''_{z_l}(z-z_l)}] \\ +ik''_{z_{ss}} (1 - e^{2ik'_{z_{ss}} t})[C^p A^{p*} e^{-2k''_{z_l}(z-z_l)} + C^p B^{p*} e^{2ik'_{z_l}(z-z_l)} \\ -D^p A^{p*} e^{-2k''_{z_l}(z-z_l)} - D^p B^{p*} e^{2k''_{z_l}(z-z_l)}] \\ +ik''_{z_{ss}} (e^{-2ik'_{z_{ss}} t} - 1)[A^p C^{p*} e^{-2k''_{z_l}(z-z_l)} + A^p D^{p*} e^{2ik'_{z_l}(z-z_l)} \\ -B^p C^{p*} e^{-2ik'_{z_l}(z-z_l)} - B^p D^{p*} e^{2k''_{z_l}(z-z_l)}] \end{pmatrix} \tag{I.35}$$

and

$$g^E_{\theta\theta} g^{H*}_{\rho\theta} = \frac{i k_l^*}{8|k_{z_{ss}}|^2 k'_{z_{ss}} k''_{z_{ss}}} \times$$
$$\begin{pmatrix} k'_{z_{ss}} (e^{2k''_{z_{ss}} - 1})[|A^s|^2 e^{-2k''_{z_l}(z-z_l)} - A^s B^{s*} e^{2ik'_{z_l}(z-z_l)} \\ +A^{s*} B^s e^{-2ik'_{z_l}(z-z_l)} - |B^s|^2 e^{2k''_{z_l}(z-z_l)}] \\ +k'_{z_{ss}} (1 - e^{-2k''_{z_{ss}} t})[|C^s|^2 e^{-2k''_{z_l}(z-z_l)} - C^s D^{s*} e^{2ik'_{z_l}(z-z_l)} \\ +D^s C^{s*} e^{-2ik'_{z_l}(z-z_l)} - |D^p|^2 e^{2k''_{z_l}(z-z_l)}] \\ +ik''_{z_{ss}} (1 - e^{2ik'_{z_{ss}} t})[C^s A^{s*} e^{-2k''_{z_l}(z-z_l)} - C^s B^{s*} e^{2ik'_{z_l}(z-z_l)} \\ +D^s A^{s*} e^{-2ik'_{z_l}(z-z_l)} - D^s B^{s*} e^{2k''_{z_l}(z-z_l)}] \\ +ik''_{z_{ss}} (e^{-2ik'_{z_{ss}} t} - 1)[A^s C^{s*} e^{-2k''_{z_l}(z-z_l)} - A^s D^{s*} e^{2ik'_{z_l}(z-z_l)} \\ +B^s C^{s*} e^{-2ik'_{z_l}(z-z_l)} - B^s D^{s*} e^{2k''_{z_l}(z-z_l)}] \end{pmatrix} \tag{I.36}$$

Injecting expressions 1.35 and I.36 into I.27 results in the expression of the monochromatic heat flux for an emitting layer with finite thickness. The only remaining unknowns to compute the monochromatic radiative heat flux are the coefficients A, B, C and D in the layer(s) where the flux is calculated. Calculation of the coefficients is performed using a S-matrix approach [1, 2], presented in Appendix A.

The FE approach and the S-matrix algorithm to calculate the Green's tensor were implemented in a simulation code. Its validity was checked for two cases: with a semi-infinite emitter and with an emitter of finite thickness. We first computed the net monochromatic and total heat flux between two semi-infinite media made of a fictitious material, and reproduced the results given in [32]. For an emitting film, we validated our code with the results given in [24], that consider the radiative heat transfer between two SiC films. The relative error between the results never exceeded 1%.

Cette thèse est accessible à l'adresse : http://theses.insa-lyon.fr/publication/2016LYSEI103/these.pdf
© [E. Blandre], [2016], INSA Lyon, tous droits réservés

I.4 Conclusions

We have presented the Planck's law of thermal radiation, that constitutes the basis of the classical blackbody model for the thermal radiation between bodies. We have then introduced the near-field regime, that appears when two bodies are separated by a distance smaller than the thermal wavelength. Several near-field effects have been introduced, and will be detailed in Chapter IV. The impact of interference phenomena will also be considered in the following: on the far-field thermal emission of few-layer structures (Chapter III), and on the radiative heat transfer in the near-to-far field transition regime (Chapter IV). Eventually, the mathematical and numerical models based on the Fluctuational Electrodynamics approach and the calculation of the Green's functions with a S-matrix algorithm have been presented. This model will be used for the calculation of the radiative heat transfer along this manuscript, in order to take into account interference and near-field effects.

Cette thèse est accessible à l'adresse : http://theses.insa-lyon.fr/publication/2016LYSEI103/these.pdf
© [E. Blandre], [2016], INSA Lyon, tous droits réservés

Cette thèse est accessible à l'adresse : http://theses.insa-lyon.fr/publication/2016LYSEI103/these.pdf
© [E. Blandre], [2016], INSA Lyon, tous droits réservés

Chapter II

Basics of photovoltaics

Contents

In this chapter, we recall the basics of the operation of a photovoltaic (PV) cell under illumination and applied voltage. We gather the different equations that will be used to model the electrical behavior of NFR-TPV cells in Chapter V.

Photovoltaics refers to conversion of radiation energy into electricity. Photons can generate free electrical charges inside a semi-conductor. If these free charges are allowed to flow, they can generate an electrical current, and if a voltage is applied to the medium supporting the electrical current, an electrical power can be provided by the system. The basic principles and equations of PV device operations given in the following are taken from textbooks [34, 35, 36, 37].

II.1 Absorption of light and generation of free charges

In a semiconductor, the minimum energy to move an electron out the valence band and promote it to the conduction band is called bandgap energy (noted E_g). It is the energy difference between

Cette thèse est accessible à l'adresse : http://theses.insa-lyon.fr/publication/2016LYSEI103/these.pdf
© [E. Blandre], [2016], INSA Lyon, tous droits réservés

the lowest energy of the conduction band E_c and the highest energy of the valence band E_v

$$E_g = E_c - E_v. \tag{II.1}$$

If a photon enters a semiconductor with an energy E smaller than the bandgap ($E < E_g$), it is likely to be absorbed by the heat carriers (i.e. by the crystalline lattice or by the free electrical charges). This absorption will generate only heat inside the semiconductor. However, if the photon has an energy larger than the bandgap of the semiconductor ($E \geq E_g$), an electron can possibly be extracted from the valence band to the conduction band, generating a negative free electrical charge. The free electron will also leave a hole in the valence band. This hole can be considered as being a positively charged free electrical carrier, and like an electron, can flow through the semiconductor. The pair of positively and negatively electrical charges generated by the absorption of a photon with sufficient energy is called electron-hole pair (EHP). A photon with an energy larger than the bandgap ($E > E_g$) will yield its energy to an electron that will reach an energy level greater than the conduction band. The excess of energy of the electron will then be transferred to the lattice and the free carriers by a process called thermalization, leading to the generation of heat.

II.2 Doping

Building a PV cell requires the doping of a semiconductor with positive or negative charges (see section II.4). In the following, we give the example of the doping process of group IV semiconductors (e.g. silicon), but the same principle can be applied to III-V semiconductors (e.g. InSb, GaSb). To dope a semiconductor negatively (n-type), pentavalent (group V) atoms (e.g. phosphorous) are inserted inside the semiconductor lattice. As the atoms of the lattice of group IV semiconductors are tetravalent, the presence of the group V atoms will lead to an excess of one electron per atom. To dope a semiconductor with holes (p-type), the same principle is used with trivalent (group III) atoms (e.g. boron). A schematic of the doping process is depicted in Fig. II.1.

As a result, a n-type semiconductor will present an excess of electrons (negatively charged electrical charges) due to a concentration of donors N_d, while a p-type material will have a default of electrons due to a concentration of acceptors N_a (or an excess of holes, positively charged electrical charges).

Cette thèse est accessible à l'adresse : http://theses.insa-lyon.fr/publication/2016LYSEI103/these.pdf
© [E. Blandre], [2016], INSA Lyon, tous droits réservés

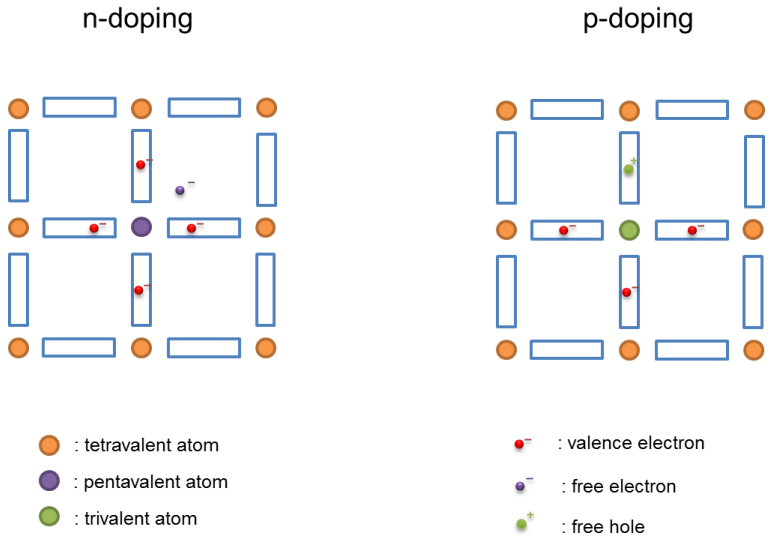

Figure II.1: Schematic representation of the p-type and n-type dopings for group IV semiconductors.

II.3 Intrinsic carrier concentration and carrier density at equilibrium

Electrical carriers can be thermally excited from the valence band to the conduction band. Therefore, at a given temperature T, the concentration of free carriers is nonzero even for an intrinsic material. This charge concentration, called the intrinsic carrier concentration, is a function of temperature, and also of the band structures of the semiconductor

$$n_i(T) = \sqrt{N_c(T)N_v(T)}e^{\frac{-E_g(T)}{2k_bT}}, \tag{II.2}$$

where N_c and N_v are the effective densities of states in the conduction and valence bands, respectively. The intrinsic concentration depends on temperature: first, the band structure (thus N_c, N_v and E_g) is affected by the variations of temperature. Second, when the temperature rises, more free carriers are likely to be thermally excited. It is also important to underline that the intrinsic carrier concentration depends on the bandgap E_g. For low-bandgap semiconductors, such as some III-V compounds (GaSb, InSb), the intrinsic carrier concentration will be larger than for semiconductors with larger bandgaps. For a doped material, the concentration of electrons and holes at equilibrium (without illumination or applied voltage), n_0 and p_0, are related to the doping level and the intrinsic carrier concentration, such that

$$n_0 = \frac{n_i^2}{N_a} \tag{II.3}$$

Cette thèse est accessible à l'adresse : http://theses.insa-lyon.fr/publication/2016LYSEI103/these.pdf
© [E. Blandre], [2016], INSA Lyon, tous droits réservés

in a p-doped material, and

$$p_0 = \frac{n_i^2}{N_d} \tag{II.4}$$

in a n-doped material. Here, N_a and N_d are the donor and acceptor concentrations.

II.4 pn-junction

To collect electrical energy from photogeneration, it is necessary to use a junction, formed by the contact of two regions with a different doping. A pn-junction is constituted of a p-doped and a n-doped region. When the two regions are put in contact (as depicted in Fig. II.2), the holes (or electrons) in excess in the p-region (n-region) diffuse to the n-region (p-region) where their concentration is less. As a result, the acceptors and donors are concentrated near the junction, leaving a zone depleted of free electrical charges, called depletion region. The variation of the spatial charge density near the junction leads to a variation of the electrostatic potential, and the creation of an electric field. The electric field induces a drift current that balances the diffusion current at equilibrium.

The spatial distribution of the electric field E or the electrostatic potential V is linked to the spatial distribution of the electrical charges through Poisson's equation

$$\frac{dE(z)}{dz} = -\frac{d^2V(z)}{dz^2} = -\frac{e}{\epsilon_r}\left\{n(z) - p(z) + N_a(z) - N_d(z)\right\}, \tag{II.5}$$

where z is the position inside the pn-junction, e is the elementary charge of the electron, ϵ_r is the relative permittivity of the semiconductor. The terms inside the brackets correspond to the spatial distribution of the electrical charge density: n is the density of free electrons, p is the density of free holes, N_a and N_d are the densities of positive and negative electrical charges due to the doping, respectively. The motion of electron and holes is ruled by transport equations. They state that the current density for both electrons and holes is the sum of two currents: the drift current corresponds to the motion of the free charges when they are pushed by the electric field. The diffusion current implies that carriers tend to diffuse inside the medium toward the region where their concentration is less. The transport equations are written in 1D and steady state as

$$J_n(z) = en(z)\mu_n E(z) + eD_n\frac{dn(z)}{dz} \tag{II.6}$$

for the electrons, and

$$J_p(z) = ep(z)\mu_p E(z) - eD_p\frac{dp(z)}{dz} \tag{II.7}$$

for the holes. In the transport equations, J_n and J_p are the electron and hole current densities, respectively. μ_n and μ_p are the mobilities of electrons and holes, D_n and D_n are their diffusion

Cette thèse est accessible à l'adresse : http://theses.insa-lyon.fr/publication/2016LYSEI103/these.pdf
© [E. Blandre], [2016], INSA Lyon, tous droits réservés

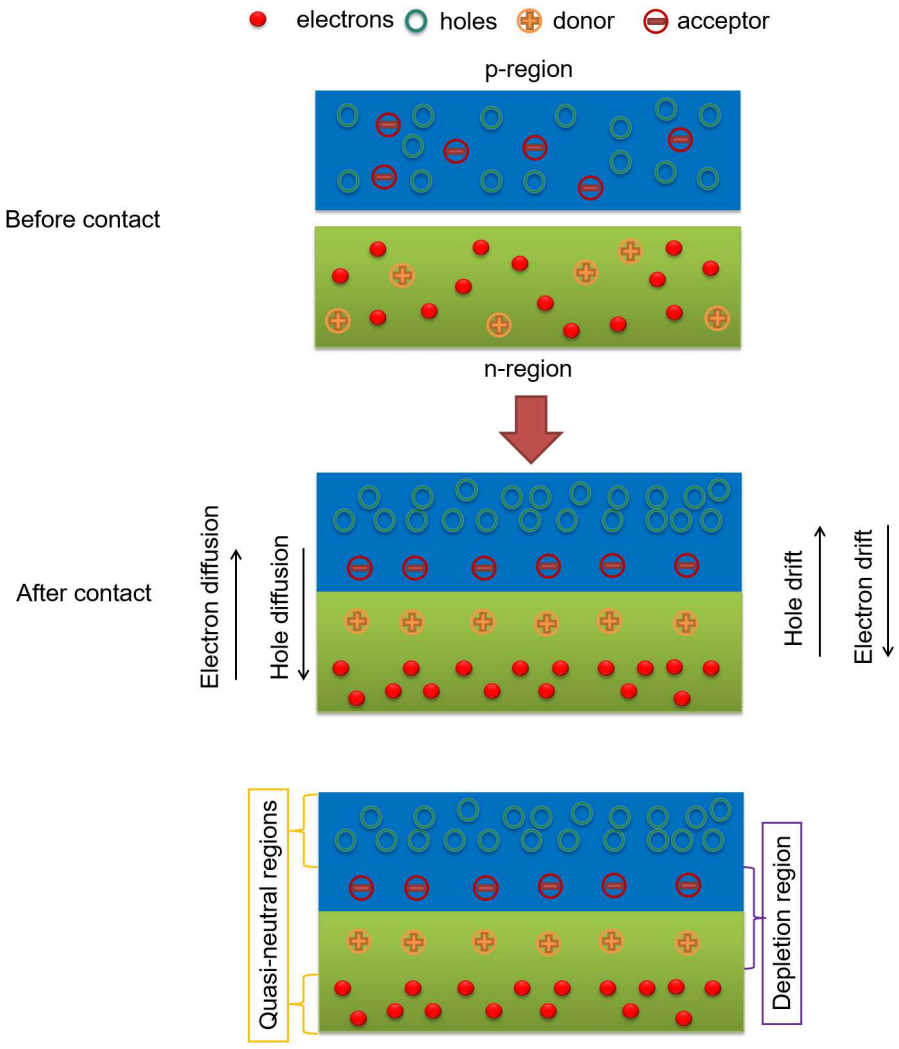

Figure II.2: Schematic representation of the formation of a pn-junction.

coefficients. The diffusion coefficients are linked to the mobilities of the electrons and holes following Einstein's relation

$$D_{n,p} = \frac{k_b T \mu_{n,p}}{e}. \tag{II.8}$$

II.5 Generation and recombination in a pn-junction

II.5.1 Generation rate of EHPs

Under illumination, EHPs are generated inside a pn-junction. For a given frequency ω, the spectral distribution of the local generation rate of EHPs (G_ω) corresponds to the number of EHPs generated per unit volume and per unit time. It is the product of the interband absorption coeffi-

Cette thèse est accessible à l'adresse : http://theses.insa-lyon.fr/publication/2016LYSEI103/these.pdf
© [E. Blandre], [2016], INSA Lyon, tous droits réservés

cient ($\kappa^{IB}(z)$) and the incident radiation power q_ω^{inc}, divided by the energy of a photon [4]

$$G_\omega(z) = \frac{q_\omega^{inc}(z)}{\hbar\omega}\kappa_\omega^{IB}. \tag{II.9}$$

The interband absorption coefficient corresponds to the absorption coefficient for frequencies above the bandgap and for the mechanism that pulls an electron from the valence band to the conduction band. The incident radiative power can be determined by means of radiative heat transfer simulations (see Chapter I). The integration over all frequencies of the spectral distribution of the local generation rate allows obtaining the total local generation rate.

II.5.2 Band-to-band (radiative) recombination

Once EHPs are generated, they have to flow to generate an electrical current. While they flow, they can fall from the conduction to the valence band through different recombination process. The first recombination process is the band-to-band recombination. In this process, a free electron meeting a free hole falls directly from the conduction band to the valence band while generating a photon. As the energy yield by the charge is equal to the bandgap of the semiconductor, the photon emitted carries the bandgap energy. The band-to-band recombination process corresponds to the spontaneous emission process opposite to the interband absorption process and thus is called radiative recombination (Fig. II.3). The radiative recombination rate can be modeled as the product of the density of electron and holes, multiplied by a coefficient of proportionality B called bimolecular recombination coefficient

$$R_{rad}(z) = B\left(n(z)p(z) - n_i^2\right). \tag{II.10}$$

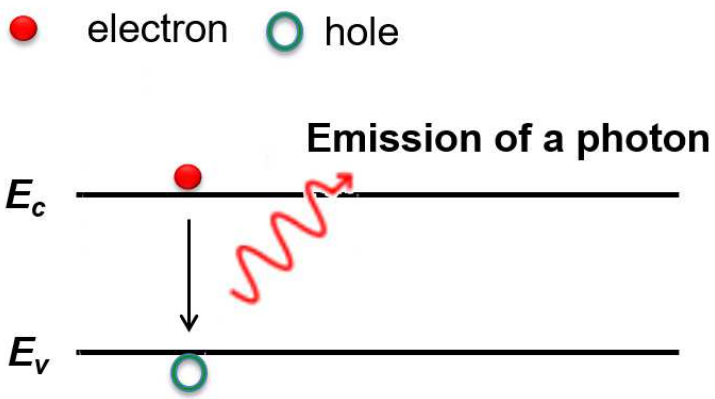

Figure II.3: Schematic representation of band-to-band (radiative) recombination.

The determination of the value of the bimolecular recombination coefficient is a complex topic, even for silicon which is the most used semiconductor for solar cells. Indeed, its value depends on the chances that an emitted photon leaves the pn-junction or is re-absorbed by the cell (photon recycling). Measurement of the radiative behavior of PV cells were performed to quantify this

Cette thèse est accessible à l'adresse : http://theses.insa-lyon.fr/publication/2016LYSEI103/these.pdf
© [E. Blandre], [2016], INSA Lyon, tous droits réservés

coefficient [38, 39, 40], but the comparison of the data of different studies exhibited a difference of orders of magnitude [38]. The problem is even more complex in near-field, where evanescent modes have to be accounted for. An accurate determination of the bimolecular radiative recombination coefficient therefore requires the calculation of the emission of the PV cell toward its environment.
The expression of the radiative recombination rate can be simplified if the density of excess of photogenerated carriers is low compared to the doping (low-injection regime). If the density of electron is lower than the doping concentration in the p-region ($N_d >> p$), the radiative recombination rate reads

$$R_{\text{rad}}(z) = B\left(N_a(z)\Delta n(z)\right) = \frac{\Delta n(z)}{\tau_n^{\text{rad}}}. \tag{II.11}$$

Similarly in the n-region if the density of holes is lower than the doping concentration ($N_a >> n$), the recombination rate can be written as

$$R_{\text{rad}}(z) = B\left(N_d(z)\Delta p(z)\right) = \frac{\Delta p(z)}{\tau_p^{\text{rad}}}. \tag{II.12}$$

In Eq. II.11 and II.12, Δn and Δp are the density in excess of electrons and holes, respectively. They are the difference between the charge density and the charge density at equilibrium:

$$\begin{aligned} \Delta n &= n - n_0, \\ \Delta p &= p - p_0. \end{aligned} \tag{II.13}$$

$\tau_{n,p}^{\text{rad}}$ are the radiative lifetime of the free electrical carriers, who are expressed as:

$$\tau_n^{\text{rad}} = \frac{1}{BN_a}, \tag{II.14}$$

$$\tau_p^{\text{rad}} = \frac{1}{BN_d}. \tag{II.15}$$

Is is important to note that with this model, it is implicitly assumed that the lifetimes do not depend on location in the cell, which is obviously debatable.

II.5.3 Shockley-Read-Hall (SRH) recombination

The second recombination process is called Shockley-Read-Hall (SRH) recombination. In this case, an electron falls into the valence band, but indirectly via a trap level (Fig. II.4). As a consequence, there is no emission of a photon, but the energy released is absorbed by the lattice,

Cette thèse est accessible à l'adresse : http://theses.insa-lyon.fr/publication/2016LYSEI103/these.pdf
© [E. Blandre], [2016], INSA Lyon, tous droits réservés

generating heat. The SRH recombination rate can be expressed as

$$R_{\mathrm{SRH}}(z) = \frac{n(z)p(z) - n_i^2}{\tau_p^{\mathrm{SRH}}(n(z) + n_i e^{\frac{E_t - E_i}{k_b T}}) + \tau_n^{\mathrm{SRH}}(p(z) + n_i e^{\frac{E_t - E_i}{k_b T}})}, \tag{II.16}$$

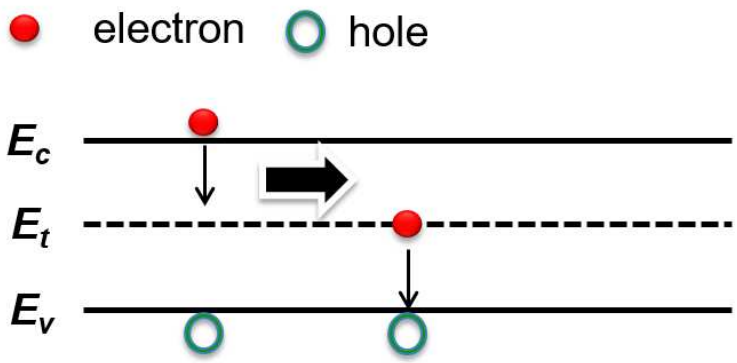

Figure II.4: Schematic representation of SRH recombination.

where τ_n^{SRH} and τ_p^{SRH} are the lifetimes of electrons and holes due to the SRH recombination process. E_t is the energy of the trap, and E_i is the intrinsic energy level. It is often considered that the traps lie in the intrinsic level in the middle of the bandgap. Therefore, $E_t - E_i = 0$ [41]. Similarly to the radiative recombination case, a simpler expression can be extracted at low-injection levels. In a n-doped region:

$$R_{\mathrm{SRH}}(z) = \frac{\Delta p(z)}{\tau_p^{\mathrm{SRH}}}, \tag{II.17}$$

while in a p-doped material ($N_a >> n$):

$$R_{\mathrm{SRH}}(z) = \frac{\Delta n(z)}{\tau_n^{\mathrm{SRH}}}. \tag{II.18}$$

II.5.4 Auger recombination

The last recombination process is called Auger recombination. It involves three electrical charges, either two electrons and one hole, or two holes and one electron. In an Auger process, an electron falls from the valence band to the conduction band, like in a band-to-band recombination. However, instead of the emission of a photon, the energy is yielded to another electron. The excited electron then releases its excess of energy through a thermalization process (Fig. II.5). The Auger recombination rate can be written as

$$R_{\mathrm{Auger}}(z) = C_n n(z)(p(z)n(z) - n_i^2) + C_p p(z)(p(z)n(z) - n_i^2). \tag{II.19}$$

The sum of the two terms corresponds to the two possible processes (two holes and one electron,

Cette thèse est accessible à l'adresse : http://theses.insa-lyon.fr/publication/2016LYSEI103/these.pdf
© [E. Blandre], [2016], INSA Lyon, tous droits réservés

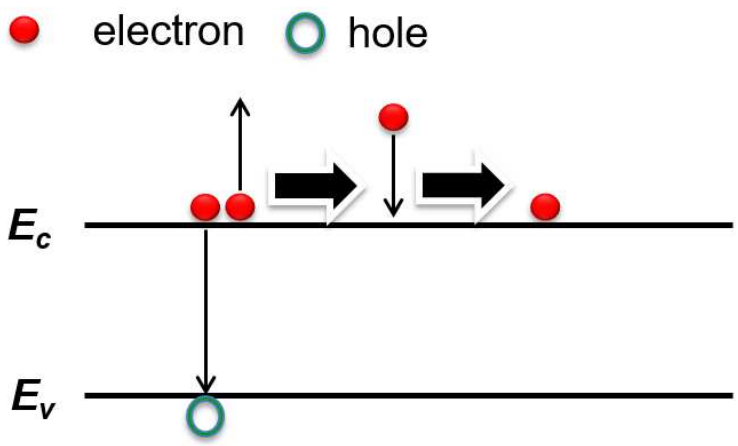

Figure II.5: Schematic representation of Auger recombination.

or two electrons and one hole). C_n and C_p are the Auger coefficients for electrons and holes. In low-injection, the Auger recombination rate reads

$$R_{\text{Auger}}(z) = C_n \Delta n(z) N_a^2 = \frac{\Delta n(z)}{\tau_n^{\text{Auger}}} \tag{II.20}$$

for a p-doped region, and

$$R_{\text{Auger}}(z) = C_p \Delta p(z) N_d^2 = \frac{\Delta p(z)}{\tau_p^{\text{Auger}}} \tag{II.21}$$

for a n-doped region. $\tau_{n,p}^{\text{Auger}}$ are the lifetimes of electrons and holes due to Auger recombination

$$\tau_n^{\text{Auger}} = \frac{1}{C_n N_a^2}, \tag{II.22}$$

$$\tau_p^{\text{Auger}} = \frac{1}{C_p N_d^2}. \tag{II.23}$$

The total recombination rate R is the sum of the recombination rates of the three different processes. If the low-injection approximation is assumed, it takes the form

$$\begin{aligned} R &= R_{\text{rad}} + R_{\text{SRH}} + R_{\text{Auger}} \\ &= \Delta n \left(\frac{1}{\tau_n^{\text{rad}}} + \frac{1}{\tau_n^{\text{SRH}}} + \frac{1}{\tau_n^{\text{Auger}}} \right) \\ &= \frac{\Delta n}{\tau_n} \end{aligned} \tag{II.24}$$

Cette thèse est accessible à l'adresse : http://theses.insa-lyon.fr/publication/2016LYSEI103/these.pdf
© [E. Blandre], [2016], INSA Lyon, tous droits réservés

in the p-region, and:

$$\begin{aligned} R &= \Delta p \left(\frac{1}{\tau_p^{\text{rad}}} + \frac{1}{\tau_p^{\text{SRH}}} + \frac{1}{\tau_p^{\text{Auger}}} \right) \\ &= \frac{\Delta p}{\tau_p} \end{aligned} \tag{II.25}$$

in the n-region. τ_n and τ_p are the total lifetimes due to the three types of recombination. One can note that they are linked to the lifetimes of the different processes by a Matthiessen's rule.

Another set of equations results from the generation and recombination inside the pn-junction. The continuity equations state that any spatial variation of the electron and hole current densities is due to the spatial distribution of the generation and recombination rate

$$-\frac{1}{e}\frac{dJ_n(z)}{dz} = G(z) - R(z) \tag{II.26}$$

for electrons, and

$$\frac{1}{e}\frac{dJ_p(z)}{dz} = G(z) - R(z) \tag{II.27}$$

for holes. The term $G-R$ is the net generation-recombination rate. Poisson's equation, continuity equations and transport equations for electrons and holes form the basic equations for modeling the transport of electrical charges inside a semiconductor, and have to be solved to determine the performances of a PV cell. The whole model is called Drift-Diffusion (DD) model.

II.6 J-V characteristic of a pn-junction

The photogeneration in a pn-junction leads to an electrical current. An electrical power P can be generated if the pn-junction is connected to a load with voltage V_f. The electrical power is for a constant intensity

$$P = J \times V_f, \tag{II.28}$$

J is the sum of the electron and hole currents

$$J = J_n + J_p. \tag{II.29}$$

When a forward bias (i.e. a positive difference of potential from the n-region to the p-region) is applied to the pn-junction, the level of carrier densities rises, inducing a recombination current that will decrease the electrical current J. At $V_f = 0$, the electrical current is called short-circuit current (J_{SC}). At a given voltage V_{OC} (open-circuit voltage), the recombination current will eventually balance the current due to the photogenerated electrical carriers. The trade-off between

Cette thèse est accessible à l'adresse : http://theses.insa-lyon.fr/publication/2016LYSEI103/these.pdf
© [E. Blandre], [2016], INSA Lyon, tous droits réservés

the decrease of the electric current and the increase of the voltage leads to a maximum of the electrical power output P_{max} at the so-called maximum power point (MPP). Fig. II.6 shows an example of J-V characteristic of a PV cell and the associated evolution of the electrical power output when voltage increases.

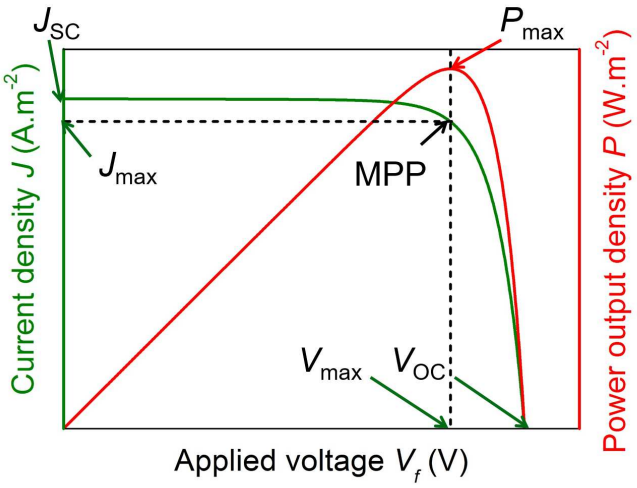

Figure II.6: Example of J-V and P-V characteristics of a PV cell.

II.7 Thermal impact on the performances of photovoltaic cells

It is known that when the temperature of PV cells increases, their performances decrease. This decay is quantified by a temperature coefficient. As in general, the decay of the maximum power output (P_{max}) with T is linear, it corresponds to the slope of the $P_{max}(T)$ curve (see Fig. II.7(a)) [3].

The increase of the temperature of a PV cell is mostly due to the different heat sources, coming for instance from the absorbed radiative energy that has not been converted into collected EHPs. One of the major consequence is the increase of the intrinsic carrier concentrations (Eq. II.1), and thus of the equilibrium carrier concentration (Eq. II.2 and II.3). It induces a stronger recombination current, which leads to a decrease of the open-circuit voltage (V_{oc}) (Fig. II.7(b)). An increase of the short-circuit current (J_{SC}) also occur when the temperature rises since the bandgap decreases with temperature, but the variations of the maximum power output are dominated by the variations of the open-circuit voltage. In the end, there is a decrease of the maximum power output of the cell. A design of TPV systems that optimizes its energy conversion performances thus requires minimizing the thermal losses in order to mitigate the cell temperature, together with the minimization of the radiative and electrical losses, or to cool the PV cell in order to decrease the temperature coefficient.

Cette thèse est accessible à l'adresse : http://theses.insa-lyon.fr/publication/2016LYSEI103/these.pdf
© [E. Blandre], [2016], INSA Lyon, tous droits réservés

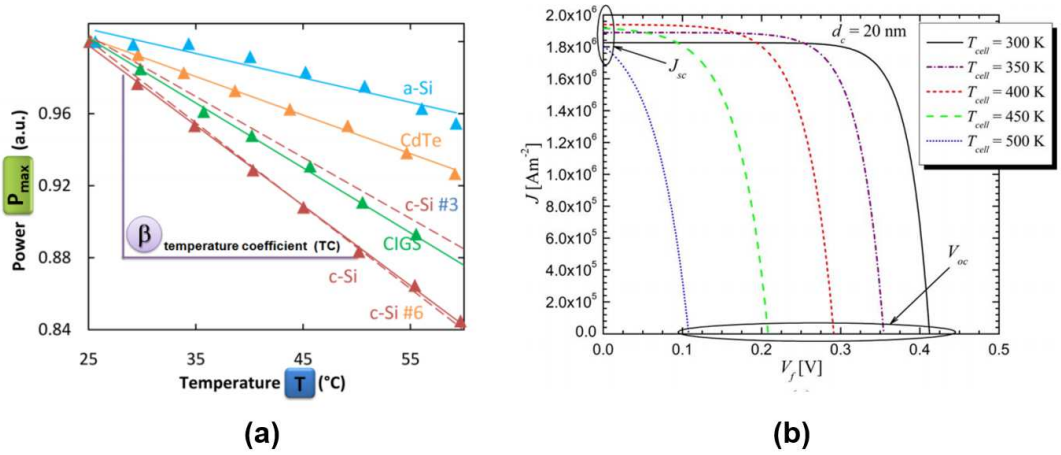

Figure II.7: (a): Relative maximum power output of different types of solar PV cell as a function of their working temperature. From [3]. (b): J-V characteristics of a InGaSb cell working under near-field regime (radiator-cell distance of 20 nm) at different cell temperatures. The radiator is made of tungsten. From [4].

II.8 Conclusions

Basics of the electrical behavior of PV cells have been presented in this chapter. The DD model will be used in Chapter V to assess the performances of selected NFR-TPV systems. In addition to simplifying the expression of the recombination rates, the low-injection approximation also allows simplifying the resolution of the DD equations (see section V.2.1). However, the validity of this approximation is questionable in the case of NFR-TPV systems, as it will be discussed in section V.2.2. By using a numerical model that solves the full DD equations (section V.2.3), the validity of the low-injection approximation will be assessed in section V.3.

Cette thèse est accessible à l'adresse : http://theses.insa-lyon.fr/publication/2016LYSEI103/these.pdf
© [E. Blandre], [2016], INSA Lyon, tous droits réservés

Chapter III

Thermal emission of few-layer structures supporting interference phenomena

Contents

Cette thèse est accessible à l'adresse : http://theses.insa-lyon.fr/publication/2016LYSEI103/these.pdf
© [E. Blandre], [2016], INSA Lyon, tous droits réservés

III.1 Introduction

The efficiency of a single p-n junction solar cell illuminated by the AM1.5 solar spectrum [15] is limited by the so-called Shockley–Queisser limit [14]. It evaluates the maximum conversion efficiency at 33% when considering a PV cell made of a material of bandgap equal to 1.34 eV. The main reason of the existence of this limit comes from the fact that the solar spectrum is broadband. Photons of energy lower than the bandgap are not harvested, and high-energy photons yield their excess of energy to the lattice and the free carriers through thermalization, generating heat. To overcome this problem, the idea to substitute the sun by another body as the source of emission of thermal radiation was introduced [42].
In solar thermophotovoltaic (STPV) systems, the sunlight radiation is converted into heat by an absorber, juxtaposed to a radiator. The radiator then re-emits thermal radiation toward a PV cell [42]. As the temperature of the emitter is much lower than the temperature of the surface of the sun ($\approx$ 5800 K), low-bandgap cells offer great potentials. According to Würfel et al. [43], STPV systems using low-bandgap cells can reach efficiencies up to 65%. Furthermore, the optical properties of the material constituting the radiator can be modified to tune its emission spectrum. Thus, the radiative losses due to absorption of sub-bandgap photons and thermalization of high-energy photons can be mitigated. A spectral filter can also be placed between the radiator and the cell to enhance the spectral selectivity of the radiative energy absorbed by the PV cell [44]. With the addition of a selective emitter and a spectral filter, the maximum conversion efficiency of STPV system was evaluated at 85% [45, 13].
To maximize the conversion of sunlight radiation into heat energy, the absorber must absorb broadband solar radiation, while mitigating its re-emission at high temperature [3]. Absorbing media made of multiwalled carbon nanotubes were considered [46]: the radiation energy is trapped inside the structure, preventing it from being reflected back to the environment. Metallo-dielectric composites [47] and one-dimensional aperiodic structures [48] were considered as well. The optical properties of rare earth materials (such as erbium and ytterbium) were used to design selective emitter [49, 50, 51]. Refractory metals (such as tungsten and molybdenum) were also considered [52]. It was shown that the spectral selectivity can be enhanced using, 1D [53, 54, 55], 2D [56], and 3D [57] photonic crystals. Especially, Nefzaoui et al. [53] emphasized the high-potential of one-dimensional multilayered structures supporting interference phenomena for selective emitter applications. Fabry-Pérot interferences occur in structures made of a periodic stacking of transparent and reflective layers, deposited on a metallic substrate. Interferences allow tailoring the spectrum of thermal radiation emitted by the radiator. Experimental demonstrations of this phenomenon were performed by the group of Zhuomin Zhang [58, 59, 60]: measurements of the spectral reflectance of a resonant layer between two metallic layer exhibits peaks due to interference phenomena.
In the first section of this Chapter, we study the spectral hemispherical emissivity of few-layers structures supporting interference phenomena, in order to design a selective radiator for TPV applications. A refractory metal with interesting intrinsic optical properties in the infrared for the TPV case under consideration constitutes the reflective layers of the radiator. The spectral selectivity of the structure is enhanced by the addition of transparent semiconductor layers inducing

Cette thèse est accessible à l'adresse : http://theses.insa-lyon.fr/publication/2016LYSEI103/these.pdf
© [E. Blandre], [2016], INSA Lyon, tous droits réservés

interference phenomena.
First, we analyze the Fabry-Pérot interferences occurring inside the different layers of the system. Then, we use the understanding of the interference phenomena to design a selective radiator for TPV applications. We quantify the efficiency of the structures by defining a figure of merit.

In the following section, we investigate the dependence on temperature of the total hemispherical emissivity of the same type of structure. Celanovic et al. [61] studied the emissivity of a simple structure composed of a Fabry-Pérot layer deposited on a substrate, and reported the increase of the spectral hemispherical emissive power of the emitter when interferences occur inside the layer. It is therefore possible to increase the total hemispherical emissivity of structures using interference phenomena. We investigate how to maximize this effect. As for the dependence on temperature of the hemispherical emissivity, it was shown that variations with temperature of the dielectric function of SiC modifies the spectral hemispherical emissivity of 2D selective emitter when the temperature varies. Especially, the broadening and the shift in frequency of the polariton resonance when temperature increases were reported, showing that calculation using the dielectric function of SiC at ambient temperature leads to inaccurate evaluation of the thermal emission. The total hemispherical emissivity of diamond-like carbon [62], copper surfaces [63] and other materials used in cryogenics [64] were experimentally investigated. A variation of the total hemispherical emissivity of the different materials when their temperature increases was reported. In our study, we calculate the temperature-dependent dielectric function of the metallic material constituting the emitter to account for the evolution with temperature of its optical properties when the temperature rises. We highlight the importance of taking into account this phenomena.

III.2 Design of a radiator for thermophotovoltaic applications

The work reported in this section was done in collaboration with Dr. Makoto Shimizu from Tohoku University in Sendai, Japan, who is working in the research group of Prof. Hiroo Yugami. Prof. Yugami's team is investigating solar thermophotovoltaic (STPV) systems by means of an experimental setup [65, 66]. During the presence of Dr. Shimizu in our research group as an invited Professor, we focused on the selective emitter of the STPV system.

III.2.1 Description of the problem

The cell used in Dr. Shimizu's experimental setup is made of gallium antimonide (GaSb) [66]. The bandgap energy of GaSb is $E_g = 0.726$ eV, which corresponds to a photon wavelength in vacuum of $\lambda_g = 1.7$ µm. Therefore, the spectrum of thermal radiation emitted by the radiator should be maximized in a spectral range between 0 and λ_g, and as low as possible above λ_g. It means that the spectral hemispherical emissivity (as defined in Chapter I) of the emitter should be a step function of value 1 below λ_g and 0 above. This defines the ideal spectral hemispherical emissivity of the perfect emitter (PE) that will be our objective (see Fig. III.1).

In the following section, it is assumed that the the optical properties of the materials under con-

Cette thèse est accessible à l'adresse : http://theses.insa-lyon.fr/publication/2016LYSEI103/these.pdf
© [E. Blandre], [2016], INSA Lyon, tous droits réservés

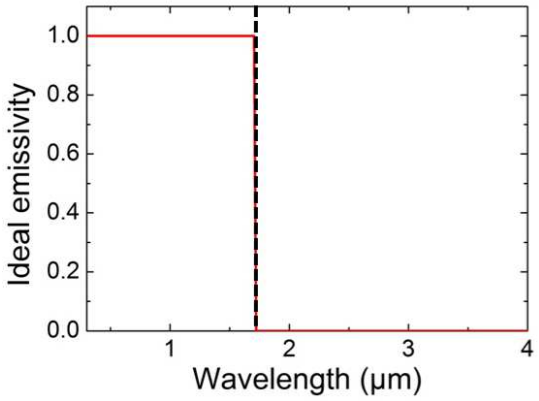

Figure III.1: Ideal spectral hemispherical emissivity for a PV cell of bandgap λ_g.

sideration are constant when temperature varies. Therefore, the spectral hemispherical emissivity of the structure will be independent of temperature.

III.2.2 Methodology for the calculation of the spectral hemispherical emissivity

The Fluctuational Electrodynamics (FE) approach presented in Chapter I is used to compute the spectral hemispherical emissivity of the structures. A schematic representation of the system is depicted in Fig. III.2. In each structure, medium 0 is the substrate and considered as semi-infinite. The far-field monochromatic radiative heat flux is computed by considering vacuum in front of the emitter, and by calculating the Poynting vector after the interface of the last layer of the system, at position z_{N+1}^{+}.

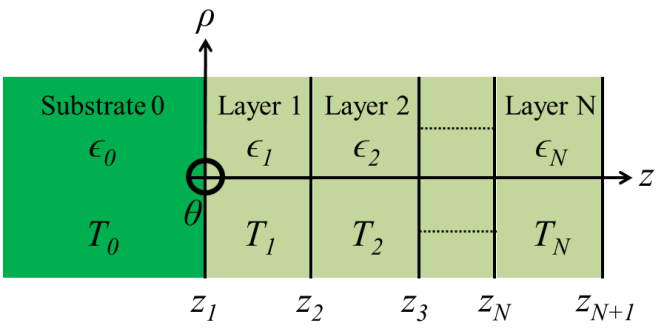

Figure III.2: Schematic representation of the one-dimensional system under consideration. Each layer l is characterized by its dielectric function ϵ_l, its temperature T_l (considered constant in section III.2) and its boundaries z_l and z_{l+1}.

Each layer is characterized by its optical properties (complex dielectric function ϵ). If an emitter constituted of several layers is considered, the total heat flux emitted by this structure is the summation of the heat fluxes emitted by each layer. This approach allows separating and analyzing the

Cette thèse est accessible à l'adresse : http://theses.insa-lyon.fr/publication/2016LYSEI103/these.pdf
© [E. Blandre], [2016], INSA Lyon, tous droits réservés

contributions of each layer to the emission. In contrast to many works, [60, 53, 67, 58, 68, 69], the Fluctuational Electrodynamics method does not rely on Kirchhoff's law, i.e. we do not compute the reflectivity to determine the absorptivity, and hence the emissivity. However, the equivalence of the two methods was emphasized in a previous work [70]. Both of them allow considering temperature profiles in the emitting layers when the multilayer structure is not at equilibrium.

In the following, we restrict ourselves to the equilibrium case: the temperature is uniform in the radiator. For simple systems, we can calculate analytically the Weyl components of the Green's tensors using the S-matrix approach (see Appendix A). In the following, we will give the example of the spectral hemispherical emissivity of a substrate and of a thin layer deposited on a substrate. The spectral hemispherical emissivity of a substrate in the absence of any other layer can be written as [71, 5]

$$\varepsilon_{\omega}^{\text{Substrate alone}} = \frac{1}{k_{\nu}^2}\int_0^{k_{\nu}} k_{\rho}\,dk_{\rho}\sum_{\gamma=s,p}(1-|r_{10}^{\gamma}|^2), \tag{III.1}$$

where s and p are respectively the transverse electric and the transverse magnetic polarizations, and r_{10}^{γ} is the reflection coefficient of the interface between medium 0 and 1. As only propagative modes participate to radiative emission in the far field, the integration over the parallel component of the wavevector k_{ρ} is performed from 0 to $k_{\nu} = \frac{\omega}{c_{\nu}}$. To determinate the spectral hemispherical emissivity of a single monolayer deposited on a substrate, we have to calculate the emission of the substrate in presence of the layer, and the emission of the layer in the presence of the substrate. The spectral hemispherical emissivity associated to the substrate taking into account the presence of the layer is given by [71, 5]

$$\varepsilon_{\omega}^{\text{Substrate}} = \frac{1}{k_{\nu}^2}\int_0^{k_{\nu}} k_{\rho}\,dk_{\rho}\sum_{\gamma=s,p}\frac{(1-|r_{10}^{\gamma}|^2)(1-|r_{12}^{\gamma}|^2)}{|1-r_{10}^{\gamma}r_{12}^{\gamma}e^{2ik_{z1}t}|^2}, \tag{III.2}$$

where r_{10}^{γ} and r_{12}^{γ} are the Fresnel reflection coefficients of the interfaces 10 and 12, respectively. k_{z1} is the component of the wavevector perpendicular to the interface in the layer, and t is the thickness of the layer. Taking into account the presence of the substrate, the spectral hemispherical emissivity of the layer is [71, 5]

$$\varepsilon_{\omega}^{\text{Layer}} = \frac{1}{k_{\nu}^2}\int_0^{k_{\nu}} k_{\rho}\,dk_{\rho}\sum_{\gamma=s,p}(1-|R_1^{\gamma}|^2-|T_1^{\gamma}|^2), \tag{III.3}$$

where R_1^{γ} and T_1^{γ} are the reflection and transmission coefficients of the film, and are functions of the Fresnel reflection and transmission coefficients [24, 71]

$$R_1^{\gamma} = \frac{r_{01}^{\gamma} + r_{12}^{\gamma}e^{2ik_{z1}t}}{1 + r_{01}^{\gamma}r_{12}^{\gamma}e^{2ik_{z1}t}}, \tag{III.4}$$

$$T_1^{\gamma} = \frac{t_{01}^{\gamma}t_{12}^{\gamma}e^{ik_{z1}t}}{1 + r_{01}^{\gamma}r_{12}^{\gamma}e^{2ik_{z1}t}}. \tag{III.5}$$

Cette thèse est accessible à l'adresse : http://theses.insa-lyon.fr/publication/2016LYSEI103/these.pdf
© [E. Blandre], [2016], INSA Lyon, tous droits réservés

Note that the terms $1 + r_{01}^{\gamma} r_{12}^{\gamma} e^{2ik_{z1}t}$ are characteristic of a Fabry-Pérot cavity, i.e. they stand for multireflections between two interfaces. Eventually, the total hemispherical emissivity of the structure is the sum $\varepsilon_{\omega}^{\text{Substrate}} + \varepsilon_{\omega}^{\text{Layer}}$.

III.2.3 Optical properties of the materials under consideration

Two different materials are considered in this section: a refractory metal, molybdenum (Mo), and a dielectric, hafnium oxide (HfO_2). The spectral values of the real part n and the imaginary part κ of the complex refractive index of both materials, taken from [72], are represented in Fig. III.3. Note that the complex refractive index N is related to the complex dielectric function ϵ

$$\epsilon = \epsilon' + i\epsilon'' = N^2 = (n + i\kappa)^2 \tag{III.6}$$

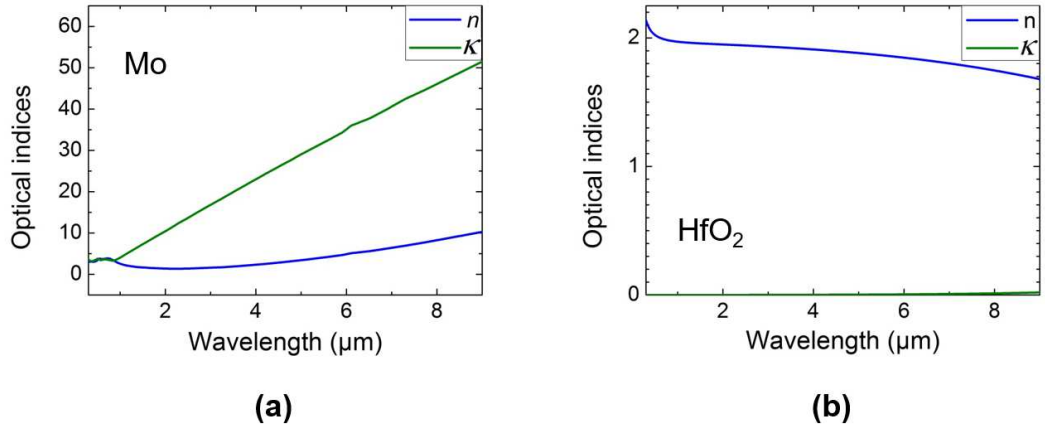

Figure III.3: Real and imaginary parts of the complex refractive index as a function of wavelength in vacuum. (a): Mo, (b): HfO_2.

Mo is a refractory metal: its fusion temperature is large (2600 K) and is thus a good candidate for constituting high-temperature radiators. For wavelengths smaller than 1 μm, its optical indices take values of the order of 3. It is rather different form classical metals (aluminum, gold or silver), that have much larger optical indices. For wavelengths larger than 1 μm the optical indices rises, and tends to these more usual metal. HfO_2 is a dielectric, and thus is very transparent in the infrared (κ is close to 0). The real part of the refractive index of HfO_2 is almost constant with wavelength. A key point to highlight is the spectral variations of the spectral reflection coefficients due to the spectral variations of the optical indices. Three types of interfaces are considered in this study:

- Mo-HfO_2
- Mo-vacuum
- HfO_2-vacuum

In Fig. III.4(a), the reflection coefficients in normal incidence for the s polarization are repre-

Cette thèse est accessible à l'adresse : http://theses.insa-lyon.fr/publication/2016LYSEI103/these.pdf
© [E. Blandre], [2016], INSA Lyon, tous droits réservés

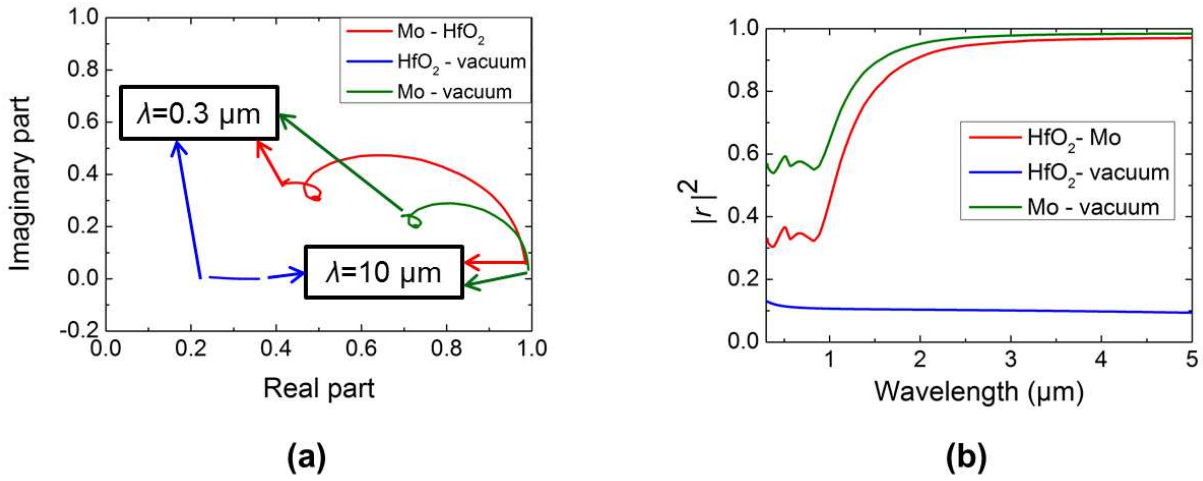

Figure III.4: (a): Reflection coefficients of the different interfaces in the complex space for a wavelength (in vacuum) range between 0.3 and 10 μm, (b): Spectral variations of the squared modulus of the reflection coefficients.

sented in the complex space. The HfO_2-vacuum reflection coefficient has small variations and it is worth noticing that the phase (represented by the argument of the complex reflection coefficient) is close to 0 for all wavelengths. Interfaces involving Mo have large spectral variations of their reflection coefficients, due to the spectral variations of the optical indices of Mo. One can note that the phase of the reflection coefficient tends to 0 for large wavelengths, in the spectral region where Mo has a metallic behavior. In Fig. III.4(b), the squared modulus of the reflection coefficient (normal incidence, *s* polarization) is represented as a function of wavelength in vacuum. The HfO_2-vacuum reflection coefficient takes values of around 0.1 on the whole spectral range, which is due to the small refractive index contrast between the two media. The Mo-vacuum and Mo-HfO_2 reflection coefficients exhibits two behaviors in accordance with the spectral variations of Mo. Below 1 μm, the reflectivity of the interfaces are moderate, and become close to 1 at larger wavelengths.

III.2.4 Emission of a Mo substrate

The emission of a single Mo substrate, computed using Eq. III.1, is represented in Fig. III.5. We observe that the spectral hemispherical emissivity of the Mo substrate alone exhibits two regimes. Below $\lambda = 1$ μm, the spectral hemispherical emissivity takes values around 0.5. Above $\lambda = 1$ μm the spectral emissivity drops to 0. The two regimes are due to the spectral variations of the optical indices of Mo. It was shown in a previous work [71] that dielectric substrates have a large emissvity as they are transparent, while metallic substrates have a low emissivity. As a consequence, the spectral variations of the optical indices of Mo induce a broadband spectrum in the spectral region where we want the flux to be maximum, and a spectral hemispherical emissivity close to 0 in the spectral range where no emission is desired. Therefore, Mo has interesting intrinsic properties for the selective emitter application under consideration. However the spec-

Cette thèse est accessible à l'adresse : http://theses.insa-lyon.fr/publication/2016LYSEI103/these.pdf
© [E. Blandre], [2016], INSA Lyon, tous droits réservés

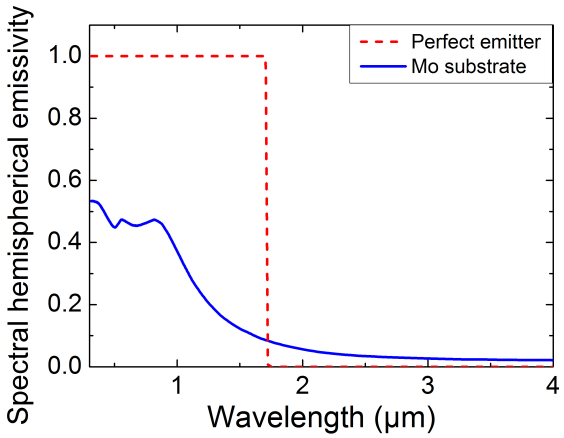

Figure III.5: Spectral hemispherical emissivity of the Mo substrate compared to the perfect emitter for the TPV application under consideration.

trum of the Mo substrate alone is still far from the ideal one (see Fig. III.5), which should emit photons that can be converted into electron-hole pairs (EHPs) and avoid low-energy photons that would potentially lead to cell heating. In the following section, we will show that it is possible to increase the spectral selectivity using structures supporting interference phenomena.

III.2.5 Emission of a HfO_2 monolayer on a Mo substrate

We now consider a structure made of a layer of HfO_2 (medium 1) of finite thickness t deposited on a Mo substrate (medium 0) and emitting towards vacuum (medium 2). The structure is referred to as monolayer on susbtrate (MOS) in the following. Fig. III.6(a) represents a schematic of the system. In Fig. III.6(b), the spectral hemispherical emissivity of the system is plotted as a function of the thickness of the oxide layer (t). Resonance branches are observed in the spectral hemispherical emissivity. They correspond to Fabry-Pérot interferences, that shift to smaller wavelengths when the thickness of the layer decreases.

Interference phenomena appear when multireflections occur in the system. In this case, multireflections can take place because HfO_2 is transparent. Therefore, waves can be reflected multiple times between the two interfaces at the boundaries of the layer before being absorbed.

A phase lag between two waves occur if their optical path is different (Fig. III.7(b)). When the phase lag between two waves is a multiple of 2π (i.e. the waves are in phase), constructive interference occurs, while waves with a phase lag that is a multiple of π interfere destructively (Fig. III.7(a)) [22]. In the following, we will derive the relation between the geometrical parameters of the systems and the wavelengths where constructive interferences occur, referred here to as conditions for constructive interference. The first approach to find them consist in analyzing the phase lags that occur for waves with different optical paths (i.e. between case 1 and 2 in Fig. I.7(b)). Phase lag can occur because of a difference of optical path length between two waves.

Cette thèse est accessible à l'adresse : http://theses.insa-lyon.fr/publication/2016LYSEI103/these.pdf
© [E. Blandre], [2016], INSA Lyon, tous droits réservés

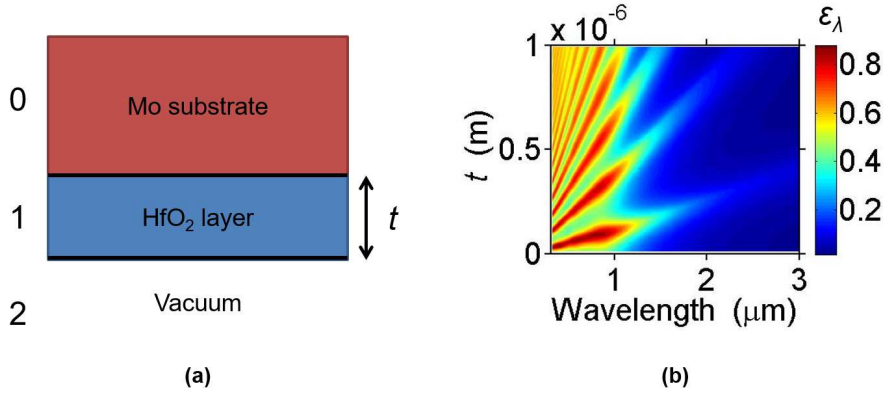

Figure III.6: (a): Schematic representation of the Mo substrate (medium 0) and the HfO_2 layer (medium 1) of thickness t emitting towards vacuum (medium 2). (b): Spectral hemispherical emissivity of the structure as a function of t.

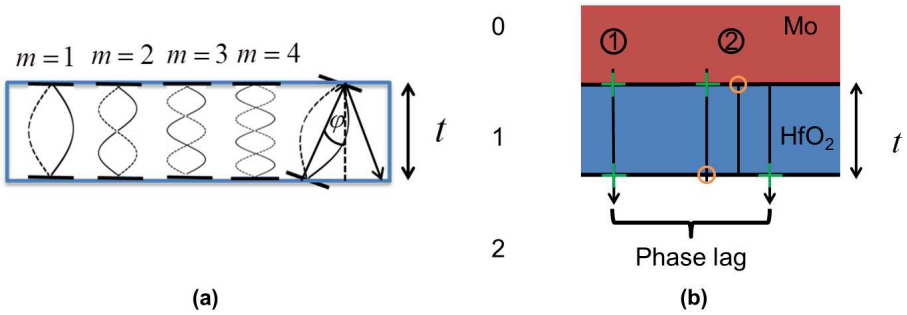

Figure III.7: (a): Schematic of interference phenomena inside a layer. (b): Schematic representation of the phase lag between two waves due to different optical paths. The green crosses represent transmissions, the orange circles represent reflections.

This phase lag δ can be written as

$$\delta = \Lambda k_\nu, \tag{III.7}$$

where k_ν is still the magnitude of the wavevector in vacuum. Λ is the optical path length, which is expressed as the distance traveled by the waves multiplied by the real part of refractive index n_1 in the layer. The phase lag due to the difference of optical path length is also the distance traveled by the wave multiplied by the magnitude of the wavevector k_i inside the medium i

$$k_i = n_i k_\nu. \tag{III.8}$$

The distance traveled by the waves between two multireflections can easily be calculated, and the optical path length is

$$\Lambda = 2nt\cos\varphi, \tag{III.9}$$

Cette thèse est accessible à l'adresse : http://theses.insa-lyon.fr/publication/2016LYSEI103/these.pdf
© [E. Blandre], [2016], INSA Lyon, tous droits réservés

where φ is the angle of incidence inside the layer where the waves are multireflected (Fig. III.7(a)). Using the fact that

$$k_\nu = \frac{\omega}{c_\nu} = \frac{2\pi}{\lambda_\nu}, \tag{III.10}$$

the phase lag due to the difference of optical path length between two waves can thus be written as

$$\delta = \frac{2nt\cos\varphi \times 2\pi}{\lambda_\nu}. \tag{III.11}$$

The second type of phase lag is that due to reflections and transmissions through interfaces between different media. The phase lags due to reflection and transmission are given by the argument of the complex reflection and transmission coefficients:

$$\phi_{\text{ref}} = \arg(r), \tag{III.12}$$

$$\phi_{\text{trans}} = \arg(t). \tag{III.13}$$

In the end, constructive interferences occur when the phase lag difference between the two waves is a multiple of 2π

$$\delta + \phi_{\text{ref}} + \phi_{\text{trans}} = 2m\pi, \tag{III.14}$$

where m is an integer. Applying this formula to the system depicted in (Fig. III.8(b)), the resonance conditions thus become

$$\frac{2nt\cos\varphi}{\lambda_\nu} + \frac{\phi_{\text{ref}}^{10} + \phi_{\text{ref}}^{12}}{2\pi} = m. \tag{III.15}$$

The relation between the thickness of the film t and the wavelength where constructive interferences occur is given by

$$t = \left(m - \frac{\phi_{\text{ref}}^{10} + \phi_{\text{ref}}^{12}}{2\pi} \right) \frac{\lambda_\nu}{2n\cos\varphi}. \tag{III.16}$$

The conditions for constructive interference depend on the angle of incidence inside the layer φ. In reality, the interference peaks in the emission spectrum are isotropic: they do not depend much on the direction [53]. To understand this phenomenon, we depicted in Fig III.8 the generic case of waves incident in a layer of refractive index n_1 and crossing an interface to a medium with a refractive index $n_2 < n_1$. The green arrow represent the normal incidence. Blue arrows corresponds to the waves that cross the interface, and therefore participate to the emission. However, above a critical angle (represented by an orange arrow), total internal reflection occur and the waves are not transmitted (red arrows).

Cette thèse est accessible à l'adresse : http://theses.insa-lyon.fr/publication/2016LYSEI103/these.pdf
© [E. Blandre], [2016], INSA Lyon, tous droits réservés

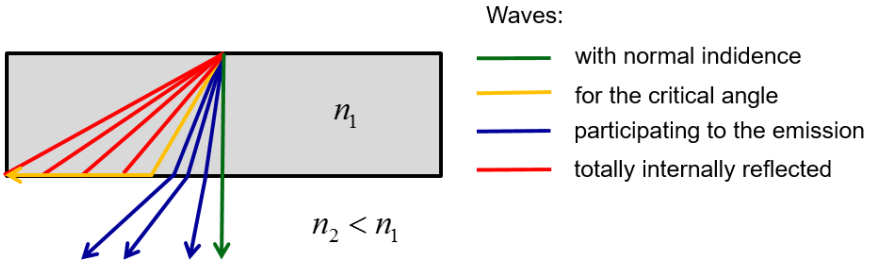

Figure III.8: Schematic representation of waves traveling from a medium of refrative index n_1 to a medium of refractive index $n_2 < n_1$. The green arrow represents the normal incidence. Blue arrows correspond to the waves that participate to the emission. The orange arrow represents the critical angle of reflection. Red arrows correspond to totally internally reflected waves.

As a result, the waves transmitted from medium 1 to medium 2 are collimated around the normal incidence. Furthermore, the cosine function has low variations close to incident angles. In conclusion, conditions for constructive interference for normal incidence is sufficient to describe the behavior of the spectral hemispherical emissivity, as following

$$t = \left(m - \frac{\phi_{\text{ref}}^{10} + \phi_{\text{ref}}^{12}}{2\pi} \right) \frac{\lambda_\nu}{2n}. \tag{III.17}$$

This constructive interference condition can also be found by analyzing the formula of the emissivity (Eqs. III.2 and III.3). The oxide layer is transparent and thin, and therefore its participation to the emission can be neglected. The emission of the substrate, given by Eq. III.2, is maximal when the denominator $|1 - r_{10}^{\gamma} r_{12}^{\gamma} e^{2ik_{z1}t_1}|^2$ is minimal. Using the trigonometric form of the complex reflection coefficients, it can be rewritten as

$$\begin{aligned} &|1 - r_{10}^{\gamma} r_{12}^{\gamma} e^{2ik_{z1}t_1}|^2 \\ &= |1 - |r_{10}^{\gamma}| e^{i\phi_{\text{ref}}^{10}} |r_{12}^{\gamma}| e^{i\phi_{\text{ref}}^{12}} e^{2ik_{z1}t_1}|^2. \\ &= |1 - |r_{10}^{\gamma}||r_{12}^{\gamma}| e^{i(2k_{z1}t_1 + \phi_{\text{ref}}^{10} + \phi_{\text{ref}}^{12})}|^2 \end{aligned} \tag{III.18}$$

The argument of the exponential is a phase term, and the denominator is minimal when it is equal to $i2\pi m$. As before the normal incidence is sufficient to describe the contructive interference behavior and k_z can reduce to k_ν. In the end, the same resonance conditions appear.

To check the validity of these constructive interference conditions, the spectral hemispherical emissivity of the MOS, superimposed with the theoretical results obtained for t with Eq. III.16 are plotted in Fig. III.9.

We observe that the theoretical conditions for constructive interference at normal incidence matches well the calculations of the spectral hemispherical emissivity. It is therefore possible to predict for a structure at which frequency the interferences will occur.

Eventually, the spectral hemispherical emissivity of the MOS is plotted in Fig. III.10. The spectral

Cette thèse est accessible à l'adresse : http://theses.insa-lyon.fr/publication/2016LYSEI103/these.pdf
© [E. Blandre], [2016], INSA Lyon, tous droits réservés

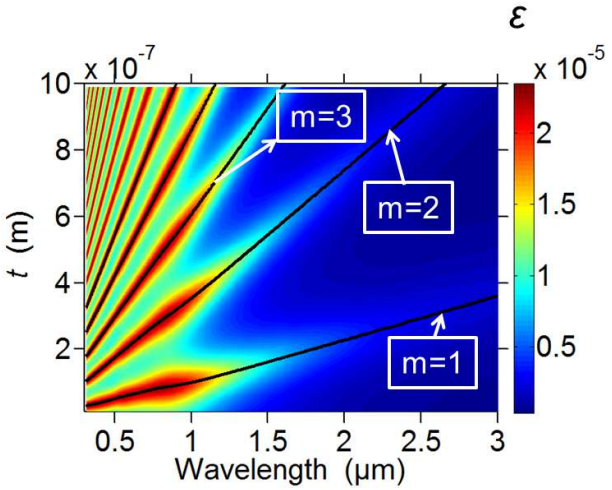

Figure III.9: Spectral hemispherical emissivity of the structure as a function of the thickness of the film t. The black lines represent the theoretical conditions for constructive interference at normal indidence.

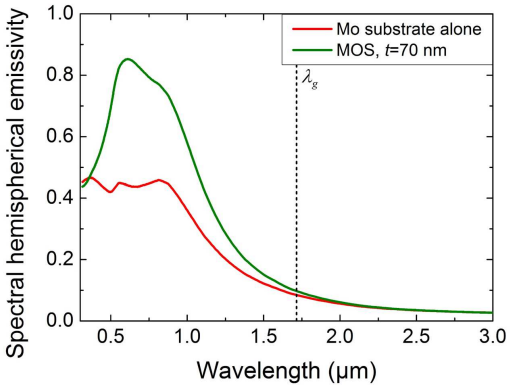

Figure III.10: Spectral hemispherical emissivity of the MOS for $t = 70$ nm, compared with the spectral hemispherical emissivity of the Mo substrate alone. The dashed line represents the cutoff wavelength λ_c.

hemispherical emissivity of the Mo substrate alone is also plotted for comparison. It is observed that with using a non-emitting oxide layer acting like a Fabry-Pérot resonator, the spectral hemispherical emissivity has been enhanced below the cutoff wavelength λ_g, while keeping low values above the cutoff.

III.2.6 Impact of a thin Mo layer on the emission of the MOS structure

To further enhance the spectral selectivity, additional layers can be considered. In this section, for the sake of simplicity, only two materials are considered. It means that a Mo layer has to be added to the system. However, as Mo is an absorbing media, the thickness of this layer has the be small,

Cette thèse est accessible à l'adresse : http://theses.insa-lyon.fr/publication/2016LYSEI103/these.pdf
© [E. Blandre], [2016], INSA Lyon, tous droits réservés

or the Mo thin film will absorb the waves that have been multireflected inside the oxide layer, and as a consequence screen the interference effects. Another issue is the dielectric function of the Mo thin layer whose values may depart from the bulk one due to spatial dispersion [73] and electron collisions with boundaries [74], that could increase the energy dissipation in the thin Mo layer. in the following, we assume that for a thickness of 10 nm, the dielectric function of Mo is not affected by the size of the layer. The bilayer on substrate (BOS) structure is depicted in Fig. III.11 (a). Its calculated spectral hemispherical emissivity as a function of the thickness of the oxide layer t_1 is shown in Fig. III.11(b).

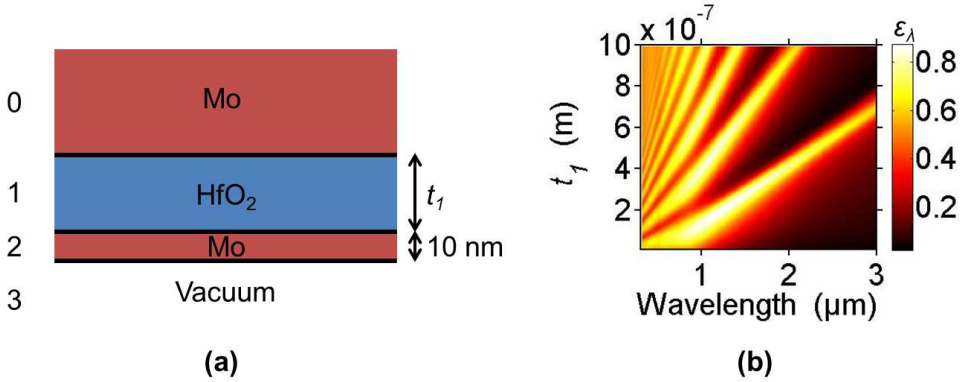

Figure III.11: (a): Schematic representation of the bilayer on substrate structure under consideration. (b): Spectral hemispherical emissivity of the structure as a function of the thickness of the oxide layer t_1.

One can notice than the conditions for constructive interference of the BOS are different to those of the MOS. First, the substitution of an oxide-vacuum interface by a Mo-vacuum interface will induce a different phase lag due to the reflections. The other factor to take into account is the optical path length of the waves when they are multireflected in both the oxide and the Mo layers. Unlike the case of the monolayer structure, a large variety of optical paths can be taken by the waves before being transmitted to vacuum. Moreover, the Mo layer and the Mo substrate are both emitting in this case. We first consider the emission of the substrate inside the structure. The amplitude of the waves emitted by the substrate (medium 0) in vacuum (medium 3) can be calculated analytically using the S-matrix formulation (see Appendix I)

$$A_3 = \frac{t_{01} T_2 e^{ik_{z_1} t_1}}{1 + r_{01} R_2 e^{2ik_{z_1} t_1}}. \tag{III.19}$$

In Eq. III.19, A_3 is the amplitude of the forward emitted waves inside medium 3, T_2 and R_2 are the global transmission and reflection coefficients of the Mo layer, defined as [24]

$$R_2 = \frac{r_{01} + r_{12} e^{2ik_{z_2} d}}{1 + r_{01} r_{12} e^{2ik_{z_2} t d}}, \tag{III.20}$$

$$T_2 = \frac{t_{01} + t_{12} e^{ik_{z_2} d}}{1 + r_{01} r_{12} e^{2ik_{z_2} d}}. \tag{III.21}$$

Cette thèse est accessible à l'adresse : http://theses.insa-lyon.fr/publication/2016LYSEI103/these.pdf
© [E. Blandre], [2016], INSA Lyon, tous droits réservés

As shown before, the denominator of Eq. III.19 can be rearranged to exhibit the phase lag difference between two reflections

$$A_3 = \frac{t_{01} T_2 e^{ik_{z_1} t_1}}{1 + |r_{01}||R_2| e^{i(2k_{z_1} t_1 + \phi_{\text{ref}}^{01} + \phi^2)}}. \tag{III.22}$$

Here, ϕ_2 is the argument of R_2 and corresponds to the phase lag induced by the infinite sum of multireflections inside the Mo layer. It means that the reflections in both the oxide and the Mo layers contribute to the final interference pattern. Conditions for constructive interferences can be determined by equalizing the argument of the exponential term to $2m\pi$. In Fig. III.12, the participation of the substrate to the emission of the BOS is plotted, and superimposed with the theoretical conditions for constructive interference at normal incidence. A good match of the interference conditions with the interference conditions and the calculated emissivity map can be observed.

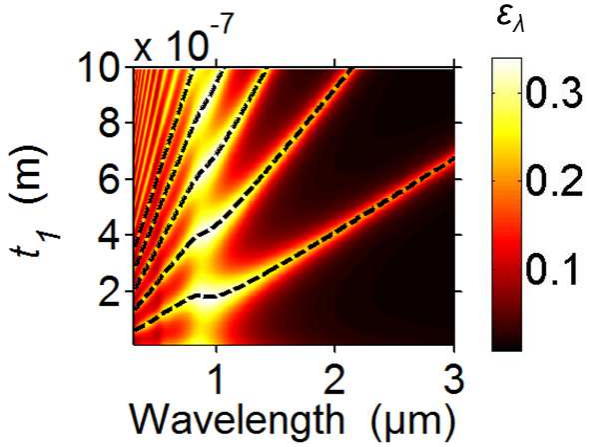

Figure III.12: Participation of the substrate to the spectral hemispherical emissivity of the BOS structure. The dashed lines represent the theoretical conditions for constructive interference at normal incidence.

The contribution of the Mo film to the overall emission is not negligible. Two types of waves have to be considered for the film emission: the forward emitted waves (i.e. emitted toward medium 3), and the backward emitted waves (i.e. emitted toward medium 1). The question we will try to answer in the following is if whether or not these waves interfere. To do this, we analyze the contributions of the forward and backward emitted waves to the emission. To estimate the contribution of the forward emitted waves, we set the value of the C and D coefficients in the S-matrix formulation to 0, while for the backward emitted waves, the coefficients A and B are set to 0 (see section I.3 and Appendix A). The contributions of the forward and backward emitted waves are plotted in Fig. III.13. For wavelengths below $\lambda = 1$ µm, forward and backward emitted waves have different interference patterns. This can be explained by the fact that the optical path of forward and backward emitted waves required to reach vacuum are different: backward emitted waves have to be reflected in the forward direction at least one time to reach vacuum.

Cette thèse est accessible à l'adresse : http://theses.insa-lyon.fr/publication/2016LYSEI103/these.pdf
© [E. Blandre], [2016], INSA Lyon, tous droits réservés

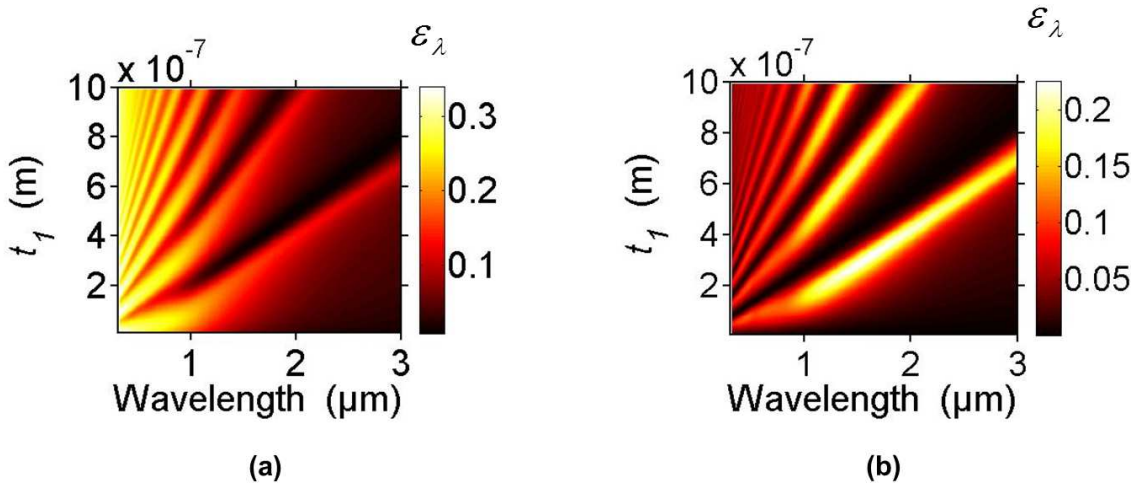

Figure III.13: Contribution of the Mo thin film to the spectral hemispherical emissivity of the BOS. (a): considering only forward emitted waves, (b): considering only backward emitted waves. Note the difference of scale between the two figures.

On the other hand, the interference patterns are the same for large wavelengths. In this case, the reflectivity of the interfaces are large, meaning that waves are more likely to be reflected multiple times before being transmitted to vacuum. The phase lag difference is therefore guided by the reflections.

To analyze the interference between forward and backward emitted waves, we compare on Fig. III.14 the incoherent addition of the spectral hemispherical emissivity of the forward and backward emitted waves with the spectral hemispherical emissivity of the structure taking into account both forward and backward emitted waves coherently. It is observed that the values of the spectral hemispherical emissivity of the structure considering the incoherent addition of the forward and backward emitted waves are much lower than the actual values of the spectral hemispherical emissivity of the structure. It means that forward and backward emitted waves actually interfere. Analytically, this can also be explained by the crossed terms (i.e. multiplications of terms corresponding to the amplitude of the forward emitted waves with terms corresponding to the backward emitted waves) in the expressions of the Green's tensors (Eq. I.35 and I.36).

We now analyze the multireflections inside the structure for two spectral regions: below $\lambda_v = 1$ μm, where the reflectivity of the interfaces are moderate, and above $\lambda = 1$ μm where the reflectivity of the interfaces are close to 1. To do this, we analyze the partial reflectivity of the structure. The partial reflectivity r_l, function of the number of secondary waves l, is defined as

$$\begin{aligned} r_0 &= R_2 \\ r_l &= T_2 \times r_{10}^l \times R_2^{l-1} \times T_2 \times e^{2lik_{z2}t_1},\ l = 1,\ 2,\ 3,\ 4... \end{aligned} \tag{III.23}$$

The infinite sum of r_l corresponds to the total reflectivity of the structure. In Fig. III.15, the partial reflectivity of a BOS structure with an oxide layer thickness $t_1 = 100$ nm is plotted as a

Cette thèse est accessible à l'adresse : http://theses.insa-lyon.fr/publication/2016LYSEI103/these.pdf
© [E. Blandre], [2016], INSA Lyon, tous droits réservés

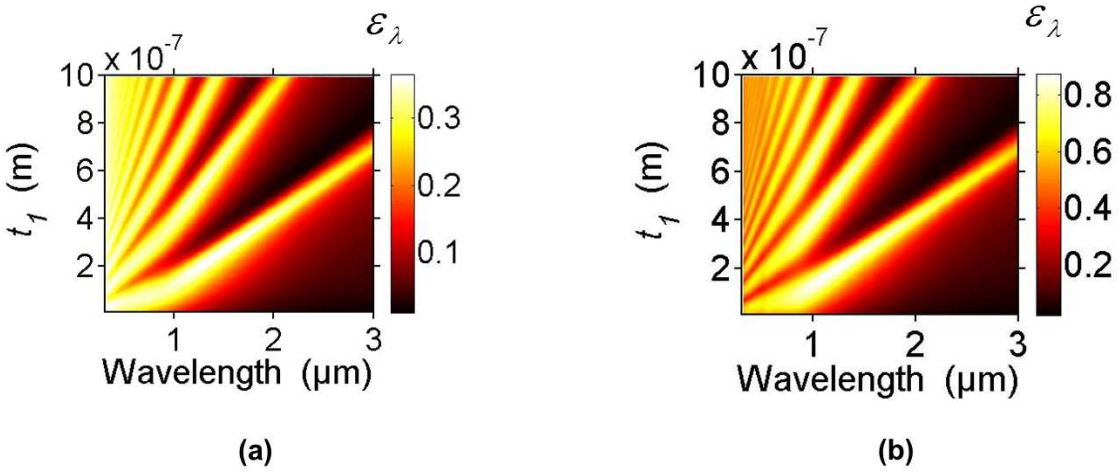

Figure III.14: (a): Incoherent addition of the spectral hemispherical emissivities of the forward and backward emitted waves for the BOS structure. (b): Spectral hemispherical emissivity of the BOS considering every types of interferences. Note the difference of scale between the two figures

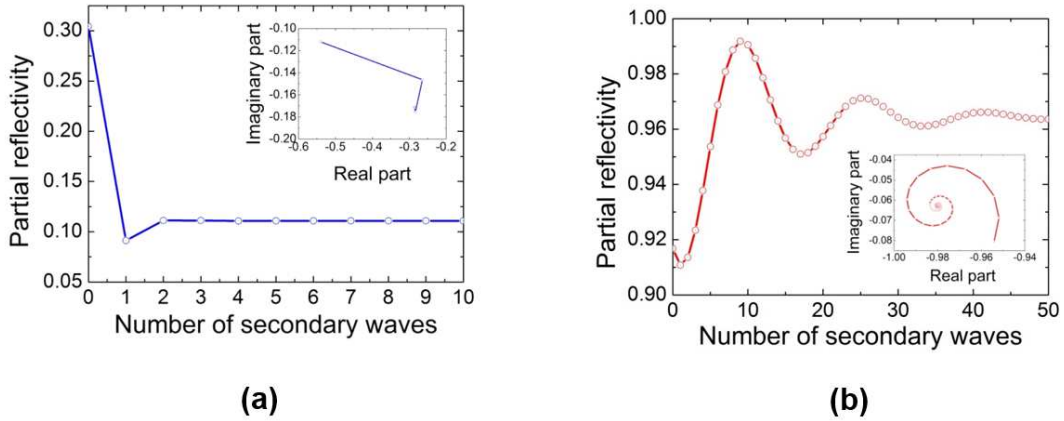

Figure III.15: Partial reflectivity r_l as a function of the number of secondary waves l for $t_1 = 100$ nm. (a): $\lambda_v = 0.3$ μm, (b): $\lambda_v = 10$ μm. The inserts represent the partial reflectivity in the complex plane.

function of the number of secondary waves included. Fig. III.15(a) is for a wavelength $\lambda_v = 0.3$ μm. It is observed that the partial reflectivity of the structure converges to its final value after a small number of reflections. The inserts represent the values of the partial reflectivity in the complex plane. The phase difference between two reflections is large, due to the large value of the argument of the reflection coefficients in this spectral region (Fig. III.4(a)). In Fig. III.15(b), the partial reflectivity is plotted for a wavelength $\lambda_v = 10$ μm. In this spectral region, the reflectivities of the interfaces are close to 1. Due to this fact, the partial reflectivity converges to its final value after a large number of reflections. However, the phase lag between two reflections is close to 0

Cette thèse est accessible à l'adresse : http://theses.insa-lyon.fr/publication/2016LYSEI103/these.pdf
© [E. Blandre], [2016], INSA Lyon, tous droits réservés

in this spectral region. It means that a large number of reflections does not necessarily induce a large reflectivity due to interferences. This phenomenon was analyzed in [68, 69], where it was demonstrated that a quarter-wavelength layer with both optical indices of the order of unity (i.e. that induces significant phase lags due to reflections) can generate so-called "perfect absorption" modes.

The spectral emissivity of the BOS structure is plotted for $t_1 = 70$ nm in Fig. III. 16, and compared with the one of the MOS obtained previously for $t = 70$ nm.

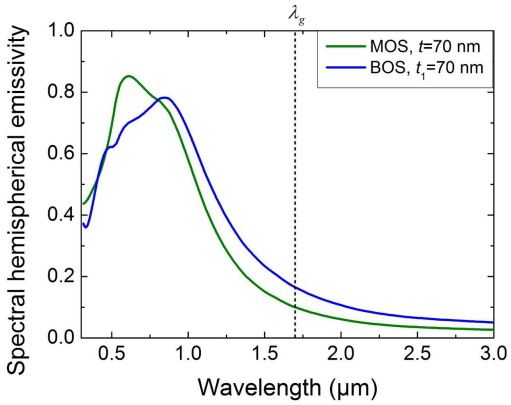

Figure III.16: Spectral hemispherical emissivity of the BOS structure ($t_1 = 70$ nm), superimposed with the one of the MOS ($t = 70$ nm).

It can be observed that the addition of the thin Mo layer does not enhance the spectral hemispherical emissivity. Additional layers have to be added to the system to further modify the emission spectrum of the radiator.

III.2.7 Spectral hemispherical emissivity of trilayer on substrate structures

A second oxide layer of thickness t_2 is added to form a trilayer on substrate (TOS) structure (see Fig. III.17(a)). The spectral hemispherical emissivity of the trilayer structure, considering that the thicknesses of the two oxide layers t_1 and t_2 are equal, is depicted in Fig. III.17(b). The number of resonant branches is increased by the addition of the second oxide layer. It worth noticing that for thicknesses lower than 100 nm, the addition of a the second interference branch generates a broad and large emission with a steep cutoff. This type of structure has therefore a high potential for tailoring the spectrum of emission close to the objective defined earlier. The origin of the different resonant branches is now analyzed. In Fig. III.17(b), the interference branches are grouped by pairs. A first reasoning would be to consider that the two branches in each pair correspond to Fabry-Pérot interferences inside each oxide layer. However, as shown in the case of the BOS structure, multireflections of waves in several layers involve complex mechanisms. We thus make an analysis on the spectral region above $\lambda_\nu = 1$ μm, where the absorption of Mo and the reflection coefficients of the interfaces are large. In this spectral region, waves cannot cross the Mo layer multiple times without being absorbed. We thus consider that the structure

Cette thèse est accessible à l'adresse : http://theses.insa-lyon.fr/publication/2016LYSEI103/these.pdf
© [E. Blandre], [2016], INSA Lyon, tous droits réservés

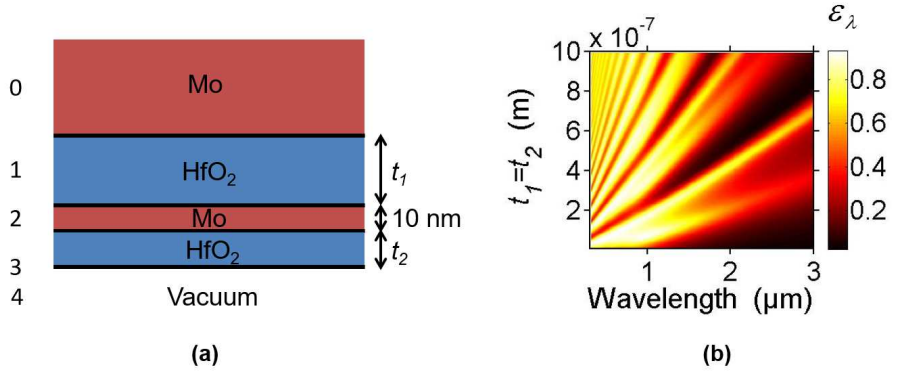

Figure III.17: (a): Schematic representation of the TOS structure. (b): Spectral hemispherical emissivity of the TOS as a function of the thicknesses of the oxide layers, considering $t_1 = t_2$.

contains two different Fabry-Pérot cavities. The first one is composed of the substrate (medium 0), the first oxide layer (medium 1) and the Mo layer (medium 2). The second cavity is composed

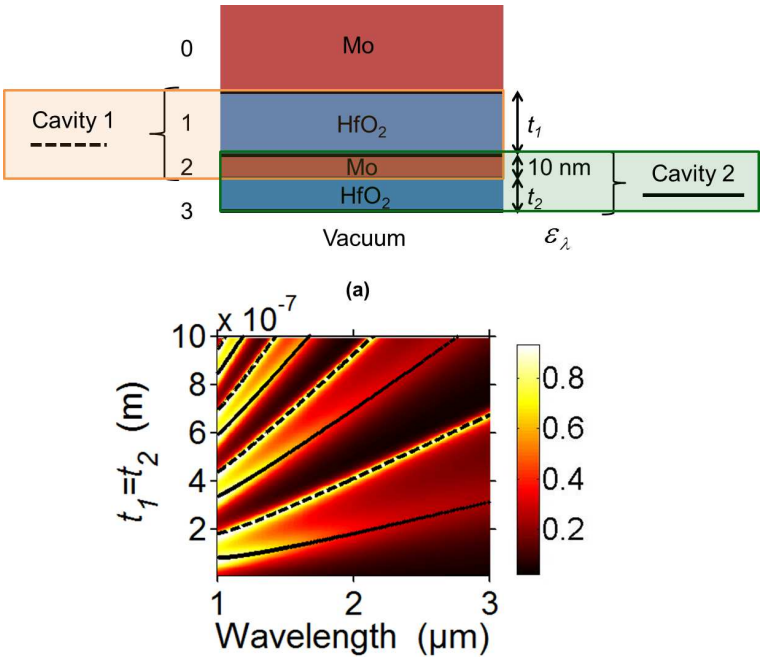

Figure III.18: Spectral hemispherical emissivity of the TOS structure. The dashed and full lines represent the constructive interference conditions at normal incidence of the two Fabry-Pérot cavities highlighted above.

of the Mo layer (medium 2) and the front oxide layer (medium 3). A schematic of the two cavities is depicted in Fig. III.18. The spectral hemispherical emissivity of the full structure and the calculated interference conditions of the two different cavities at normal incidence are also plotted. A good agreement between the calculated emissivity map and the theoretical conditions for constructive interference at normal incidence can be observed. However, it was not possible to retrieve the correct interference conditions for wavelengths smaller than $\lambda_v = 1$ µm using

Cette thèse est accessible à l'adresse : http://theses.insa-lyon.fr/publication/2016LYSEI103/these.pdf
© [E. Blandre], [2016], INSA Lyon, tous droits réservés

this method. The interpretation is the following: for wavelengths smaller than $\lambda_v = 1$ µm, the reflectivity of the interfaces are moderate, and the absorption coefficient of the thin Mo layer is low. In this case, waves can cross multiple times the Mo layer, inducing multireflections, and thus complex patterns inside the three layers of the structure. Therefore, for small thicknesses of the oxide layers, a broad emission is generated. For wavelengths larger than $\lambda_v = 1$ µm, the interfaces have a reflectivity close to 1, and the absorption coefficient of the Mo layer is large. It means that waves are more likely to be reflected inside the oxide layers without crossing multiple times the Mo layer. In this case, the decomposition in two cavities is consistent. To validate this hypothesis, we plot in Fig. III.19 the emission of the film inside the structure considering only forward emitted waves (Fig. III.19(a)) and only backward emitted waves (Fig. III.19(b)). For forward emitted

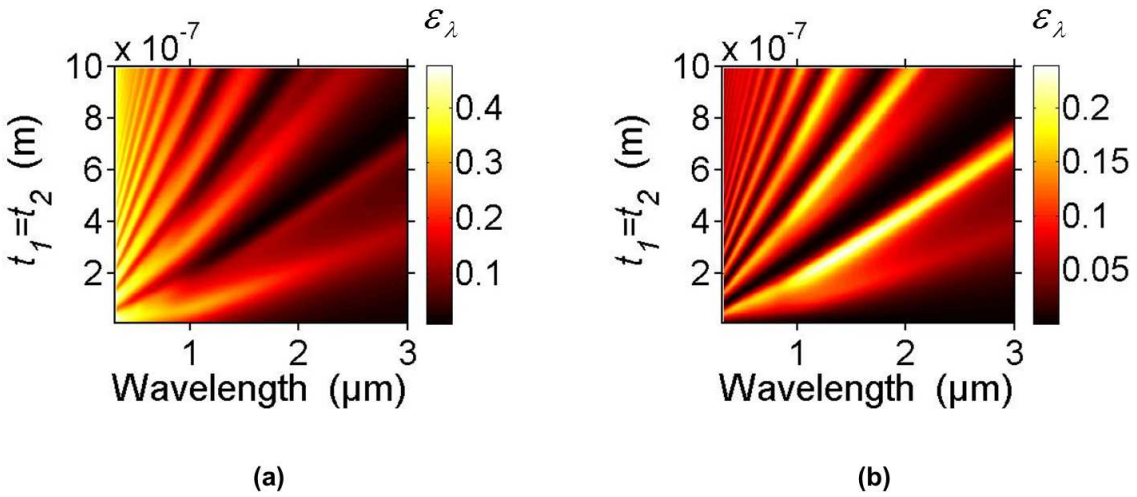

Figure III.19: Contribution of the Mo film to the spectral hemispherical emissivity of the TOS structure considering $t_1 = t_2$. (a): considering only forward emitted waves. (b): considering only backward emitted waves.

waves, the lower branch has a larger intensity. The resonance conditions of the lower branch correspond to cavity 2, which is directly in the path of emission of the waves. The opposite happens for the case of the backward emitted waves: the branches whose resonance conditions correspond to cavity 1 have a larger intensity. Again, this is due to the fact that the cavity is in the path of the emitted waves. Thus, we can conclude that the two branches corresponds to one cavity. The spectral hemispherical emissivity of the TOS structure for $t_1 = t_2 = 70$ nm is plotted in Fig. III. 20. It is observed that the addition of the second oxide layer allows increasing significantly the spectral hemispherical emissivity of the structure below the wavelength corresponding to the bandgap energy of GaSb, while keeping low values above it.

As a conclusion for this part, the addition of a second transparent oxide layer allowed increasing the number of interfering modes. It results in a broadband emission with a steep cutoff, which is the kind of spectrum needed for the TPV application under consideration.

Cette thèse est accessible à l'adresse : http://theses.insa-lyon.fr/publication/2016LYSEI103/these.pdf
© [E. Blandre], [2016], INSA Lyon, tous droits réservés

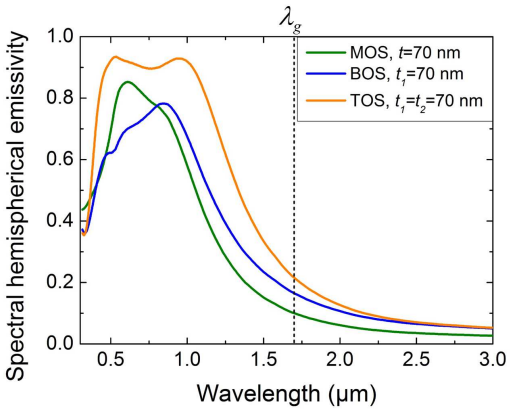

Figure III.20: Spectral hemispherical emissivity of the MOS structure ($t = 70$ nm), BOS ($t_1 = 70$ nm) and TOS ($t_1 = t_2 = 70$ nm) structures.

III.2.8 Optimization of the layer size of the few-layer structures for the TPV application

This section is dedicated to the optimization of the few-layer structures for the TPV application presented previously. To quantify the performance of the TPV emitter, we define a figure of merit FM that assesses how close to the ideal emission the emissivity of the structure is. We recall that the perfect emitter has a spectral hemispherical emissivity defined as

$$\varepsilon_\lambda = \begin{cases} 1 \text{ for} \lambda \leq \lambda_c \\ 0 \text{ for} \lambda > \lambda_c \end{cases} \tag{III.24}$$

λ_c is the cutoff wavelength corresponding the the bandgap of GaSb (0.726 eV at 300 K), and is equal to 1.7 μm. To define the figure of merit, we introduce the function $\psi(\lambda)$ that represents the deviation to the ideal emission, defined as

$$\psi(\lambda) = \begin{cases} q_\lambda^{bb}(T)(1-\epsilon_\lambda) \text{ for} \lambda \leq \lambda_c \\ q_\lambda^{bb}(T)\epsilon_\lambda \text{ for} \lambda > \lambda_c \end{cases}, \tag{III.25}$$

where $q_\lambda^{bb}(T)$ is the spectral emissive power of a blackbody at temperature T (see Chapter I). Experimentally, a temperature $T = 1500$ K for the emitter can be achieved [66]. At this temperature, the wavelength where the blackbody intensity is maximum (λ_{Wien}) is close to the wavelength corresponding to the bandgap of GaSb λ_g at 300 K. In the following, we choose this value for the temperature, knowing that the same procedure can of course be applied for other temperatures. For a given wavelength λ, the function E represents the fraction of energy that is below the ideal emission for the wavelengths below the cutoff (1), and the fraction of energy that is above the

Cette thèse est accessible à l'adresse : http://theses.insa-lyon.fr/publication/2016LYSEI103/these.pdf
© [E. Blandre], [2016], INSA Lyon, tous droits réservés

ideal emission (0) for wavelengths above the cutoff

$$FM_{\text{tot}} = 1 - \frac{\int_{\lambda_{\min}}^{\lambda_{\max}} \psi(\lambda) d\lambda}{\int_{\lambda_{\min}}^{\lambda_{\max}} q_{\lambda}^{bb}(T) d\lambda}. \tag{III.26}$$

This ratio provides a number between 0 and 1, that represents the deviation to ideality in terms of energy integrated over the wavelengths. As a consequence, the figure of merit FM_{tot} takes its highest values when the spectral hemispherical emissivity of the structure is close to the ideal emitter. The subscript "tot" in Eq. III.26 means that the figure of merit is defined for the spectral range between $\lambda_{\min} = 0.3$ µm and $\lambda_{\max} = 10$ µm. It is important to note that the values of $\lambda_{\min}$ and $\lambda_{\max}$ correspond to the boundaries of the spectral range where the optical indices are tabulated in [72]. A second figure of merit is defined for wavelengths below λ_c to ensure that the emitter still has a large emissivity in this spectral range, in order to maximize the energy yield by the TPV system.

$$FM_{\text{below}} = 1 - \frac{\int_{\lambda_{\min}}^{\lambda_c} \psi(\lambda) d\lambda}{\int_{\lambda_{\min}}^{\lambda_c} q_{\lambda}^{bb}(T) d\lambda}. \tag{III.27}$$

In the same way, a figure of merit FM_{above} could be defined. Using these definitions, we find a figure of merit for the single Mo substrate of $FM_{\text{tot}} = 0.82$ for the whole spectrum, and $FM_{\text{below}} = 0.19$ below the cutoff. It means that the Mo substrate takes small values of spectral hemispherical emissivity above the cutoff, which leads to a large total figure of merit. However, in the wavelength range below the cutoff, the emissivity is also small. Therefore, the figure of merit below the cutoff takes low values.

Is has been shown in the previous section that the spectral selectivity can be enhanced using interferences. For the MOS structure (section III.2.5), Fig. III.21. depicts the figures of merit as a function of the thickness of the oxide layer t. The figure of merit oscillates as a function of the thickness of the oxide layer t. It is due the constructive interference peaks in the spectral hemispherical emissivity that shift to larger wavelengths when the thickness of the oxide layer (t) increases. Compared to the Mo substrate alone, the spectral selectivity of the monolayer on substrate emitter significantly increases the figure of merit. For the optimal size of the oxide layer thickness $t = 148$ nm, the total figure of merit reaches a value of $FM_{\text{tot}} = 0.85$, and the value of the figure of merit for wavelengths below the the cutoff is $FM_{\text{below}} = 0.38$. Since the BOS structure did not exhibit an enhancement of the spectral emissivity compared to the MOS strucutre, performances of the TOS are investigated next. The size of the thin Mo layer is still set at 10 nm. The figures of merit of this emitter are plotted in Fig. III.22, as a function of the sizes of the two oxide layers. The figures of merit exhibit peaks and dips for the same reasons as for the MOS: since both cavities (as defined in the previous section) generate two different interference peaks, local maxima can be found when varying both thicknesses. As for the values, the maximum figure of merit for wavelengths below the cutoff is 0.60, while the maximum total figure of merit is 0.86. One should note that the maxima of FM_{tot} and FM_{below} occur at different thicknesses. To compare the figures of merit of the different structures, we gather the results in Table III.1. The addition of

Cette thèse est accessible à l'adresse : http://theses.insa-lyon.fr/publication/2016LYSEI103/these.pdf
© [E. Blandre], [2016], INSA Lyon, tous droits réservés

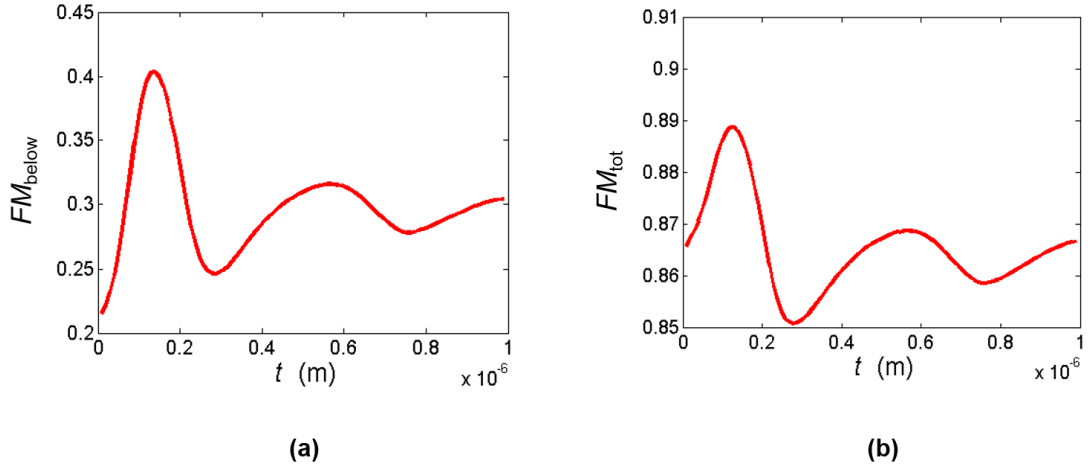

Figure III.21: Figure of merit for the MOS structure as a function of the thickness of the oxide layer t. (a): for wavelengths below the cutoff. (b): for the whole wavelength range.

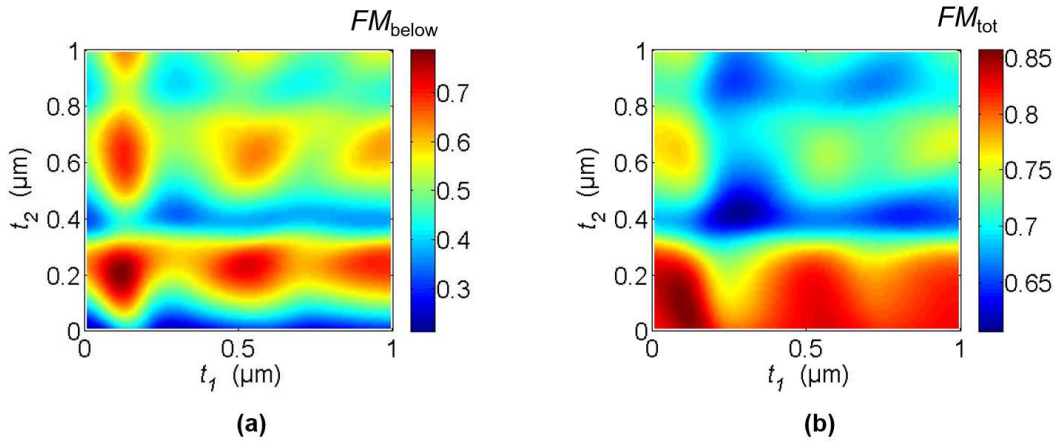

Figure III.22: Figure of merit for the trilayer on substrate structure as a function of the thickness of the oxide layers t_1 and t_2. (a): for wavelengths below the cutoff. (b): for the whole wavelength range. The thickness of the thin Mo layer is 10 nm.

the different layers and optimization of the thicknesses of the layers allows enhancing the figure of merit for wavelengths below the cutoff by a factor 2 for the monolayer structure, and by a factor 3 for the trilayer structure compared to the Mo substrate alone. This means that potentially three times more photons could be converted into EHP. The optimal spectral hemispherical emissivities of the different structures maximizing the figure of merit FM_{below} are plotted in Fig. III.23 for comparison. The total figure of merit does not benefit much the addition of layers. This is due to two facts: first, the Mo substrate has intrinsically a low spectral hemispherical emissivity above the cutoff. Second, the Mo thin layer induces a small enhancement of the spectral hemispherical emissivity in the wavelength range above the cutoff, as illustrated by the orange curve

Cette thèse est accessible à l'adresse : http://theses.insa-lyon.fr/publication/2016LYSEI103/these.pdf
© [E. Blandre], [2016], INSA Lyon, tous droits réservés

Table III.1: Maximum values of the figures of merit for the different structures

	Mo substrate	MOS	TOS
maximum FM_{below}	0.19	0.38	0.60
maximum FM_{tot}	0.82	0.85	0.86

in Fig. III.23. Here, the useful energy (below the cutoff) and the detrimental one are considered on equal footing in FM_{tot}. Considering how detrimental energy could affect the TPV conversion could allow introducing weights factors, and probably show strong variations of FM_{tot}.

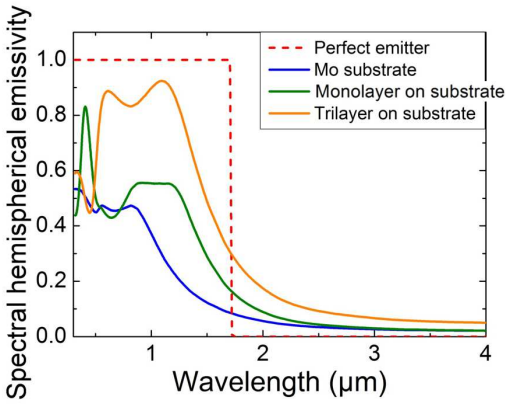

Figure III.23: Spectral hemispherical emissivity of the Mo substrate, the optimal bilayer and the optimal trilayer structures, compared with the ideal emitter.

To conclude this section, we have studied interference phenomena in few-layer structures using numerical simulations. The spectral variations of the optical indices of Mo induce different regimes of interference that we have analyzed in depth. The understanding of those phenomena allows modifying the spectral hemispherical emissivity of the structure. We have then used this analysis to design a TPV selective emitter. Mo has intrinsic optical properties that generate a spectral hemispherical emissivity that fits with the TPV application under consideration. To enhance spectral selectivity, interference phenomena have been used by adding different layers onto the substrate. For a trilayer structure, the spectral hemispherical emissivity is broadband with large values and a steep cutoff near the cutoff wavelength, which is close to the desired spectrum. For the perspectives, it is important to mention that the spectral hemispherical emissivities were calculated by using the optical properties of the materials at $T = 300$ K. In reality, the temperature of the emitter is much higher for a TPV system, and the optical properties of the materials may vary. However, because of a lack of data, it is difficult to quantify this variation. Note that the criterion used to define the figure of merit is purely optical: we only take into account radiative losses, and neglect the electrical and thermal losses. In reality, high-energy photons can be detrimental to the PV conversion, because of their excess of energy generating heat through thermalization and many other processes, that were studied in detail in [3]. Furthermore, low-energy photons can be reflected back to the radiator, which can prove useful. Therefore, the ideal spectral hemi-

Cette thèse est accessible à l'adresse : http://theses.insa-lyon.fr/publication/2016LYSEI103/these.pdf
© [E. Blandre], [2016], INSA Lyon, tous droits réservés

spherical emissivity may not be a step-like function, but a band function [75], and the low cutoff wavelength would depend on the thermal behavior of the TPV system. In the future, numerical simulations of the coupled radiative heat transfer, electrical charge transport and thermal phenomena in the whole TPV system should be considered.

III.3 Temperature dependence of the spectral and total emissivities of Al-Si few-layer structures

In TPV applications, the temperature of the radiator is obviously not the ambient temperature and may vary. This will have an impact on the conversion efficiency of the system. Another example is thermal rectification between two bodies. This phenomena takes place when a thermal diode can be observed, i.e. when different heat fluxes are transferred when the temperatures of the two bodies are inverted. The key point for making such systems is to have bodies with strong variations of their total emissivity when their temperature changes [67]. In this section, we study the temperature dependence of the emission properties of Al-Si few-layer structures for lower temperatures than in section III.2 (from 0 to 500 K), especially the total hemispherical emissivity. We also analyze how interferences can enhance the total hemispherical emissivity of these structures, and how to maximize it. The results and the text of this section are taken from [5].

III.3.1 Optical properties of Al and Si and their temperature dependence

Two materials are considered in this section: aluminum and silicon. Aluminum is a metal, and will therefore act as a reflector (this time over the whole frequency range) inside the emitting structures. Its optical properties are well described by a Drude model [73, 23]

$$\epsilon(\omega) = 1 - \frac{\omega_p^2}{\omega(\omega + i\Gamma)}, \tag{III.28}$$

where ω_p is the plasma frequency and Γ is the damping constant. To account for the variations of the dielectric function of aluminum as a function of temperature, temperature-dependent Drude parameters ω_p and Γ are considered. The plasma frequency can be written as

$$\omega_p^2 = \frac{\eta e^2}{m^* \epsilon_0}, \tag{III.29}$$

where η is the density of electrons in aluminum, ϵ_ν is the permittivity of vacuum, m^* is the optical effective mass of the electron, and e its electrical charge. The damping constant is related to the electrical resistivity ρ through [76]

$$\Gamma = \frac{\eta e^2 \rho}{m^*}. \tag{III.30}$$

The physical parameters that depend on temperature are the optical mass m^* and the electrical

Cette thèse est accessible à l'adresse : http://theses.insa-lyon.fr/publication/2016LYSEI103/these.pdf
© [E. Blandre], [2016], INSA Lyon, tous droits réservés

resistivity ρ. Variations of the electrical resistivity as a function of temperature can be found in [77], and those of the optical effective mass of the electron as a function of temperature are taken from [78]. Using these values, we can fully take into account the effect of temperature variation on the dielectric function of aluminum. Intrinsic silicon, or weakly doped silicon, has a constant refractive index in the infrared, and is almost lossless (it never absorbs significantly). Thus, it is a good material for building Fabry-Pérot layers, because waves can be multireflected inside this material, thus maximizing interference effects. Its dielectric function is also calculated with a Drude model, whose parameters are doping dependent [76, 79]. Pure intrinsic silicon is difficult to obtain because there is always a residual doping. Therefore, we consider weakly doped silicon (with 10^{14} dopants per cm^{-3}) with a corresponding dielectric function close to pure intrinsic silicon. Silicon thin layers are almost non-emitting due to their high transparency in the infrared. Moreover, variations of the refractive index of silicon with temperature are weak [80], and thus are not taken into account. The optical indices of both materials are depicted in Fig. III.24.

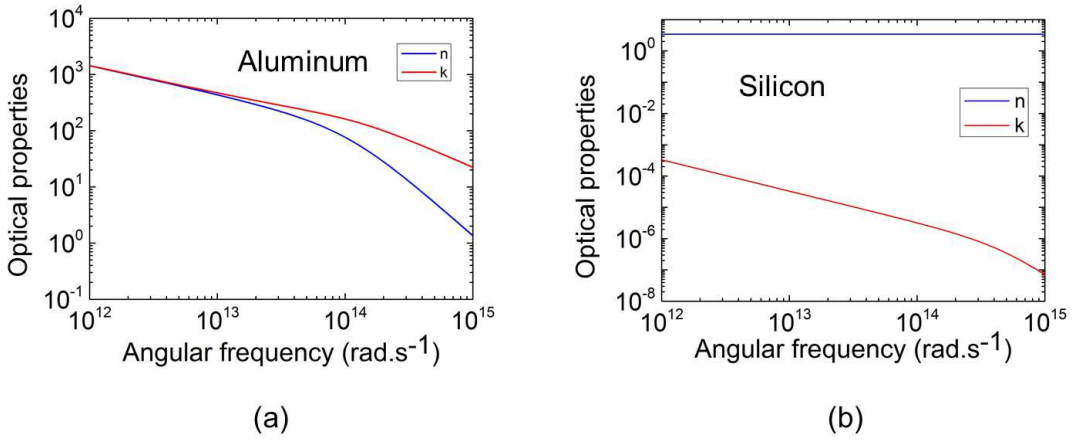

Figure III.24: Optical indices of the two materials under consideration at room temperature. (a): aluminum, (b): silicon.

III.3.2 Variations with temperature of the total hemispherical emissivity of an Al substrate

The importance of the temperature dependence of the optical properties of Al is in illustrated Fig. III.25. The total hemispherical emissivity of a single Al substrate alone is plotted as a function of temperature. We compare the results when using the dielectric function of Al at ambient temperature, and when accounting for the variations of the dielectric function of Al as a function of temperature. We observe that the results are significantly different. When using a non-temperature dependent dielectric function, the variations of emissivity as a function of temperature are only due to the frequency shift of Planck's blackbody spectrum. When temperature increases, it shifts toward larger frequencies. It can be observed in Fig. III.25(b) that the spectral emissivity of an Al substrate increases with frequency. In reality, the dielectric function of Al is also modified when

Cette thèse est accessible à l'adresse : http://theses.insa-lyon.fr/publication/2016LYSEI103/these.pdf
© [E. Blandre], [2016], INSA Lyon, tous droits réservés

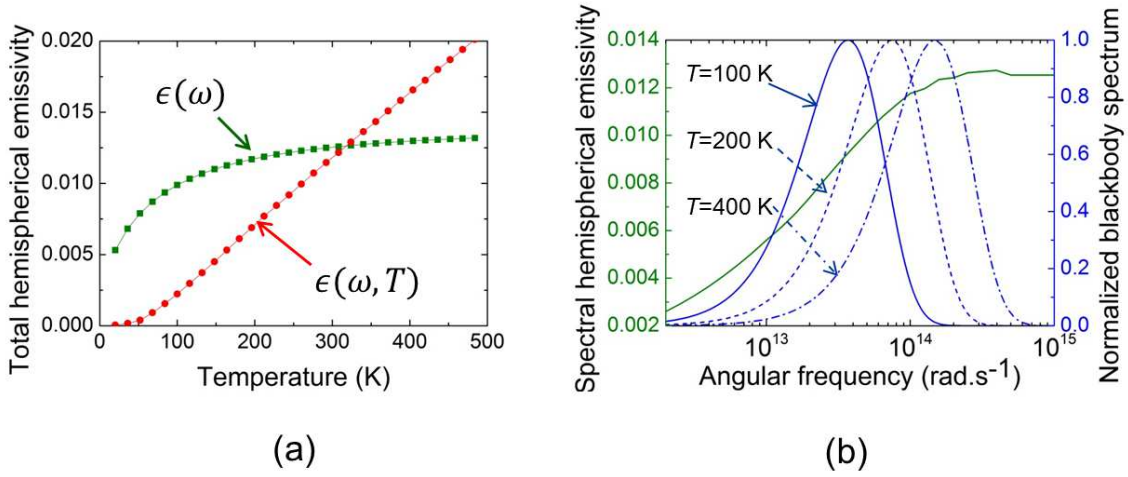

Figure III.25: (a): Total hemispherical emissivity of an aluminum susbtrate as a function of temperature. The green line represents the values calculated with the dielectric function of Al at ambient temperature. The red line represents the values calculated with the temperature-dependent dielectric function for Al. (b): Spectral hemispherical emissivity of an Al susbtrate at $T = 300$ K (green curve) and normalized blackbody spectra at different temperatures (blue curves). From [5].

temperature varies. We observe that the dependence on temperature of the total hemispherical emissivity becomes proportional to the electrical resistivity of Al. As the electrical resistivity varies proportionally to temperature, a rise of temperature induces an increase of the damping coefficient, leading to an increase of the spectral and total hemispherical emissivities. Accounting for the variations of the dielectric function of Al due to temperature is therefore crucial to study the temperature dependence of the emissivity of metallic emitters.

III.3.3 Spectral amplification of the emission of a substrate with interference phenomena

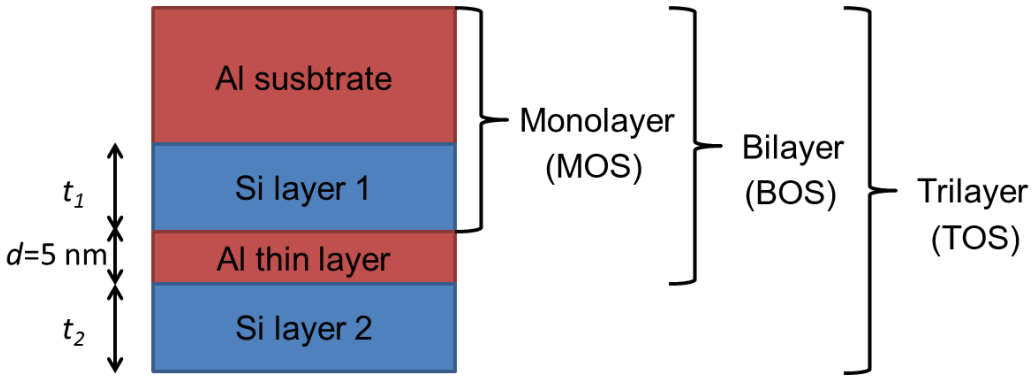

Figure III.26: Schematic representation of the investigated structures.

Cette thèse est accessible à l'adresse : http://theses.insa-lyon.fr/publication/2016LYSEI103/these.pdf
© [E. Blandre], [2016], INSA Lyon, tous droits réservés

In the previous section, we have mentioned that interferences in a resonant layer strongly affect the spectral hemispherical emissivity of the system over a large frequency range. Here, we are interested in analyzing the total hemispherical emissivity of layered structures and its dependence on temperature. When increasing the temperature of the system, the blackbody spectrum shifts to larger frequencies. The dependence on temperature of the hemispherical emissivity of the structure should be affected by interferences.

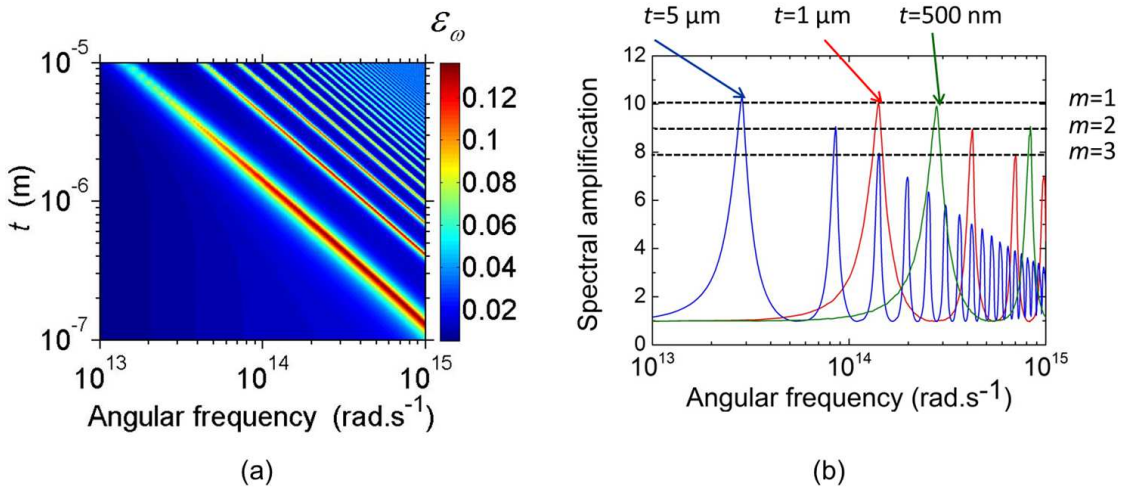

Figure III.27: (a): Spectral hemispherical emissivity of the monolayer structure as a function of the thickness of the Si film t_1. (b): Spectral amplification for different sizes of the Si layer.

As in the previous section, three types of structures are investigated: the monolayer, bilayer and trilayer structures deposited on an Al substrate (Fig. III.26).

The monolayer structure is first considered. In Fig. III.27(a), its spectral hemispherical emissivity is plotted as a function of the thickness of the Si layer t_1. We observe the apparition of interference modes, like in the case of the Mo-HfO_2 structures. However, as Al is a highly reflective material in the whole frequency range under consideration, the interference peaks are much sharper. In Fig. III.27(b), the spectral amplification, as defined as the emission of the MOS divided by the emission of the substrate, is plotted for different thicknesses of the Si layer. The spectral hemispherical emissivity can be enhanced at specific frequencies by a factor up to 10 compared to that of the single Al substrate.

III.3.4 Dependence on temperature of the total hemispherical emissivity of a monolayer on substrate

In this section, we are also interested by the total hemispherical emissivity of the structures. Fig. III.28 depicts the variations the total hemispherical emissivity of the structure as a function of the thickness of the Si layer for different temperatures. We compare the results when considering a temperature-independent dielectric function for Al at room temperature (Fig. III.28(a)) and when accounting for the variations of the dielectric function of Al as a function of temperature

Cette thèse est accessible à l'adresse : http://theses.insa-lyon.fr/publication/2016LYSEI103/these.pdf
© [E. Blandre], [2016], INSA Lyon, tous droits réservés

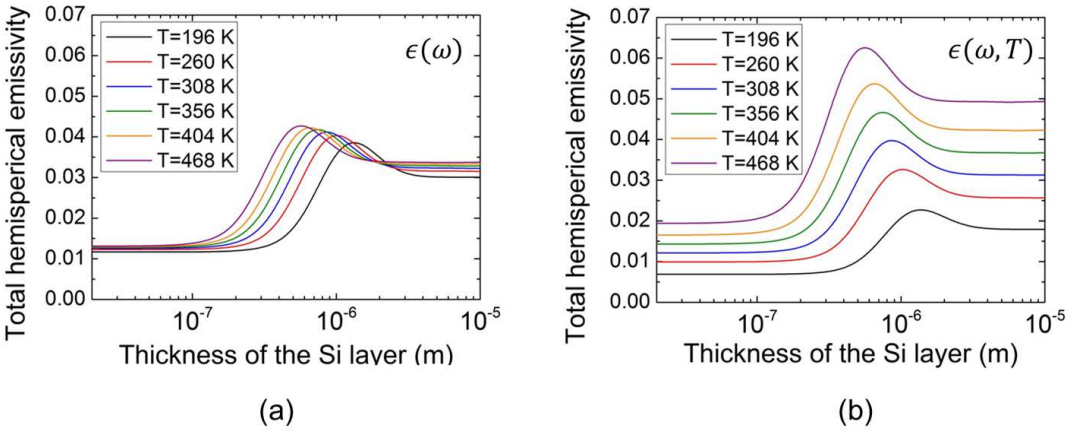

Figure III.28: Total hemispherical emissivity of a Si film coated on an Al substrate. (a): Considering the dielectric function of aluminum at room temperature. (b): Considering the temperature-dependent dielectric function of aluminum. From [5].

(Fig. III.28(b)). First, we observe that in both figures, the addition of a Si coating on an Al substrate increases the total hemispherical emissivity of the substrate alone (Fig. III.25(a)), despite the fact that the Si layer is transparent and therefore non-emitting. The total hemispherical emissivity exhibits several regimes: a plateau of low emissivity for low thicknesses, then a maximum at a given thickness that shifts toward lower thicknesses when the temperature increases, and a second plateau at larger thicknesses. If we now compare the results with and without the dependence on temperature of the dielectric function of Al, we observe that the optimal thickness that maximizes the emissivity at one temperature is the same for both cases. However, accounting for the variations of the Drude parameters of Al when the temperature increases leads to a significant increase of emissivity. The total hemispherical emissivity of the structures is thus strongly affected by the temperature-dependence of the optical properties of the emitting layer. It is also

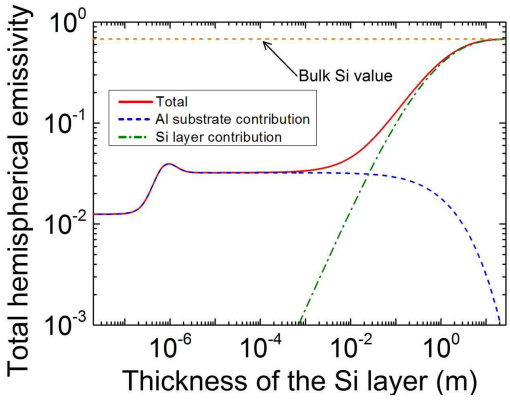

Figure III.29: Total hemispherical emissivity of the Si monolayer on substrate for $T = 300$ K. The contributions of each layer to the emission are also plotted.

Cette thèse est accessible à l'adresse : http://theses.insa-lyon.fr/publication/2016LYSEI103/these.pdf
© [E. Blandre], [2016], INSA Lyon, tous droits réservés

interesting to analyze the total hemispherical emissivity of the structure for very large thicknesses of the Si layer. In Fig. III.29, the total hemispherical emissivity of the structure for $T = 300$ K is plotted as a function of the thickness of the Si layer. The contributions of the different layers to the emissions are also plotted. Several regimes are exhibited. For very low thicknesses of the Si layer (t), the emission is driven by the Al substrate, with no impact of the Si layer, because the thicknesses are too small for interference to occur in the frequency range where the blackbody extends. For thicknesses of several dozens of nanometers, the interferences are modifying the total hemispherical emissivity of the Al substrate, as described before. For thicknesses close to 1 mm, the contribution of the Si layer starts to increase. In between, the contribution of the Al layer starts to decrease because the Si layer becomes progressively optically thick. Therefore, waves emitted by the Al substrate are more likely to be absorbed inside the Si layer. For the largest thicknesses, the emissivity reaches that of the bulk Si value.

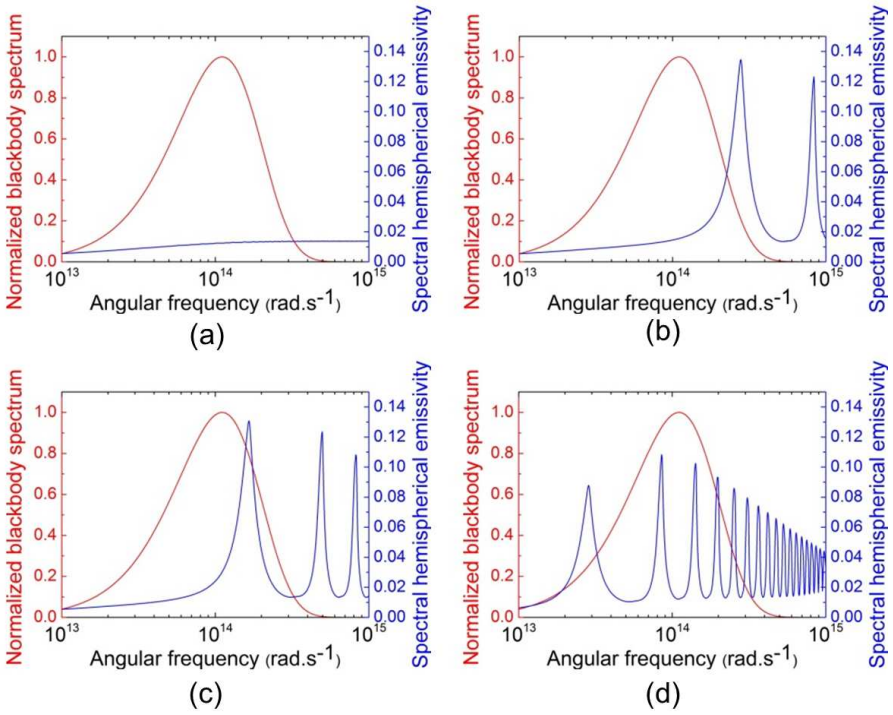

Figure III.30: Spectral emissivity of the structures (blue lines) and blackbody spectrum at $T = 300$ K for different thicknesses of the Si layer. (a): $t = 10$ nm (b): $t = 500$ nm (c): $t = 874$ nm (d): t=5 μm. From [5].

The optimal thickness (t_{max}) that maximizes the total hemispherical emissivity can be determined by analyzing the frequency of the first-order peak (smallest frequency) of interference and the frequency of the maximum intensity of Planck's blackbody spectrum at the considered temperature. At a given temperature T, Planck's blackbody intensity is maximum at a frequency $\omega_{max} = C \times T$, according to Wien's law, where C is a constant equal to $3.6971 \times 10^{11} \mathrm{s}^{-1}\mathrm{K}^{-1}$ when Planck's distribution function is expressed in terms of angular frequency (see Chapter I). In Fig. III.30, the spectral hemispherical emissivity of the structure under consideration (a Si film on an Al substrate) is plotted for different Si film thicknesses. The normalized Planck blackbody spectrum at

Cette thèse est accessible à l'adresse : http://theses.insa-lyon.fr/publication/2016LYSEI103/these.pdf
© [E. Blandre], [2016], INSA Lyon, tous droits réservés

$T = 300$ K is also plotted. For $t = 10$ nm (Fig. III.30(a)), the Si film is too thin for interferences to occur in the spectral range where the blackbody spectrum at 300 K extends. Analyzing the denominator of Eq. III.2 which includes the term that accounts for multireflections, we find that the argument of the exponential term is close to 0 when $t << \frac{c}{n\omega_{max}}$ and interferences cannot occur at the considered temperature. When the thickness of the film reaches $t \sim \frac{c}{n\omega_{max}}$, the first peak of interference in the spectral hemispherical emissivity starts to overlap with the Planck blackbody spectrum (Fig. III.30(b)), and the total hemispherical emissivity of the structure increases. At the thickness where the total hemispherical emissivity is maximum, the first peak of interference is close to the frequency ω_{max} (Fig. III.30(c)). For each temperature, the ratio between the frequency ω_{max} and the frequency of the first-order peak of interference ω_{fp} was numerically found to have almost the same value ($\frac{\omega_{max}}{\omega_{fp}} \sim 0.72$ - 0.74). When the thickness of the film increases even more, a larger number of interfering modes overlap the blackbody spectrum (Fig. III.30(d)), and the total hemispherical emissivity reaches a plateau. In Eq. III.2, we observe that when t becomes much larger than $\frac{c}{n\omega_{max}}$, the factor that accounts for multireflections in the Fabry-Pérot layer reduces to 1 meaning a lot of multireflections occur in the spectral range where the blackbody extends, leading to a constant value of the total hemispherical emissivity.

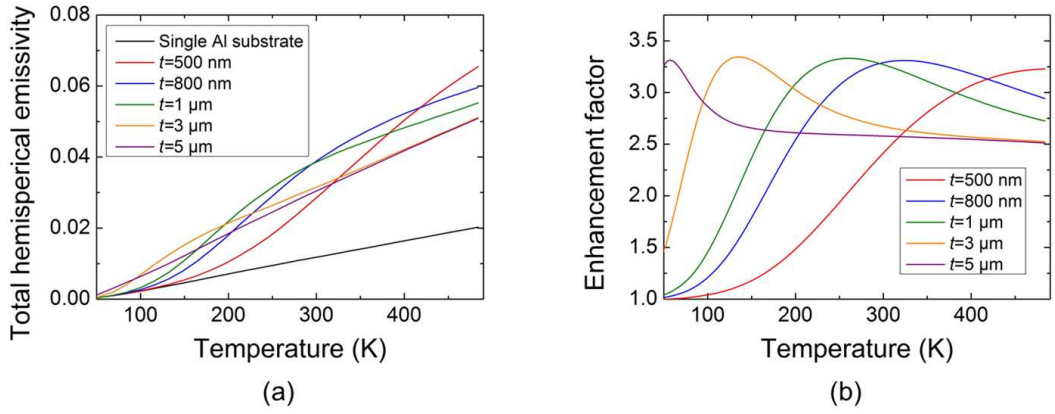

Figure III.31: (a): Total hemispherical emissivity of the Si monolayer on Al substrate as a function of temperature for different Si layer thickesses. (b): Enhancement factor as a function of temperature for different thicknesses. From [5].

We now focus on the temperature dependence of the emissivity of the structures under consideration. Total hemispherical emissivities of the Si monolayer on the Al substrate are plotted as a function of temperature in Fig. III.31(a) for different Si layer thicknesses. Total hemispherical emissivities increase with temperature, but at different rates when considering different layer thicknesses. Again, this increase is due to two separate effects: the frequency shift of the blackbody spectrum and the variations of the optical properties of Al with temperature. To separate the two effects, we define the enhancement factor of a given structure as the total hemispherical emissivity of the structure divided by the total hemispherical emissivity of a single Al substrate at

Cette thèse est accessible à l'adresse : http://theses.insa-lyon.fr/publication/2016LYSEI103/these.pdf
© [E. Blandre], [2016], INSA Lyon, tous droits réservés

a given temperature

$$E_f = \frac{\varepsilon^{\text{Substrate}} + \varepsilon^{\text{Layer}}}{\varepsilon^{\text{Substrate}}}. \tag{III.31}$$

By doing this, we can analyze the impact of the frequency shift of the blackbody spectrum without the impact of the variations of the optical properties of Al when temperature increases. In Fig. III.31(b), we plot the enhancement factor as a function of temperature for different layer thicknesses. For each thickness, the enhancement factor reaches a maximum at a given temperature, close to 3.3. Like previously, this temperature can be related to the spectral position of the maximum intensity of Planck's blackbody spectrum and of the first peak of interference. As a conclusion, interferences affect the total hemispherical emissivity of the structure and also its temperature dependence, and it is possible to determine the Si layer thickness that maximizes it for each temperature. The enhancement factor depends on the real part of the refractive index of the transparent layer. In Fig. III. 32, the maximum enhancement factors are reported as a function of the real part of the refractive index of the transparent layer.

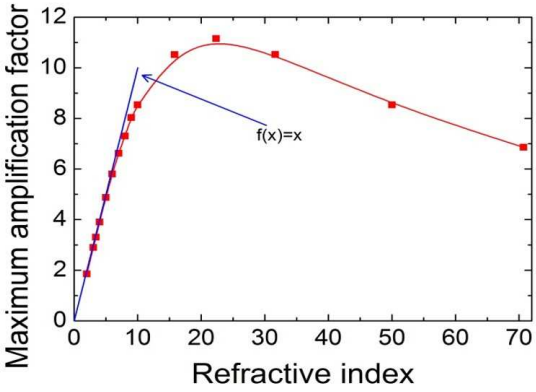

Figure III.32: Maximum enhancement factor of a monolayer on substrate as of function of the refractive index of the transparent layer.

It is observed that the maximum enhancement factor depends linearly on the real part of the refractive index of the transparent layer until it reaches a value around 10. Then, the maximum amplification factor reaches a maximum before decreasing when the real part of the refractive index decreases. Note that the layer of refractive index n is assumed lossless. In reality, the real and imaginary parts of the complex refractive index are linked by the Kramers-Kronig relation [30], and therefore the material considered in this example may be unrealistic. However, it provides a guideline to enhance the total hemispherical emissivity of this type of structure using interference phenomena.

Cette thèse est accessible à l'adresse : http://theses.insa-lyon.fr/publication/2016LYSEI103/these.pdf
© [E. Blandre], [2016], INSA Lyon, tous droits réservés

III.3.5 Maximizing the total hemispherical emissivity of few-layer structures using interference phenomena

A thin Al layer of thickness 5 nm is then added to the structure to enhance interference effects, forming an asymmetric Fabry-Pérot cavity [58, 60, 59], also referred to as Salisbury screen in the literature [81]. Unlike semiconductors, the hemispherical emissivity of metallic thin layers increases exponentially below a critical thickness. This effect was described in [71], where the threshold thickness was estimated to be a few dozens of nanometers. Using a thin metallic layer, it is possible to both increase the emissivity and enhance interferences effects in the Si layer. In

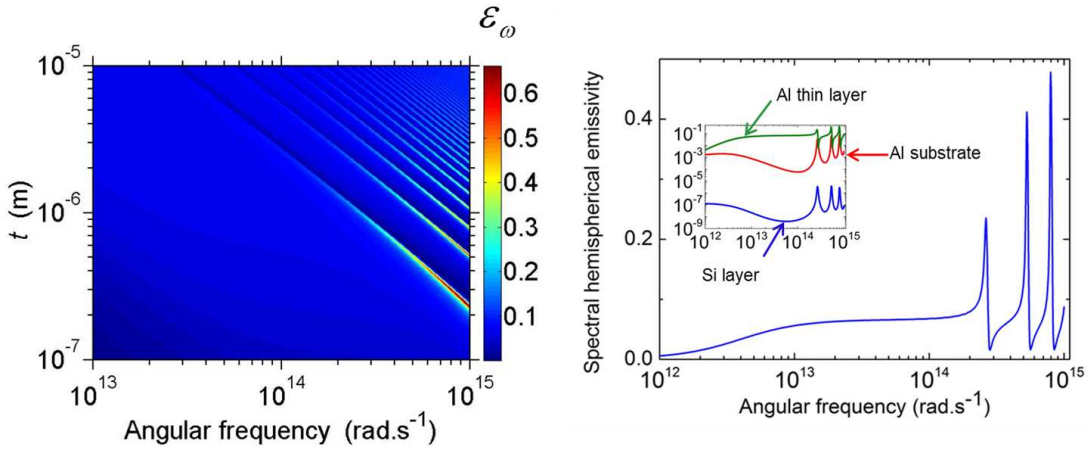

Figure III.33: Spectral hemispherical emissivity of the bilayer on substrate. (a): as a function of the thickness of the Si layer t_1. (b): for $t_1 = 1$ µm and $d = 5$ nm. The insert represents the participation of each layer to the emissivity.

Fig. III.33(a), the spectral hemispherical emissivity of the bilayer structure is reported as a function of the thickness of the silicon layer. It is observed that interferences have a larger amplitude, and also that the overall hemispherical emissivity of the structure is larger than the hemispherical emissivity of the monolayer. The spectral hemispherical emissivity of the structure for $t_1 = 1$ µm is reported on Fig. III.33(b). The shape of the interference peaks is now asymmetric. Furthermore, the spectral hemispherical emissivity of the structure reaches a minimum right after the maximum. An explanation of this phenomenon can be found in [58], where the analytic function of the reflectance of the structure was analyzed. Participation of each layer to the hemispherical emissivity of the structure is plotted in the insert. It is worth noticing that most of the emission, as well as the asymmetric shape of the interference peaks, comes now from the thin aluminum layer. In summary, the Al thin layer is the main source of emission in this structure, and waves emitted by this film are interfering inside the Si layer. This structure exhibits therefore larger values of spectral hemispherical emissivity, and interference peaks with larger amplitudes.
Finally, a second silicon layer is added onto the aluminum thin film to build a trilayer structure. We report in Fig. III.34(a) the total hemispherical emissivity of the structure as a function of the thicknesses t_1 and t_2 of the two Si layers. For a given thickness t_1, there is a thickness t_2 that maximizes the total hemispherical emissivity of the structure, and vice versa. The maximum of

Cette thèse est accessible à l'adresse : http://theses.insa-lyon.fr/publication/2016LYSEI103/these.pdf
© [E. Blandre], [2016], INSA Lyon, tous droits réservés

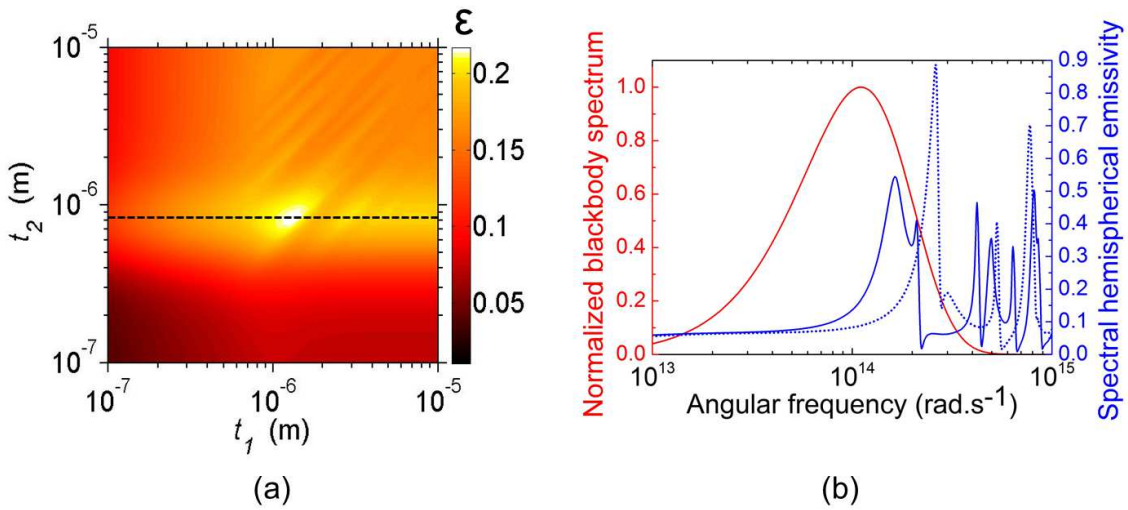

Figure III.34: (a): Total hemispherical emissivity of the trilayer on substrate structure for $T = 300$ K, as a function of t_1 and t_2. (b): Spectral hemispherical emissivity of the structure maximizing the total hemispherical, and normalized blackbody intensity at $T = 300$ K. From [5].

total hemispherical emissivity of the structure corresponds to the intersection of the optimal thicknesses for both t_1 and t_2. On Fig. III.34(a), the horizontal dashed line represents the thickness that maximizes the total hemispherical emissivity of the MOS structure at the same temperature. We observe that the optimal thickness t_1 is very close to this value, which is consistent after noticing that the second layer of thickness t_2 of the trilayer structure is equivalent to the layer of the monolayer structure in terms of interfaces, and therefore of conditions for constructive interference. It can indeed be expected that the maximum of the total hemispherical emissivity of the structure corresponds to the case where the first-order peaks of interference for both cavities occur at the same frequency, to form a large peak of emission as described in [53]. Using the constructive interference conditions (Eq. III.16) for both cavities gives

$$\lambda_n = \frac{2t_1 \cos\varphi}{(m - \frac{\phi_1}{2\pi})} = \frac{2t_2 \cos\varphi}{(m - \frac{\phi_2}{2\pi})}, \tag{III.32}$$

where ϕ_1 and ϕ_2 are the phase lags due to reflections at the interfaces at the boundaries of the layers, that take a value close to 0 and π respectively. Using this expression for $m = 1$, the first peak of interference in each layer overlaps when the thickness of the first layer t_1 is twice larger than the thickness of the second layer t_2, as depicted in Fig. III.34(b) (dotted line). In this case, the spectral hemispherical emissivity exhibits a large peak, that reaches a value close to 0.9. But according to Fig. III.34(a), this is not the configuration that maximizes the total hemispherical emissivity of the structure. In fact, the maximum of emissivity occurs when the first-order peaks of interference of both layers do not occur at the exact same frequency, but still overlap with the envelope of the blackbody at the considered temperature, as depicted in Fig. III.34(b) (full blue line), where the spectral hemispherical emissivity of the structure with the optimal architecture

Cette thèse est accessible à l'adresse : http://theses.insa-lyon.fr/publication/2016LYSEI103/these.pdf
© [E. Blandre], [2016], INSA Lyon, tous droits réservés

Table III.2: Maximum values of the spectral and total hemispherical emissivities at $T = 300$ K for each structure. The values for a simple Al substrate and a single Al thin layer are given for comparison.

	Al substrate	Al thin layer	Monolayer	Bilayer	Trilayer
Spectral maxima	0.01	0.06	0.13	0.48	0.89
Total maxima	0.01	0.06	0.03	0.07	0.21

is plotted.

The addition of a second Fabry-Pérot layer can therefore enhance the emissivity even more, and the successive addition of layers on the aluminum substrate increases the total hemispherical emissivity of the structure by one order of magnitude when using the optimal parameters of the system, as shown in Table III.2.

As a conclusion for this section, the influence of interferences on the spectral hemispherical emissivity and on the total hemispherical emissivity of layered structures as a function of temperature has been investigated. We have highlighted the impact of the variations with temperature of the optical properties of metallic layers on the hemispherical emissivity. We have shown that when interferences occur in an emitting layer, the spectral hemispherical emissivity of the structure exhibits sharp peaks, whose frequencies depend on the size of the layer and its refractive index. Hemispherical emissivities are increased, and an optimal film thickness that maximizes the hemispherical emissivity has been highlighted. We have also investigated how multilayered structures can enhance these effects, using an additional thin metallic film and a second layer to enhance interference effects. In the end, we have been able to increase the total hemispherical emissivity by a factor 20 in comparison to the bulk, and by a factor 6 in comparison to the thin metallic film. With the understanding of these phenomena, we have demonstrated that it is possible to provide a method with physical bases for maximizing the total hemispherical emissivity of few-layer structures.

III.4 Conclusions

We have investigated the far-field thermal emission of few-layer structures supporting interference phenomena. In the first section, dedicated to the design of a selective radiator for TPV applications, the spectral hemispherical emissivity of structures made of molybdenum and hafnium oxide layers deposited on a molybdenum substrate has been analyzed. Because of spectral variations of its optical properties, a Mo substrate exhibits a broadband emission in the spectral region below the wavelength corresponding to the bandgap energy of GaSb, while keeping low values above it. Mo is therefore a good candidate for building a selective TPV radiator to convert energy in a GaSb PV cell. We have focused on the understanding of the interference phenomena occurring in the radiator induced by the addition of transparent HfO_2 layer, in order to control the spectral hemispherical emissivity using constructive interferences. By defining a figure of merit, the design of a TPV radiator has then been performed. The addition of layers has proven to increase

Cette thèse est accessible à l'adresse : http://theses.insa-lyon.fr/publication/2016LYSEI103/these.pdf
© [E. Blandre], [2016], INSA Lyon, tous droits réservés

the figure of merit below the cutoff wavelength by a factor 4 compared to the Mo substrate alone, and reach a figure of merit defined over the whole wavelength range under consideration of 0.86. To sum up, we have demonstrated that using only three layers deposited on a substrate and the understanding of interference phenomena, emission spectra close to the one wanted can be obtained. The work in this section can be used as a guideline for designing TPV radiators.
In the second section, the variation with temperature of the same kind of structure has been investigated. By calculating the temperature-dependent dielectric function of Al, we have highlighted the importance of taking into account the variations of the optical properties of the materials constituting the radiator when calculating the thermal emission of structures. Eventually, the enhancement of the total hemispherical using interferences has been demonstrated. We have shown how to use the understanding of the impact of interferences to maximize the total hemispherical emissivity of few-layer structures, that can reach values up to 20 times larger than the one of a single Al substrate.
The work in this chapter constitutes a solid theoretical basis for the control of thermal emission of metallo-dielectric layered structures calculated from the Fluctuational Electrodynamics, and paves the way for the optimization of systems which require controlling the total radiative heat transfer between two bodies (for instance radiative rectification and radiative cooling) or the spectral distribution of the radiative heat flux emitted by a body, such as radiator in thermophotovoltaics.

Cette thèse est accessible à l'adresse : http://theses.insa-lyon.fr/publication/2016LYSEI103/these.pdf
© [E. Blandre], [2016], INSA Lyon, tous droits réservés

Cette thèse est accessible à l'adresse : http://theses.insa-lyon.fr/publication/2016LYSEI103/these.pdf
© [E. Blandre], [2016], INSA Lyon, tous droits réservés

Chapter IV

Near-field thermal radiation between a semi-infinite emitter and a film

Contents

IV.1 Introduction

In this manuscript, the analysis of the performances of thermophotovoltaic (TPV) systems is split into studies of three major phenomena that take place them: the radiative heat transfer from the hot source (radiator) to the PV cell, the generation and transport of electrical charges leading to an electrical current, and variations with temperature of the PV cell performances. We focus here on the analysis of the radiative behavior of near-field radiation mediated thermophotovoltaic (NFR-TPV) systems. In this frame, the near-field radiative heat transfer between a semi-infinite body and a thin film of finite thickness is under consideration in this chapter. This configuration is chosen because it is geometrically the closest to a NFR-TPV system. Indeed, the simplest radiator is a semi-infinite medium, while PV cells are films. The numerical modeling of radiative heat transfer in this configuration therefore allows analyzing the different phenomena that occur in the near field, that can impact the performances of energy conversion of NFR-TPV systems. In particular, we are interested on the phenomena that drive the spectral distribution of the radiative heat flux such as SPhP and interferences. The spatial distribution of the absorbed radiative power is also important. Indeed, the local absorption of radiative power is related to the local

Cette thèse est accessible à l'adresse : http://theses.insa-lyon.fr/publication/2016LYSEI103/these.pdf
© [E. Blandre], [2016], INSA Lyon, tous droits réservés

generation of electron-hole pairs (EHP) in a photovoltaic cell.

The first complete mathematical model for the calculation of near-field radiative heat transfer between two parallel plates was developed by Polder and Van Hove [17], and is based on the Fluctuational Electrodynamics approach [31] (see Chapter I). In the case of radiative heat transfer between two plates, it was highlighted in [17, 32] that the radiative heat flux between the two semi-infinite bodies increases when the distance between them decreases, due to the increasing contribution of evanescent waves. The role of surface polaritons on the spectral distribution of the radiative heat flux in the near-field was underlined in [23]. For very small vacuum gap sizes between the two plates, the authors observed resonances in the spectrum of thermal radiation, leading to the concentration of the energy exchanged by the two bodies in a narrow spectral band. Near-field thermal radiation therefore allows to increase the radiative power absorbed by a body, and to control the spectrum of the thermal radiation using surface polaritons. Both of those properties are interesting for the main application under study in this thesis: thermophotovoltaics.

After these discoveries, many studies were conducted on the topic of near-field thermal radiation between planar bodies, in order to characterize the near-field radiative heat transfer regime. It was shown that because of their large momentum, evanescent modes have a very low penetration depth, that was evaluated as approximately $0.2d$ in the case of two parallel plates separated by a vacuum gap of size d [82]. Another group [83, 84] studied hyperbolic metamaterials, and their ability to increase the penetration depth of near-field radiative heat flux. In those materials, the impact of frustrated modes (see Chapter I) on the spatial absorption is significant. Furthermore, these modes are propagating inside the absorber, so they are expected to have a larger penetration depth than surface modes. Studies involving the radiative transfer between two thin films [85, 24] showed that the hybridization of surface waves of the two interfaces of the film can impact the spectral shape at the resonances, and increase the number of evanescent modes participating to the radiative heat flux, therefore increasing the radiative heat flux at the resonances. The same principle was applied to substrates coated with a dielectric [86] or a metallic [87] film, with the same conclusions. More complex geometries were also studied. In [23], a sphere plane configuration is considered, while in [88], the near-field radiative heat transfer between two spheres was calculated.
Experimental proofs of those phenomena were obtained over the years. The increase of the radiative heat flux for a tip-plane geometry was demonstrated in [30, 89], and for a surface-sphere configuration in [90, 91, 92, 93]. These configurations are based on the use of an atomic force microscope (AFM), except for [30] that used a scanning tunneling microscope (STM). Experimental works considering a plane-plane configuration were also considered [94, 95, 96, 97]. Indeed, building and controlling a good parallelism between two plates separated by a nanometer sized vacuum gap is a technical challenge. However, it is interesting to note that for some sphere-plane configuration, experimental values were confronted with theoretical calculations using the Derjaguin approximation [98], which is an extrapolation of the calculation in the plane-plane geometry. Theoretical and experimental results showed a good agreement, meaning that the

Cette thèse est accessible à l'adresse : http://theses.insa-lyon.fr/publication/2016LYSEI103/these.pdf
© [E. Blandre], [2016], INSA Lyon, tous droits réservés

simulation of the near-field radiative heat transfer between plane bodies is sufficient to describe these specific cases of radiative heat transfer between a sphere and a plate. Possible spectral resonance of the near-field radiation was also demonstrated in [99, 100, 101] using scanning near-field optical microscopy in the scattering configurations.
In the first section of this chapter, we analyze the variations of the different modes (propagative, frustrated and evanescent) as a function of the thickness of the film t and the size of the vacuum gap d. We also pay a particular attention to the number and shapes of the resonance branches. Then, we investigate the spatial distribution of the absorbed radiative power inside thin absorbing films. We focus on the penetration depth of the different modes, and underline the role of surface modes on the spatial absorption of very thin films. Eventually, we study the near-to-far field transition regime, where interference phenomena can occur due to coherence effects, and we emphasize on the impact of interferences on the spatial and spectral distributions of the radiative heat flux inside the absorbing film. In the following figures and the text are partially taken from [6].

IV.2 Description of the problem

We consider the case of a semi-infinite body emitting towards a film of thickness t, as depicted in Fig. IV.1. The emitter and the film are made of the same material. The depth inside the film is called z and the origin of this axis is set such that the entrance of the film corresponds to $z = 0$. In NFR-TPV systems, the radiator is usually at a much higher temperature than the PV cell, such that the net radiative heat flux between the two bodies is close to the radiative heat flux emitted by the radiator and absorbed by the PV cell. Therefore, to simplify the problem, we consider the film to be non-emitting: its temperature is set to 0 K.

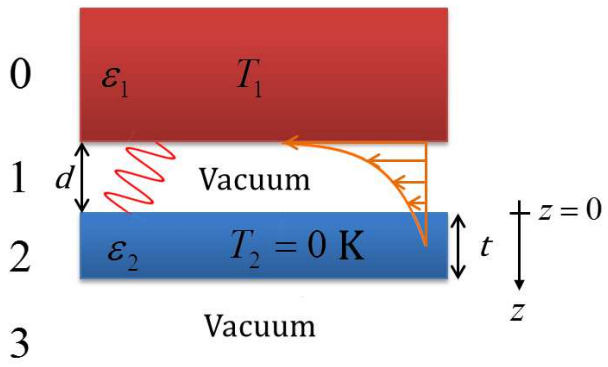

Figure IV.1: Case of a semi-infinite emitter separated by a vacuum gap of size d from a film of thickness t. The film is considered as non-emitting.

The radiative heat flux between the semi-infinite emitter and the film is computed with the Fluctuational Electrodynamics approach, and the Green's functions are computed using the S-matrix approach (section I.4). Since this case is rather simple, we can use the analytical formulation from [24] to compare our results. The analytical calculation of the coefficients A, B, C and D leads to the

Cette thèse est accessible à l'adresse : http://theses.insa-lyon.fr/publication/2016LYSEI103/these.pdf
© [E. Blandre], [2016], INSA Lyon, tous droits réservés

following equation for the monochromatic heat flux at the entrance of the film ($z = 0$) [24]

$$q_\omega^{prop}(z=0) = \frac{\Theta(\omega, T_{emit})}{4\pi^2} \times \int_0^{\frac{\omega}{c}} k_\rho dk_\rho \sum_{\gamma=s,p} \frac{(1-|r_{21}^\gamma|^2)(1-|R_3^\gamma|^2)}{|1-r_{21}^\gamma R_3^\gamma e^{2ik_{z_2}d}|^2}, \tag{IV.1}$$

$$q_\omega^{evan}(z=0) = \frac{\Theta(\omega, T_{emit})}{\pi^2} \times \int_{\frac{\omega}{c}}^{\infty} k_\rho dk_\rho e^{-2k''_{z_2}d} \sum_{\gamma=s,p} \frac{Im(r_{21}^\gamma) Im(R_3^\gamma)}{|1-r_{21}^\gamma R_3^\gamma e^{2ik_{z_2}d}|^2}, \tag{IV.2}$$

where:

- γ stands for to the polarization s or p,
- r_{ij}^γ are the reflection coefficients for the s and p polarizations for the interface between media i and j,
- R_3^γ represents the total reflection coefficient of the film, and its expression is given by [24]

$$R_3^\gamma = \frac{r_{12}^\gamma + r_{23}^\gamma e^{2ik_{z_3}t}}{1 + r_{12}^\gamma r_{23}^\gamma e^{2ik_{z_3}t}}. \tag{IV.3}$$

The red terms represent the transmission coefficient T_e^γ. The total monochromatic heat flux is the summation of the two components q_ω^{prop} and q_ω^{evan}. In order to analyze the participations of the propagative, frustrated and surface modes to the radiative heat transfer, we divide the monochromatic heat flux into three components, by splitting the integration of k_ρ into three parts (Fig. IV.2):

- from $k_\rho = 0$ to $k_\rho = \frac{\omega}{c}$ for the purely propagative modes,
- from $k_\rho = \frac{\omega}{c}$ to $k_\rho = \frac{\omega n}{c}$, where n is the real part of the complex refractive index of the material [102] for the frustrated modes,
- from $k_\rho = \frac{\omega n}{c}$ to $k_\rho = \infty$ for the surface (or purely evanescent) modes.

To analyze the distribution of absorption of the radiative heat flux, we discretize the film into N control volumes (CV). The radiative heat flux at the boundaries of each CV is then calculated, and the radiative power absorbed (q_{vol}) by a sublayer of size Δz of the film located between z and $z + \Delta z$ is given by:

$$q_{\text{vol}}(z) = \frac{q(z) - q(z+\Delta_z)}{\Delta z}. \tag{IV.4}$$

Silicon carbide, that supports SPhP in the infrared, will be the material under consideration. The dielectric function of SiC can be approximated by a damped oscillator model (Lorentz model) as [24]

$$\epsilon(\omega) = \epsilon_\infty \left[\frac{\omega^2 - \omega_{LO}^2 + i\Gamma\omega}{\omega^2 - \omega_{TO}^2 + i\Gamma\omega} \right] \tag{IV.5}$$

Cette thèse est accessible à l'adresse : http://theses.insa-lyon.fr/publication/2016LYSEI103/these.pdf
© [E. Blandre], [2016], INSA Lyon, tous droits réservés

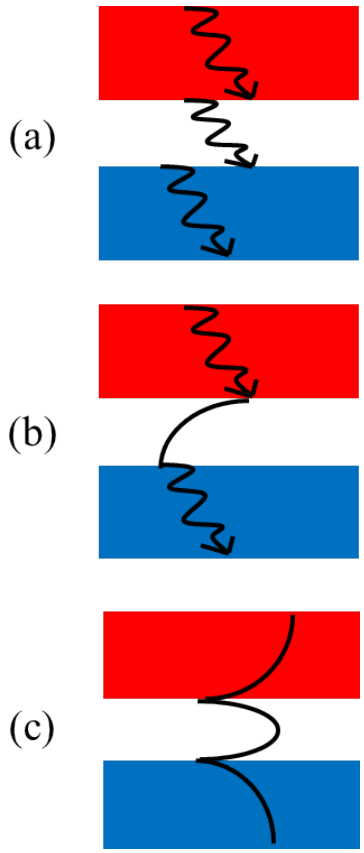

Figure IV.2: Schematic representation of the different components of the radiative heat flux:
(a): the modes are purely propagative,
(b): the modes are frustrated, i.e. propagative in the material and evanescent in vacuum,
(c): the modes are purely evanescent.

For SiC, $\epsilon_\infty = 6.7$, $\omega_{LO} = 1.827 \times 10^{14}$ rad/s, $\omega_{TO} = 1.495 \times 10^{14}$ rad/s, and $\Gamma = 8.971 \times 10^{11}$ rad/s.

IV.3 Spectral and directional analyses

First, we analyze the values of the transmission coefficient T_e^γ as a function of k_ρ and ω. Fig. IV.3 represents these values in the case of a SiC emitter separated by a vacuum gap of size $d = 100$ nm from a SiC film of thickness $t = 100$ nm.

The $(k_\rho,\ \omega)$ plane can be decomposed into three parts. The blue dashed line is the curve of equation $\omega = k_\rho c$. It means that the region on the left of this blue line represents the propagative modes. The green dashed line is the curve of equation $\omega = \frac{k_\rho c}{n}$, it means that the region on the right of this line corresponds to the fully evanescent modes. Eventually, in-between the two curves, the last region corresponds to the frustrated modes. We observe that there is a spectral band where $k_\rho c > \frac{k_\rho c}{n}$. In this case, the frustrated modes cannot exist. This means that frustrated modes can only exist if $n > 1$.

For large k_ρ, the values of the transmission coefficients tend to 0. This is due to the exponential

Cette thèse est accessible à l'adresse : http://theses.insa-lyon.fr/publication/2016LYSEI103/these.pdf
© [E. Blandre], [2016], INSA Lyon, tous droits réservés

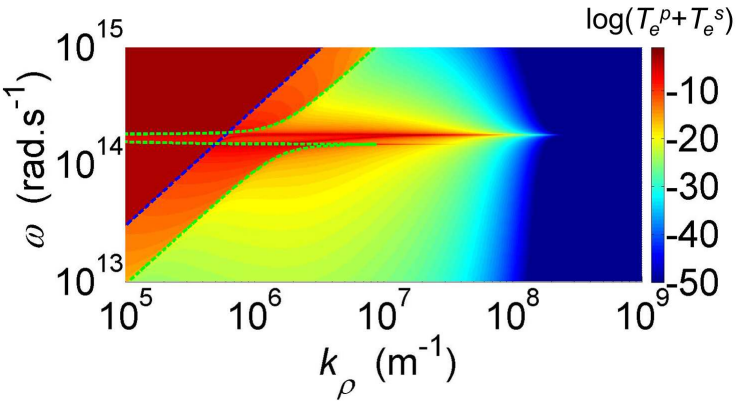

Figure IV.3: Plot of the p and s polarized transmission coefficients T_e^p and T_e^p, as a function of k_ρ and ω, in the case of SiC for $d = t = 100$ nm. The blue dashed line is the curve of equation $\omega = k_\rho c$ and the green dashed line is the curve of equation $\omega = \frac{k_\rho c}{n}$

factor $e^{-2ik_z'' d}$ in the expression of the transmission coefficient for evanescent modes. When k_ρ is large, k_z is approximately equal to ik_ρ, and the exponential term becomes $e^{-2k_\rho d}$. When k_ρ becomes larger than $\frac{5}{d}$, the exponential factor becomes much smaller than 1. In summary, the radiative heat flux becomes negligible when $k_\rho > \frac{5}{d}$, and in the following, the integration over k_ρ will be performed from $k_\rho = 0$ to $k_\rho = \frac{5}{d}$.
The spectral band where $n > 1$, between $\omega = \omega_{LO}$ and $\omega = \omega_{TO}$, is the spectral region where SPhPs can exist. The resonance branches of the surface modes clearly appear in this frequency band. We are interested in the evolution of the strengths of the different modes when the film thickness (t) varies.

In Fig. IV.4, the size of the vacuum gap (d) is still set at 100 nm, and the thickness of the film is varied. The most striking fact is that when the film thickness decreases, the values of T_e for the frustrated modes decrease. Variations of the resonance branches are also observed. The next section focus on this phenomenon.

IV.4 Behaviour of the SPhP resonances for SiC

The behaviors of the resonances are studied as a function of the parameters d and t. First, we investigate the case of a semi-infinite SiC body emitting toward a thick layer.

In Fig. IV.5, we observe the dispersion relation of the SPhP for a single SiC-vacuum interface. This dispersion relation can be analytically determined using the continuity relations of the electromagnetic field at the SiC-vacuum interface. Following the development made in [23], the dispersion relation can be written as

$$k = \frac{\omega}{c}\sqrt{\frac{\epsilon_{SiC}(\omega)}{\epsilon_{SiC}(\omega)-1}}. \tag{IV.6}$$

Cette thèse est accessible à l'adresse : http://theses.insa-lyon.fr/publication/2016LYSEI103/these.pdf
© [E. Blandre], [2016], INSA Lyon, tous droits réservés

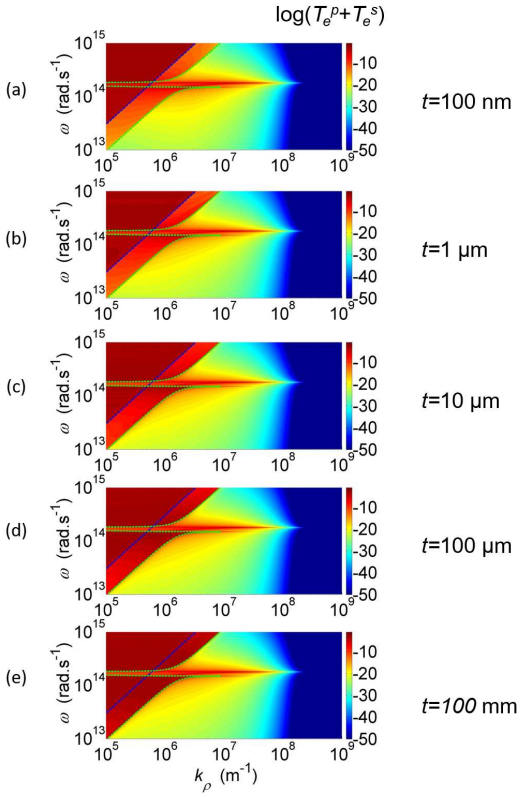

Figure IV.4: Sum of the p and s polarized transmission coefficients T_e^p and T_e^p, as a function of k_ρ and ω, in the case of SiC for $d = 100$ nm and several thicknesses t. (a): $t = 100$ nm, (b): $t = 1$ µm, (c): $t = 10$ µm, (d): $t = 100$ µm and (e): $t = 100$ mm.

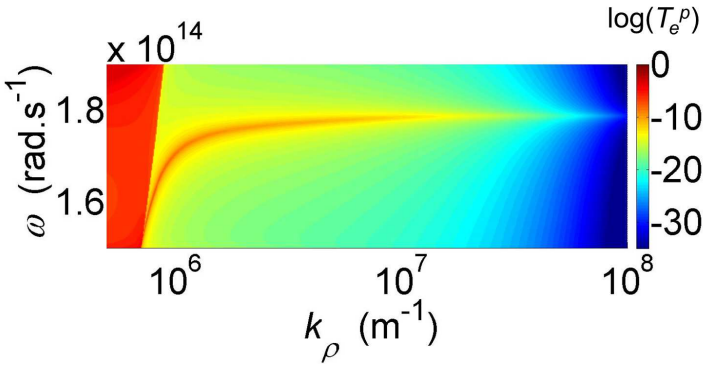

Figure IV.5: p-polarized transmission coefficient T_e^p, as a function of k_ρ and ω, in the case of a semi-finite SiC emitter and a semi-infinite black absorber for $d = 100$ nm. Note the logarithmic scale.

The case of two semi-infinite bodies of SiC is depicted next. In Fig. IV.6, the p-polarized transmission coefficient T_e^p is plotted for the case of two semi-infinite SiC bodies separated by a vacuum gap of size $d = 100$ nm.

We observe the splitting of the resonance branch of the single SiC-vacuum interface into two

Cette thèse est accessible à l'adresse : http://theses.insa-lyon.fr/publication/2016LYSEI103/these.pdf
© [E. Blandre], [2016], INSA Lyon, tous droits réservés

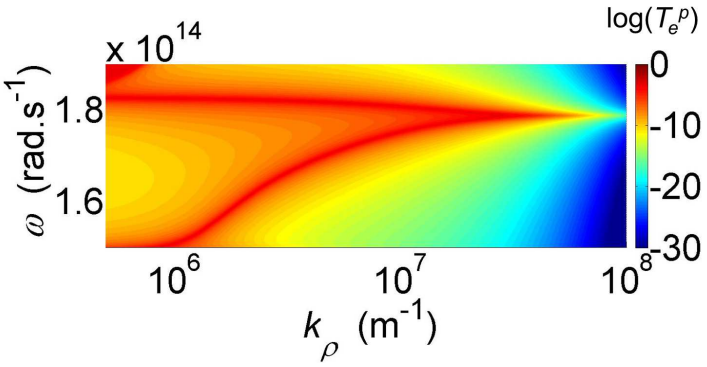

Figure IV.6: p-polarized transmission coefficient T_e^p, as a function of k_ρ and ω, in the case of two semi-finite SiC bodies for $d = 100$ nm. Note the logarithmic scale.

branches. It is known that the surface waves of two bodies that are close enough from each other can couple inside the cavity between them. If their resonance branches match, they split into symmetric and antisymmetric modes [23, 103, 104]. The upper branch corresponds to the symmetric mode, and the lower branch to the antisymmetric mode. The two branches merge at large k_ρ into the asymptotic value for the single SiC-vacuum interface case. When k_ρ is large, the denominator of T_e^p ($|1 - r_{21}^\gamma R_3^\gamma e^{2ik_{z_2}d}|^2$) is equal to 1 because of the exponential term, and as a consequence, T_e^p becomes close to the single SiC-vacuum interface case. We can interpret this using the penetration depth of evanescent waves δ. It can be written as a function of k_z [82]

$$\delta = \frac{1}{Im(2k_z)}. \tag{IV.7}$$

At large k_ρ, $k_z = ik_\rho$, thus

$$\delta = \frac{1}{2k_\rho}, \tag{IV.8}$$

meaning that a surface wave cannot penetrate further than $\frac{1}{2k_\rho}$. The penetration depth of surface waves is therefore of the same order of magnitude as the size of the vacuum gap d. If the penetration depth is smaller than the size of the vacuum gap (i.e. $k_\rho > \frac{1}{d}$), the surface waves cannot couple, and the two resonance branches merge into the single one associated to a single SiC-vacuum interface.

Two surface waves can also couple inside a film if it is thin enough [87, 85, 24]. This is shown in Fig. IV.7 where T_e^p is plotted in the case of a blackbody half-space emitting on a thin SiC film. Again, we observe the splitting of the coupled surface waves, but inside the thin film. The two branches merge into the single branch associated to the case of the single SiC-vacuum interface. Using the same analysis as before, we can physically interpret this using the penetration depth of SPhPs, but this time inside the film. In addition, using the reflection coefficient of the film R_3, we notice again that when k_ρ is large, we get back to the case of the single SiC-vacuum

Cette thèse est accessible à l'adresse : http://theses.insa-lyon.fr/publication/2016LYSEI103/these.pdf
© [E. Blandre], [2016], INSA Lyon, tous droits réservés

interface.

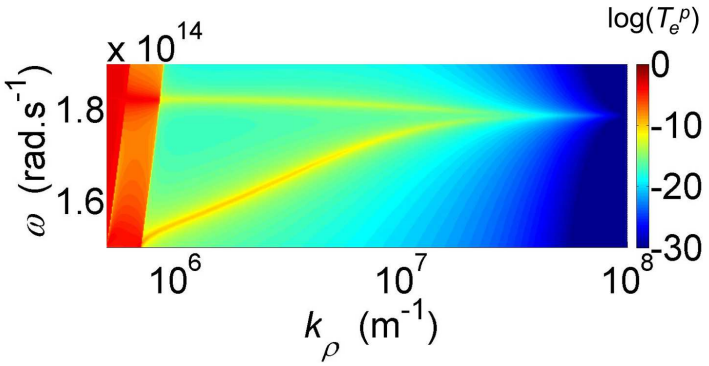

Figure IV.7: p polarized transmission coefficient T_e^p, as a function of k_ρ and ω, in the case of a blackbody emitting half space separated by a vacuum gap size $d = 100$ nm of a thin SiC film $t = 100$ nm. Note the logarithmic scale.

To sum up, two surface waves from two close interfaces can couple, either in vacuum (case of a cavity between two materials) or in a material (case of a thin film).
The case of a SiC half-space emitting on a SiC film is thus analyzed next. We first study the influence of the film thickness on the resonances.

In Fig. IV.8, the p-polarized transmission coefficient is plotted as a function of k_ρ and ω for $d = 100$ nm and several thicknesses (t). When the film is thick ($t = 10$ µm, (a)), the shape of the resonances is close to the case of two semi-infinite SiC media. When the thickness of the film decreases, we observe the apparition of a third resonance branch, due to the thermal excitation of the interface at the rear of the film. We notice that this branch disappears when k_ρ reaches approximately $\frac{5}{t}$, and that its dispersion relation is the same as in the case of a single SiC-vacuum interface. The shapes of the upper and lower branches are also slightly modified.
We then calculate the dispersion relations of the three branches, following the reasoning used in [24]. The condition for resonance is that for p-modes, the transmission coefficient becomes large

$$\frac{(1-|r_{21}^\gamma|^2)(1-|R_3^\gamma|^2)}{|1-r_{21}^\gamma R_3^\gamma e^{2ik_{z_2}d}|^2} >> 1 \tag{IV.9}$$

It means that either

$$(1-|r_{21}^\gamma|^2)(1-|R_3^\gamma|^2) >> 1 \tag{IV.10}$$

or that

$$|1-r_{21}^\gamma R_3^\gamma e^{2ik_{z_2}d}|^2 \to 0 \tag{IV.11}$$

First, we search the couples (ω, k_ρ) that fulfill Eq. IV.11. To simplify the calculations, we use the

Cette thèse est accessible à l'adresse : http://theses.insa-lyon.fr/publication/2016LYSEI103/these.pdf
© [E. Blandre], [2016], INSA Lyon, tous droits réservés

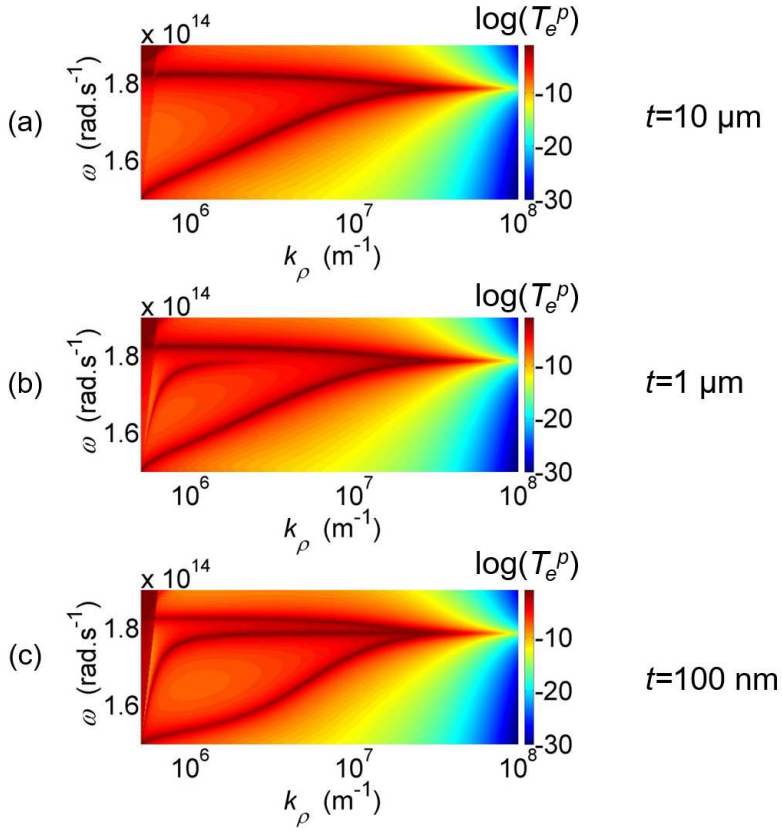

Figure IV.8: p-polarized transmission coefficient T_e^p as a function of k_ρ and ω in the case of a SiC emitting half space separated by a vacuum gap of size $d = 100$ nm from a film of different thicknesses t. (a): $t = 10$ µm (b): $t = 1$ µm (c): $t = 100$ nm. Note the logarithmic scale.

approximation which assumes that for surface modes, k_ρ is large, such that:

$$k_z = \sqrt{\epsilon_{SiC} k^2 - k_\rho^2} \approx i k_\rho. \tag{IV.12}$$

Using this approximation, the reflection coefficients r_{ij} becomes

$$r_{21}^p = \frac{\epsilon_{SiC} - 1}{\epsilon_{SiC} + 1} \tag{IV.13}$$

Eventually, if the losses are neglected in the dielectric function of SiC, the reflection coefficients become pure real numbers, and solving Eq. IV.11 becomes straightforward. Substituting Eq. IV.13 into Eq. IV.11 leads to two solutions for $\omega(k_\rho)$

$$\omega^\pm = \left[\frac{\epsilon_\infty \omega_{LO}^2 - \Phi^\pm \omega_{TO}^2}{\epsilon_\infty - \Phi^\pm} \right]^{1/2} \tag{IV.14}$$

where

$$\Phi^+ = \frac{\sqrt{h} + 1}{\sqrt{h} - 1} \tag{IV.15}$$

Cette thèse est accessible à l'adresse : http://theses.insa-lyon.fr/publication/2016LYSEI103/these.pdf
© [E. Blandre], [2016], INSA Lyon, tous droits réservés

and

$$\Phi^- = \frac{\sqrt{h}-1}{\sqrt{h}+1} \tag{IV.16}$$

h is a function of the geometric parameters of the system

$$h = e^{-2k_\rho t} + e^{-2k_\rho d} - e^{-2k_\rho (t+d)} \tag{IV.17}$$

ω^+ and ω^- are the dispersion relations for the upper and lower branches, respectively. To find the equation of the middle branch, Eq. IV.10 must be satisfied. This condition is the same as for the case of a single SiC-vacuum interface, and so its dispersion relation is given by

$$k_\rho = Re\left(\frac{\omega}{c}\sqrt{\frac{\epsilon_{SiC}}{\epsilon_{SiC}+1}}\right). \tag{IV.18}$$

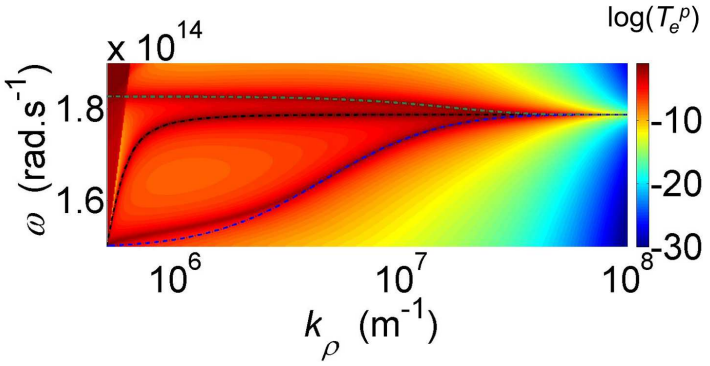

Figure IV.9: p-polarized transmission coefficient T_e^p as a function of k_ρ and ω in the case of a SiC emitting half space separated by a vacuum gap of size $d = 100$ nm from a film of thickness $t = 100$ nm. The black dashed line is the dispersion relation given by Eq. IV.18, and the blue and green lines are the ones given by Eq. IV.14. Note the logarithmic scale.

In Fig. IV.9, we plot the p-polarized transmission coefficients as a function of k_ρ and ω for $t = d = 100$ nm. The curves representing the calculated dispersion relations are superimposed. We observe that these curves fit pretty well the resonances, with just a little discrepancy at low k_ρ, where the high-k_ρ approximation is probably not valid. We conclude that the upper and lower branches are the result of the coupling of the SPhPs of two interfaces of the system. They overlap and split into symmetric and antisymmetric modes. The middle branch comes from the last interface. Its equation is the same as in the case of a single SiC-vacuum interface. For a deeper analysis, the dispersion relations are plotted for $d = 100$ nm and several thicknesses t, with the condition that $d > t$. Results are gathered in Fig. IV.10. First, we observe that all curves merges into the case of the single SiC-vacuum interface at $k_\rho = \frac{5}{d}$. Then, when the film thicknesses increase, the dispersion relations merge into the bulk-bulk case at lower k_ρ.

We show that the limit k_ρ where a curve for a film thickness t merge into the curve assciated to the case of a semi-infinite absorber is approximately $\frac{5}{t}$, which again is related to the penetration depth inside the film. Therefore, when $k_\rho < \frac{5}{t}$, the evanescent waves have a sufficient penetra-

Cette thèse est accessible à l'adresse : http://theses.insa-lyon.fr/publication/2016LYSEI103/these.pdf
© [E. Blandre], [2016], INSA Lyon, tous droits réservés

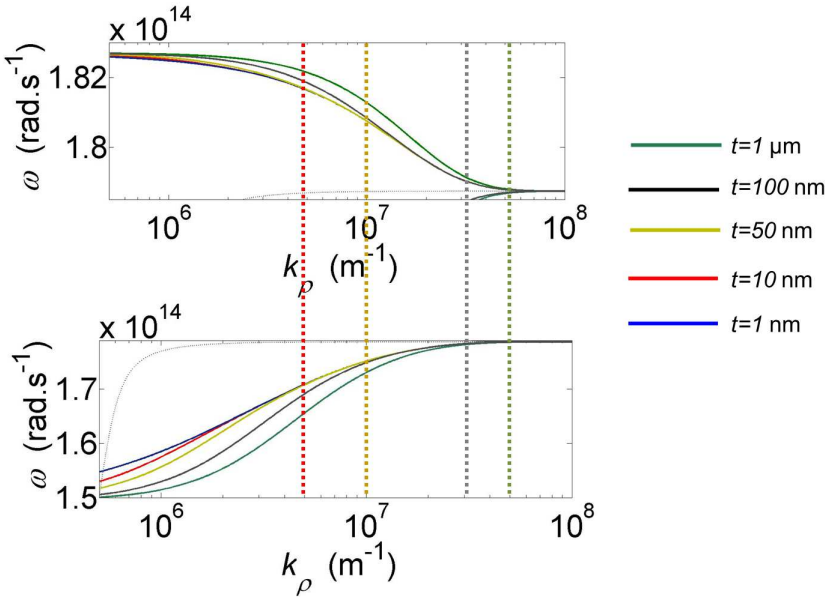

Figure IV.10: Dispersion relations for $d = 100$ nm and several thicknesses t. The vertical lines represent the abscissa $k_\rho = \frac{5}{t}$, where t is the thickness of the film for the curve of the same color.

tion depth to excite the rear interface of the film. After this limit, the surface modes at the rear of the film cannot be excited, so there is a coupling only between the interface of the emitter and the top interface of the film: the case of two semi-infinite bodies is reached.
Because the resonance branches merge into each other at $k_\rho = \frac{5}{t}$, and the values of the transmission coefficient become close to 0 at $k_\rho = \frac{5}{d}$, a regime appears if t becomes smaller than d. In this regime, the branches do not merge into the curve associated to a single SiC-vacuum interface other before the cutoff value $k_\rho = \frac{5}{d}$ is reached. This phenomena is depicted in Fig. IV.11.

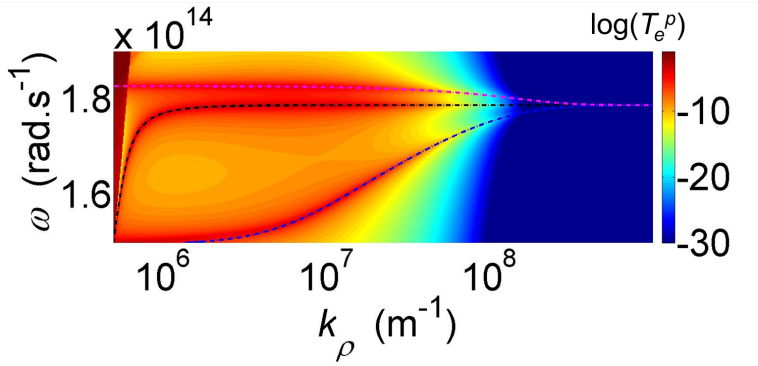

Figure IV.11: p-polarized transmission coefficient T_e^p, as a function of k_ρ and ω for $t = 10$ nm and $d = 100$ nm. The dotted lines represent the dispersion relations of the SPhPs.

The dispersion relations merge into each other at about $k_\rho = \frac{5}{t}$, but the values of k_ρ in this region are larger than $\frac{5}{d}$, and therefore the transmission coefficient becomes negligible. As a consequence, two regimes are possible, defined by either $\frac{t}{d} \geq 1$ or $\frac{t}{d} < 1$.

Cette thèse est accessible à l'adresse : http://theses.insa-lyon.fr/publication/2016LYSEI103/these.pdf
© [E. Blandre], [2016], INSA Lyon, tous droits réservés

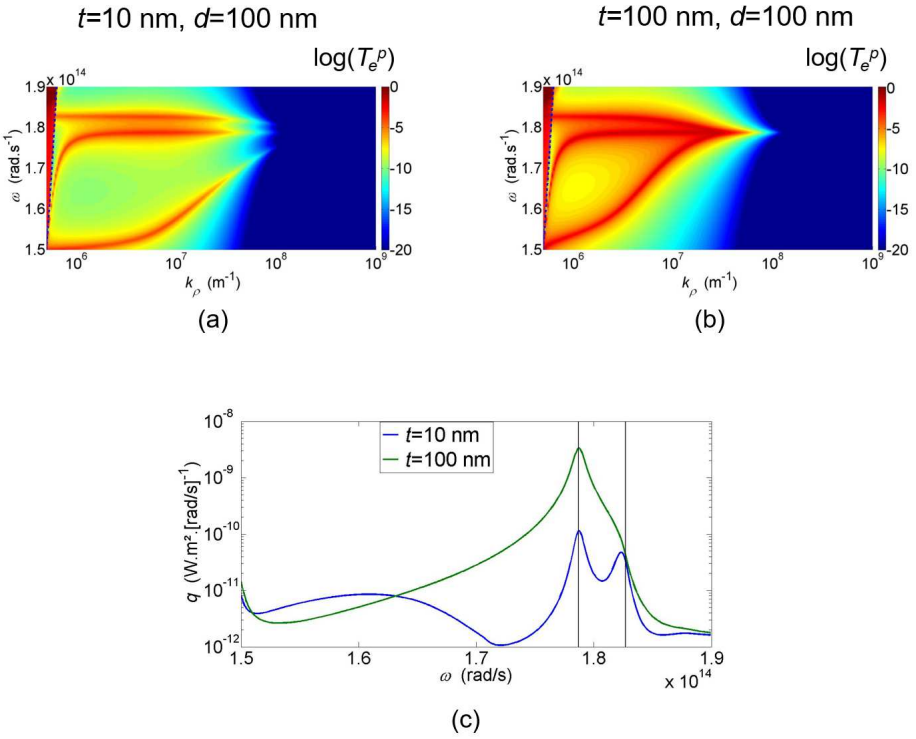

Figure IV.12: p-polarized transmission coefficient T_e^p, as a function of k_ρ and ω. (a): for $t = 10$ nm and $d = 100$ nm. (b): for $t = 100$ nm and $d = 100$ nm. (c) Monochromatic radiative heat flux for $d = 100$ nm and for $t = 10$ nm and $t = 100$ nm.

The impact on the emission spectrum of the two regimes is depicted in Fig. IV.12. In Fig. IV.12(a) and (b), the p-polarized transmission coefficient T_e^p is depicted for $d = 100$ nm for the two regimes: $\frac{t}{d} < 1$ (Fig. IV.12(a)), and $\frac{t}{d} \geq 1$ (Fig. IV.12(b)). In Fig. IV.12(c), the monochromatic radiative heat flux in the two cases is depicted. It is observed that for the case $\frac{t}{d} < 1$, the peak due to the surface phonon-polaritons is attenuated and split into two peaks. On the other hand when $\frac{t}{d} \geq 1$, the spectrum of emission still exhibits a large peak.

As a conclusion for this section, we have investigated the SPhP resonances in the case of a semi-infinite emitter and an absorbing film. Especially, the dispersion relations have been analyzed when varying the size of the vacuum gap (d) and the thickness of the film (t). The coupling of the surface modes of the different interfaces induces different dispersion relations, that have been calculated. In particular, we have analyzed the impact of the dispersion relations on the spectrum of emission. If the size of the film t is smaller than the size of the vacuum gap d, the peak of emission due to SPhP resonances is attenuated.

Cette thèse est accessible à l'adresse : http://theses.insa-lyon.fr/publication/2016LYSEI103/these.pdf
© [E. Blandre], [2016], INSA Lyon, tous droits réservés

IV.5 Spatial absorption of the radiative power inside the film

In this section, we study the spatial distribution of the absorption of the radiative power inside the film. The spatial distribution of the generation of electrical charges is impacting the performances of the PV cell. Therefore, controlling where the radiative power is absorbed is an important topic to control the performances of NFR-TPV systems. The case of a film of infinite thickness (i.e. the near-field radiative heat transfer between two bulks) is considered first.

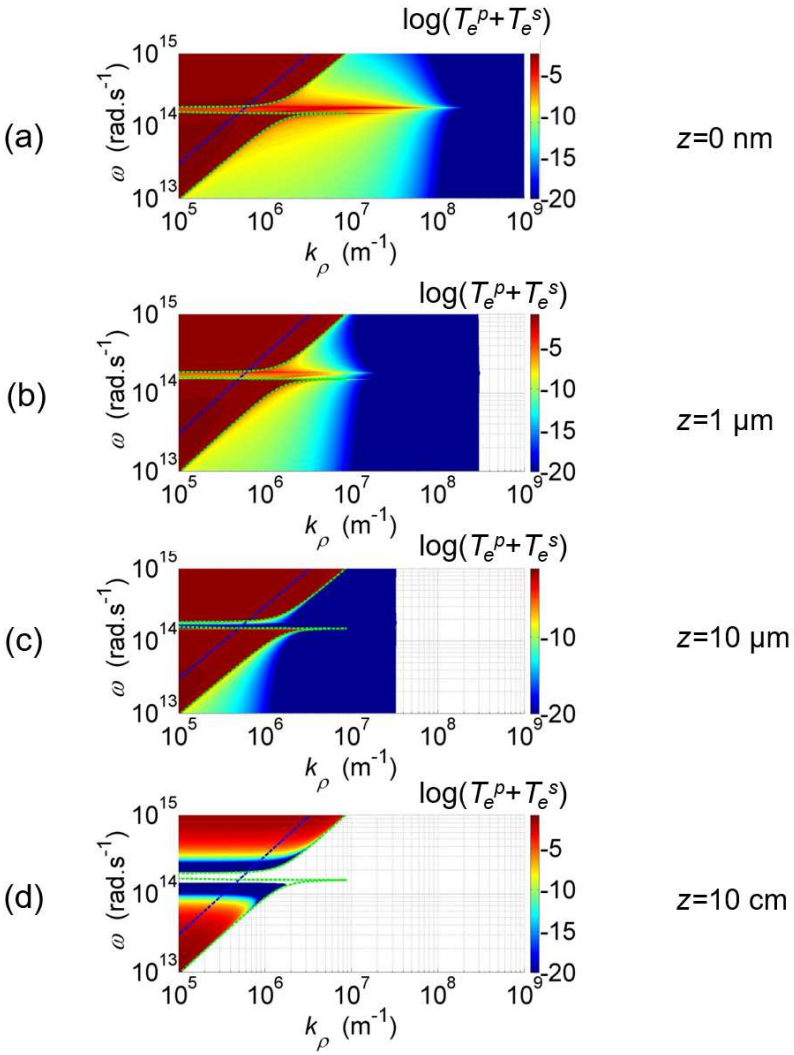

Figure IV.13: Sum of the p and s polarized transmission coefficients T_e^p and T_e^p as a function of k_ρ and ω at different depths inside the absorber z, in the case of two SiC bulks separated by a vacuum gap of size $d = 100$ nm. (a): $z = 0$ nm, (b): $z = 1$ µm. (c): $z = 10$ µm, (d): $z = 10$ cm. The white color means that the numerical value was rounded to 0, and therefore not represented on the logarithmic scaled figure.

In Fig. IV.13, we plot the transmission coefficient $T_e^p + T_e^s$ as a function of k_ρ and ω for two SiC bulks separated by a vacuum gap of size $d = 100$ nm, for several depths inside the film. It is observed that the evanescent modes with the largest values of k_ρ are absorbed close to the

Cette thèse est accessible à l'adresse : http://theses.insa-lyon.fr/publication/2016LYSEI103/these.pdf
© [E. Blandre], [2016], INSA Lyon, tous droits réservés

surface. As mentioned before, these modes have the smallest penetration depth. When the depth increases, evanescent modes are fully absorbed, and only the propagative and frustrated modes are participating to the absorption.

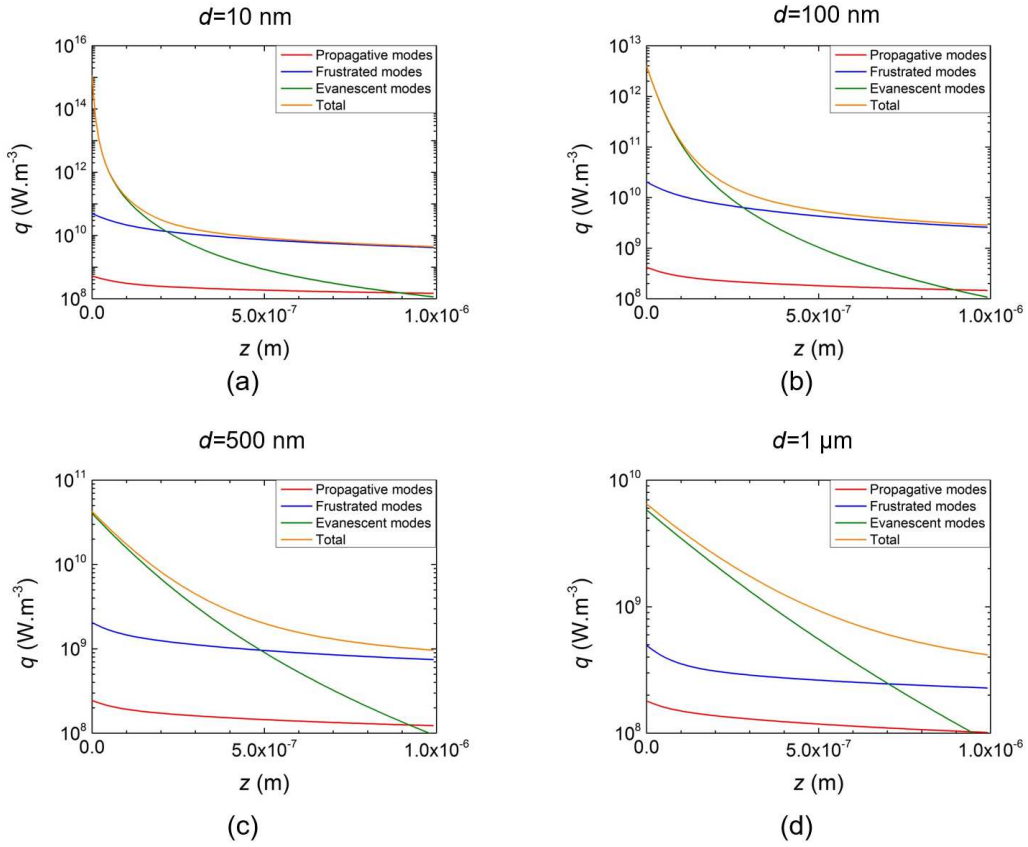

Figure IV.14: Absorbed volumetric radiative power as a function of depth inside the film z in the case of two SiC bulks. (a): $d = 10$ nm, (b): $d = 100$ nm, (c): $d = 500$ nm, (d): $d = 1$ µm. The contributions of the propagative, frustrated and evanescent modes are highlighted.

The spatial distribution of the absorbed radiative power is analyzed in Fig. IV.14. The contributions of the propagative, frustrated and evanescent modes are separated. It is observed that near the surface of the film, purely evanescent waves dominate the absorption. After they are absorbed, a second regime appears where absorption is dominated by the frustrated modes. This second regime occurs from at depths when the distance d decreases, due to the stronger contribution of the frustrated modes. Contribution of the propagative modes is negligible for the distances d considered. It is also observed that when the distance between the two bodies d decreases, the decay of the evanescent modes when z increases is stronger. This is due to the fact that for small values of d, the large k_ρ modes are excited, and therefore the purely evanescent modes have a smaller penetration depth. On the other hand, the penetration depth of the frustrated modes does not vary much when the distance d varies.

The case of an absorbing film of thickness t is now considered. In Fig. IV.15, the spatial distribu-

Cette thèse est accessible à l'adresse : http://theses.insa-lyon.fr/publication/2016LYSEI103/these.pdf
© [E. Blandre], [2016], INSA Lyon, tous droits réservés

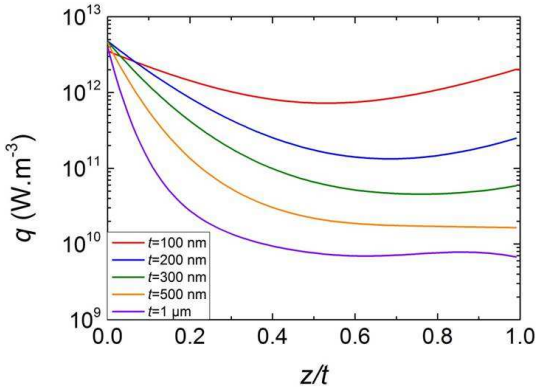

Figure IV.15: Absorbed volumetric radiative power as a function of the depth inside the film z normalized by the size of the film t, for several thicknesses.

tion of the absorbed radiative power is plotted as a function of depth inside the film normalized by its size, for several thicknesses t. In this figure, we observe that the absorbed radiative power is exponentially decreasing as a function of depth in the film. However, for the smallest thicknesses, it re-increases near the rear interface of the film. This phenomenon is clear for $t = 100$ nm, and becomes hardly visible when the film thickness increases. The rise of the absorbed radiative power is due to the excitation of the surface wave at the rear interface of the film. To analyze this phenomenon, we define a term $M(k_\rho, \omega, z)$ which is a function of the p-polarized transmission coefficient T_e^p at locations z and $z + \Delta z$, such as

$$M(k_\rho, \omega, z) = T_e^p(k_\rho, \omega, z) - T_e^p(k_\rho, \omega, z + \Delta z) \tag{IV.19}$$

This term allows analyzing the absorption of the radiative power at location z.

We plot in Fig IV.16 the values of M as a function of k_ρ and ω for several depths inside the film of thickness $t = 100$ nm, and a distance separating the emitter and the absorber $d = 100$ nm. An animated version of this figure can be found in the supplemental materials section of [6]. At the entrance of the film (Fig IV.16(a)), absorption is dominated by the SPhP modes, especially the upper and lower branches. Their contribution decreases when the depth increases. Near the rear interface of the film, the absorption increases by means of the middle branch. The conclusion is that the single-interface resonant mode comes from the rear interface of the film. The upper and lower branches are the result of the splitting of the symmetric and antisymmetric modes of the surface waves of the two interfaces of the cavity, and are slightly affected by the remaining interface inside the film.

As a conclusion for this section, the spatial distribution of the near-field radiative power is dominated by the purely evanescent modes with a low penetration depth, at the surface of the absorbing media. The frustrated modes have a larger penetration length, and therefore play an important role away from the surface. It is important to mention here that because SiC is supporting SPhPs, the contribution of the evanescent modes is large. For materials that do not support

Cette thèse est accessible à l'adresse : http://theses.insa-lyon.fr/publication/2016LYSEI103/these.pdf
© [E. Blandre], [2016], INSA Lyon, tous droits réservés

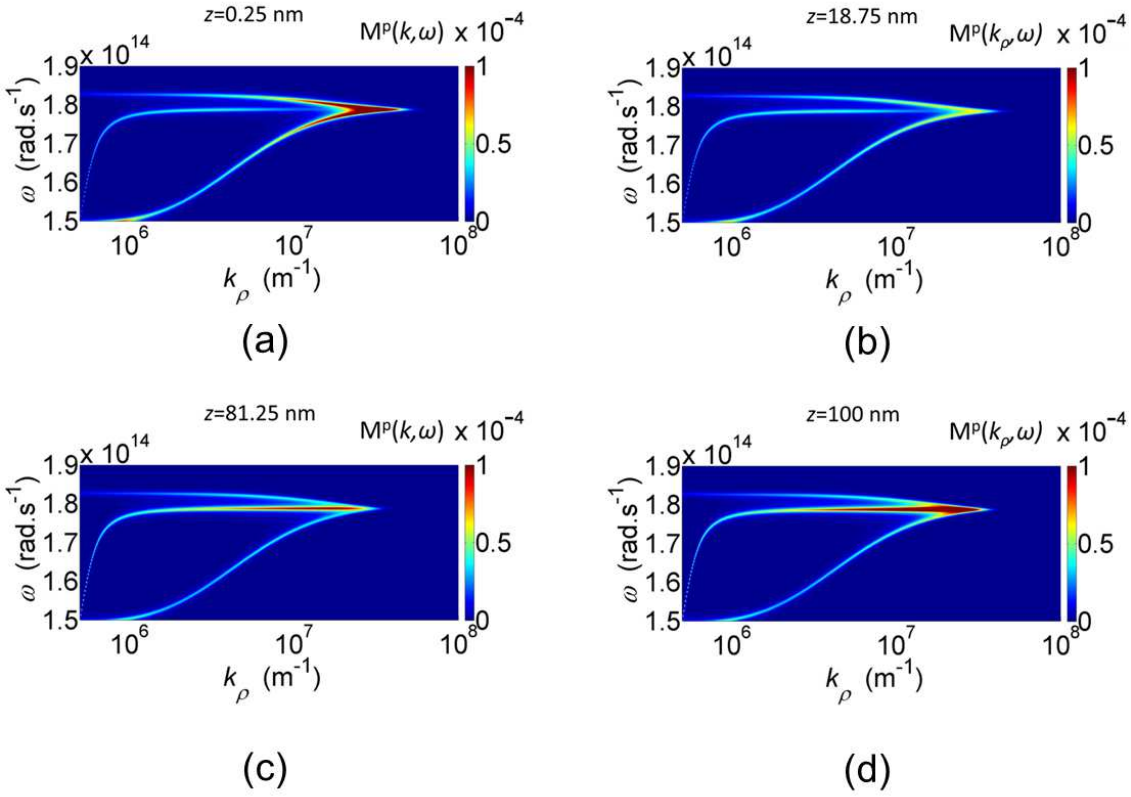

Figure IV.16: Plot of M as a function of k_ρ and ω at several depths inside the film.

surface polaritons in the infrared, the impact of frustrated modes is expected be more important. In the case of an absorbing film, the absorption can be modified for small thicknesses. The excitation of the surface modes at the rear of the film can induce an increase of the absorption near to it. This analysis allows understanding how the near-field radiative power inside the film is absorbed.

IV.6 Interferences phenomena in the near-to-far field transition regime

The regime between the near field and the far field is now under consideration. We define the transition regime by the zone of the vacuum gap size d where evanescent waves are not dominant yet, but temporal coherence effects of thermal radiation start to appear, causing propagative waves to interfere [105, 106]. This regime occurs when the size of a cavity is of the same order of magnitude as the maximum wavelength of the Planck blackbody distribution λ_{Wien}, given by Wien's law (see Chapter I). The conflict between constructive and destructive interferences results in the presence of minima and maxima in the thermally radiated flux transferred between the two bodies in this regime. For highly reflective materials, like metals, this effect is particularly important [105, 26]. First, the transmission coefficient is plotted in the transition regime ($d = 10$ μm) for two aluminum half-spaces (Fig. IV.17).

Cette thèse est accessible à l'adresse : http://theses.insa-lyon.fr/publication/2016LYSEI103/these.pdf
© [E. Blandre], [2016], INSA Lyon, tous droits réservés

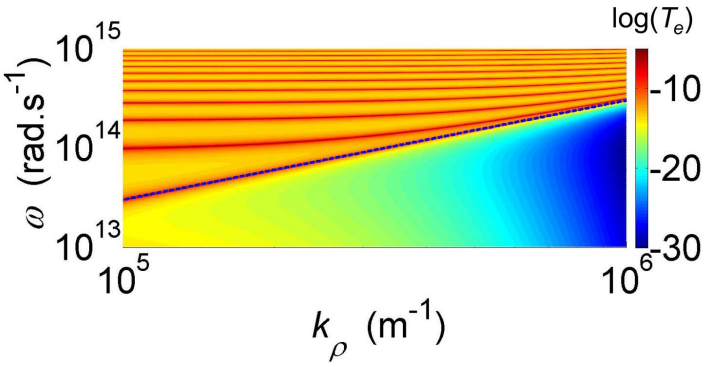

Figure IV.17: Transmission coefficient T_e as a function of k_ρ and ω for $d = 10$ µm between two aluminum half spaces. The blue dashed line represents the curve of equation $\omega = kc$ and sets the limit between propagative and evanescent modes.

In this figure, propagative modes are located before the blue dashed line of equation $\omega = k_\rho c$. In the propagative modes region, we observe peaks and dips due to interferences. As a result, the spectrum of thermal radiation is strongly affected, as depicted in Fig. IV.18.

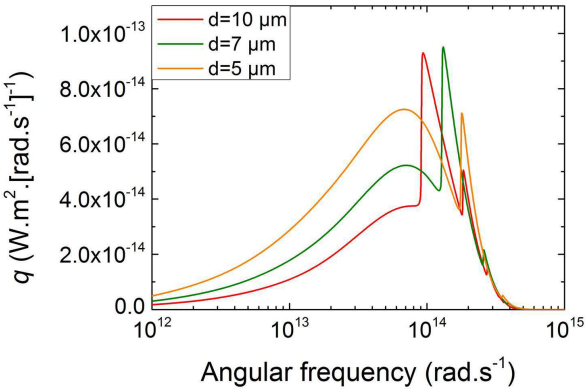

Figure IV.18: Monochromatic emissive power emitted by an aluminum half-space at $T = 300$ K and absorbed by another one at $T = 0$ K separated by a vacuum gap of size d.

In particular, interferences lead to a spectral selection on the radiative heat flux: a large peak of emission occurs around a frequency. As this frequency depends on the size of the vacuum gap, it is possible to enhance the radiative heat transfer between two planar bodies for a selected wavelength. Tuning the spectrum of the thermal radiation may thus be possible using interference phenomena.

Propagative waves can also interfere due to multireflections inside a film. Interferences inside a film with a reflective index n should appear when the thickness of the film t is of the same order of magnitude as the dominant wavelength inside the film $\frac{\lambda_{Wien}}{n}$. In order to study this phenomenon, the optical properties of the half-space and the film are modeled by a flat (non-frequency dependent) dielectric function, such as $\epsilon = 20 + 0.01i$. Results are represented in Fig. IV.19.

Cette thèse est accessible à l'adresse : http://theses.insa-lyon.fr/publication/2016LYSEI103/these.pdf
© [E. Blandre], [2016], INSA Lyon, tous droits réservés

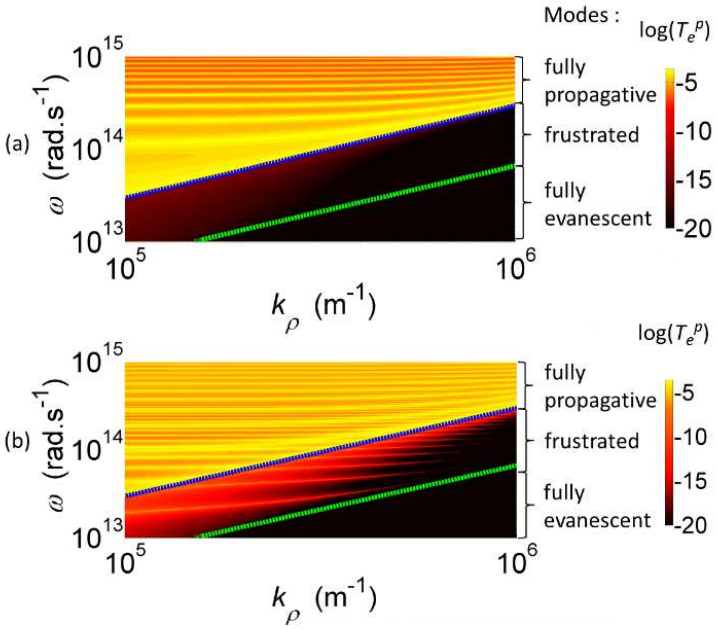

Figure IV.19: p-polarized component of the transmission factor T_e^p for a constant dielectric function, as a function of k_ρ and ω. The blue dashed line represents the curve of equation $\omega = k_\rho c$ and the green dashed line represents the curve of equation $\omega = \frac{k_\rho c}{n}$. (a) $d = 10$ µm and $t = 100$ nm (b) $d = 10$ µm and $t = 10$ µm. From [6].

In the propagative area of the (k_ρ, ω) plots (Figs. IV.19(a) and b), we observe the apparition of fringes that are caused by interferences inside the vacuum cavity. In the second configuration (Fig. IV.19(b)), the thickness of the film is set at 10 µm as well as the size of the vacuum gap. As the characteristic wavelength of thermal radiation inside the film $\frac{\lambda_v}{n}$ is close to the thickness of the film, interferences can also occur in the film. In the T_e^p representation, we observe the apparition of peaks and dips due to interferences in the component related to the frustrated modes.

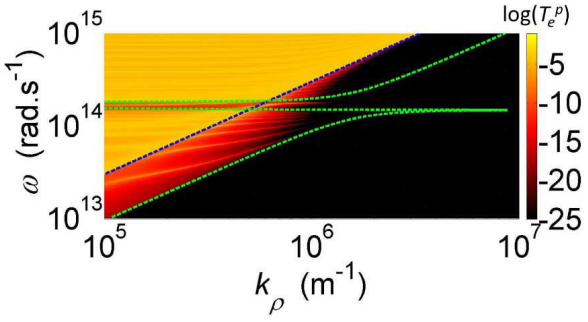

Figure IV.20: p-polarized component of the transmission factor T_e^p for SiC, as a function of k_ρ and ω, $d = 10$ µm and $t = 10$ µm. From [6].

The same phenomenon can of course occur with realistic materials. For instance, the real and imaginary parts of the dielectric function of SiC is almost constant outside the reststrahlen band (between ω_{LO} and ω_{LO}), and the values are of the same order as that of our example. We depict

Cette thèse est accessible à l'adresse : http://theses.insa-lyon.fr/publication/2016LYSEI103/these.pdf
© [E. Blandre], [2016], INSA Lyon, tous droits réservés

this for SiC in Fig. IV.20, where the transmission coefficient T_e^p is plotted for $t = d = 10$ µm. Interferences occur in the area of the frustrated modes, except in the reststrahlen band, where the absorption coefficient of SiC is large.

As a conclusion for this section, the impact of interferences in the near-to-far field transition regime can be enhanced with selected film thickness, and could improve the spectral control of the radiative energy transferred between two bodies. The possibility of spectral control using film of selected thickness could be a way to enhance those phenomena. If an absorbing film is considered, frustrated modes can interfere because they are propagative inside it. The potential of frustrated modes for NFR-TPV conversion was highlighted in [7]. Two radiators were considered. The first one is a fictitious radiator supporting surface SPhPs, and optimized to generate a spectrum of emission that maximizes the conversion of radiation into EHPs when the distance between the radiator and the cell is 10 nm. As its optical properties are described by a Drude model, it is referred to as optimized Drude radiator. The second one is made of tungsten and supports mostly frustrated modes. The power output enhancement due to near-field effects as a function of the vacuum gap thickness separating the radiator and the PV cell is plotted for the two radiators. The contributions of the propagating, frustrated and surface modes are depicted. The power output enhancements of the NFR-TPV system for the two radiators are plotted as a function of the distance separating the radiator and the cell in Fig. IV.21. The contributions of the propagating, evanescent and surface modes are depicted.

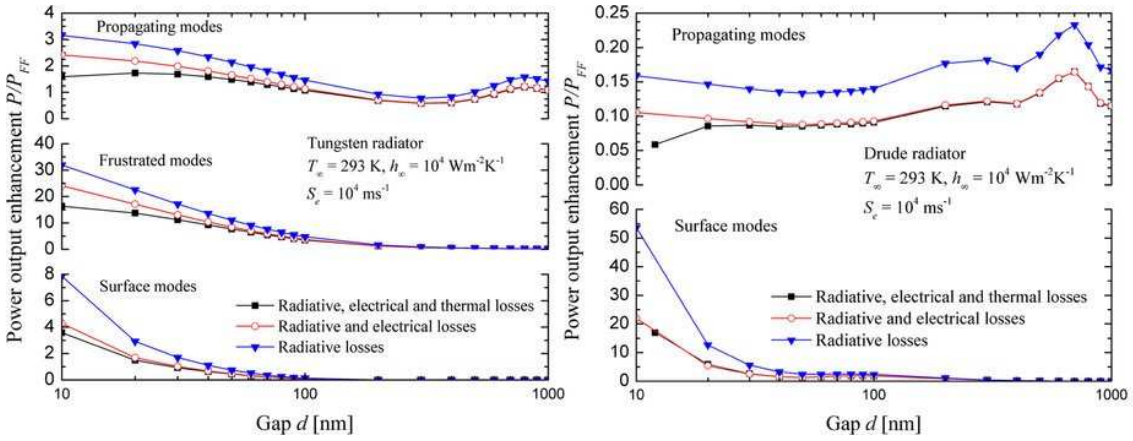

Figure IV.21: Power output enhancement of NFR-TPV system as a function of the vacuum gap thickness separating the radiator and the PV cell and the type of losses considered showing the contributions of propagating, frustrated and surface modes. From [7].

It is observed that the power output enhancement is larger when considering the tungsten radiator than when considering the optimized Drude radiator. The analysis of the different losses performed in this study showed that the limiting factor in the case of the optimized Drude radiator is surface recombination. Indeed, the small penetration depth of SPhP induces a generation rate of EHPs localized at the top surface of the cell. Frustrated modes have a larger penetration, and therefore when using the tungsten radiator, the impact of surface recombination is mitigated. This emphasizes the fact that the spatial distribution of the absorption is a important factor that

Cette thèse est accessible à l'adresse : http://theses.insa-lyon.fr/publication/2016LYSEI103/these.pdf
© [E. Blandre], [2016], INSA Lyon, tous droits réservés

impacts the performances of NFR-TPV systems. Furthermore, it is observed that the power output enhancement oscillates when the distance between the emitter and the cell varies, due to interference modes. This proves that interference phenomena are also impacting the performances of NFR-TPV systems.

IV.7 Conclusions and prospects

Near-field and interference effects on the radiative heat transfer between a semi-infinite medium and a flat film of finite thickness have been studied. Three important phenomena for NFR-TPV have been analyzed. First, the behavior of the SPhP resonances when the geometrical parameters t and d of the system vary, and especially the coupling of the surface waves of the different interfaces of the system have been studied. The impact of the behavior of the SPhP resonances on the emission spectrum has then been analyzed. It has been observed that when the thickness of the film is smaller than the size of the vacuum gap, the peak due to SPhPs in the spectrum of emission is attenuated.
The second phenomenon that has been investigated is the spatial distribution of the absorbed radiative power inside the film. Control of the spatial distribution of absorption of radiative power is key to enhance the performances of NFR-TPV systems. Indeed, the local generation rate of electron-hole pairs is related to the amount of radiative power absorbed locally in the PV cell. Besides, electron-hole pairs generated near the surface of the cell are likely to be lost by surface recombination. In the near field, the evanescent waves dominate absorption for the first hundreds nanometers after the interface. Frustrated modes are absorbed at larger depths. The penetration depth of the radiative heat flux decreases when the vacuum gap size decreases because of the excitation of modes with large k_ρ values. These results have led to a better understanding of the performances of NFR-TPV systems [7]. Indeed, the small penetration depth of SPhPs induces large surface recombinations. As frustrated modes have a larger penetration depth, this problem is mitigated when using a tungsten radiator that supports mostly frustrated modes. For very thin films, the absorption can be enhanced near the rear interface of the film. Thus, localizing the spatial absorption of the near-field radiative power away from the surface of the cell by means of the excitation of the surface waves, could be a powerful tool to reduce surface recombination and increase the performances of the NFR-TPV systems. This could be applied for example in the case of heterojunctions, where the p and n-regions are made of different semiconductors. If the surface modes at the interface between the two regions participate to the absorption of radiative power, the generation of electron-hole pairs could be enhanced near the junction, where the electric field extends. These photogenerated electrical charges would likely be collected directly after being generated, leading to a decrease of the recombination rates.
Eventually, the near-to-far field transition regime has been analyzed. In the case of two metallic plates, interferences allow selecting frequencies that can be modified by controlling the size of the vacuum gap. For dielectrics, waves can interfere inside the cavity and inside the film. This phenomenon occurs for propagating modes, but also for frustrated waves, that participate to radiative heat transfer in the near field. Indeed, frustrated modes are propagating inside the film.

Cette thèse est accessible à l'adresse : http://theses.insa-lyon.fr/publication/2016LYSEI103/these.pdf
© [E. Blandre], [2016], INSA Lyon, tous droits réservés

Interferences of frustrated modes could thus be a way to enhance the performances of NFR-TPV systems, and constitute an alternative to the spectral tuning using SPhPs. In the future, more complex configurations should be investigated. Indeed, the spectral selectivity due to SPhPs can be enhanced for example by using a thin film instead of a semi-infinite emitter as a radiator [85, 24]. Studies like those investigated in Chapter III for far-field emitters may thus be useful for NFR-TPV. The control of the penetration depth of the near-field thermal radiation can be achieved with multilayer structures, known in the literature as hyperbolic metamaterials [83, 84]. It has also been shown that multilayer structures can be used to enhance the spectral selectivity of emitters supporting Fabry-Pérot interferences (see Chapter III) in the far-field [5, 53]. The same principles should be applicable to the near-to-far field transition regime.
The results reported in this section have provided new understanding and shed new lights on the radiative behavior on NFR-TPV systems. New tools and ideas have been provided to optimize thermal radiation between the radiator and the cell, and could be a new step forward for the design of high-efficiency NFR-TPV prototypes.

Cette thèse est accessible à l'adresse : http://theses.insa-lyon.fr/publication/2016LYSEI103/these.pdf
© [E. Blandre], [2016], INSA Lyon, tous droits réservés

Chapter V

High-injection effects on near-field radiation mediated thermophotovoltaics

Contents

Cette thèse est accessible à l'adresse : http://theses.insa-lyon.fr/publication/2016LYSEI103/these.pdf
© [E. Blandre], [2016], INSA Lyon, tous droits réservés

V.1 Introduction

The concept that a TPV system could benefit from the modification of radiative heat transfer due to near-field effects, by decreasing the distance between the radiator and the cell to a subwavelength distance, was introduced by Whale and Cravalho [19]. These systems are referred to as near-field radiation mediated thermophotovoltaic (NFR-TPV). The first experimental work on this topic was conducted by the team of DiMatteo [20, 107, 108]. A silicon radiator and an InAs cell, placed inside a vacuum chamber, were used. The distance between the radiator and the cell was controlled by a piezoelectric device. Variations of the short-circuit current were observed when varying the size of the vacuum gap. More precisely, the authors reported an increase of the short-circuit current by a factor 5. A dynamic test was performed, where the vacuum gap size was oscillating. In-phase variations of the short-circuit current with the gap size suggested that the increase of the short-circuit current was due to near-field effects. The second experimental study on this subject was conducted by Hanamura [21], and presented only in a scientific conference. A marginal enhancement of the performances of the system when decreasing the distance between the radiator and the cell was reported, and the size of the vacuum gap could not be controlled below 10 μm. Numerical studies of the performances of NFR-TPV systems began with Whale and Cravalho's work [19]. The radiator and the cell were considered semi-infinite. The optical properties of the radiator were described by a Drude model, while the cell was made of an alloy of InAs and GaAs. Fluctuational Electrodynamics was used to model radiative heat transfer between the radiator and the cell. A 100% quantum efficiency was considered to avoid modeling transport of electrical charges inside the PV cell. No thermal effects were accounted for. They reported a large increase of the electrical power output of the system due to near-field effects, but only a marginal gain on conversion efficiency. Narayanaswamy and Chen [109] introduced the idea that surface phonon-polaritons supported by a cBN substrate could enhance the efficiency of NFR-TPV systems, by considering a cell made a of a fictitious semiconductor, with a bandgap energy corresponding to the frequency of the SPhP resonance of cBN. Laroche et al. [110] analyzed the performances of NFR-TPV systems using a tungsten radiator and a source with an emission spectrum concentrated in a narrow spectral band, referred to as "quasi-monochromatic" heat source. They reported a maximum efficiency of the system of 35 % using the quasi-monochromatic heat source, and also analyzed the impact of near-field effects on the dark current. Park et al. [27] introduced in the modeling of NFR-TPV systems an electrical model with a spatial distribution of the generation rate of electron-hole pairs inside the PV cell. With a tungsten radiator and a cell made of an alloy of InSb and GaSb, they reported a maximum conversion efficiency of 23 %. The most complete model to simulate the performances of NFR-TPV systems up to now was presented by Francoeur et al. [4]. A thermal model was added, allowing the analysis of the performances of the NFR-TPV systems while accounting for the thermal behavior of the PV device on the performances of the system. By calculating the different heat sources inside the cell, the authors calculated the temperature of the cell, and evaluated the impact on the maximum power output of the systems. It was shown that to maintain the cell at ambient temperature, a convective heat transfer coefficient up to 10^5 is required due to the important heat sources arising inside the PV cell. With smaller values of the convective heat transfer coefficient, the cell temperature increases

Cette thèse est accessible à l'adresse : http://theses.insa-lyon.fr/publication/2016LYSEI103/these.pdf
© [E. Blandre], [2016], INSA Lyon, tous droits réservés

and the energy conversion performances drop significantly. Attemps of optimizations of NFR-TPV systems were also performed. Bright et al. [25] studied the impact of a backside gold reflector to increase the amount of radiative energy absorbed by the cell. They also reported the impact of the small penetration depth of evanescent waves on the increase of surface recombinations. This phenomenon was later studied in depth in [7]. The contributions of the propagating, frustrated and surface modes were analyzed. It was shown that a radiator supporting mostly frustrated modes generates a stronger electrical power output than a radiator supporting surface modes, despite the fact that SPhPs were used to enhance radiative heat transfer from the radiator to the cell in a narrow spectral range. This is mostly due to the fact that optical optimization is not sufficient: electrical and thermal losses have to be taken into account to optimize the system. The idea of a spectral filter to cut high-energy photons was also introduced: photons of energy much larger than the bandgap generate electron-hole pairs (EHP) but also heat through thermalization. Therefore, due to thermal impact, high-energy photons can be detrimental. Other optimizations were performed using graphene [111, 112, 113, 28] in order to increase the near-field thermal radiation between the radiator and the cell, or radiators supporting hyperbolic modes with large penetration depth [114]. Eventually, more exploratory systems, such as solar NFR-TPV systems were investigated [115], where the radiator is heated by the sunlight radiation.

Up to now, no convincing experimental demonstration proving the efficiency of the concept of NFR-TPV systems could be performed. The only two experimental works exhibited marginal increases of the energy conversion performances due to near-field effects. This is due to two facts. First, the control of the distance between the radiator and the cell is a technological challenge. Successful experiments on the measurement of thermal radiation between objects separated by subwavelength distances were performed only recently (e.g. [91, 90, 96]). The second fact is that without optimization of the PV cell, any increase of the performances due near-field effects is likely to be marginal because of the impact of the radiative, electric and thermal losses in the PV device. Understanding the different phenomena occurring in the PV cell and optimizations of the full NFR-TPV system are thus required to design an efficient prototype, that could allow demonstrating that a TPV system can benefit from near-field effects.

In this chapter, we first present the numerical model that allows simulating properly the transport of the photogenerated electrical charges inside the PV cell. The usually applied low-injection approximation will be introduced first. This model was already used in many theoretical works on NFR-TPV systems [27, 4, 25, 7, 28]. However, no one ever questioned the validity of these approximations in the case of NFR-TPV converters where the injection of carriers is high due to the near-field radiation enhancement. Thus, we present the model we have implemented in our simulation code that solves the transport of electrical charges problem in NFR-TPV cells without taking into account the low-injection approximation. The domains of validity of the different approximations are then assessed. The following section is dedicated to new optimizations using the appropriate charge transport model of two parameters of the PV cell, the doping levels and the thicknesses of the p and n-regions, in order to increase the performances of the NFR-TPV systems. Eventually, we end this chapter by analyzing the performances of InSb cells with a PIN architecture, that are PV cell candidates for the conversion of thermal energy emitted by relatively low-temperature ($\approx$ 800K) sources, and for which a full Drift-Diffusion modeling is

Cette thèse est accessible à l'adresse : http://theses.insa-lyon.fr/publication/2016LYSEI103/these.pdf
© [E. Blandre], [2016], INSA Lyon, tous droits réservés

required.

V.2 Numerical solutions of the full and approximate Drift-Diffusion equations

As mentioned in Chapter II, in order to evaluate the performances of a NFR-TPV system, its electrical behavior under illumination and applied voltage has to be modeled. We recall the basic equations of the Drift-Diffusion (DD) model, in the 1D and steady state. First, Poisson's equation relates the electric field (or the electrostatic potential profile) to the spatial distribution of the electrical charges inside the PV cell writes

$$\frac{dE(z)}{dz} = -\frac{d^2V(z)}{dz^2} = -\frac{e}{\varepsilon}\left\{n(z) - p(z) + N_a(z) - N_d(z)\right\}. \tag{V.1}$$

The transport equations state that the electrical current is due to the motion of the electrical charges that are either swept by the electric field or diffusing from high to low concentration regions

$$J_n = en(z)\mu_n E(z) + eD_n\frac{dn}{dz} \tag{V.2}$$

for the electrons, and

$$J_p = ep(z)\mu_p E(z) - eD_p\frac{dp}{dz} \tag{V.3}$$

for the holes. Eventually, the continuity equations relate the spatial variations of the electrical currents with the net generation-recombination rates

$$-\frac{1}{e}\frac{dJ_n(z)}{dz} = G(z) - R(z), \tag{V.4}$$

for the electrons, and

$$\frac{1}{e}\frac{dJ_p(z)}{dz} = G(z) - R(z). \tag{V.5}$$

for the holes. The number of equations can be lowered from 5 to 3 by combining the continuity and transport equations, thus eliminating the electrical currents J_n and J_p

$$D_n\frac{d^2n(z)}{dz^2} + \mu_n E(z)\frac{dn(z)}{dz} + \mu_n\frac{dE(z)}{dz}n(z) = R(z) - G(z), \tag{V.6}$$

$$D_p\frac{d^2p(z)}{dz^2} - \mu_p E(z)\frac{dp(z)}{dz} - \mu_p\frac{dE(z)}{dz}p(z) = R(z) - G(z). \tag{V.7}$$

In Eq. V.6 and V.7, it is assumed that the mobilities μ_n and μ_p and the diffusion coefficient D_n and D_p do not vary spatially in each region. Mobilities and diffusion coefficients depend on the

Cette thèse est accessible à l'adresse : http://theses.insa-lyon.fr/publication/2016LYSEI103/these.pdf
© [E. Blandre], [2016], INSA Lyon, tous droits réservés

temperature and the doping levels. As the PV cell is thin, its spatial temperature distribution is almost uniform. Furthermore, we consider abrupt doping profiles, which means that the number of donors and acceptors are constant in each region of the PV cell. To solve the charge transport problem, Eqs. V.1, V.6 and V.7 have to be solved for the electric field E and the carrier densities n and p. These three equations are non-linear, because the recombination terms are carrier-density dependent (Eqs. II.16, II.17, II.19). Moreover, they are coupled by the fact that the electric field depends on the carrier density and vice-versa. Two methods can be used to solve the Drift-Diffusion equations. The simplest case is to assume a set of hypotheses, called under the naming low-injection approximation, that simplifies the problem. However, the low-injection approximation is questionable in the case of NFR-TPV systems. To solve the problem without applying the low-injection approximation, an iterative method can be used. In the following, we will present the two approaches, starting by the low-injection approximation.

V.2.1 The low-injection approximation and the separation of the minority and majority carriers (MCS model)

A schematic of the pn-junction under consideration is depicted in Fig. V.1.

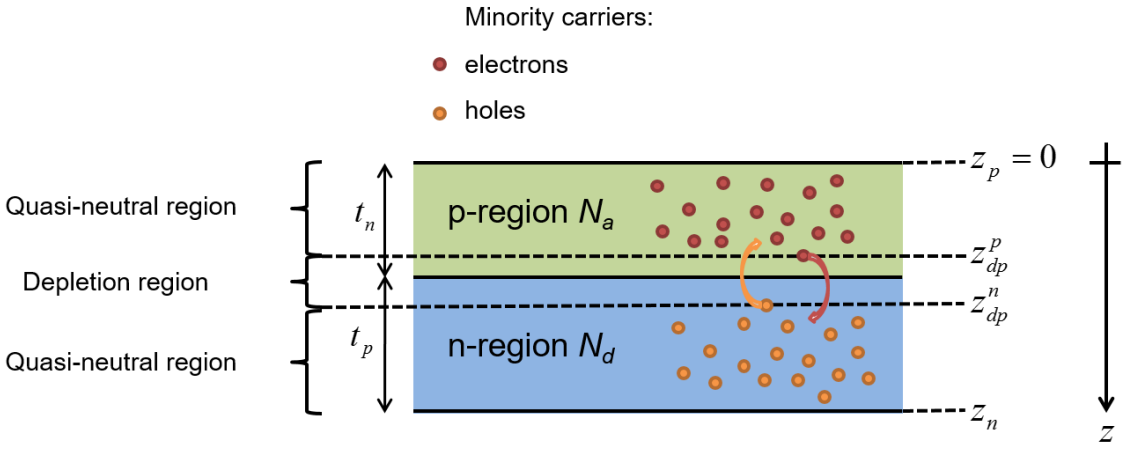

Figure V.1: Schematic representation of the pn-junction under consideration, assuming the low-injection approximation.

In the p-region, the concentration of holes in larger than the concentration of electrons, due to the doping. In this case, the electrons are the minority carriers in this region, and the holes are the majority carriers. In the n-region, the electrons are the majority carriers and the holes are the minority carriers. The low-injection approximation consists in assuming that the minority carrier densities n and p are always much lower than the doping levels N_a and N_d in each region. It means that these approximations are valid only under some level of illumination, or if the doping level is high enough. The first impact of this approximation can be seen on Poisson's equation,

Cette thèse est accessible à l'adresse : http://theses.insa-lyon.fr/publication/2016LYSEI103/these.pdf
© [E. Blandre], [2016], INSA Lyon, tous droits réservés

that becomes

$$\frac{dE(z)}{dz} = \frac{d^2V(z)}{dz^2} = \frac{e}{\varepsilon}\left(N_a(z) - N_d(z)\right). \tag{V.8}$$

The dependence of the electric field on carrier densities is removed, meaning that it is now independent of the illumination and the applied voltage. The new Poisson's equation can now be solved for the electric field. As an abrupt doping profile in considered, N_a and N_d are constant in each region. As a consequence, the electric field is nil outside the depletion region, in the quasi-neutral regions. The size of the depletion region can be calculated as [34]

$$L_{dp} = l_p + l_n = \sqrt{\frac{2\varepsilon}{e} V_0 \left(\frac{1}{N_a} + \frac{1}{N_d}\right)} \tag{V.9}$$

where V_0 is the built-in voltage

$$V_0 = \frac{k_b T}{e} \ln\left(\frac{N_a N_d}{n_i^2}\right). \tag{V.10}$$

The thickness of the depletion region in the p and n-regions l_p and l_n can be expressed as

$$l_p = L_{dp}\frac{N_d}{N_a + N_d},\ l_n = L_{dp}\frac{N_a}{N_a + N_d}. \tag{V.11}$$

When a forward bias V_f is imposed on the PV cell, the thickness of the depletion is calculated as [34]

$$L_{dp} = l_p + l_n = \sqrt{\frac{2\varepsilon}{e}(V_0 - V_f)\left(\frac{1}{N_a} + \frac{1}{N_d}\right)}. \tag{V.12}$$

The next approximation is the full depletion approximation: if an electrical charge reaches the depletion region, the electric field sweeps it toward the region where it is a majority carrier and no recombination occurs. The electrical carrier generates a current. As a consequence, Eqs. V.6 and V.7 need to be solved in the quasi-neutral regions, more specifically in the p-region for electrons and in the n-region for holes. As E is nil outside the depletion region, Eqs V.6 and V.7 become

$$D_n \frac{d^2 n(z)}{dz^2} = R(z) - G(z) \tag{V.13}$$

for the p-region, and

$$D_p \frac{d^2 p(z)}{dz^2} = R(z) - G(z) \tag{V.14}$$

for the n-region. As shown in Chapter II, when the low-injection approximation is considered,

Cette thèse est accessible à l'adresse : http://theses.insa-lyon.fr/publication/2016LYSEI103/these.pdf
© [E. Blandre], [2016], INSA Lyon, tous droits réservés

the recombination rate can reduce to

$$R = \frac{\Delta n}{\tau_n} \tag{V.15}$$

for electrons in the p-region, and

$$R = \frac{\Delta p}{\tau_p} \tag{V.16}$$

for holes in the n-region.

Equations V.13 and V.14 can then be written as

$$D_n \frac{d^2 \Delta n(z)}{dz^2} - \frac{\Delta n}{\tau_n} + G(z) = 0 \tag{V.17}$$

for the p-region, and

$$D_p \frac{d^2 \Delta p(z)}{dz^2} - \frac{\Delta p}{\tau_p} + G(z) = 0 \tag{V.18}$$

for the n-region. Eq. V.18 and V.19 are two second-order non-coupled and linear differential equations, that can easily be solved numerically using the finite element method and a tridiagonal matrix algorithm (TDMA) [116], or even analytically if an analytic expression of the generation rate of electron-hole pair (G) can be provided (as in [28]). Because Eqs. V.18 and V.19 are decoupled, it is assumed that the behavior of the minority and majority carriers are independent in each region. Boundary conditions are required to solve these equations. At the boundaries of the depletion region, the excess of carriers Δn and Δp is assumed to be nil due to the electric field

$$\Delta n(z = z_{dp}^p) = \Delta p(z = z_{dp}^n) = 0, \tag{V.19}$$

where z_{dp}^p and z_{dp}^n are the spatial positions of the edges of the depletion region on the p-side and n-side, respectively (Fig. V.1).

At the boundaries of the cell, the electrical current is balanced by the surface recombinations

$$D_n \frac{d\Delta p(z = z_p)}{dz} = S_n \Delta n, \tag{V.20}$$

in the n-region, and

$$D_p \frac{d\Delta p(z = z_n)}{dz} = S_p \Delta p, \tag{V.21}$$

in the p-region. S_p and S_n are the surface recombination velocities for holes and electrons, respectively. z_n is the position of the boundary of the cell in the n-region, and z_p is the position of the boundary of the cell in the p-region. Once the spatial distribution of the excess carrier concen-

Cette thèse est accessible à l'adresse : http://theses.insa-lyon.fr/publication/2016LYSEI103/these.pdf
© [E. Blandre], [2016], INSA Lyon, tous droits réservés

trations are found, the electrical currents can be derived. If electrical charges are photogenerated in the depletion region, they are assumed to be collected. The corresponding electrical current is:

$$J_{dp} = e \int_{z_{dp}^p}^{z_{dp}^n} G(z). \tag{V.22}$$

As explained before, if charges are photogenerated in the quasi-neutral regions, they are assumed to be collected if they reach the depletion region. The current of electron and holes can therefore be written as proportional to the gradient of Δp and Δn at the edges of the depletion region

$$J_n = eD_n \frac{d\Delta n(z_{dp}^p)}{dz}, \tag{V.23}$$

$$J_p = -eD_p \frac{d\Delta p(z_{dp}^n)}{dz}. \tag{V.24}$$

The photogenerated current is then the sum of the three components

$$J_{\text{ph}} = J_n + J_p + J_{dp}. \tag{V.25}$$

To evaluate the performances of NFR-TPV devices, the problem has to be solved for different applied voltages V_f. When the cell is under dark conditions (i.e. not illuminated), a current appear when the voltage increases, called dark current (J_{dark}). To save computation time, only the dark current is computed as a function of V_f. The dark current is obtained by solving the transport equations (Eqs. V.17 and V.18) without illumination ($G = 0$). Once the J-V characteristic under dark conditions is obtained, the total current is the calculated as

$$J_{\text{tot}}(V_f) = J_{\text{ph}} + J_{\text{dark}}(V_f). \tag{V.26}$$

Here, it is assumed that the dark current does not depend on the level of illumination. This is possible by means of the superposition principle.

V.2.2 Questioning the low-injection approximation for NFR-TPV devices

In the preceding section, several approximations have been made to simplify the resolution of the Drift-Diffusion equations:

- The density of minority carriers is much smaller than the doping everywhere,
- The electric field is not dependent on the level of illumination,
- The expressions of the recombination rates can be simplified using a spatially constant lifetime,
- The recombination current depends only on the applied voltage, and not on the level of illumination.

Cette thèse est accessible à l'adresse : http://theses.insa-lyon.fr/publication/2016LYSEI103/these.pdf
© [E. Blandre], [2016], INSA Lyon, tous droits réservés

In the case of non-concentrated solar PV, these approximations can been made because of the level of illumination is relatively low. Furthermore, in the case of silicon solar cells (the most commonly used type of solar cell), because of the large bandgap of silicon, the intrinsic carrier concentration is small. It induces smaller carrier concentrations at equilibrium, and therefore smaller carrier concentrations under illumination and applied voltage. However in NFR-TPV systems, the semiconductors under consideration (III-V compounds) have smaller bandgap energies. In addition, the levels of illumination are larger than in non-concentrated solar PV, as depicted in Fig. V.2(a). In this figure, the radiative power emitted by a radiator at 2000 K and absorbed by a GaSb cell as a function of the distance between the two bodies is presented. One can observe that the values

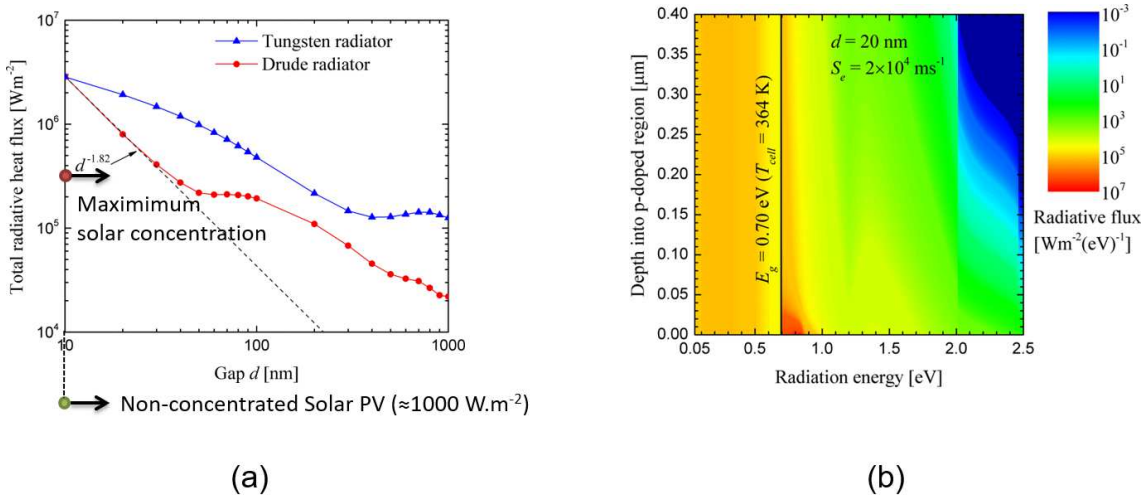

Figure V.2: (a): Radiative power absorbed by a 10.4 µm thick GaSb cell in the vicinity of a radiator at 2000 K as a function of the distance separating them. From [7]. (b): Map of the radiative heat flux as a function of the radiation energy and the depth inside p-region of a Gasb cell. The radiator (2000 K) supporting surface polaritons is placed at 20 nm from the cell. From [8].

increase exponentially when the distance between the two bodies decreases, up to an absorbed total radiative heat flux of $\approx 3.10^6$ W.m^{-2}. In comparison, the value of the incident radiative power from the sun at the sea is 10^3 W.m^{-2} for the standard AM1.5 spectrum [15]. It means that the amount of photogenerated electrical charges inside a PV cell is much larger in NFR-TPV devices than in non-concentrated solar PV devices. Even in concentrated solar photovoltaics where the illumination can reach 46000 suns, the radiative power absorbed by the cell is lower than in TPV systems in the extreme near-field. Moreover, it can be observed in Fig. V.2(b) that absorption is very local, especially when using radiators supporting SPhPs. It is observed that most of the radiative power is absorbed in the first dozens of nanometers due to the small penetration depth of evanescent waves. Because of this, the validity of the low-injection approximation has to be verified.

Cette thèse est accessible à l'adresse : http://theses.insa-lyon.fr/publication/2016LYSEI103/these.pdf
© [E. Blandre], [2016], INSA Lyon, tous droits réservés

V.2.3 Numerical solution of the full Drift-Diffusion equations (FDD)

If the low-injection approximation is not used, the Drift-Diffusion equations cannot be solved directly, but rather with an iterative method. In this section, we will present Gummel's iterative procedure [117] used to solve the problem. It consists in taking an initial guess on the electric field (or the electrostatic potential) and the carrier densities. Using the values of the carrier densities, Poisson's equation can be solved for the electrostatic potential, and the electrostatic potential is then used to solve the transport equation for the carrier densities. The process is repeated until convergence.

V.2.3.1 Variables, normalization and scaling

The first step is to redefine a set of variables to solve the problem. The unknowns are the electric field E and the carrier densities n and p. However these variables are not convenient to solve the full Drift-Diffusion problem. Therefore, we solve the Drift-Diffusion equations for the electrostatic potential V, and the quasi-Fermi levels for the electrons and holes ϕ_n and ϕ_p. The quasi-Fermi levels describe the population of electrons and holes in the conduction and valence bands in non-equilibrium (i.e. when a voltage is applied or under illumination). They represent the shift in potential due to the excess of electrical carriers. They are related to the carrier concentrations as

$$n(z) = n_i \exp\left(\frac{eV(z)}{k_b T}\right)\left(\frac{-e\phi_n(z)}{k_b T},\right), \tag{V.27}$$

$$p(z) = n_i \exp\left(\frac{-eV(z)}{k_b T}\right)\left(\frac{e\phi_p(z)}{k_b T}\right). \tag{V.28}$$

The red terms in Eqs. V.28 and V.29 correspond to the equilibrium carrier concentrations of the electrons and holes inside the PV cell. To simplify the equations, normalized variables are introduced. The electrostatic potential can be normalized by the thermal voltage $V^* = \frac{k_b T}{e}$ to define a new variable

$$\bar{V} = \frac{V}{V^*}, \tag{V.29}$$

called normalized electrostatic potential. The quasi-Fermi levels can be written in the form of the so-called Slotboom variables [118]

$$\Phi_n = \exp\frac{-e\phi_n}{k_b T}, \tag{V.30}$$

$$\Phi_p = \exp\frac{e\phi_p}{k_b T}, \tag{V.31}$$

Cette thèse est accessible à l'adresse : http://theses.insa-lyon.fr/publication/2016LYSEI103/these.pdf
© [E. Blandre], [2016], INSA Lyon, tous droits réservés

where Φ_n and Φ_p are the Slotboom variables for electrons and holes, respectively. Using these notations, the carrier densities become

$$n(z) = n_i \exp\left(\bar{V}\right)\Phi_n, \tag{V.32}$$

$$p(z) = n_i \exp\left(-\bar{V}\right)\Phi_p. \tag{V.33}$$

The space variable can be normalized by the intrinsic Debye length $z^* = \sqrt{\frac{\varepsilon k_b T}{e^2 n_i}}$

$$\bar{z} = \frac{z}{z^*}. \tag{V.34}$$

V.2.3.2 Solving the Poisson equation

Poisson's equation can be rewritten using the variables introduced before

$$\frac{V^*}{z^{*2}}\frac{d^2\bar{V}}{d\bar{z}^2} = \frac{en_i}{\varepsilon}\left(\exp(\bar{V}(z))\Phi_n(z) - \exp(-\bar{V}(z))\Phi_p(z) + \frac{N_a(z) - N_d(z)}{n_i}\right). \tag{V.35}$$

By noticing that the factor $\frac{V^*}{z^{*2}}$ is equal to $\frac{en_i}{\varepsilon}$, Poisson's equation takes the form

$$\frac{d^2\bar{V}}{d^2\bar{z}^2} = \left(\exp(\bar{V}(z))\Phi_n(z) - \exp(-\bar{V}(z))\Phi_p(z) + \frac{N_a(z) - N_d(z)}{n_i}\right). \tag{V.36}$$

This differential equation is non-linear, meaning that an iterative method has to be used once again. First, an initial guess on $\bar{V}$ is chosen. Then, at the next iteration, a new potential is written as $\bar{V}^{i+1} = \bar{V}^i + \delta\bar{V}$. Injecting this in Eq. II.37, we have

$$\begin{aligned}&\frac{d^2\bar{V}}{d\bar{z}^2} + \frac{d\delta\bar{V}}{d\bar{z}^2} = \\ &\left(\exp(\bar{V}(z))\exp(\delta\bar{V}(z))\Phi_n(z) - \exp(-\bar{V}(z))\exp(-\delta\bar{V}(z))\Phi_p(z) + \frac{N_a(z) - N_d(z)}{n_i}\right).\end{aligned} \tag{V.37}$$

To linearize this equation, we can use the first order Taylor expansion $\exp(\pm\delta\bar{V}) = 1 \pm \delta\bar{V}$

$$\begin{aligned}&\frac{d^2\bar{V}}{d^2\bar{z}^2} + \frac{d\delta\bar{V}}{d\bar{z}^2} = \\ &\left(\exp(\bar{V}(z))(1 + \delta\bar{V(z)})\Phi_n(z) - \exp(-\bar{V}(z))(1 - \delta\bar{V(z)})\Phi_p(z) + \frac{N_a(z) - N_d(z)}{n_i}\right).\end{aligned} \tag{V.38}$$

The linearized Poisson's equation can be solved for $\delta\bar{V}$ using a TDMA procedure. The potential at iteration $i+1$ can then be calculated as a function of that at step i. The process is then repeated until $\delta\bar{V}$ reaches a value close to 0 at each spatial node of the system (i.e. lower than a prescribed convergence criterion).

Cette thèse est accessible à l'adresse : http://theses.insa-lyon.fr/publication/2016LYSEI103/these.pdf
© [E. Blandre], [2016], INSA Lyon, tous droits réservés

Boundary conditions are required to solve Poisson's equation. At the boundaries of the cell, we assume that charge neutrality holds, meaning that the right hand side of Poisson's equation is equal to 0 [117]:

$$\left(\exp(\bar{V}(z))\Phi_n(z) - \exp(-\bar{V}(z))\Phi_p(z) + \frac{N_a(z) - N_d(z)}{n_i}\right) = 0. \tag{V.39}$$

We need to solve this equation for $\bar{V}$. Introducing the variable $X = \exp(\bar{V})$, Eq. V.39 becomes

$$\begin{aligned} X\Phi_n(z) - \frac{1}{X}\Phi_p(z) + \frac{N_a(z) - N_d(z)}{n_i} &= 0 \\ \Rightarrow X^2\Phi_n(z) - \Phi_p(z) + X\frac{N_a(z) - N_d(z)}{n_i} &= 0. \end{aligned} \tag{V.40}$$

Eq. V.40 is a second order polynomial equation that can easily be solved for X. The potential at the boundaries of the cell is therefore

$$\bar{V}(z = z_p) = -\ln\left((\Phi_p(z = z_p)\right) - \ln\left(\sqrt{\left(\frac{N_a}{2n_i}\right)^2 + \Phi_n(z = z_p)\Phi_p(z = z_p)} - \frac{N_a}{2n_i}\right), \tag{V.41}$$

$$\bar{V}(z = z_n) = -\ln\left(\Phi_n(z = z_n)\right) + \ln\left(\sqrt{\left(\frac{N_d}{2n_i}\right)^2 + \Phi_n(z = z_n)\Phi_p(z = z_n)} - \frac{N_d}{2n_i}\right). \tag{V.42}$$

The electrostatic potential profile is then used in the next step, that consists in solving the continuity/transport equations.

V.2.3.3 Solving the continuity/transport equations

Once the potential and the electric field are known, they can be injected in the expression of the electron current density

$$J_n = -e\mu_n n(z)\frac{dV}{dz} + e\mu_n \frac{k_b T}{e}\frac{d}{dz}\left[n_i \exp\left(\frac{e(V - \phi_e)}{k_b T}\right)\right]. \tag{V.43}$$

where the Einstein's relation for the diffusion coefficients D_n and D_p was inserted. The derivative term is

$$\frac{dn(z)}{dz} = \frac{d}{dz}\left[n_i \exp\left(\frac{e(V - \phi_n)}{k_b T}\right)\right] = \frac{en(z)}{k_b T}\left(\frac{dV}{dz} - \frac{d\phi_n}{dz}\right). \tag{V.44}$$

Cette thèse est accessible à l'adresse : http://theses.insa-lyon.fr/publication/2016LYSEI103/these.pdf
© [E. Blandre], [2016], INSA Lyon, tous droits réservés

The electron current density becomes

$$\begin{aligned} J_n &= -e\mu_n n(z)\frac{d\phi_n}{dz} \\ &= -e\mu_n n_i \exp\left[\frac{e(V-\phi_n)}{k_b T}\right]\frac{d\phi_n}{dz} \\ &= -e\mu_n n_i \exp\left(\frac{qV}{k_b T}\right)\exp\left(-\frac{e\phi_n}{k_b T}\right)\frac{d\phi_n}{dz}. \end{aligned} \tag{V.45}$$

By noticing that

$$\exp\left(-\frac{e\phi_n}{k_b T}\right)\frac{d\phi_n}{dz} = -\frac{k_b T}{e}\frac{d}{dz}\left[\exp\left(-\frac{e\phi_n}{k_b T}\right)\right], \tag{V.46}$$

we can then write

$$J_n = \mu_n n_i k_b T \exp\left(\frac{eV}{k_b T}\right)\frac{d}{dz}\left[\exp\left(-\frac{e\phi_n}{k_b T}\right)\right]. \tag{V.47}$$

Finally

$$J_n = a_n(z)\frac{d\Phi_n}{dz}, \tag{V.48}$$

where

$$\begin{aligned} a_n(z) &= \mu_n n_i k_b T \exp\left(\frac{eV}{k_b T}\right) \\ &= \mu_n n_i k_b T \exp(\bar{V}). \end{aligned} \tag{V.49}$$

For holes, the transport equation is:

$$J_p = -e\mu_p p(z)\frac{dV}{dz} - e\mu_p \frac{k_b T}{e}\frac{d}{dz}\left[n_i \exp\left(\frac{e(\phi_p - V)}{k_b T}\right)\right]. \tag{V.50}$$

Similarly, one finds

$$J_p = a_p(z)\frac{d\Phi_p}{dz}, \tag{V.51}$$

where

$$a_p(z) = -\mu_p n_i k_b T \exp\left(-\frac{eV}{k_b T}\right) = -\mu_p n_i k_b T \exp(-\bar{V}). \tag{V.52}$$

Cette thèse est accessible à l'adresse : http://theses.insa-lyon.fr/publication/2016LYSEI103/these.pdf
© [E. Blandre], [2016], INSA Lyon, tous droits réservés

Now we can inject the current density into the continuity equations, which gives

$$\frac{d}{dz}\left[a_n(z)\frac{d\Phi_n}{dz}\right] = e\,(R(z)-G(z)) \tag{V.53}$$

for the electrons, and

$$\frac{d}{dz}\left[a_p(z)\frac{d\Phi_p}{dz}\right] = -e\,(R(z)-G(z)) \tag{V.54}$$

for the holes. Equations V.57 and V.58 are now linear and non-coupled and can be solved for the quasi-Fermi levels Φ_n and Φ_p using a TDMA procedure. Once they are known, equations V.27 and V.28 are used to compute the carrier density profiles. Then, the carrier dependent terms, like those for the recombinations, are updated. The process is iterated until convergence, i.e. when the relative difference between the quasi-Fermi levels and the electrostatic potential between two iterations is close to zero. Boundary conditions are required to solve the continuity/transport equations. At the boundaries of the cell, if the carriers are the majority ones, the quasi-Fermi levels are equal to the potential applied at each side of the PV cell

$$\Phi_n(z_n) = \exp\left(\frac{-eV_n}{k_bT}\right), \tag{V.55}$$

$$\Phi_p(z_p) = \exp\left(\frac{eV_p}{k_bT}\right). \tag{V.56}$$

Here V_n is the potential applied at the boundary of the n-region, and V_p is the potential applied at the boundary of the p-region. The applied voltage is the potential difference between the edges of the cell. To apply a forward bias on the cell in the following, we consider the potential on the p-side of the cell to be zero, and the potential on the n-side of the cell to be $-V_f$, such that the voltage applied on the cell is V_f. For the region where the carriers are the minority ones, the current of electrical charges is balanced by a surface recombination current at the boundaries of the cell

$$J_n(z=z_p) = -e\frac{S_nS_p(n(z=z_p)p(z=z_p)-n_i^2)}{S_n(n(z=z_p)+n_i)+S_p(p(z=z_p)+n_i)}, \tag{V.57}$$

$$J_p(z=z_n) = e\frac{S_nS_p(n(z=z_n)p(z=z_n)-n_i^2)}{S_n(n(z=z_n)+n_i)+S_p(p(z=z_n)+n_i)}. \tag{V.58}$$

The algorithm used to solve the Drift-Diffusion equations with the Gummel iteration method is depicted in Fig. V.3.

Cette thèse est accessible à l'adresse : http://theses.insa-lyon.fr/publication/2016LYSEI103/these.pdf
© [E. Blandre], [2016], INSA Lyon, tous droits réservés

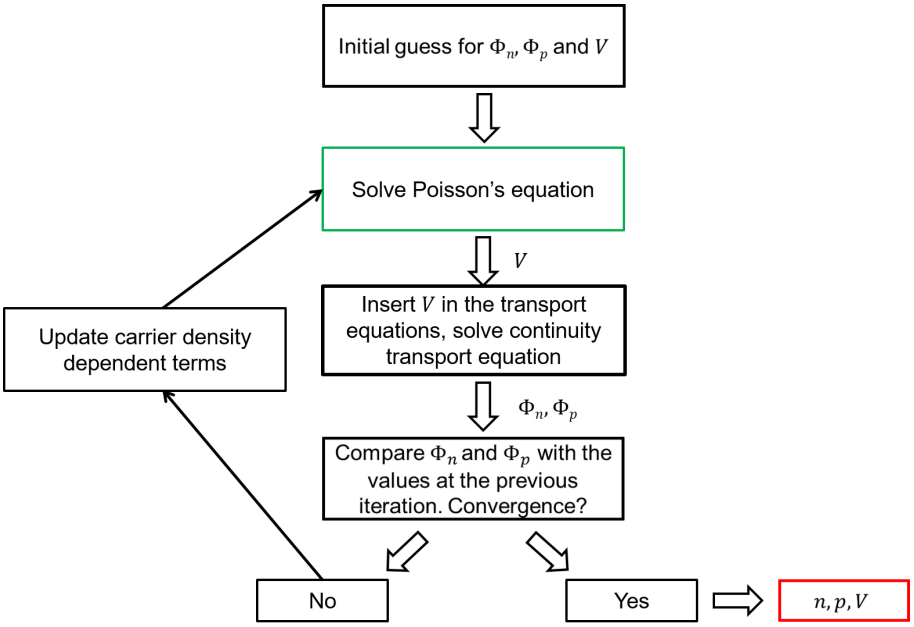

Figure V.3: Algorithm used to solve the Drift-Diffusion equations with Gummel's iteration method. The green frame represents the algorithm to solve Poisson's equation.

V.2.3.4 Algorithm for the computation of the J-V characteristic of the PV cell

Poisson's equation is first solved at equilibrium (ϕ_n and ϕ_p equal to 0, Φ_n and Φ_p equal to 1), i.e. in absence of illumination ($G = 0$) and applied voltage ($V_f = 0$). The carrier density profiles at equilibrium are retrieved. When an illumination is applied, the values of $\bar{V}$, Φ_n and Φ_p at equilibrium are used as initial guess. Once the algorithm has converged, the applied voltage is gradually increased by a step ΔV_f that is much smaller than the built-in voltage (Eq. V.10), avoiding numerical issues. Again, it is very important to use the values of $\bar{V}$, Φ_n and Φ_p that have been calculated at the previous step for the bias ΔV_f as the initial guesses for the next step, or the algorithm may not converge. The process is repeated until the open-circuit voltage V_{oc} is reached. The algorithm used to compute the J-V characteristic of the cell is depicted in Fig. V.4.

Once the J-V characteristic is calculated, the analysis of the product $J \times V_f$ allows finding the maximum power output $P_{\max}$ of the system. The validation of the FDD model implemented in our simulation code can be found in Appendix C.

Cette thèse est accessible à l'adresse : http://theses.insa-lyon.fr/publication/2016LYSEI103/these.pdf
© [E. Blandre], [2016], INSA Lyon, tous droits réservés

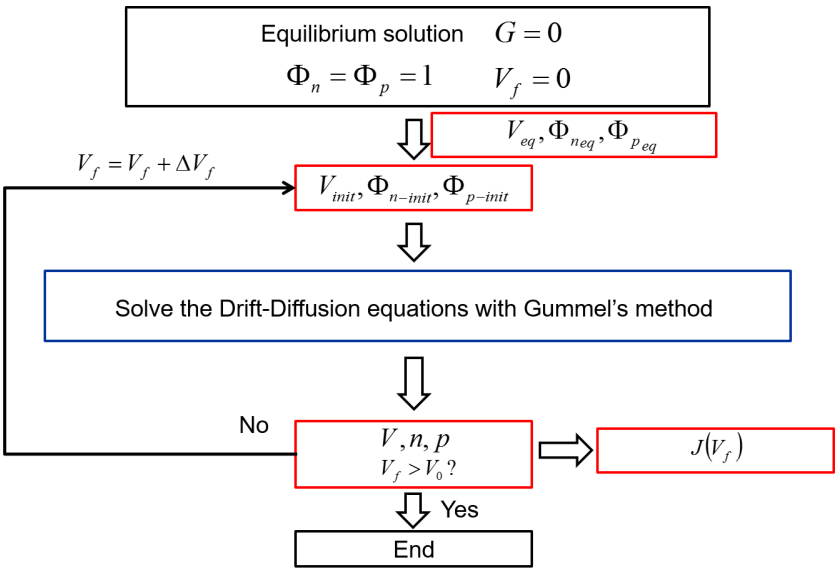

Figure V.4: Algorithm used to compute the J-V characteristic of the cell. The blue frame represents the resolution of the Drift-Diffusion equations with Gummel's iteration method (Fig. V.3).

V.3 Analysis of low and high-injection regimes in NFR-TPV

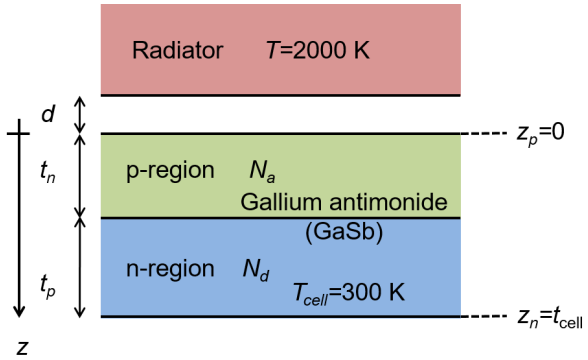

Figure V.5: Schematic representation of the NFR-TPV system under consideration.

In this section, we analyze the low-injection approximation in different cases. We study the same system as in [7]: the radiator is at 2000 K, and emits thermal radiation toward a GaSb cell, composed of a pn-junction (p over n) of size t_{cell}. The p-region of size t_p has a doping N_a, while the n-region of size t_n has a doping N_d. The radiator and the cell are separated by a distance d. The cell is assumed to be at ambient temperature ($T_{\text{cell}} = 300$) K. A schematic of that NFR-TPV system is depicted in Fig. V.5.

The optical properties of the radiator are described by a Drude model. The Drude parameters have been chosen such that at $d = 10$ nm, the polariton resonance generates a peak in the radiation heat flux spectrum at a frequency which is a little bit larger than the frequency corresponding to the bandgap energy of GaSb [111, 7]. To start with, the size of the p-region is set at $t_p = 400$ nm,

Cette thèse est accessible à l'adresse : http://theses.insa-lyon.fr/publication/2016LYSEI103/these.pdf
© [E. Blandre], [2016], INSA Lyon, tous droits réservés

the size of the n-region at $t_n = 10$ µm, and the doping of the n-region at $N_d = 10^{17}$ cm^{-3}. High-injection phenomena are likely to occur when the density of excess minority carriers is of the same order as the level of majority carriers (or the doping). Therefore it may happen either when the local generation rate is large, or when the doping level is low. In the following, unless specified otherwise, we consider an extreme case where the distance d is fixed at 10 nm, such that the generation rate in the PV cell is large ($\approx 10^{33}$ m^{-3}s^{-1} near to the top surface). Furthermore, as the radiator supports surface polaritons, the generation rate of EHPs is localized near the surface of the PV cell (Fig. V.2(b)). It is worth noticing that a distance of 10 nm between the radiator and the cell is experimentally difficult to achieve in a plane-plane configuration. However, as the radiator is optically optimized for this distance, it constitutes a interesting study case. Two doping levels are considered for the p-region: $N_a = 10^{19}$ cm^{-3} and $N_a = 10^{15}$ cm^{-3}.

V.3.1 Carrier concentrations under illumination

The spatial distribution of the excess electron and hole densities are plotted in Fig. V.6.

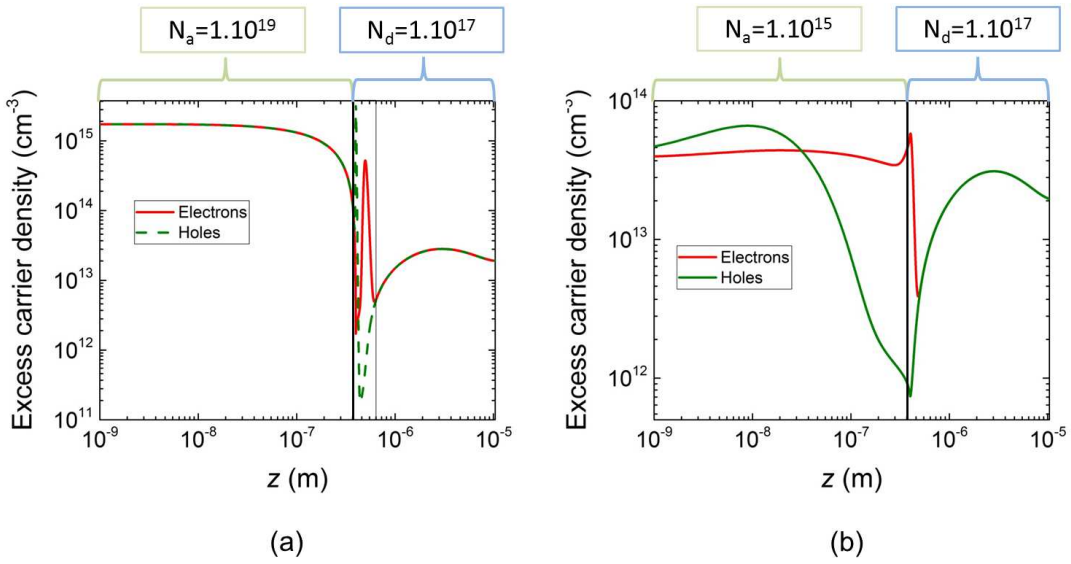

Figure V.6: Spatial distribution of excess electron and hole densities inside the cell. (a): the doping of the p-region is high ($N_a = 10^{19}$ cm^{-3}). (b): the doping of the p-region is low ($N_a = 10^{15}$ cm^{-3}). $d = 10$ nm

When the doping level is N_a is equal to 10^{19} cm^{-3} (Fig. V.6(a)), it is observed that the excess of carriers is three orders of magnitude larger in the p-region than in the n-region. This is due to the extremely localized spatial distribution of the generation rate. However, the values (10^{15} at maximum) never exceed the doping level. It is worth noticing that except in the depletion region (represented by a black frame in the figure), the excess eletron and hole densities are equal. This fact is taken as an hypothesis in the "Ambipolar Transport Equations" model [35], that is another way to simplify the Drift-Diffusion equations. As the density of photogenerated carriers is smaller than the doping, the low-injection regime prevails when the doping of the p-region is

Cette thèse est accessible à l'adresse : http://theses.insa-lyon.fr/publication/2016LYSEI103/these.pdf
© [E. Blandre], [2016], INSA Lyon, tous droits réservés

$N_a = 10^{19}$ cm^{-3}. In Fig. V.6(b), a lower doping level for the p-region is considered. It can be observed that in the p-region, the values of the excess carrier densities are close to the doping level, but only in the p-region. It is also worth noticing that in the p-region, the excess of electron and holes densities are no longer equal. For a doping level of $N_a = 10^{15}$ cm^{-3}, the p-region is therefore in high injection. In the following, we will test the validity of the approximations listed in section V.2.2., in the cases of high and low injection.

V.3.2 Spatial distribution of the electric field

The electric field variations are analyzed first. In Fig. V.7, the electric field at $V_f = 0$ for the two different values of N_a is plotted. We compare the electric field under dark conditions and under illumination. In both cases, the electric field spatial distribution is the same for both configurations. It is interesting to observe that that in Fig. V.7(b), the electric field extends to the top boundary of the p-region z_p. It is due to the fact that, according to Eq. V.11, the electric field extends toward the region with the lowest doping. As the doping level of the p-region is low compared to the one in the n-region, the electric field extends to the top boundary of the cell.

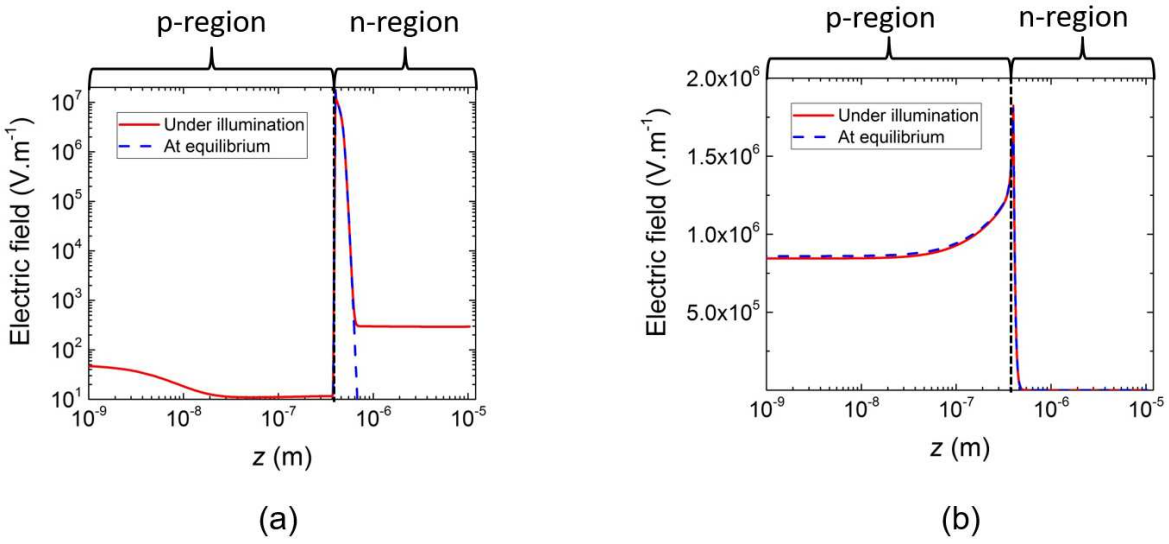

Figure V.7: Spatial distribution of the electric field. (a): $N_a = 10^{19}$ cm^{-3}. (b): $N_a = 10^{15}$ cm^{-3}. $d = 10$ nm.

V.3.3 Recombination rate and lifetimes of electrial carriers

Next, we analyze the lifetime approximation for the recombinations. According to Eq. II. 25, the recombination rate can be approximated as being proportional to the excess of minority carriers. The coefficient of proportionality is the inverse of the lifetime $\frac{1}{\tau}$ of the electrical carriers, and is spatially constant. The calculated recombination rates of the Auger, SRH and radiative processes inside the p-region are plotted in Fig. V.8 as a function of the excess electron density Δn at the same position.

Cette thèse est accessible à l'adresse : http://theses.insa-lyon.fr/publication/2016LYSEI103/these.pdf
© [E. Blandre], [2016], INSA Lyon, tous droits réservés

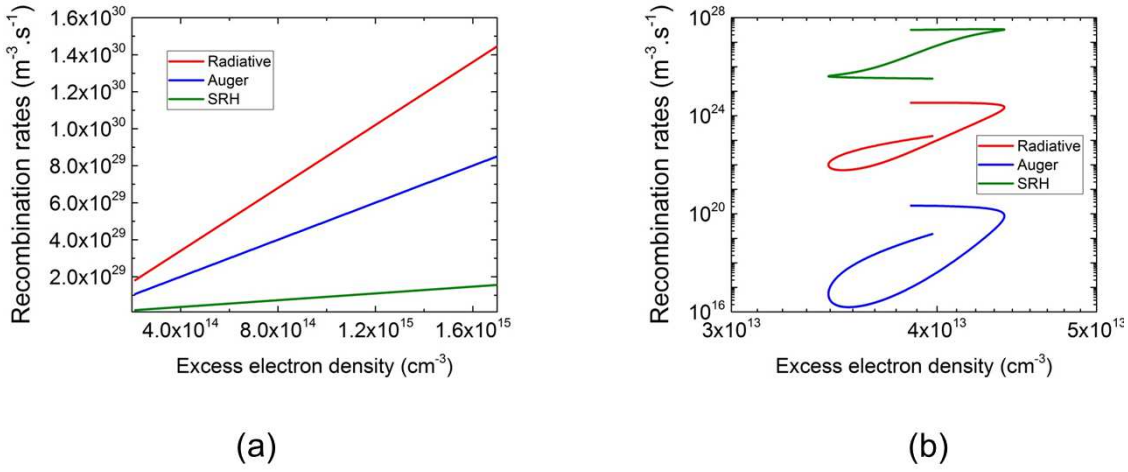

Figure V.8: Recombination rates of the different processes as a function of the carrier minority carrier (electron) density in the p-region. (a): $N_a = 10^{19}$ cm^{-3}. (b): $N_a = 10^{15}$ cm^{-3}. $d = 10$ nm.

In Fig. I.8(a), we observe a linear relationship between the recombination rates and the excess carrier density. Furthermore, we perform a linear interpolation on the three curves: the slopes are equal to the lifetimes calculated using the low-injection approximation, whose expressions are given in Eqs. II.15, II.18 and II.23. We conclude that the hypothesis of the spatially constant lifetime to describe the recombination rates is valid in this case. In high-injection (Fig. I.8(b)), there is no linear relationship between the excess electron density and the recombination rates: the lifetime approximation is not valid anymore. Furthermore, the curves are not bijective, which means that the recombination rates depend not only on the excess of minority carrier (electrons), but also on the excess of majority carrier (holes). It is also interesting to note that this phenomenon

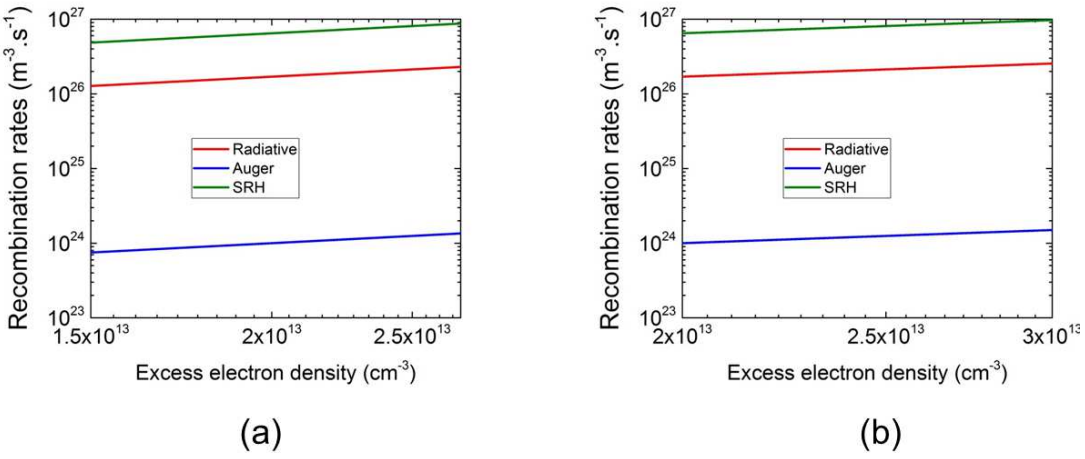

Figure V.9: Recombination rates of the different processes as a function of the minority carrier (holes) density in the n-region. (a): $N_a = 10^{19}$ cm^{-3}. (b): $N_a = 10^{15}$ cm^{-3}. $d = 10$ nm.

Cette thèse est accessible à l'adresse : http://theses.insa-lyon.fr/publication/2016LYSEI103/these.pdf
© [E. Blandre], [2016], INSA Lyon, tous droits réservés

occurs only in the p-region (compare Fig. V.9 with Fig. V.8), which means that high-injection phenomena can be localized in a single region of the PV cell.

V.3.4 Superposition principle

Next, we analyze the validity of the superposition principle. The recombination currents are plotted as a function of the applied voltage for the two doping levels under consideration, under illumination and dark conditions. The recombination current under dark conditions is calculated by simply computing the J-V characteristic of the cell with a nil generation rate ($G = 0$). Under illumination, the recombination current is calculated as $J(V_f) - J_{SC}$. Under low-injection (Fig. I.10(a)), the recombination currents under illumination and dark conditions are almost equal, which means that the superposition principle is applicable. However, it is observed that in high-injection (Fig. I.10(b)), the recombinations currents are not the same under illumination and under dark conditions. In this case, the superposition principle is not valid anymore.

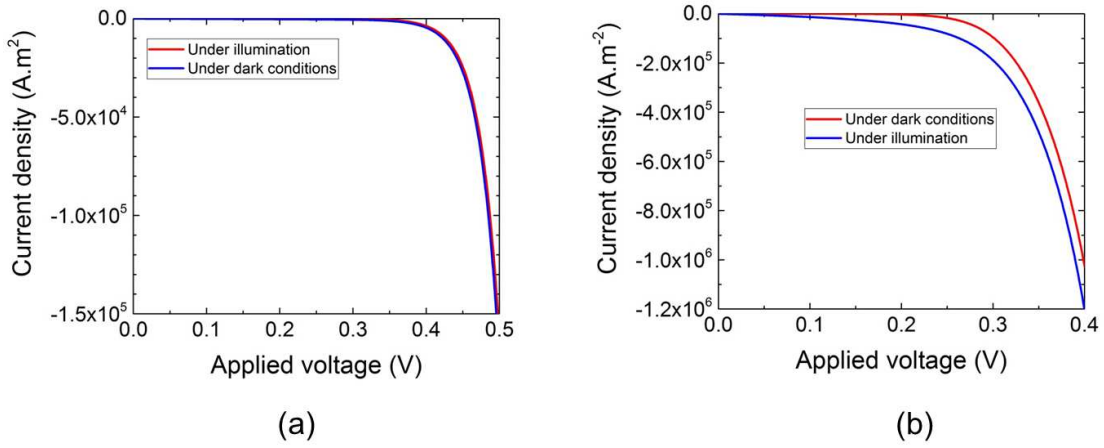

Figure V.10: Recombination current under illumination and under dark conditions as a function of the applied voltage. (a): $N_a = 10^{19}$ cm^{-3}. (b): $N_a = 10^{15}$ cm^{-3}. $d = 10$ nm. $d = 10$ nm.

V.3.5 Maximum power output

Ultimately, to prove the necessity of taking care of high-injection phenomena in NFR-TPV, we compare in the two cases the results obtained using the MCS model (low-injection approximation) and the FDD model (all injections). In Fig. V.11(a), the current-voltage (J-V) and power-voltage (P-V) characteristics are plotted in the case of low-injection.

A good agreement between the two models is observed, leading to a relative error on $P_{\max}$ less than 2%. In the case of high-injection (Fig. V.11(b)), we observe a significant difference between the results obtained with the two models (relative difference of 15%). Furthermore, the maximum power output is largely underestimated when using the MCS mode. This emphasizes the fact that the MCS model can be used only if no high-injection phenomena occur. As mentioned before, the case where the distance separating the radiator and the cell is equal to 10 nm is an extreme

Cette thèse est accessible à l'adresse : http://theses.insa-lyon.fr/publication/2016LYSEI103/these.pdf
© [E. Blandre], [2016], INSA Lyon, tous droits réservés

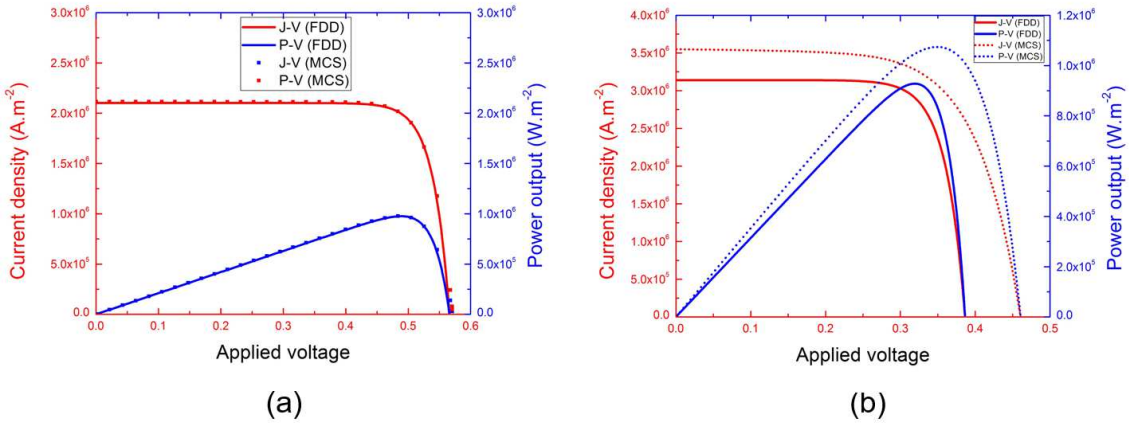

Figure V.11: Comparaison of the J-V and P-V characteristics obtained with the FDD model with the one obtained using the MCS. (a): $N_a = 10^{19}$ cm^{-3}. (b): $N_a = 10^{15}$ cm^{-3}. $d = 10$ nm

case, hardly feasible experimentally. In Fig. V.12, the current-voltage (J-V) and power-voltage (P-V) characteristics are plotted in the same configurations as before, except that the distance between the radiator and the cell is fixed at 200 nm. In this case, the difference between the results obtained with the FDD and MCS models are relatively low ($\approx$ 1.8%), even for low a doping level of the p-region ($N_a = 10^{15}$ cm^{-3}), meaning that high-injection effects are negligible on the performances of the NFR-TPV system. This emphasizes that high-injection effects of course depend also on the level on illumination.

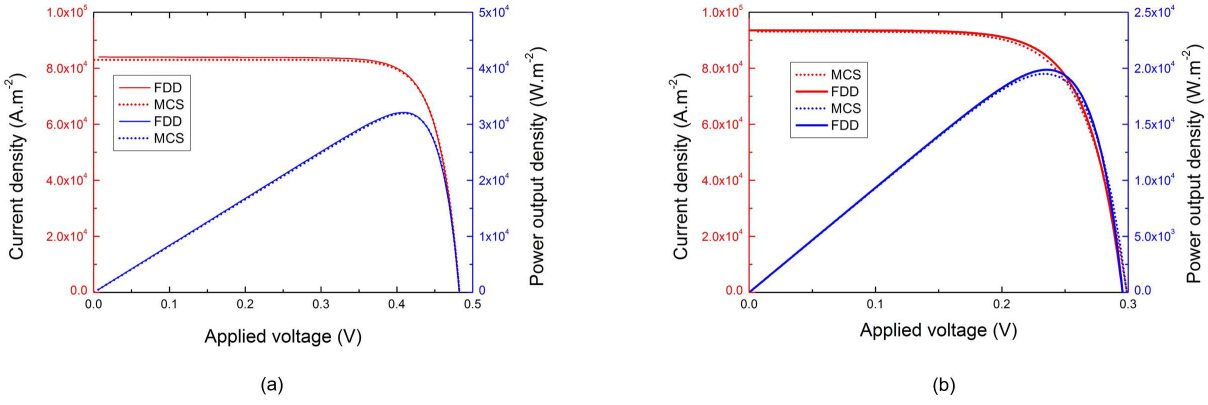

Figure V.12: Comparaison of the J-V and P-V characteristics obtained with the FDD model with the one obtained using the MCS. (a): $N_a = 10^{19}$ cm^{-3}. (b): $N_a = 10^{15}$ cm^{-3}. The distance d between the radiator and the cell is 200 nm.

Cette thèse est accessible à l'adresse : http://theses.insa-lyon.fr/publication/2016LYSEI103/these.pdf
© [E. Blandre], [2016], INSA Lyon, tous droits réservés

V.3.6 Spatial variations of the quasi-Fermi levels

To end this section, we analyze another approximation that relates the local difference of the quasi-Fermi levels of electrons and holes. As mentioned in section V.2, the difference of the quasi-Fermi levels at the boundaries of the cell should be equal to the applied voltage on the cell V_f. However, it is often assumed that the local difference of the quasi-Fermi levels at any position z inside is constant and equal to the applied voltage:

$$\phi_n(z) - \phi_p(z) = V_f, \tag{V.59}$$

meaning that the shift of potential due to the excess of electrical carriers is always negligible compared to the one due to the increase of the applied voltage.

This approximation is commonly assumed to describe the emission of a body in the presence of a non-zero chemical potential [36]. The Planck function in the presence a non-zero chemical potential in the emitting body can be used to calculate emission from radiative recombination of a PV cell in a system in order to evaluate the bimolecular recombination coefficient B. Recently, this approximation has also been assumed for the calculation of the radiative emission of bodies for radiative cooling applications [119]. The fact that the quasi-Fermi levels are solved in the FDD model to compute the performances of the system offers the opportunity to check the validity of this approximation.

The differences of the quasi-Fermi levels for electrons and holes are depicted in Fig. V.13, for different applied voltages V_f, represented on the plots by a black dashed line. On the left, we considered the extreme near-field regime ($d = 10$ nm), while on the right, the far-field regime ($d = 1$ mm) is considered. It is observed that the difference of the quasi-Fermi levels is always equal to the applied voltage in the depletion region (around $z = 400$ nm): in this region, due to the electric field, the excess carrier densities are low. Outside the depletion region, $\phi_n - \phi_p$ is almost never equal to the applied voltage V_f. The two values get however closer when the applied voltage increases, or when the carrier densities are decreased (i.e. when the doping becomes lower or when the distance between the radiator and the cell d decreases). The important case is at the maximum power point (MPP) of the J-V characteristics of the pn-junction. The MPP is around 0.5 V for the cell under consideration: at this applied voltage, the local difference of the quasi-Fermi levels are approximately equal to the applied voltage in far-field, but not in the extreme near-field. This emphasizes the fact that to compute the emission of a body under high illumination, the use of a model that allows calculating the local values of the quasi-Fermi levels for electrons and holes might be required.

As a conclusion for this section, we studied two cases, one where the cell is under low-injection regime, and one where high-injection phenomena occur inside the p-region. The hypotheses made in the low-injection approximation have been confronted in both cases. When the injection is large, except for the electric field, they are not valid anymore. This leads to a significant difference between the results obtained with the FDD model and the MCS model.

Cette thèse est accessible à l'adresse : http://theses.insa-lyon.fr/publication/2016LYSEI103/these.pdf
© [E. Blandre], [2016], INSA Lyon, tous droits réservés

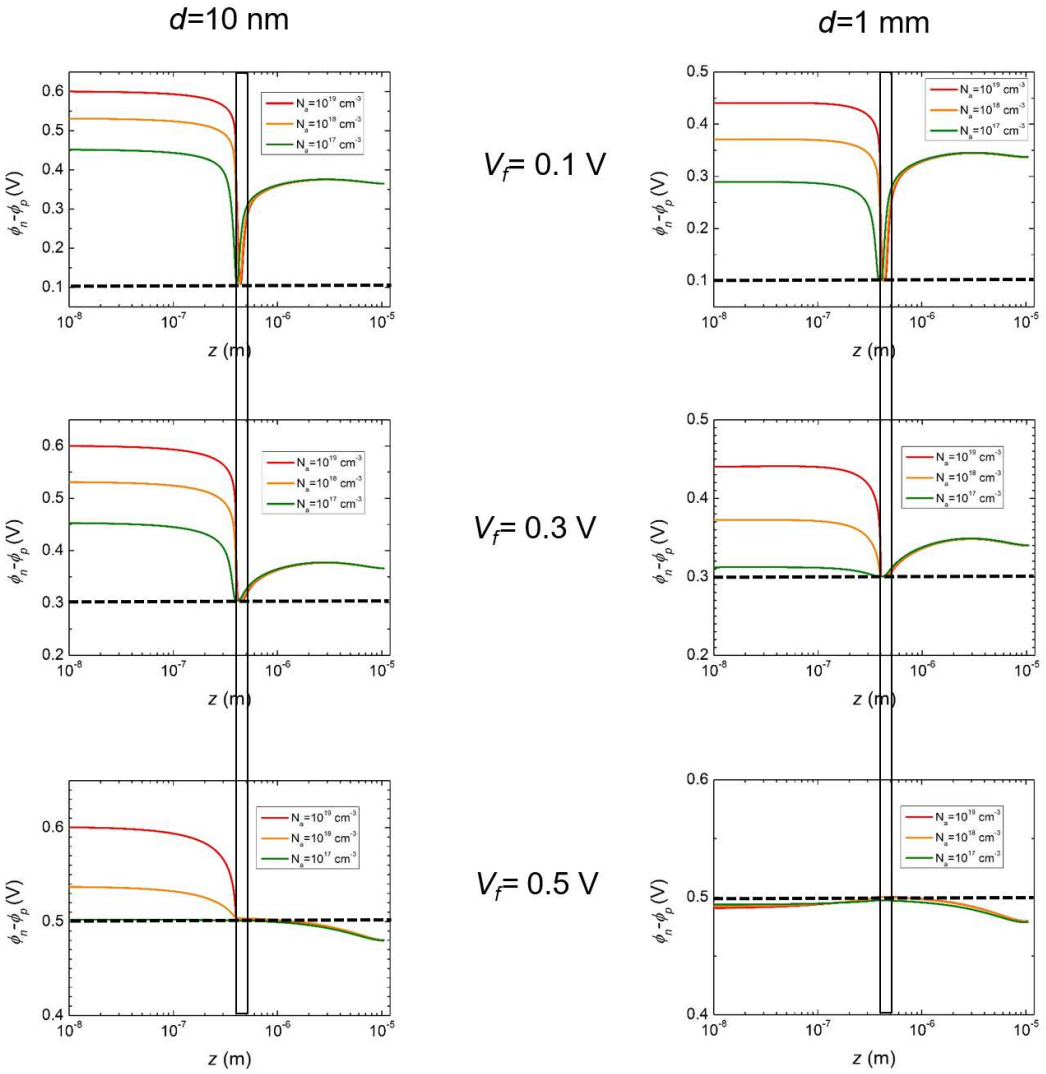

Figure V.13: Local difference of the quasi-Fermi level for electrons and holes $\phi_n - \phi_p$ for different doping levels of the p-region N_a and different applied voltages V_f (represented by the dashed horizontal lines). An extreme near-field case (left figures, $d = 10$ nm) and a far-field case (right figures, $d = 1$ mm) are depicted. The black lines represent the edges of the depletion region.

V.4 Optimization of the doping levels and the thickness of the doped regions for NFR-TPV systems

V.4.1 Optimization of the doping levels of the doped regions

As mentioned in the introductory section of this chapter, an experimental setup that would allow to prove that a TPV system can benefit greatly of near-field effects requires an optimization of the PV device. For example, [7, 25] showed that surface-phonon polariton mediated NFR-TPV systems exhibit large electrical losses due to surface recombinations. In this section, we propose to analyze the impact of the doping levels and the thicknesses of the doped regions, to optimize

Cette thèse est accessible à l'adresse : http://theses.insa-lyon.fr/publication/2016LYSEI103/these.pdf
© [E. Blandre], [2016], INSA Lyon, tous droits réservés

the performances of the NFR-TPV cell. The analysis of the doping levels could not be made before because of the validity of the MCS modeling could be questioned. Here, we use the full solution of the DD equations.

The same radiator as before is consired. The distance between the radiator and the cell d is set at 10 nm. The impact of the doping levels is investigated first. By setting the doping of the n-region (N_d) at 10^{17} cm^{-3}, we plot in Fig. V.14 the J-V (Fig. V.14(a)) and P-V (Fig. V.14(b)) characteristics of the NFR-TPV system. In Fig. V.14(a), it is observed that varying the doping level of the p-region makes the maximum power output of the PV cell vary. The maximum power output of the cell reaches a maximum at a value close to $N_a = 10^{17}$ cm^{-3}. Two phenomena occur when decreasing the doping level. First, the mobility of the electrons and holes depends on the doping level: the mobility decreases with the number of impurities brought by the doping (Fig. V.15). The effect is the strongest for electrons (minority carriers in the p-region). The increase of the mobility induces an increase of the short-circuit current (J_{SC}), as observed in Fig. V.14(b). This tends to increase the performances of the system. However, when the doping decreases, the equilibrium carrier concentration of electrons and holes increases (according to Eqs. II.3 and II.4). The increase of the equilibrium carrier concentrations induces a larger carrier concentration under illumination and applied voltage, and therefore larger recombination rates. The stronger recombination current leads to a decrease of the open-circuit voltage (V_{OC}), which results in a decrease of the performance of the NFR-TPV system. The maximum of the maximum power output when the doping varies is the result of the trade-off induced by these two phenomena. The results obtained with the FDD and MCS models are compared in this Fig. V.14. For the larger values of the doping level, a good agreement is observed between the MCS and the FDD models. For the smallest doping levels, the values are departing from each others. This emphasizes that the optimization of the doping level may need to be performed using the resolution of the full Drift-Diffusion equations, especially in the extreme near-field.

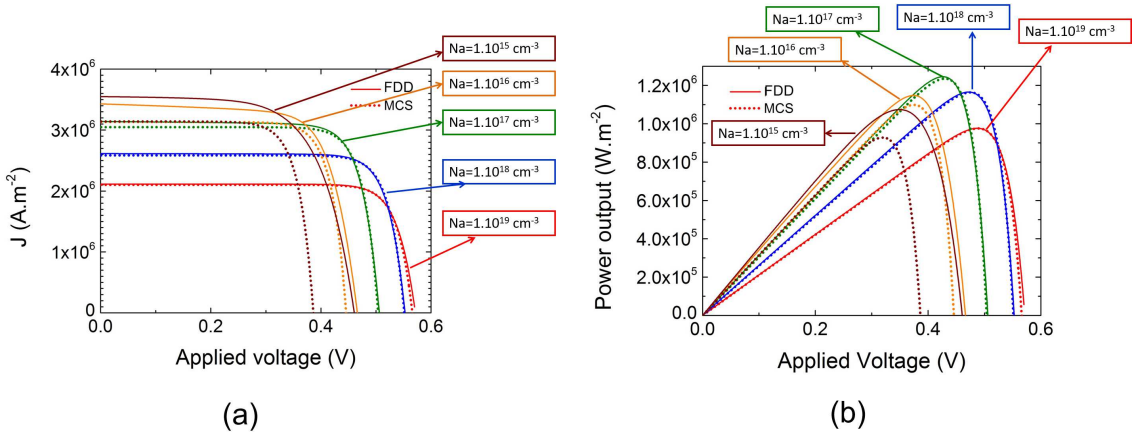

Figure V.14: (a): J-V characteristics for different doping levels of the p-region. (b): Power output as a function of the applied voltage for different doping levels of the p-region. $d = 10$ nm. $d = 10$ nm.

To emphasize the gain of performances due to the optimization of doping, the values of $P_{\max}$

Cette thèse est accessible à l'adresse : http://theses.insa-lyon.fr/publication/2016LYSEI103/these.pdf
© [E. Blandre], [2016], INSA Lyon, tous droits réservés

are plotted in Fig. V.16(a) as a function of the doping level of the p-region. An increase of the values of $P_{\max}$ is observed, up to 30% compared with the initial doping level. In order to analyze this increase, the excess electron densities are plotted for different doping levels of the p-region are depicted in Fig. V.16(b). For each case, the surface recombination rates at the front surface of the cell are provided. It is observed that the electron density is decreasing when the doping level decreases. This leads to a decrease of the surface recombination rates. As mentioned in [7], surface recombinations are the most limiting factor for SPhP mediated NFR-TPV systems. Therefore, the choice of an optimal doping to reduce this phenomenon is key to optimize the performances of the system.

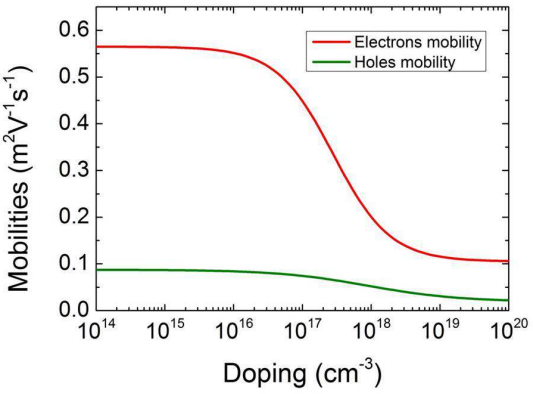

Figure V.15: Mobility of the electrons and holes as a function of the doping level, for $T = 300$ K.

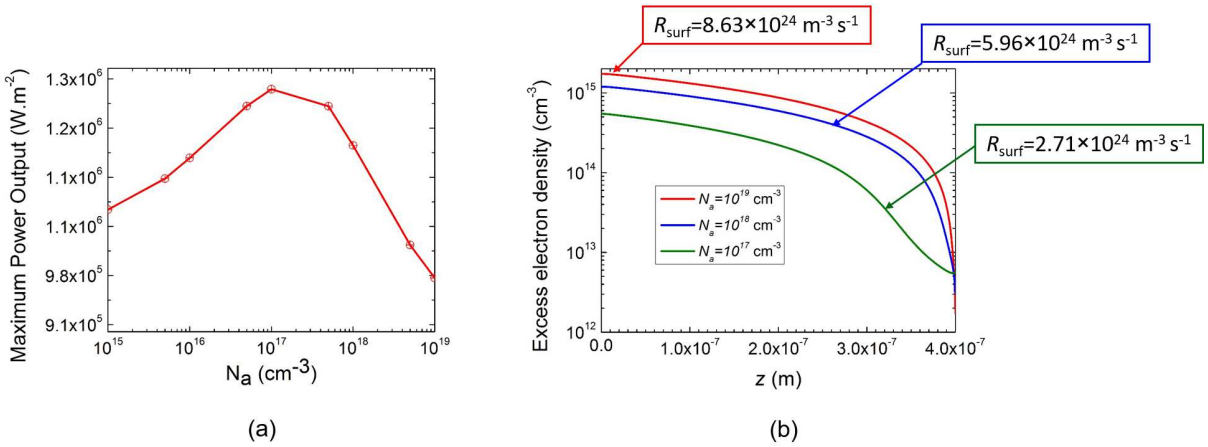

Figure V.16: (a): Maximum power output $P_{\max}$ as a function of the doping level of the p-region N_a. (b): Spatial distribution of the excess electron density in the p-region for different doping levels N_a. $d = 10$ nm.

The doping level of the n-region is now under consideration. The values of the power output ($P_{\max}$) as a function of the doping level of the n-region are reported in Fig. V.17, with a doping level of the p-region set at $N_a = 10^{17}$ cm^{-3}. Unlike the case of the p-region, the maximum power

Cette thèse est accessible à l'adresse : http://theses.insa-lyon.fr/publication/2016LYSEI103/these.pdf
© [E. Blandre], [2016], INSA Lyon, tous droits réservés

output reaches a constant value at a doping level of $N_d \simeq 10^{17}$ cm^{-3}. Since the size of the n-region is large (10 μm), the surface recombination rate at the back of the cell is small, and the system does not benefit from the increase of the mobility of holes. Moreover, the hole mobility is not very sensitive to the doping level (Fig. V.15).

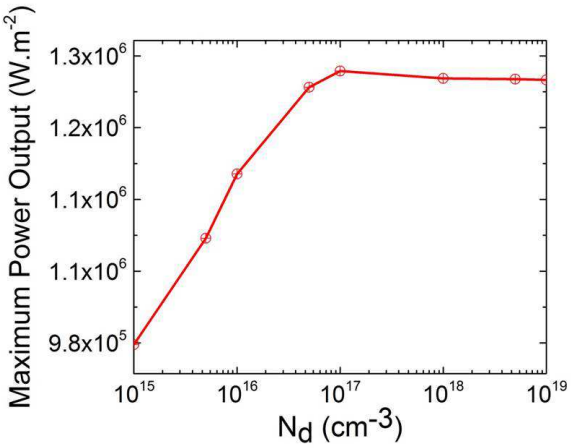

Figure V.17: Maximum power output of the cell as a function of the doping level of the n-region. $d = 10$ nm.

V.4.2 Optimization of the thickness of the doped regions

Eventually, the impact of the sizes of the p and n-region is analyzed. The thickness of the p-region is varied first (Fig. V.18).

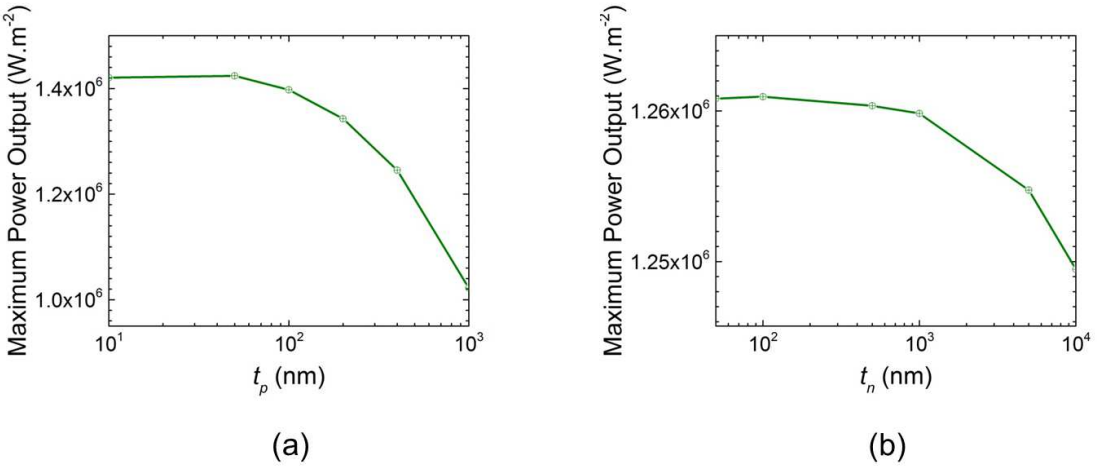

Figure V.18: (a): Maximum power output of the cell as a function of the size of the p-region t_p ($t_n = 10$ μm). (b): Maximum power output of the cell as a function of the size of the n-region t_n ($t_p = 400$ nm).

When the thickness of the p-region decreases, the maximum power output of the cell increases

Cette thèse est accessible à l'adresse : http://theses.insa-lyon.fr/publication/2016LYSEI103/these.pdf
© [E. Blandre], [2016], INSA Lyon, tous droits réservés

until it reaches a plateau at a given value of t_p (around 50 nm as depicted in Fig. V.18(a)). The same phenomenon occurs for the thickness of the n-region, for a thickness t_n around 200 nm (Fig. V.18(b)), but the increase of the power output is smaller. Reducing the size of the a region allows decreasing the distance between the region where the carriers are photogenerated and the depletion region. Therefore, it decreases the bulk recombination rates. Indeed, in NFR-TPV systems, due to the small penetration depth of the SPhPs, the majority of the radiation is absorbed by the PV cell if its thickness is larger than the penetration depth of the thermal radiation ($\simeq \frac{5}{d}$). Therefore, reducing the thickness of the PV cell should be a way to improve the performances of NFR-TPV systems. One should however pay attention to additional phenomena that could play a role when the sizes become too small.

V.5 Toward an experimental configuration: simulations of the performances of an InSb PIN photodiode in the near field

In this last section, we have presented an idealistic configuration for NFR-TPV. Experimentally, a temperature of 2000 K is difficult to achieve for the radiator. Instead, a temperature around 800 K is reasonable. At this temperature, a low bandgap semiconductor has to be used. InSb has a bandgap in the mid-infrared (0.17 eV). Therefore, we will consider the cell to be made of InSb. To collect radiative energy and convert it into electricity, InSb PIN junctions are used as infrared photodectectors. A PIN photodiode is constituted of an intentionally undoped region (i-region) sandwiched between a p and a n-region. The principle of the PIN photodiode is that because of the large doping difference between the intrinsic region and the two doped region, the electric field extends inside the i-region, forming a large depletion region [34, 35]. The p and n-region are generally very thin and the i-region thick, such as the radiative heat flux from the radiator to the far field is mostly absorbed inside the i-region, where the EHPs are separated and swept by the electric field toward the regions where they are in minority.

The configuration studied is based on the architecture of a standard InSb photodetector, and is depicted in Fig. V.19. The radiator is made of SiC, and its working temperature is 800 K. Note that we did not consider SiC because it supports SPhPs in the infrared, but because it has a large emissivity (unlike metals for example). Indeed, as the radiator is at a temperature of only 800 K, the radiative power emitted by a metal could have been too small to generate a significant photocurrent. The PIN diode is constituted of a top p-region of thickness $t_n = 400$ nm, and of doping $N_a = 4 \times 10^{17}$ cm^{-3}. The i-region is 4 µm thick. A semiconductor in never fully intrinsic: defects inside its crystalline lattice induce a residual doping. In this case, the doping of the i-region is a n-doping of value $N_d = 5 \times 10^{14}$ cm^{-3}. The bottom n-region is 200 nm thick, and its doping level is set as $N_d = 5 \times 10^{14}$ cm^{-3}. As InSb has a low bandgap, large levels of equilibrium carrier concentrations will appear (Eqs. II.2, II.3 and II.4), leading to a large thermal noise that will affect the performances of the system. As a consequence, cooling the cell may be required to observe an electrical photocurrent. We consider a temperature range from 300 K (ambient temperature) to 77 K (temperature of liquid nitrogen). We underline that because of the presence of the i-region, high-injection phenomena are very likely to take place inside the PIN diode. In this framework,

Cette thèse est accessible à l'adresse : http://theses.insa-lyon.fr/publication/2016LYSEI103/these.pdf
© [E. Blandre], [2016], INSA Lyon, tous droits réservés

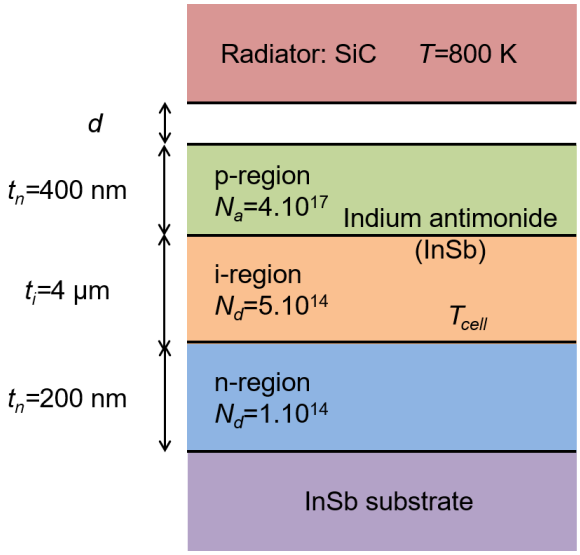

Figure V.19: Schematic representation of the NFR-TPV system with a generic PIN photodiode.

the low-injection approximation cannot be applied, and the full resolution of the Drift-Diffusion equations is required.

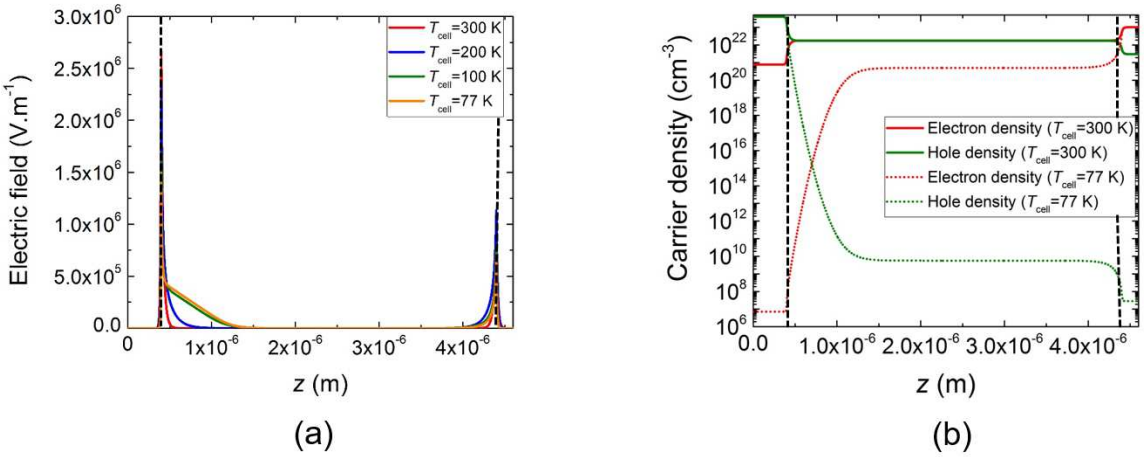

Figure V.20: (a): Spatial distribution of the electric field inside the PIN diode for different temperatures. (b): Spatial distribution carrier densities. The dashed vertical lines represent the spatial position of the interfaces between the different regions.

The spatial distribution of the electric field within the InSb cell in considered first. In Fig. V. 20(a) the electric field inside the PIN photodiode is depicted at equilibrium (no illumination nor applied voltage) for different temperatures of the cell. It is observed that at a temperature of 300 K, the electric field does not extend far into the i-region. When the cell temperature decreases, the electric field starts to extend in the i-region, especially near the interface between the p and the i-region, where the difference of doping is large. In Fig. V.20(b), the carrier concentrations are plotted inside the PIN cell, for two temperatures (300 K and 77 K). The relative difference

Cette thèse est accessible à l'adresse : http://theses.insa-lyon.fr/publication/2016LYSEI103/these.pdf
© [E. Blandre], [2016], INSA Lyon, tous droits réservés

between the carrier densities and the doping is rather large when the cell is at 77 K, but at ambient temperature (300 K), the carrier concentrations at equilibrium are only between one and two orders of magnitude smaller than the doping levels. As the spatial variations of the charge density are small, the electric field is not extending far inside the i-region. With the present configuration, the PIN photodiode is not expected to produce large photocurrents at 300 K. Doping levels and thicknesses of the different regions should be optimized for allowing the operation of the cell at 300 K.

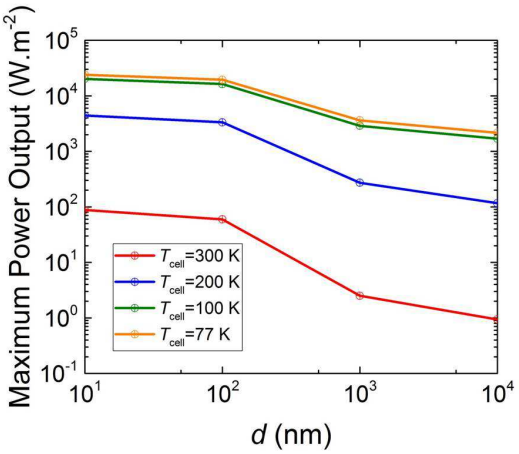

Figure V.21: Maximum power output of the PIN photodiode as a function of the distance separating the radiator and the cell d.

The observation of the near-field enhancement is analyzed in Fig. V.21. The maximum power output of the system is plotted as a function of the distance between the radiator and the cell (d), for several temperatures of the PV cell. The enhancement of the energy conversion performances due to near-field effects is observed when the distance decreases. When the cell temperature decreases, the maximum power output also increases, up to 2 orders of magnitude larger than that at ambient temperature. It emphasizes the fact that the design of the PIN photodiode is not relevant for an operating temperatures close to ambient. Is is worth noticing that the maximum power output does not follow the same behavior than the absorbed radiative power absorbed by the PV device, which is generally a power law. In order to make a deeper analysis of the performances for the different operating temperatures, Fig. V.21 depicts the J-V (Fig. V.22(a)) and P-V (Fig. V.22(b)) characteristics of the PIN cell ($d = 10$ nm).

It is observed that the open-circuit voltage (V_{OC}) of the cell at ambient temperature is extremely small, due to the small bandgap energy of InSb (large thermal recombination current). The short-circuit current also increases between 300 and 200 K, until it stabilizes at a value of around 1.5×10^5 W.m^{-2} for low temperatures. Eventually, the impact of the decrease of the short-circuit currents on the energy conversion performances can be observed in the P-V characteristic. Although, the short-circuit current are of the same order of magnitude for the different temperatures, the decrease of the open-circuit voltage induces a large drop of maximum power output ($P_{\max}$). As explained before, the case where the distance d separating the radiator and the cell is

Cette thèse est accessible à l'adresse : http://theses.insa-lyon.fr/publication/2016LYSEI103/these.pdf
© [E. Blandre], [2016], INSA Lyon, tous droits réservés

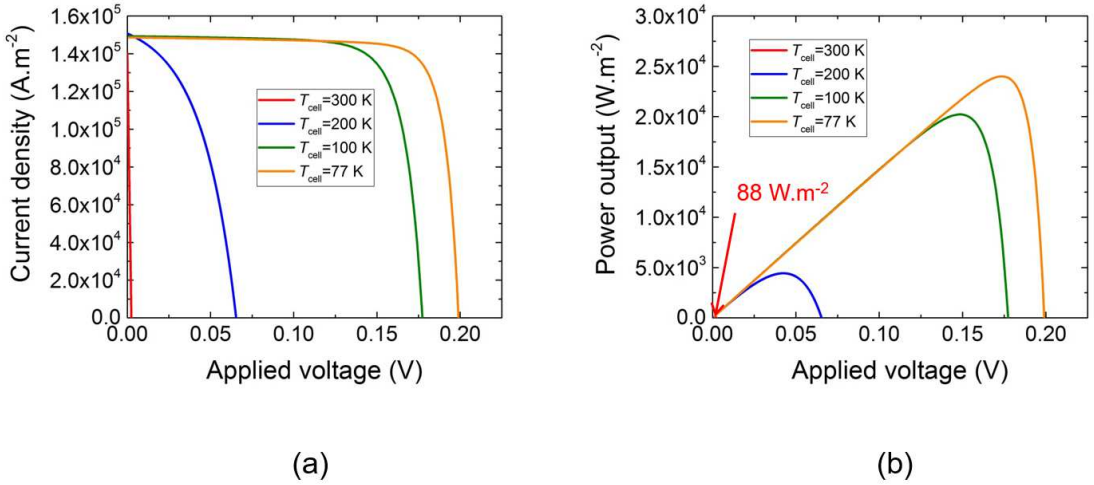

Figure V.22: (a): J-V characteristics of the PIN photodiode for $d = 10$ nm and different cell temperatures. (b): Power outputs of the PIN diode as a function of the applied voltage for several temperatures. For $T = 300$ K, the value of $P_{\max}$ is indicated in red.

10 nm may be difficult the achieve experimentally. Therefore, we report in Fig. V.23 the J-V (Fig. V.23(a)) and P-V (Fig. V.23(b)) characteristics of the PIN cell for $d = 200$ nm.

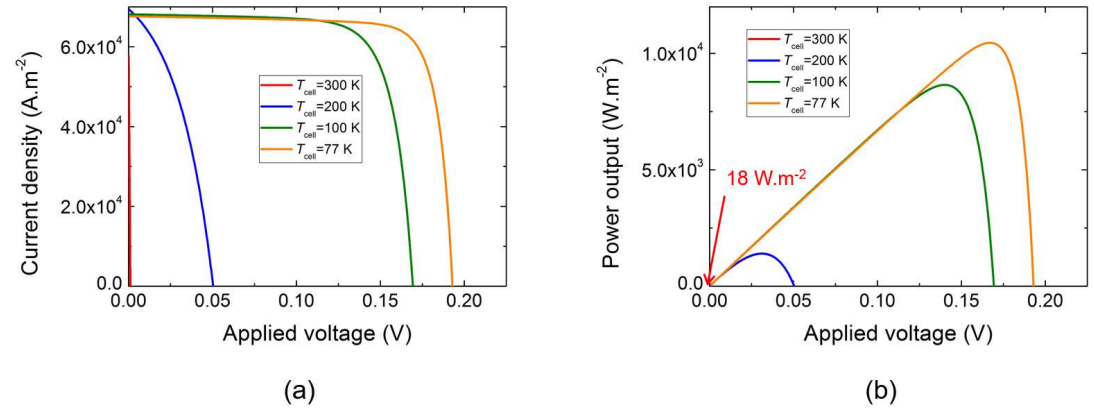

Figure V.23: (a): J-V characteristics of the PIN photodiode for $d = 200$ nm and different cell temperatures. (b): Power outputs of the PIN diode as a function of the applied voltage for several temperatures. For $T = 300$ K, the value of $P_{\max}$ is indicated in red.

The same behaviors as before are observed. The values of current and power output are lower than the previous case, due to the lower illumination induced by the larger distance between the radiator and the PV cell.

As a conclusion for this section, we have introduced an architecture of a NFR-TPV system for making the experimental demonstration of near-field radiation enhancement using a radiator at moderate temperature (800 K). The initial choice of an InSb PIN photodiode used for infrared photodetection has been presented. The preliminary results have shown that the PIN diode is

Cette thèse est accessible à l'adresse : http://theses.insa-lyon.fr/publication/2016LYSEI103/these.pdf
© [E. Blandre], [2016], INSA Lyon, tous droits réservés

efficient at low temperature (77 K), but in order to work at ambient temperature, its parameters have to be optimized. In particular, we have shown in the previous section that the doping levels of the different regions could enhance the performances of the NFR-TPV system.

V.6 Conclusions and prospects on the simulations of NFR-TPV devices

In this chapter, we have presented original numerical simulations of NFR-TPV systems. Our first objective has been to point out the impact of high-injection phenomena inside PV cells illuminated by a body in the near field. The development of a numerical model has allowed analyzing if high-injection phenomena could occur inside PV cells in the near field. Results have shown that high-injection phenomena can take place in the extreme near-field, depending on the doping level or the level of illumination of the PV cell. The impact of this phenomenon on the different approximations used to simplify the resolution of the Drift-Diffusion equations has then been analyzed. The final result has shown that the MCS model is not appropriate for calculating accurately the electrical performances of the PV cell when high-injection phenomena occur.
The second topic under consideration has been the optimization of the doping levels and the thicknesses of the doped region. We have demonstrated that with appropriate values of the doping levels and the region thicknesses, the maximum power output can be enhanced by about 30% compared to the configuration presented in [7].
Eventually, simulations of an InSb PIN photodiode designed initially for infrared photodetectors have been presented. We have highlighted that the parameters of the PIN junction have to be optimized in order to enhance the energy conversion performances of the system at ambient temperature.
In the future, several improvements of the modeling should be considered, in order to take into account different effects neglected until now. First, in our simulations, the cell temperature has not been allowed to vary. The impact of the different heat sources was studied previously in [4, 7]. The model used by the authors was in the meantime improved in [3]. The improved thermal model should be implemented in the future. The dependences on carrier concentrations and on temperature of several parameters are currently neglected because of a lack of data. For example, the dependence on temperature of the optical properties (dielectric functions) of the different materials is difficult to evaluate. As for the dependence on carrier concentration, bandgap narrowing effects due to large doping levels [120] are currently neglected. It affects optical properties of the semiconductor, by shifting the interband transition, and also the electrical properties, such as the intrinsic carrier concentration that depends on the bandgap of the semiconductor. Until now only doping-dependent mobilities were used. Carrier-carrier scattering effects could be accounted for by using mobility models that account for the carrier concentrations, but again, the lack of data for III-V semiconductors are limiting the advances in this topic.
Eventually, a proper calculation of the radiative recombination rate should be implemented. Until now, we used tabulated values of the bimolecular recombinations coefficients for GaSb and InSb. As mentioned in Chapter II, the calculation of this coefficient requires the calculation of the

Cette thèse est accessible à l'adresse : http://theses.insa-lyon.fr/publication/2016LYSEI103/these.pdf
© [E. Blandre], [2016], INSA Lyon, tous droits réservés

emission of the PV cell toward its environment.
There is room for improvements of the performances of the NFR-TPV systems: only basic configurations have been studied. Other PV cells, such as multijunctions and heterojunctions, could be explored in the future. Especially, the use of a semiconductor transparent in the infrared and dopable for the top region of the cell like CIGS solar cells are for Sun light, that would let the thermal radiation penetrate deeper into the cell to avoid surface recombination, could be a way to reach high efficiency NFR-TPV systems with radiators supporting surface polaritons. To conclude, this work paves a way to the conception of an experimental setup, that could demonstrate the efficiency of the concept of NFR-TPV energy converters.

Cette thèse est accessible à l'adresse : http://theses.insa-lyon.fr/publication/2016LYSEI103/these.pdf
© [E. Blandre], [2016], INSA Lyon, tous droits réservés

General conclusions

This manuscript has dealt with the tailoring of the thermal emission of few-layer structures using interference phenomena, and the dependence on temperature of the spectral and total hemispherical emissivities of these structures. The near-field thermal radiation between a semi-infinite emitter and a flat film as then been analyzed. In the last chapter, we have focused on high-injection phenomena in NFR-TPV systems. Optimizations of the doping levels and of the thicknesses of the doped regions have been performed in order to increase the performances of NFR-TPV systems. Eventually, a NFR-TPV system close to an experimental configuration using an InSb PV cell based on a PIN architecture has been proposed, and the first results of the performances of such systems have been presented. This conclusion section summarizes the main results presented in this thesis, and provides prospects for future works in this field.

We have first analyzed the interference phenomena inside few-layers structures. We have considered structures made of a refractory metal, molybdenum, and a transparent semiconductor, hafnium oxide. The addition of hafnium oxide layers induces the appearance of interference phenomena that allows enhancing the spectral hemispherical emissivity for selected wavelengths. We have provided a detailed analysis of interference phenomena occurring inside multiple layers. By means of the comprehension of these phenomena, the optimization of a selective radiator for a TPV system using a gallium antimonide cell has been performed. We have defined a criterion that maximizes the conversion of radiation power into electrical power, by maximizing the spectral hemispherical emissivity for photons with energy larger than the bandgap energy of GaSb, and minimizing the emission of the radiator for photons with energy lower than the bandgap. We have presented two figures of merit based on this criterion. The figure of merit defined over the whole frequency range under consideration reaches a rather high value, 0.82, for a molybdenum substrate. This emphasizes the large potential of molybdenum (and other refractory metals as well) for building selective radiator for TPV applications. The same figure of merit reaches a value of 86 when considering a trilayer structure deposited on a substrate for the optimal architecture. The second figure of merit, defined over the wavelength range below the wavelength corresponding to the bandgap of GaSb is only 0.19 for a single molybdenum substrate because of its rather low spectral hemispherical emissivity in this wavelength range. However, with the optimal architecture of the trilayer structure deposited on a substrate, this value is tripled (0.60). We have provided a methodology to design radiators for TPV systems that can be used as a guideline for future optimizations.
The impact of variations of the optical properties with temperature of the materials constituting an

Cette thèse est accessible à l'adresse : http://theses.insa-lyon.fr/publication/2016LYSEI103/these.pdf
© [E. Blandre], [2016], INSA Lyon, tous droits réservés

emitter on its thermal emission is often omitted in the literature. We have analyzed this phenomena by calculating the thermal emission of aluminum-silicon few-layer structures as a function of temperature. Comparison of the results obtained using dielectric function of aluminum with the temperature-dependent one that with have calculated shows significant differences. The relative difference between the two reaches 60% at 500 K. This emphasizes the fact that the calculation of the emission of thermal emitters should be performed using the dielectric function at the corresponding temperature. Even if the maximum temperature considered was 500 K, which is much lower than the operation temperature of a TPV radiator, this work highlight that variations with temperature of the optical properties of a materials constituting this emitter should be accounted for, especially in the case of metallic materials.
We have also investigated the total hemispherical emissivity of few-layer structures supporting interference phenomena. An enhancement of the total hemispherical emissivity of a trilayer on substrate structure by a factor 20 has been found for the optimal architecture. The results gathered in this section can be used for applications which require controlling the total radiative heat flux between two bodies, for example radiative rectification [67].
The performance of TPV systems using the optimized radiator designed in this chapter should be evaluated in the future using the coupled radiative, electrical and thermal model presented for example in [4]. The impact of heat sources due to thermalization of high-energy photons should be analyzed as well. According to [75], the optimal spectral hemispherical emissivity that maximizes the energy yield by TPV systems is a step function only when the temperature of the cell is not allowed to vary. The criterion used to optimize the emission spectrum of the radiator may thus be modified.

The next chapter has been dedicated to the analysis of near-field radiative heat transfer between a semi-infinite emitter and a flat film. The polariton resonances have been analyzed in the case of silicon carbide. We have shown that to conserve a large peak in the emission spectrum due to surface phonon-polaritons, the size of the thin film should be always larger than the size of the vacuum gap. The spatial distribution of the near-field radiative power has then been analyzed. Frustrated modes have a larger penetration depth than surface modes, and therefore are absorbed deeper in the film. However if the film is thin enough, the excitation of the surface waves at the rear of the film induces a raise of the absorption at this location. This phenomenon could be interesting in the case of heterojunction cells, where the p- and n-regions are made with different materials. If the surface wave at the interface between the two regions can be excited, the absorption would be increased inside the depletion region, leading to the generation of electron-hole pairs that would be collected right after being generated, thus mitigating the recombination processes.
Eventually, interference phenomena occurring in the near-to-far field transition regime have been under consideration. As they are propagating inside the film, frustrated modes can interfere. Therefore, as demonstrated in Chapter III, it is possible to spectrally tune the radiative heat transfer between the emitter and the film in the near-to-far field transition regime. Furthermore, frustrated waves are propagative inside the film, and therefore have a larger penetration depth than surface modes. This induces a mitigation of the surface recombination problems, that are

Cette thèse est accessible à l'adresse : http://theses.insa-lyon.fr/publication/2016LYSEI103/these.pdf
© [E. Blandre], [2016], INSA Lyon, tous droits réservés

currently the limiting factor for SPhP mediated NFR-TPV system. This emphasizes the fact that frustrated modes mediated NFR-TPV systems have a great potential [7].
The work in this section has brought a deeper understanding near-field thermal radiation between bodies, and has shed new light on the radiative behavior of NFR-TPV systems, that will allow analyzing and optimizing the radiative heat transfer between the radiator and the cell in NFR-TPV devices.

In the last chapter, we have focused on high-injection phenomena in NFR-TPV systems. After having recalled the charge transport model commonly used to evaluate the performances of NFR-TPV systems that assumes the low-injection approximation (MCS model), we have presented a model that accounts for high-injection phenomena (FDD model). By means of this model, we have assessed the validity of the low-injection approximation in the case of NFR-TPV systems. We have demonstrated that high-injection phenomena can occur in the extreme near field for low doping levels of the top region of the PV cell. In this case, the MCS model can not describe accurately the performances of the NFR-TPV system: a relative difference of 15% between the results obtained with the two models have been highlighted. This emphasizes that the validity of the low-injection approximations should be tested extensively in future works. One of the future goal will be to define a criterion on the level of illumination and the doping level that assesses if whether or not the low-injection approximation is valid.
Using the FDD model, we have then performed numerical optimizations of two parameters: the size and the doping level of the p and n-regions. The doping level of the top p-region is a crucial parameter for SPhP mediated NFR-TPV systems: decreasing the doping allows mitigating the impact of surface recombinations. We also have shown that the size of the PV device should be as small as possible to maximize its efficiency. In the extreme near field, an increase of the power density yield by 30% is possible with optimal parameters (i.e. for the smallest sizes of the p and n-regions, and a doping level of the p-region equal to 10^{17} cm^{-3}).
Finally, we have introduced a new kind of NFR-TPV system with a cell made of an InSb PIN junction, designed initially for infrared photodetectors. The simulations of the electrical behavior of PIN junctions have been possible with the development of the FDD model, because of the presence of the intrinsic region where high-injection phenomena are likely to occur. We have presented our very first results on the simulations of such NFR-TPV systems. We have demonstrated that the PIN cell is not efficient at ambient temperature, but rather at low temperature: a maximum power output of 88 $W.m^{-2}$ at ambient temperature, and of 24000 $W.m^{-2}$ at at 77 K have been found for a distance separating the radiator and the cell of 10 nm. This may be due to the spatial distribution of the electric field, supposed to extend inside the i-region in the case of PIN junctions, that is restricted near the interfaces between the different regions. Further optimizations using the results obtained in the previous sections should be performed in the future to design a high-efficiency prototype.

Numerous parameters impacting the performances of NFR-TPV systems are yet to analyze. For example, only one temperature of the radiator for each semiconductor constituting the PV cell has been considered. For GaSb, the temperature of the radiator (2000 K) may be difficult to reach

Cette thèse est accessible à l'adresse : http://theses.insa-lyon.fr/publication/2016LYSEI103/these.pdf
© [E. Blandre], [2016], INSA Lyon, tous droits réservés

experimentally. Evaluation of the performances of NFR-TPV systems with lower radiator temperature should be performed. The comparison between metallic and dielectric radiators should also be done. At a longer term, the contacts at the sides of the PV cell should be accounted for to get closer from experimental PV devices. Eventually, moving from 1D to 2D simulations would allow considering different geometries of the PV cells, and accounting for side effects.

All the results presented in this manuscript have shed new light on thermal radiation at nanoscale inside multilayers, and their application to thermophotovoltaic energy conversion, as well as the electrical behavior of PV cells under near-field illumination. This report provides new tools and understanding for the analysis of the performances of NFR-TPV systems. We believe this could lead to the first convincing experimental demonstration of the efficiency of the concept of NFR-TPV energy converters.

Cette thèse est accessible à l'adresse : http://theses.insa-lyon.fr/publication/2016LYSEI103/these.pdf
© [E. Blandre], [2016], INSA Lyon, tous droits réservés

Appendices

Cette thèse est accessible à l'adresse : http://theses.insa-lyon.fr/publication/2016LYSEI103/these.pdf
© [E. Blandre], [2016], INSA Lyon, tous droits réservés

Cette thèse est accessible à l'adresse : http://theses.insa-lyon.fr/publication/2016LYSEI103/these.pdf
© [E. Blandre], [2016], INSA Lyon, tous droits réservés

Appendices

A Determination of the amplitudes of the field: the scattering matrix method

A.1 From the T-matrix method to the S-matrix method [1, 2]

In this appendix, the S-matrix for the calculation of the Green's functions is presented.
To determine the Weyl components of the Green's tensor, the coefficients A, B, C and D must be determined for the two polarizations s and p in each layer. An efficient way to determine those coefficients is the transfer matrix method (T-matrix). The amplitudes of the fields in layer l at a location z just after the interface $l, l+1$ (denoted $z = z_l^+$) are linked with the amplitudes in layer $l+1$ at location $z = z_{l+1}^+$ with the transfer matrix $\bar{\bar{U}}_l$

$$\begin{bmatrix} A_l \\ B_l \end{bmatrix} = \begin{bmatrix} u_{l,11} & u_{l,12} \\ u_{l,21} & u_{l,22} \end{bmatrix} \begin{bmatrix} A_{l+1} \\ B_{l+1} \end{bmatrix} \tag{A.60}$$

$$\begin{bmatrix} C_l \\ D_l \end{bmatrix} = \begin{bmatrix} u_{l,11} & u_{l,12} \\ u_{l,21} & u_{l,22} \end{bmatrix} \begin{bmatrix} C_{l+1} \\ D_{l+1} \end{bmatrix} \tag{A.61}$$

where $u_{l,ij}$ are the components of the T-matrix $\bar{\bar{U}}_l$. The T-matrix in layer l can be expressed as the product of the transmission matrix $\bar{\bar{V}}_{l,l+1}$ at the interface $l, l+1$ and the propagation matrix $\bar{\bar{P}}_l$ in layer l (Fig. A.1)

$$\bar{\bar{V}}_{l,l+1} = \frac{1}{t_{l,l+1}} \begin{bmatrix} 1 & r_{l,l+1} \\ r_{l,l+1} & 1 \end{bmatrix} \tag{A.62}$$

$$\bar{\bar{P}}_l = \begin{bmatrix} e^{-ik_{z_l}(z_{l+1}-z_l)} & 0 \\ 0 & e^{ik_{z_l}(z_{l+1}-z_l)} \end{bmatrix} \tag{A.63}$$

$$\bar{\bar{U}}_l = \frac{1}{t_{l,l+1}} \begin{bmatrix} e^{-ik_{z_l}(z_{l+1}-z_l)} & r_{l,l+1}e^{-ik_{z_l}(z_{l+1}-z_l)} \\ r_{l,l+1}e^{ik_{z_l}(z_{l+1}-z_l)} & e^{ik_{z_l}(z_{l+1}-z_l)} \end{bmatrix} \tag{A.64}$$

where $r_{l,l+1}$ and $t_{l,l+1}$ are respectively the Fresnel reflection and transmission coefficients at the interface separating layers l and $l+1$. It is important to mention here that the s and p polarized field amplitudes are calculated by using respectively the s and p polarizations of the Fresnel

Cette thèse est accessible à l'adresse : http://theses.insa-lyon.fr/publication/2016LYSEI103/these.pdf
© [E. Blandre], [2016], INSA Lyon, tous droits réservés

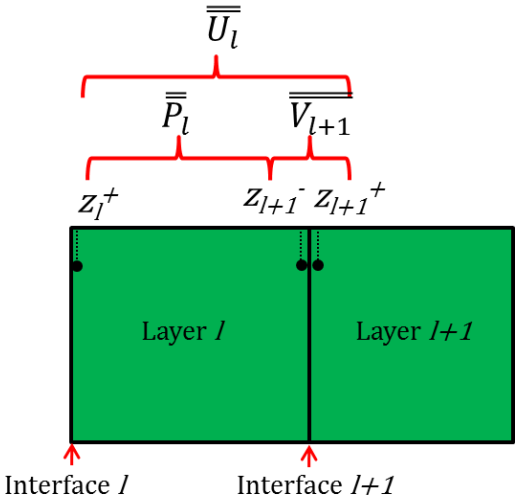

Figure A.1: Schematic representation of the T-matrix between a layer l and a layer $l+1$.

reflection and transmission coefficients.

The transmission matrix $\bar{\bar{V}}_{l,l+1}$ links the amplitude of the field just before and just after the interface $l, l+1$. The propagation matrix $\bar{\bar{P}}_l$ represents the wave propagation in layer l. The transfer matrix $\bar{\bar{U}}_l$ describes the fact that to propagate from a position z_l^+ in layer l to a position z_{l+1}^+ in layer $l+1$, a wave must propagate in the medium of layer l from z_l^+ to z_{l+1}^-, and then cross the interface $l, l+1$ from z_{l+1}^- to z_{l+1}^+ (as depicted in Fig. I.5). The relation between the amplitudes in layer 0 and layer L where the flux is calculated becomes

$$\begin{bmatrix} A_0 \\ B_0 \end{bmatrix} = \left(\prod_{l=0}^{L-2} \bar{\bar{V}}_{l,l+1} \bar{\bar{P}}_{l+1} \right) \bar{\bar{V}}_{L-1,L} \begin{bmatrix} A_L \\ B_L \end{bmatrix} \tag{A.65}$$

$$\begin{bmatrix} C_0 \\ D_0 \end{bmatrix} = \left(\prod_{l=0}^{L-2} \bar{\bar{V}}_{l,l+1} \bar{\bar{P}}_{l+1} \right) \bar{\bar{V}}_{L-1,L} \begin{bmatrix} C_L \\ D_L \end{bmatrix} \tag{A.66}$$

This relation shows that the calculation of the coefficients in layer 0 and layer L where the flux is calculated requires multiple products of the elements of the transfer matrix $\bar{\bar{U}}$, and therefore of the complex increasing and decreasing exponential terms $e^{\pm i k_{z_l}(z_{l+1}-z_l)}$, which can be very small or very large depending of the value of k_z, and of the thickness of the layer $z_{l+1}-z_l$. This leads to numerical difficulties when k_z is large (case of evanescent waves), and when the number of layers between layers s and l or when the film thicknesses are too large. This is why the T-matrix method is not appropriate for numerical calculations of near-field thermal radiation in one-dimensional layered media.

To solve the problem of numerical instabilities, we use a modified version of the T-matrix method, called scattering matrix method (S-matrix). This method was applied by Drevillon [1] and Francoeur [2] for the calculation of near-field thermal radiation in 1D-layered media. The S-matrix method consists in expressing the coefficient in layer l directly as a function of the coefficient in

Cette thèse est accessible à l'adresse : http://theses.insa-lyon.fr/publication/2016LYSEI103/these.pdf
© [E. Blandre], [2016], INSA Lyon, tous droits réservés

layer 0

$$\begin{bmatrix} A_l \\ B_0 \end{bmatrix} = \bar{\bar{S}}(0,l) \begin{bmatrix} A_0 \\ B_l \end{bmatrix} \tag{A.67}$$

The relations linking the S-matrix between 0 and l, $\bar{\bar{S}}(0,l)$, and between 0 and $l+1$, $\bar{\bar{S}}(0,l+1)$, need to be determined. The matrix relation between A_0, B_0, A_l and B_l can be written as the following system

$$\begin{cases} A_l = S_{11}(0,l)A_0 + S_{12}(0,l)B_l \\ B_0 = S_{21}(0,l)A_0 + S_{22}(0,l)B_l \end{cases} \tag{A.68}$$

The T-matrix relation between coefficients in layer l and $l+1$ (Eq. A.41) gives

$$\begin{cases} A_l = u_{l,11}A_{l+1} + u_{l,12}B_{l+1} \\ B_l = u_{l,21}A_{l+1} + u_{l,22}B_{l+1} \end{cases} \tag{A.69}$$

Substituting A_l and B_l from Eq. A.45 into Eq. A.46 gives a system that links the coefficients in layer l with the coefficients in layer $l+1$ and the elements of the S-matrix $\bar{\bar{S}}(0,l)$

$$\begin{cases} u_{l,11}A_{l+1} + u_{l,12}B_{l+1} = S_{11}(0,l)A_0 + S_{12}(0,l)(u_{l,21}A_{l+1} + u_{l,22}B_{l+1}) \\ B_0 = S_{21}(0,l)A_0 + S_{22}(0,l)(u_{l,21}A_{l+1} + u_{l,22}B_{l+1}) \end{cases} \tag{A.70}$$

$$\Leftrightarrow \begin{cases} u_{l,11}A_{l+1} - S_{12}(0,l)(u_{l,11}A_{l+1}) = S_{11}(0,l)A_0 + B_{l+1}(S_{12}(0,l)u_{l,22} - u_{l,21}) \\ B_0 - S_{22}(0,l)u_{l,21}A_{l+1} = S_{21}(0,l)A_0 + S_{22}(0,l)u_{l,22}B_{l+1} \end{cases} \tag{A.71}$$

Equation A.48 can be written as a matrix system

$$\begin{bmatrix} A_{l+1} \\ B_0 \end{bmatrix} \begin{bmatrix} u_{l,11} - S_{21}(0,l) & 0 \\ -S_{22}(0,l)u_{l,21} & 1 \end{bmatrix} = \begin{bmatrix} S_{11}(0,l) & S_{21}(0,l)u_{l,22} - u_{l,21} \\ S_{21}(0,l) & S_{22}(0,l) \end{bmatrix} \begin{bmatrix} A_0 \\ B_{l+1} \end{bmatrix} \tag{A.72}$$

$$\Leftrightarrow \begin{bmatrix} A_{l+1} \\ B_0 \end{bmatrix} = \begin{bmatrix} u_{l,11} - S_{21}(0,l) & 0 \\ -S_{22}(0,l)u_{l,21} & 1 \end{bmatrix}^{-1} \begin{bmatrix} S_{11}(0,l) & S_{21}(0,l)u_{l,22} - u_{l,21} \\ S_{21}(0,l) & S_{22}(0,l) \end{bmatrix} \begin{bmatrix} A_0 \\ B_{l+1} \end{bmatrix} \tag{A.73}$$

where the product of the two matrices

$$\begin{bmatrix} u_{l,11} - S_{21}(0,l) & 0 \\ -S_{22}(0,l)u_{l,21} & 1 \end{bmatrix}^{-1} \begin{bmatrix} S_{11}(0,l) & S_{21}(0,l)u_{l,22} - u_{l,21} \\ S_{21}(0,l) & S_{22}(0,l) \end{bmatrix} \tag{A.74}$$

can be identified as the scattering matrix between layer 0 and $l+1$.
The inversion of the first matrix is straightforward, and gives

$$\begin{bmatrix} u_{l,11} - S_{21}(0,l) & 0 \\ -S_{22}(0,l)u_{l,21} & 1 \end{bmatrix}^{-1} = \begin{bmatrix} (u_{l,11} - S_{12}(0,l)u_{l,21})^{-1} & 0 \\ S_{22}(0,l)u_{l,21}(u_{l,11} - S_{21}(0,l)u_{l,21})^{-1} & 1 \end{bmatrix} \tag{A.75}$$

Cette thèse est accessible à l'adresse : http://theses.insa-lyon.fr/publication/2016LYSEI103/these.pdf
© [E. Blandre], [2016], INSA Lyon, tous droits réservés

Multiplying the two matrices in Eq. A.51 gives the expression of the S-matrix between layer 0 and $l+1$ as a function of the elements of the S-matrix between 0 and l and the elements of the transfer matrix $\bar{\bar{U}}_l$

$$\bar{\bar{S}}(0,l+1)=\begin{bmatrix} S_{11}(0,l+1) & S_{12}(0,l+1) \\ S_{21}(0,l+1) & S_{22}(0,l+1) \end{bmatrix} \tag{A.76}$$

where:

$$S_{11}(0,l+1)=\frac{S_{11}(0,l)}{u_{l,11}-S_{21}(0,l)u_{l,11}} \tag{A.77}$$

$$S_{12}(0,l+1)=\frac{S_{21}(0,l)u_{l,22}-u_{l,21}}{u_{l,11}-S_{21}(0,l)u_{l,21}} \tag{A.78}$$

$$S_{21}(0,l+1)=\frac{S_{11}(0,l)S_{22}(0,l)u_{l,21}}{u_{l,11}-S_{21}(0,l)u_{l,21}}+S_{21}(0,l) \tag{A.79}$$

$$S_{22}(0,l+1)=\frac{(S_{21}(0,l)u_{l,22}-u_{l,21})(S_{22}(0,l)u_{l,21})}{u_{l,11}-S_{21}(0,l)u_{l,21}}+S_{22}(0,l)u_{l,22} \tag{A.80}$$

Substituting the elements of the transfer matrix $\bar{\bar{U}}_l$ given by Eq. A.41, the elements of the S-matrix between 0 and $l+1$, $\bar{\bar{S}}(0,l+1)$, become

$$S_{11}(0,l+1)=\frac{S_{11}(0,l)t_{l,l+1}e^{ik_{z_l}(z_{l+1}-z_l)}}{1-S_{12}(0,l)r_{l,l+1}e^{2ik_{z_l}(z_{l+1}-z_l)}} \tag{A.81}$$

$$S_{12}(0,l+1)=\frac{S_{12}(0,l)e^{2ik_{z_l}(z_{l+1}-z_l)}-r_{l,l+1}}{1-S_{12}(0,l)r_{l,l+1}e^{2ik_{z_l}(z_{l+1}-z_l)}} \tag{A.82}$$

$$S_{21}(0,l+1)=\frac{S_{11}(0,l)S_{22}r_{l,l+1}e^{ik_{z_l}(z_{l+1}-z_l)}}{t_{l,l+1}} \tag{A.83}$$

$$S_{22}(0,l+1)=\frac{S_{22}(0,l)[S_{22}r_{l,l+1}+1]e^{ik_{z_l}(z_{l+1}-z_l)}}{t_{l,l+1}} \tag{A.84}$$

where only $e^{ik_{z_l}(z_{l+1}-z_l)}$ terms appear, which demonstrates that the S-matrix algorithm is stable regardless of the values of k_ρ and $z_{l+1}-z_l$. Indeed, no product of factors in required.

The S-matrix can be initialized in any layer l using the relation

$$\begin{bmatrix} S_{11}(l,l) & S_{12}(l,l) \\ S_{21}(l,l) & S_{22}(l,l) \end{bmatrix}=\begin{bmatrix} 1 & 0 \\ 0 & 1 \end{bmatrix} \tag{A.85}$$

Cette thèse est accessible à l'adresse : http://theses.insa-lyon.fr/publication/2016LYSEI103/these.pdf
© [E. Blandre], [2016], INSA Lyon, tous droits réservés

A.2 Algorithm for the determination of the coefficients

The general case of an emitting layer of finite thickness is under consideration. Coefficients A, B, C and D must be determined. Given the fact that layers 0 and N are semi-infinite, there cannot be z-negative and z-positive traveling waves respectively in layers 0 and N. It results that coefficients A_0, C_0, B_N and C_N are equal to 0, regardless of the emitting layer. We start with coefficients A and B related to the field emitting in the z-positive direction.
For the coefficients between layer 0 and the emitting layer ss ($l \leq ss$), the S-matrix relation gives

$$\begin{bmatrix} A_{ss} \\ B_0 \end{bmatrix} = \bar{\bar{S}}(0,ss) \begin{bmatrix} A_0 \\ B_{ss} \end{bmatrix} \tag{A.86}$$

As $A_0 = 0$, this gives the following system:

$$\Leftrightarrow \begin{cases} A_{ss} = S_{12}(0,ss) B_{ss} \\ B_0 = S_{22}(0,ss) B_{ss} \end{cases} \tag{A.87}$$

Note that here, the S-matrix between 0 and l for $l \leq ss$ must be initialized in layer 0.

For the coefficients between the emitting layer ss and layer N ($l \geq ss$), the S-matrix relation must account for the source for the forward (z-positive) traveling waves. The S-matrix relation gives

$$\begin{bmatrix} A_N \\ B_{ss} \end{bmatrix} = \bar{\bar{S}}(ss,N) \begin{bmatrix} A_{ss} + S^+ \\ B_N \end{bmatrix} \tag{A.88}$$

where S^+ is the unit amplitude ($S^+ = 1$) of the field related to the forward traveling waves. As B_N is equal to zero, this gives the following system

$$\Leftrightarrow \begin{cases} A_N = S_{11}(ss,N)(A_{ss} + S^+) \\ B_{ss} = S_{21}(0,ss)(A_{ss} + S^+) \end{cases} \tag{A.89}$$

Note that here, the S-matrix between ss and l for $l \geq ss$ must be initialized in layer ss.

Substituting A_{ss} from Eq. A.64 into Eq. A.66, we are able to determine the expression of B_{ss}

$$B_{ss} = \frac{S_{21}(ss,N) S^+}{1 - S_{21}(ss,N) S_{21}(0,ss)} \tag{A.90}$$

and the expression of A_{ss} is given by

$$A_{ss} = \frac{S_{12}(0,ss) S_{21}(ss,N) S^+}{1 - S_{21}(ss,N) S_{21}(0,ss)} \tag{A.91}$$

The relation that gives the expression of coefficients A_l and B_l in layer l can now be determined.

Cette thèse est accessible à l'adresse : http://theses.insa-lyon.fr/publication/2016LYSEI103/these.pdf
© [E. Blandre], [2016], INSA Lyon, tous droits réservés

For the layers located before the emitting layer ($l \leq ss$), the S-matrix relation gives

$$\begin{pmatrix} A_l \\ B_0 \end{pmatrix} = \bar{\bar{S}}(0,l) \begin{pmatrix} A_0 \\ B_l \end{pmatrix} \tag{A.92}$$

providing the following system

$$\begin{cases} B_l = \dfrac{B_0}{S_{22}(0,l)} \\ A_l = S_{22}(0,l) B_l \end{cases} \tag{A.93}$$

where $B_0 = S_{22}(0,ss)B_{ss}$. For layers located after the emitting layer ss ($l \geq ss$), the S-matrix relation gives

$$\begin{pmatrix} A_l \\ B_{ss} \end{pmatrix} = \bar{\bar{S}}(0,l) \begin{pmatrix} A_{ss} + S^+ \\ B_l \end{pmatrix} \tag{A.94}$$

leading to the following system

$$\begin{cases} B_l = \dfrac{B_{ss} - S_{21}(ss,l)(A_{ss} + S^+)}{S_{22}(ss,l)} \\ A_l = S_{11}(ss,l)(A_{ss} + S^+) + S_{12}(ss,l) B_l \end{cases} \tag{A.95}$$

Using this algorithm, coefficients A and B can now be determined in each layer l. For coefficients C and D related to the field emitted in the backward (z-negative) direction, the process is similar. For layers located between layer 0 and layer ss ($l \leq ss$), the S-matrix relation must account for the source related to the backward traveling waves

$$\begin{bmatrix} C_{ss} \\ D_0 \end{bmatrix} = \bar{\bar{S}}(0,ss) \begin{bmatrix} C_0 \\ D_{ss} + S^- \end{bmatrix} \tag{A.96}$$

where S^- is the unit amplitude ($S^- = 1$) of the field related to the backward traveling waves. As C_0 is equal to zero, this provides the following system

$$\Leftrightarrow \begin{cases} C_{ss} = S_{12}(0,ss)(D_{ss} + S^-) \\ D_0 = S_{21}(0,ss)(D_{ss} + S^-) \end{cases} \tag{A.97}$$

For the layers located after the emitting layer ($l \geq ss$), the S-matrix relation can be written as

$$\begin{pmatrix} C_N \\ D_{ss} \end{pmatrix} = \bar{\bar{S}}(s,l) \begin{pmatrix} C_{ss} \\ D_N \end{pmatrix} \tag{A.98}$$

Cette thèse est accessible à l'adresse : http://theses.insa-lyon.fr/publication/2016LYSEI103/these.pdf
© [E. Blandre], [2016], INSA Lyon, tous droits réservés

so that it reduces the following system

$$\begin{cases} C_N = S_{11}(s,N)C_{ss} \\ D_{ss} = S_{22}(0,ss)C_{ss} \end{cases} \tag{A.99}$$

Substituting D_{ss} from Eq. A.74 into Eq. A.76, we are able to determine the expression of C_{ss}

$$C_{ss} = \frac{S_{21}(0,ss)S^-}{1-S_{12}(0,ss)S_{21}(ss,N)} \tag{A.100}$$

and the expression of D_{ss} is given by

$$D_{ss} = \frac{S_{22}(0,ss)S_{21}S^-}{1-S_{12}(0,ss)S_{21}(ss,N)} \tag{A.101}$$

The relation that gives the expressions of coefficient C_l and D_l in layer l can now be determined. For the layers located before the emitting layer ($l \leq ss$), the S-matrix relation brings

$$\begin{pmatrix} C_l \\ D_0 \end{pmatrix} = \bar{\bar{S}}(0,l)\begin{pmatrix} C_0 \\ D_l \end{pmatrix} \tag{A.102}$$

leading to the following system

$$\begin{cases} C_l = S_{12}(0,l)D_l \\ D_l = \dfrac{D_0}{S_{22}(0,l)} \end{cases} \tag{A.103}$$

where $D_0 = S_{22}(0,ss)(D_{ss} + S^-)$. For the layers located after the emitting layer ss ($l \geq ss$), the S-matrix relation reads

$$\begin{pmatrix} C_l \\ D_{ss} \end{pmatrix} = \bar{\bar{S}}(ss,l)\begin{pmatrix} A_{ss} \\ B_l \end{pmatrix} \tag{A.104}$$

providing the following system

$$\begin{cases} C_l = S_{11}(ss,l)C_{ss} + S_{12}(ss,l)D_l \\ D_l = \dfrac{D_{ss} - S_{21}(ss,l)C_{ss}}{S_{22}(s,l)}. \end{cases} \tag{A.105}$$

Using this algorithm, coefficients C and D can now be determined in each layer l. The problem is simplified for the case of an emitting half space. Since the emitting layer is semi-infinite, the amplitude of the waves emitted in the backward direction is 0, implying that $C_l = D_l = 0$. The S-matrix relation between layer 0 and N writes:

$$\begin{pmatrix} A_N \\ B_0 \end{pmatrix} = \bar{\bar{S}}(ss,l)\begin{pmatrix} A_0 + S^+ \\ B_N \end{pmatrix} \tag{A.106}$$

Cette thèse est accessible à l'adresse : http://theses.insa-lyon.fr/publication/2016LYSEI103/these.pdf
© [E. Blandre], [2016], INSA Lyon, tous droits réservés

As $A_0 = B_N = 0$, it provides the following system

$$\begin{cases} A_N = S_{11}(0,N) \\ B_0 = S_{21}(0,N) \end{cases} \tag{A.107}$$

The S-matrix relation between layer 0 and l gives

$$\begin{pmatrix} A_l \\ B_0 \end{pmatrix} = \bar{\bar{S}}(0,l) \begin{pmatrix} A_0 \\ B_l \end{pmatrix} \tag{A.108}$$

Finally the expression of A_l and B_l in each layer l can be determined

$$\begin{cases} A_l = S_{11}(0,l) + S_{12}(0,l)B_l \\ B_l = \dfrac{B_0 - S_{21}(0,l)}{S_{22}(0,l)} \end{cases} \tag{A.109}$$

With the values of coefficients A, B, C and D, the Weyl components of the Green's tensors can now be determined, and the radiative heat flux can be calculated.

Cette thèse est accessible à l'adresse : http://theses.insa-lyon.fr/publication/2016LYSEI103/these.pdf
© [E. Blandre], [2016], INSA Lyon, tous droits réservés

B Validation of the full Drift-Diffusion resolution model

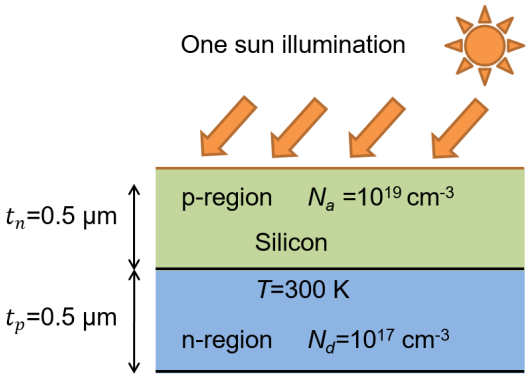

Figure B.1: Schematic representation of the test case used for the validation.

To validate the numerical model that solves the full Drift-Diffusion equations, we used the well-known PC-1D software [121] that is usually used to solve charge transport problems in solar cells. We compared the results obtained with PC-1D and our simulation code on a test case (Fig. B.1).

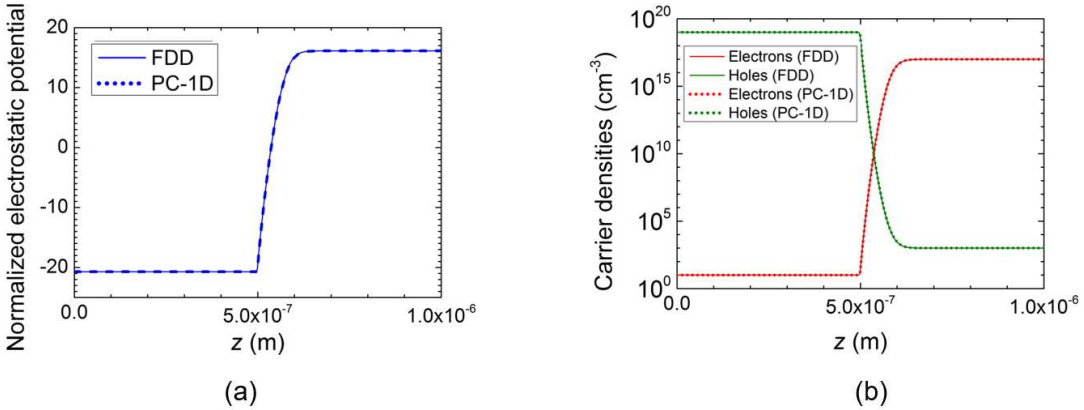

Figure B.2: (a): Spatial distribution of the normalized electrostatic potential. (b): Spatial distribution of the electron and hole densities. $V_f = 0$ V, no illumination.

We considered a silicon pn-junction, where the thicknesses of the p and n-regions are both equal to 0.5 µm. The doping level of the p-region is $N_a = 10^{19}$ cm^{-3} and the doping level of the n-region is $N_d = 10^{17}$ cm^{-3}. The electrical parameters of silicon have been extracted from PC-1D and implemented in our simulation code. We considered a one sun illumination. The spatial distribution of the generation rate was calculated with PC-1D and imported in our simulation code. The calculated spatial distribution of the carrier densities (n and p), and of the normalized electrostatic potential ($\bar{V}$) are depicted in the following figures: at equilibrium (no applied voltage and illumination) in Fig. B.2, with applied voltage and no illumination in Fig. B.3, and with

Cette thèse est accessible à l'adresse : http://theses.insa-lyon.fr/publication/2016LYSEI103/these.pdf
© [E. Blandre], [2016], INSA Lyon, tous droits réservés

illumination and applied voltage in Fig. B.4.

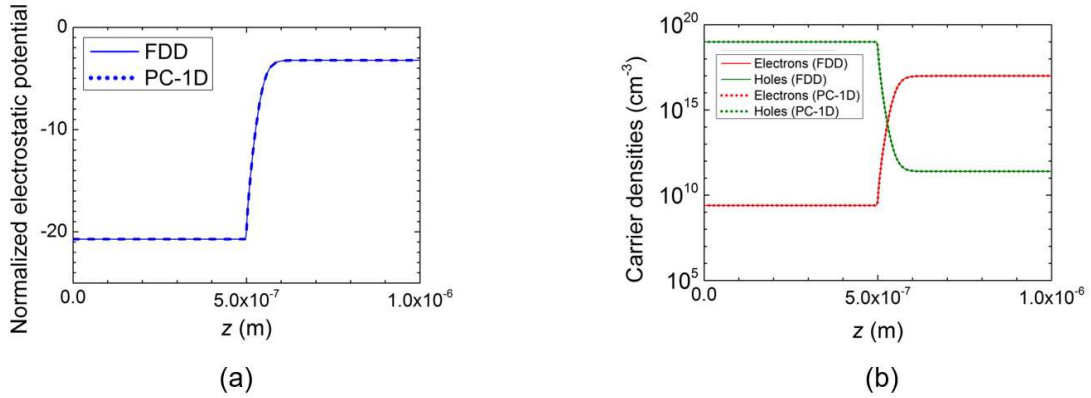

Figure B.3: (a): Spatial distribution of the normalized electrostatic potential. (b): Spatial distribution of the electron and hole densities. $V_f = 0.5$ V, no illumination.

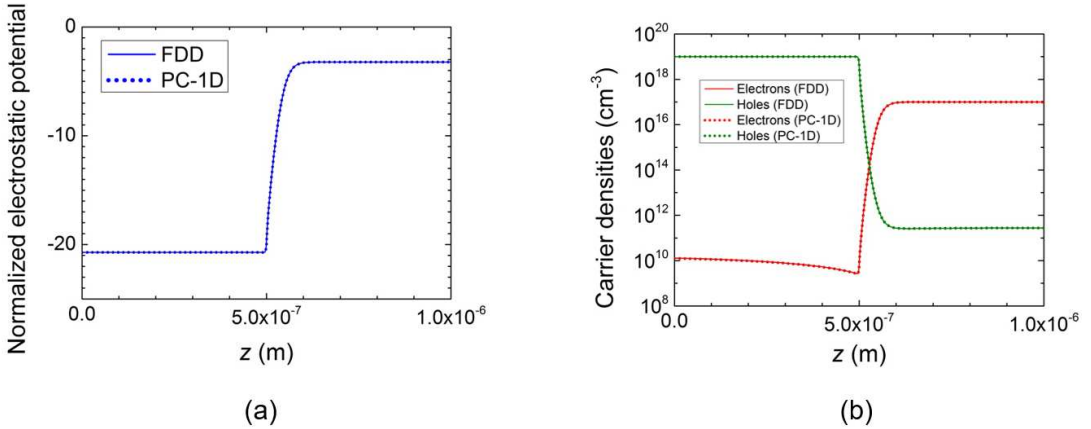

Figure B.4: (a): Spatial distribution of the normalized electrostatic potential. (b): Spatial distribution of the electron and hole densities. $V_f = 0.3$ V, one sun illumination.

The J-V characteristics of the cell obtained with the two simulation tools are compared in Fig. B.5. The slight difference between the two J-V characteristics represents a relative error of only 2%, and the relative difference on the maximum power output is less than 1%.

Cette thèse est accessible à l'adresse : http://theses.insa-lyon.fr/publication/2016LYSEI103/these.pdf
© [E. Blandre], [2016], INSA Lyon, tous droits réservés

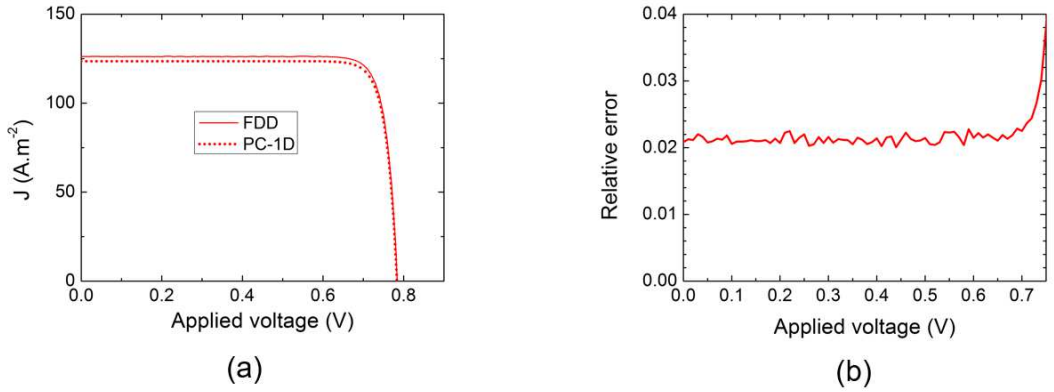

Figure B.5: (a): J-V characteristics of the PV cell. (b): Relative error between the currents obtained with the FDD model and PC-1D as a function of the applied voltage.

C Physical properties of GaSb and InSb

In this section, the physical properties of InSb and GaSb used for the calculations performed in Chapter V are detailed.

C.1 Dielectric function

For $E < E_g$, the absorption is dominated by the absorption of the lattice and free carriers while for $E > E_g$, it is the interband process that dominates the absorption. The interband absorption coefficient is calculated with the model proposed in [122]. The lattice and free carriers absorption is calculated using a Lorentz-Drude model, and the parameters for GaSb can be found in [123], and in [124] for InSb. It is worth noticing that the dielectric functions of GaSb and InSb depend on the bandgap E_g.

C.2 Dependence on temperature of the bandgap

The temperature dependent bandgap energy for InSb and GaSb are calculated using Varshni's equation [125]. The parameters for InSb and GaSb are taken from [126].

C.3 Mobility of electrons and holes

The doping and temperature-dependent mobility of the electrons and holes is calculated with the Caughey-Thomas model [127]. The parameters for InSb and GaSb are provided in [126]. It is important to note that in [126], the parameters related to the temperature dependence for InSb are not provided. Therefore, we did not account for the variations with temperature of the mobility of InSb.

Cette thèse est accessible à l'adresse : http://theses.insa-lyon.fr/publication/2016LYSEI103/these.pdf
© [E. Blandre], [2016], INSA Lyon, tous droits réservés

C.4 Recombination coefficients

The SRH recombination parameters $\tau_{n,p}^{\mathrm{SRH}}$ are calculated using the model provided in [126]. The bimolecular recombination coefficients B are taken from [127]. Auger coefficients C_n and C_p are given in [128]. As for the surface recombination velocities S_n and S_p, their value is difficult to evaluate, because it depends on the surface treatment of the PV cell. For the purpose of simulations, we chose to set S_n and S_p at 5.10^3 m.s^{-1}.

Cette thèse est accessible à l'adresse : http://theses.insa-lyon.fr/publication/2016LYSEI103/these.pdf
© [E. Blandre], [2016], INSA Lyon, tous droits réservés

D Numerical details

D.1 Radiative heat transfer calculations

Integrations over the frequencies or the wavelengths are performed using the trapezoidal integration algorithm. The frequency mesh is uniform, and 1000 frequencies are considered in each calculations to obtain well defined spectra and avoid numerical error on the integrations, especially in the case of materials supporting SPhPs that induce a large peak of emission in the spectrum of the energy exchanged. Integrations over the parallel wavevectors k_ρ are performed using the Simpson method. Indeed, near the light line ($k_\rho \approx \frac{\omega}{c_v}$), the values of the radiative heat flux can be highly oscillatory.
To compute the spatial distribution of absorption, the absorbing medium is divided into control volumes. The incident heat flux at node j, which is required to compute the generation rate of electron hole pairs is calculated as [4]

$$q^j_{\text{inc}} = \frac{q^j_{\text{abs}}}{\Delta z^j \kappa^j}, \tag{D.1}$$

where κ is the absorption coefficient, Δz is the distance between two nodes, and q_{abs} is the radiative power absorbed by a control volume (see Chapter 2).

D.2 Charge transport calculations

The resolution of the linear differential equations are performed using the TDMA approach [116]. The system is discretized into control volumes. We considered a uniform mesh for both the MCS and FDD models. However in the future, an exponential mesh should be implemented in the FDD model to reduce the number of nodes required to ensure numerical stability because of the strong exponential decay of the generation rate when the depth inside the PV cell increases. The derivative are approximated with a central differencing scheme.

The generation rate at node j is written as

$$G^j = \frac{\kappa^{\text{IB}^j}}{\hbar\omega}\left(\frac{q^j_{\text{abs}}}{\Delta z^j \kappa^j}\right), \tag{D.2}$$

where the terms in bracket correspond to the incident heat flux on a control volume. For the MCS model, the radiative heat transfer grid corresponds to the electrical grid. 1200 nodes are considered. However for the FDD model, the number of nodes required to obtain accurate results has to be much larger. To ensure numerical stability, we considered 25000 nodes in all our calculations. In terms of calculation time, computing the near-field radiative heat flux for 25000 nodes would require a large computation time. This is why we considered a less refined grid for the radiative heat transfer calculations. The spatial distribution of the generation rate is then interpolated on the electric grid.

Cette thèse est accessible à l'adresse : http://theses.insa-lyon.fr/publication/2016LYSEI103/these.pdf
© [E. Blandre], [2016], INSA Lyon, tous droits réservés

The solution of the charge transport model using Gummel's iteration procedure is much larger than when using the MCS model. However, it still represents only a few minutes. Radiative heat transfer calculation are much longer, especially in the near field. In the end, the two coupled NFR-TPV model have almost the same computation times.

Cette thèse est accessible à l'adresse : http://theses.insa-lyon.fr/publication/2016LYSEI103/these.pdf
© [E. Blandre], [2016], INSA Lyon, tous droits réservés

Bibliography

[1] J. Drevillon. *Design ab-initio de matériaux micro et nanostructurés pour l'émission thermique cohérente en champ proche et en champ lointain*. Theses, Université de Nantes, December 2007.

[2] M. Francoeur, M.P. Mengüç, and R. Vaillon. Solution of near-field thermal radiation in one-dimensional layered media using dyadic green's functions and the scattering matrix method. *J. Quant. Spectrosc. Radiat. Transfer*, 110(18):2002 – 2018, 2009.

[3] Olivier Dupré. *Physics of the thermal behavior of photovoltaic devices*. PhD thesis, Institut National des Sciences Appliquées de Lyon, 2015.

[4] M. Francoeur, R. Vaillon, and M.P. Mengüç. Thermal impacts on the performance of nanoscale-gap thermophotovoltaic power generators. *IEEE Trans. Ener. Conv.*, 26(2):686–698, June 2011.

[5] E. Blandre, P.O. Chapuis, and R. Vaillon. Spectral and total temperature-dependent emissivities of few-layer structures on a metallic substrate. *Opt. Express*, 24(2):A374–A387, Jan 2016.

[6] E. Blandre, P.O. Chapuis, M. Francoeur, and R. Vaillon. Spatial and spectral distributions of thermal radiation emitted by a semi-infinite body and absorbed by a flat film. *AIP Adv.*, 5(5), 2015.

[7] M P. Bernardi, O. Dupré, E. Blandre, P.O. Chapuis, R. Vaillon, and M. Francoeur. Impacts of propagating, frustrated and surface modes on radiative, electrical and thermal losses in nanoscale-gap thermophotovoltaic power generators. *Sci. Rep.*, 5(11626), 2015.

[8] M. P. Bernardi, O. Dupré, R. Vaillon, and M. Francoeur. Surface polariton mediated thermophotovoltaic power generation. *arXiv e-prints*, 2013.

[9] Lawrence Livermore National Laboratory. 2014 energy flow chart. 2015.

[10] Z.G. Chen, G. Han, L. Yang, L. Cheng, and J. Zou. Nanostructured thermoelectric materials: Current research and future challenge. *Prog. Nat. Sci: Mat.*, 22(6):535 – 549, 2012.

[11] S.C. Baker-Finch, K.R. McIntosh, and M.L. Terry. Isotextured silicon solar cell analysis and modeling 1: Optics. *IEEE J. Photovolt*, 2(4):457 – 464, 2012.

Cette thèse est accessible à l'adresse : http://theses.insa-lyon.fr/publication/2016LYSEI103/these.pdf
© [E. Blandre], [2016], INSA Lyon, tous droits réservés

[12] Z. Zhou, E. Sakr, Y. Sun, and P. Bermel. Solar thermophotovoltaics: reshaping the solar spectrum. *Nanophotonics*, 5(1):1–21, 2016.

[13] N.P. Harder and P. Würfel. Theoretical limits of thermophotovoltaic solar energy conversion. *Semicond. Sci. Technol.*, 18(5):S151, 2003.

[14] W. Shockley and H. J. Queisser. Detailed balance limit of efficiency of p-n junction solar cells. *J. Appl. Phys.*, 32(3):510–519, 1961.

[15] 2008 IEC. *Photovoltaic Devices—Part 3: Measurement Principles for Terrestrial Photovoltaic (PV) Solar Devices With Reference Spectral Irradiance Data. In Int. Stand., IEC 60904–3*. 2008.

[16] C. Ungaro, S.K. Gray, and M.C. Gupta. Solar thermophotovoltaic system using nanostructures. *Opt. Express*, 23(19):A1149–A1156, Sep 2015.

[17] D. Polder and M. Van Hove. Theory of radiative heat transfer between closely spaced bodies. *Phys. Rev. B*, 4:3303–3314, Nov 1971.

[18] J.-P. Mulet. *Modélisation du rayonnement thermique par une approche électromagnétique. Rôle des ondes de surface dans le transfert d'énergie aux courtes échelles et dans les forces de Casimir*. These, Université Paris Sud - Paris XI, March 2003.

[19] M. D. Whale and E. G. Cravalho. Modeling and performance of microscale thermophotovoltaic energy conversion devices. *IEEE Trans. Energy Convers.*, 17:130–142, 2002.

[20] R. S. DiMatteo, P. Greiff, S. L. Finberg, K. A. Young-Waithe, H. K. H. Choy, M. M. Masaki, and C. G. Fonstad. Enhanced photogeneration of carriers in a semiconductor via coupling across a nonisothermal nanoscale vacuum gap. *Appl. Phys. Lett.*, 79(12):1894–1896, 2001.

[21] K. Hanamura and Mori. K. Nano-gap tpv generation of electricity though evanescent wave in near-field above emitter surface. *Proceedings of the 7 th Conference on Thermophotovoltaic Generation of Electricity.*, 2007.

[22] E. Hecht. *Optics 2nd edition*. Addison-Wesley, 1987.

[23] K. Joulain, J-P. Mulet, F. Marquier, R. Carminati, and J-J. Greffet. Surface electromagnetic waves thermally excited: Radiative heat transfer, coherence properties and casimir forces revisited in the near field. *Surf. Sci. Rep.*, 57(3–4):59 – 112, 2005.

[24] M. Francoeur, M.P. Mengüç, and R. Vaillon. Spectral tuning of near-field radiative heat flux between two thin silicon carbide films. *J. Phys. D: Appl. Phys*, 43(7):075501, 2010.

[25] T.J. Bright, L.P. Wang, and Z.M. Zhang. Performance of near-field thermophotovoltaic cells enhanced with a backside reflector. *J. Heat Transfer*, 6(136):062701, 2014.

[26] Y. Tsurimaki, P.O. Chapuis, J. Okajima, A. Komiya, S. Maruyama, and R. Vaillon. Coherent regime and far-to-near-field transition for radiative heat transfer. *J. Quant. Spectrosc. Radiat. Transfer*, 2016. Accepted for publication.

Cette thèse est accessible à l'adresse : http://theses.insa-lyon.fr/publication/2016LYSEI103/these.pdf
© [E. Blandre], [2016], INSA Lyon, tous droits réservés

[27] K. Park, S. Basu, W.P. King, and Z.M. Zhang. Performance analysis of near-field thermophotovoltaic devices considering absorption distribution. *J. Quant. Spectrosc. Radiat. Transfer*, 109(2):305 – 316, 2008. The Fifth International Symposium on Radiative Transfer.

[28] L. Mikyung, J. Seokmin, Seung S. L., and Bong J. L. Graphene-assisted si-insb thermophotovoltaic system for low temperature applications. *Opt. Express*, 23(7):A240–A253, Apr 2015.

[29] J.R. Howell, M.P. Menguc, and R. Siegel. *Thermal Radiation Heat Transfer* 5^{th} *edition*. CRC Press, 2011.

[30] A. Kittel, W. Müller-Hirsch, J. Parisi, S.-A. Biehs, D. Reddig, and M. Holthaus. Near-field heat transfer in a scanning thermal microscope. *Phys. Rev. Lett.*, 95:224301, 2005.

[31] S.M. Rytov, I.U.A. Kravtsov, and V.I. Tatarskii. *Principles of Statistical Radiophysics: Elements of random fields*. Principles of Statistical Radiophysics. Springer-Verlag, 1989.

[32] M. Francoeur and M.P. Mengüç. Role of fluctuational electrodynamics in near-field radiative heat transfer. *J. Quant. Spectrosc. Radiat. Transfer*, 109(2):280 – 293, 2008.

[33] J. E. Sipe. New green-function formalism for surface optics. *J. Opt. Soc. Am. B*, 4(4):481–489, Apr 1987.

[34] B. Streetman and S. Banerjee. *Solid State Electronic Devices* 6^{th} *edition*. Pearson Prentice Hall, 2006.

[35] E. Rosencher and B. Vinter. *Optoélectronique* $2^{ème}$ *édition*. Dunod, 2002.

[36] P. Würfel. *Physics of Solar Cells: From Basic Principles to Advanced Concepts* 2^{nd} *edition*. Wiley, 2009.

[37] M. Green. *Solar Cells : Operating Principles, Technology and System Applications*. University of New South Wales, 1986.

[38] T. Trupke, M. A. Green, P. Würfel, P. P. Altermatt, A. Wang, J. Zhao, and R. Corkish. Temperature dependence of the radiative recombination coefficient of intrinsic crystalline silicon. *J. Appl. Phys*, 94(8):4930–4937, 2003.

[39] H. T. Nguyen, S. C. Baker-Finch, and D. Macdonald. Temperature dependence of the radiative recombination coefficient in crystalline silicon from spectral photoluminescence. *Appl. Phys. Lett.*, 104(11), 2014.

[40] H. T. Nguyen, F. E. Rougieux, B. Mitchell, and D. Macdonald. Temperature dependence of the band-band absorption coefficient in crystalline silicon from photoluminescence. *J. Appl. Phys*, 115(4), 2014.

[41] D. Vasileska, S.M. Goodnick, and G. Klimeck. *Computational Electronics : Semiclassical and Quantum Device Modeling and Simulation*. CRC Press, 2016.

Cette thèse est accessible à l'adresse : http://theses.insa-lyon.fr/publication/2016LYSEI103/these.pdf
© [E. Blandre], [2016], INSA Lyon, tous droits réservés

[42] R.M. Swanson. A proposed thermophotovoltaic solar energy conversion system. *Proc. IEEE*, 67:446–447, 1979.

[43] P. Würfel and W. Ruppel. Upper limit of thermophotovoltaic solar-energy conversion. *IEEE. T. Electron. Dev.*, 27:745–750, 1980.

[44] H. Höfler, H.J. Paul, W. Ruppel, and P. Würfel. Interference filters for thermophotovoltaic solar energy conversion. *Sol. Cells*, 10(3):273 – 286, 1983.

[45] W. Spirkl and H. Ries. Solar thermophotovoltaics: An assessment. *J. Appl. Phys.*, 57(9):4409–4414, 1985.

[46] A. Lenert, D.M. Bierman, Y. Nam, W.R. Chan, I Celanovic, M. Soljacic, and E.N. Wang. A nanophotonic solar thermophotovoltaic device. *Nature Nanotech.*, 1:1 – 5, 2014.

[47] Q.Z. Zhang. High efficiency al-n cermet solar coatings with double cermet layer film structures. *J. Phys. D: Appl. Phys.*, 32(15):1938, 1999.

[48] N.P. Sergeant, O. Pincon, M. Agrawal, and P. Peumans. Design of wide-angle solar-selective absorbers using aperiodic metal-dielectric stacks. *Opt. Express*, 17(25):22800–22812, Dec 2009.

[49] G.E. Guazzoni. High-temperature spectral emittance of oxides of erbium, samarium, neodymium and ytterbium. *Appl. Spectrosc.*, 26(1):60–65, Jan 1972.

[50] D.L. Chubb, A.T. Pal, M.O. Patton, and P.P. Jenkins. Rare earth doped high temperature ceramic selective emitters. *J. Eur. Ceram. Soc.*, 19(13–14):2551 – 2562, 1999.

[51] B. Bitnar, W. Durisch, J.C. Mayor, H. Sigg, and H.R. Tschudi. Characterisation of rare earth selective emitters for thermophotovoltaic applications. *Sol. Energ. Mat. Sol. Cells*, 73(3):221 – 234, 2002.

[52] Z. Zhou, Q. Chen, and P. Bermel. Prospects for high-performance thermophotovoltaic conversion efficiencies exceeding the shockley–queisser limit. *Energ. Convers. Manage.*, 97:63 – 69, 2015.

[53] E. Nefzaoui, J. Drevillon, and K. Joulain. Selective emitters design and optimization for thermophotovoltaic applications. *Journal of Applied Physics*, 111(8), 2012.

[54] J. Drevillon, K. Joulain, P. Ben-Abdallah, and E. Nefzaoui. Far field coherent thermal emission from a bilayer structure. *J. Appl. Phys.*, 109(3), 2011.

[55] D. Chester, P. Bermel, J.D. Joannopoulos, M. Soljacic, and I. Celanovic. Design and global optimization of high-efficiency solar thermal systems with tungsten cermets. *Opt. Express*, 19(S3):A245–A257, May 2011.

[56] C. Arnold, F. Marquier, M. Garin, F. Pardo, S. Collin, N. Bardou, J.L. Pelouard, and J.J. Greffet. Coherent thermal infrared emission by two-dimensional silicon carbide gratings. *Phys. Rev. B*, 86:035316, Jul 2012.

Cette thèse est accessible à l'adresse : http://theses.insa-lyon.fr/publication/2016LYSEI103/these.pdf
© [E. Blandre], [2016], INSA Lyon, tous droits réservés

[57] J.G. Fleming, S.Y. Lin, I. El Kady, and K.M. Ho. All-metallic three-dimensional photonic crystals with a large infrared bandgap. *Nature*, 417:52–55, 2002.

[58] L.P. Wang, B.J. Lee, X.J. Wang, and Z.M. Zhang. Spatial and temporal coherence of thermal radiation in asymmetric Fabry-Pérot resonance cavities. *Int. J. Heat Mass Transfer*, 52(13–14):3024 – 3031, 2009.

[59] B.J. Lee and Z.M. Zhang. Design and fabrication of planar multilayer structures with coherent thermal emission characteristics. *Journal of Applied Physics*, 100(6):–, 2006.

[60] L.P. Wang, S. Basu, and Z.M. Zhang. Direct measurement of thermal emission from a fabry–perot cavity resonator. *J. Heat Transfer*, 134, 2012.

[61] I. Celanovic, D. Perreault, and J. Kassakian. Resonant-cavity enhanced thermal emission. *Phys. Rev. B*, 72:075127, Aug. 2005.

[62] P. Hanzelka, T. Kralik, A. Maskova, V. Musilova, and J. Vyskocil. Thermal radiative properties of a DLC coating. *Cryogenics*, 48(9-10):455 – 457, 2008.

[63] V. Musilova, T. Kralik, P. Hanzelka, and A. Srnka. Effect of different treatments of copper surface on its total hemispherical absorptivity below 77 k. *Cryogenics*, 47(4):257 – 261, 2007.

[64] V. Musilova, P. Hanzelka, T. Kralik, and A. Srnka. Low temperature radiative properties of materials used in cryogenics. *Cryogenics*, 45(8):529 – 536, 2005.

[65] M. Shimizu, A. Kohiyama, and H. Yugami. High-efficiency solar-thermophotovoltaic system equipped with a monolithic planar selective absorber/emitter. *J. Photon Ener.*, 5(1):053099, 2015.

[66] A. Kohiyama, M. Shimizu, H. Kobayashi, F. Iguchi, and H. Yugami. Spectrally controlled thermal radiation based on surface microstructures for high-efficiency solar thermophotovoltaic system. *Energy Procedia*, 57:517 – 523, 2014.

[67] E. Nefzaoui, J. Drevillon, Y. Ezzahri, and K. Joulain. Simple far-field radiative thermal rectifier using Fabry-Pérot cavities based infrared selective emitters. *Appl. Opt.*, 53(16):3479–3485, Jun. 2014.

[68] M. A. Kats, D. Sharma, J. Lin, P. Genevet, R. Blanchard, Z. Yang, M. M. Qazilbash, D. N. Basov, S. Ramanathan, and F. Capasso. Ultra-thin perfect absorber employing a tunable phase change material. *Appl. Phys. Lett.*, 101(22), 2012.

[69] M. A. Kats, P. Genevet, R. Blanchard, and F. Capasso. Nanometre optical coatings based on strong interference effects in highly absorbing media. *Nat. Mater.*, 12:20–24, 2012.

[70] L.P. Wang, S. Basu, and Z.M. Zhang. Direct and indirect methods for calculating thermal emission from layered structures with nonuniform temperatures. *J. Heat Transfer*, 133, 2011.

Cette thèse est accessible à l'adresse : http://theses.insa-lyon.fr/publication/2016LYSEI103/these.pdf
© [E. Blandre], [2016], INSA Lyon, tous droits réservés

[71] S. Edalatpour and M. Francoeur. Size effect on the emissivity of thin films. *Journal of Quantitative Spectroscopy and Radiative Transfer*, 118(0):75 – 85, 2013.

[72] E. Palik. *Handbook of Optical Constants of Solids* 1^{rst} *edition*. Academic Press, 1987.

[73] P.O. Chapuis, S. Volz, C. Henkel, K. Joulain, and J.J. Greffet. Effects of spatial dispersion in near-field radiative heat transfer between two parallel metallic surfaces. *Phys. Rev. B*, 77:035431, Jan. 2008.

[74] A. Bid, A. Bora, and A. K. Raychaudhuri. Temperature dependence of the resistance of metallic nanowires of diameter ≥15 nm : Applicability of Bloch-Grüneisen theorem. *Phys. Rev. B*, 74(3):035426, Jul. 2006.

[75] J. DeSutter, M.P. Bernardi, and M. Francoeur. Determination of thermal emission spectra maximizing thermophotovoltaic performance using a genetic algorithm. *Energ. Convers. Manage.*, 108:429 – 438, 2016.

[76] F. Marquier, K. Joulain, J.P. Mulet, R. Carminati, and J.J. Greffet. Engineering infrared emission properties of silicon in the near field and the far field. *Opt. Commun.*, 237(4–6):379 – 388, 2004.

[77] R. Bauer, A. Schmid, P. Pavone, and D. Strauch. Electron-phonon coupling in the metallic elements Al, Au, Na, and Nb: A first-principles study. *Phys. Rev. B*, 57:11276–11282, May 1998.

[78] A G Mathewson and H P Myers. Optical absorption in aluminium and the effect of temperature. *J.Phys. F: Metal Physics*, 2(2):403, 1972.

[79] C.J. Fu and Z.M. Zhang. Nanoscale radiation heat transfer for silicon at different doping levels. *Int. J. Heat Mass Transfer*, 49(9–10):1703 – 1718, 2006.

[80] H. H. Li. Refractive index of silicon and germanium and its wavelength and temperature derivatives. *J. Phys. Chem. Ref. Data*, 9(3):561–658, 1980.

[81] M. Laroche, F. Marquier, R. Carminati, and J.-J. Greffet. Tailoring silicon radiative properties. *Opt. Commun.*, 250(4–6):316 – 320, 2005.

[82] S. Basu and Z M. Zhang. Ultrasmall penetration depth in nanoscale thermal radiation. *Appl. Phys. Lett.*, 95(13):–, 2009.

[83] M. Tschikin, S.-A. Biehs, P. Ben-Abdallah, S. Lang, A. Petrov, and M. Eich. Transport of radiative heat flux by hyperbolic metamaterials. *ArXiv e-prints*, 2014.

[84] S. Lang, M. Tschikin, S.-A. Biehs, A.-Y. Petrov, and M. Eich. Large penetration depth of near-field heat flux in hyperbolic media. *Appl. Phys. Lett.*, 104(12):121903, 2014.

[85] P. Ben-Abdallah, K. Joulain, J. Drevillon, and G. Domingues. Near-field heat transfer mediated by surface wave hybridization between two films. *J. Appl. Phys.*, 106(4):–, 2009.

Cette thèse est accessible à l'adresse : http://theses.insa-lyon.fr/publication/2016LYSEI103/these.pdf
© [E. Blandre], [2016], INSA Lyon, tous droits réservés

[86] M. Francoeur, M. P. Mengüç, and R. Vaillon. Near-field radiative heat transfer enhancement via surface phonon polaritons coupling in thin films. *Appl. Phys. Lett.*, 93(4):043109, 2008.

[87] S-A. Biehs. Thermal heat radiation, near-field energy density and near-field radiative heat transfer of coated materials. *The European Physical Journal B*, 58(4):423–431, 2007.

[88] A. Narayanaswamy and G. Chen. Thermal near-field radiative transfer between two spheres. *Phys. Rev. B*, 77:075125, 2008.

[89] K. Kim, B. Song, V. Fernandez-Hurtado, W. Lee, W. Jeong, L. Cui, D. Thompson, J. Feist, M.T. Homer Reid, F.J. Garcia-Vidal, J.C. Cuevas, E. Meyhofer, and P. Reddy. Radiative heat transfer in the extreme near field. *Nature*, 528:387–391, 2015.

[90] S. Shen, A. Narayanaswamy, and G. Chen. Surface phonon polaritons mediated energy transfer between nanoscale gaps. *Nano Lett.*, 9(8):2909–2913, 2009.

[91] E. Rousseau, A. Siria, G. Jourdan, S. Volz, F. Comin, J. Chevrier, and J-J. Greffet. Radiative heat transfer at the nanoscale. *Nature Photon.*, 2009.

[92] S. Shen, A. Mavrokefalos, P. Sambegoro, and G. Chen. Nanoscale thermal radiation between two gold surfaces. *Appl. Phys. Lett.*, 100(23):233114, 2012.

[93] B. Song, Y. Ganjeh, S. Sadat, D. Thompson, A. Fiorino, V. Fernandez-Hurtado, J. Feist, F.J. Garcia-Vidal, J.C. Cuevas, P. Reddy, and E. Meyhofer. Enhancement of near-field radiative heat transfer using polar dielectric thin films. *Nat. Nanotechnol.*, 2015.

[94] M. Lim, S. S. Lee, and B. J. Lee. Near-field thermal radiation between doped silicon plates at nanoscale gaps. *Phys. Rev. B*, 91:195136, May 2015.

[95] T. Ijiro and N. Yamada. Near-field radiative heat transfer between two parallel Sio_2 plates with and without microcavities. *Appl. Phys. Lett.*, 106(2), 2015.

[96] B. Song, D. Thompson, A. Fiorino, Y. Ganjeh, P. Reddy, and E. Meyhofer. Radiative heat conductances between dielectric and metallic parallel plates with nanoscale gaps. *Nature Nanotech.*, 11:509 – 514, 2016.

[97] R. St-Gelais, L. Zhu, S. Fan, and M. Lipson. Near-field radiative heat transfer between parallel structures in the deep subwavelength regime. *Nature Nanotech.*, 11:515–519, 2016.

[98] B. V. Derjaguin, I. I. Abrikosova, and E. M. Lifshitz. Direct measurement of molecular attraction between solids separated by a narrow gap. *Q. Rev. Chem. Soc.*, 10:295–329, 1956.

[99] A. C. Jones and M. B. Raschke. Thermal infrared near-field spectroscopy. *Nano Lett.*, 12(3):1475–1481, 2012.

[100] A. Babuty, K. Joulain, P.O. Chapuis, J.J. Greffet, and Y. De Wilde. Blackbody spectrum revisited in the near field. *Phys. Rev. Lett.*, 110:146103, Apr 2013.

Cette thèse est accessible à l'adresse : http://theses.insa-lyon.fr/publication/2016LYSEI103/these.pdf
© [E. Blandre], [2016], INSA Lyon, tous droits réservés

[101] B. T. O'Callahan, W. E. Lewis, A. C. Jones, and M. B. Raschke. Spectral frustration and spatial coherence in thermal near-field spectroscopy. *Phys. Rev. B*, 89:245446, Jun 2014.

[102] E. Rousseau, M. Laroche, and J-J. Greffet. Asymptotic expressions describing radiative heat transfer between polar materials from the far-field regime to the nanoscale regime. *J. Appl. Phys.*, 111(1):–, 2012.

[103] D. Sarid. Long-range surface-plasma waves on very thin metal films. *Phys. Rev. Lett.*, 47:1927–1930, Dec 1981.

[104] E. N. Economou. Surface plasmons in thin films. *Phys. Rev.*, 182:539–554, Jun 1969.

[105] Y. Tsurimaki, P.O. Chapuis, R. Vaillon, J. Okajima, A. Komiya, and S. Murayama. Reducing thermal radiation between parallel plates in the far-to-near field transition regime. In *Proceedings of the 15th International Heat Transfer Conference, Kyoto, Japan*, Aug. 10-15, 2014.

[106] J. Mayo and A. Narayanaswamy. Minimum radiative transfer between two metallic planar surfaces. In *Proceedings of the 11th AIAA/ASME Joint Thermophysics and Heat Transfer Conference, Atlanta, USA*, June 16-20, 2014.

[107] R. S. DiMatteo, P. Greiff, S. L. Finberg, K. A. Young-Waithe, H. K. H. Choy, M. M. Masaki, and C. G. Fonstad. Micron-gap thermophotovoltaics (mtpv). *AIP Conference Proceedings*, 653(1):232–240, 2003.

[108] R.S. DiMatteo, P. Greiff, D. Seltzer, D. Meulenberg, E. Brown, E. Carlen, K. Kaiser, S. Finberg, H. Nguyen, J. Azarkevich, P. Baldasaro, J. Beausang, L. Danielson, M. Dashiell, D. DePoy, H. Ehsani, W. Topper, K. Rahner, and R. Siergiej. Micron-gap thermophotovoltaics (mtpv). *AIP Conference Proceedings*, 738(1):42–51, 2004.

[109] A. Narayanaswamy and G. Chen. Surface modes for near field thermophotovoltaics. *Appl. Phys. Lett.*, 82(20):3544–3546, 2003.

[110] M. Laroche, R. Carminati, and J.-J. Greffet. Near-field thermophotovoltaic energy conversion. *J. Appl. Phys.*, 100(6), 2006.

[111] O. Ilic, M. Jablan, J.D. Joannopoulos, I. Celanovic, and M. Soljačić. Overcoming the black body limit in plasmonic and graphene near-field thermophotovoltaic systems. *Opt. Express*, 20(S3):A366–A384, 2012.

[112] R. Messina and P. Ben-Abdallah. Graphene-based photovoltaic cells for near-field thermal energy conversion. *Sci. Rep.*, 3(1383), 2012.

[113] V. B. Svetovoy and G. Palasantzas. Graphene-on-silicon near-field thermophotovoltaic cell. *Phys. Rev. Applied*, 2:034006, 2014.

[114] S. Jin, M. Lim, S.S. Lee, and B.J. Lee. Hyperbolic metamaterial-based near-field thermophotovoltaic system for hundreds of nanometer vacuum gap. *Opt. Express*, 24(6):A635–A649, 2016.

Cette thèse est accessible à l'adresse : http://theses.insa-lyon.fr/publication/2016LYSEI103/these.pdf
© [E. Blandre], [2016], INSA Lyon, tous droits réservés

[115] M. Elzouka and S. Ndao. Towards a near-field concentrated solar thermophotovoltaic microsystem: Part i – modeling. *Solar Energy*, 2015.

[116] S.V. Patankar. *Numerical Heat Transfer and Fluid Flow*. CRC Press, 1980.

[117] H.K. Gummel. A self-consistent iterative scheme for one-dimensional steady state transistor calculations. *IEEE T. Electron Dev.*, 11(10):455–465, Oct 1964.

[118] J.W. Slotboom and N.V. Philips. Computer-aided two-dimensional analysis of bipolar transistors. *IEEE. T. Electron. Dev.*, 20(8):669–679, 1973.

[119] K. Chen, P. Santhanam, S. Sandhu, L. Zhu, and S. Fan. Heat-flux control and solid-state cooling by regulating chemical potential of photons in near-field electromagnetic heat transfer. *Phys. Rev. B*, 91:134301, Apr 2015.

[120] J.W. Slotboom and H.C. de Graaff. Bandgap narrowing in silicon bipolar transistors. *IEEE. T. Electron. Dev.*, 24(8):1123 – 1125, 1977.

[121] P.A. Basore. Numerical modeling of textured silicon solar cells using pc-1d. *IEEE. T. Electron. Dev.*, 37(2):337 – 343, 1990.

[122] S. Adachi. Optical dispersion relations for GaP, GaAs, GaSb, InP, InAs, InSb, AlGaAs, and InGaAs. *J. Appl. Phys*, 66(12):6030–6040, 1989.

[123] M. Patrini, G. Guizzetti, M. Galli, R. Ferrini, A. Bosacchi, S. Franchi, and R. Magnanini. Optical functions of bulk and epitaxial gasb from 0.0025 to 6 eV. *Solid State Commun.*, 101(2):93 – 98, 1997.

[124] S. Adachi. *Optical Properties of Crystalline and Amorphous Semiconductors*. Springer, 1999.

[125] Y.P. Varshni. Temperature dependence of the energy gap in semiconductors. *Physica*, 34(1):149 – 154, 1967.

[126] J.A. Gonzalez-Cuevas, T.F. Refaat, M.N. Abedin, and H.E. Elsayed-Ali. Calculations of the temperature and alloy composition effects on the optical properties of AlGaAsSb and GaInAsSb in the spectral range 0.5-6 ev. *J. Appl. Phys*, 102(1), 2007.

[127] D. Martín and C. Algora. Temperature-dependent GaSb material parameters for reliable thermophotovoltaic cell modelling. *Semicond. Sci. Technol.*, 19(8):1040, 2004.

[128] G. Stollwerck, O.V. Sulima, and A.W. Bett. Characterization and simulation of GaSb device-related properties. *IEEE. T. Electron. Dev.*, 47(2):448 – 457, 2000.

Cette thèse est accessible à l'adresse : http://theses.insa-lyon.fr/publication/2016LYSEI103/these.pdf
© [E. Blandre], [2016], INSA Lyon, tous droits réservés

Cette thèse est accessible à l'adresse : http://theses.insa-lyon.fr/publication/2016LYSEI103/these.pdf
© [E. Blandre], [2016], INSA Lyon, tous droits réservés